Studies of Electroweak Interactions and Searches for New Physics Using Photonic Events with Missing Energy at the Large Electron-Positron Collider

Thesis by

Marat I. Gataullin

In Partial Fulfillment of the Requirements

for the Degree of

Doctor of Philosophy

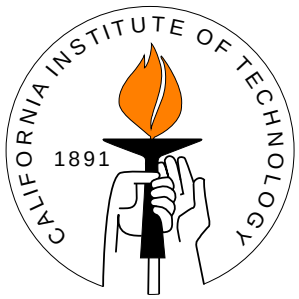

California Institute of Technology

Pasadena, California

2006

(Defended November 22, 2005)

Acknowledgments

First and foremost, I would like to thank my advisor, Professor Harvey B. Newman. Thank you, Harvey, for your guidance and support throughout my graduate career and for carefully reading my thesis, in spite of your extremely busy schedule.

I am profoundly grateful to Dr. Salvatore Mele for the time he invested in my single-photon paper and for his contributions to the analysis I am presenting here. I would also like to thank members of my paper committee, Drs. Jean-Jacques Blaising and Wes Metzger, for their valuable suggestions and advice.

This thesis would not have been complete without the contributions of many past and present L3 collaboration members. I would especially like to thank Drs. Sergey Shevchenko and Alex Shvorob for getting me started in L3 and for all the interesting conversations we had. I am deeply indebted to Dr. Alvise Favara for helping me develop my single-photon analysis and RFQ calibration algorithm. I am also very grateful to my companions in the RFQ calibration project: Dr. Renyuan Zhu at Caltech and Drs. Chris Tully, Utsawa Chaturvedi, and Lei Xia at CERN. In addition, I benefited a great deal from working with Drs. Juan Alcaraz, Stefan Ask, Michel Chemarin, Jean Fay, Dominique Duchesneau, Martin Gruenewald, Andre Holzner, John Langford, Vladimir Litvin, Luca Malgeri, Marco Musy, Sylvie Rosier, Daniel Ruschmeier, Stefano Villa, Alfons Weber, and Stephan Wynhoff.

I wish to thank Drs. Simon Blyth, Abdel Boucham, David Kirkby, and Gerhard Raven for providing me with their results and plots, and Dr. Zbigniew Was for answering my numerous questions on his Monte Carlo program. In preparing this thesis, I greatly benefited from the constructive criticisms of Mr. Tony Lee and Dr. Stephen Pappas. I also thank Professor Alan Weinstein for his comments and suggestions.

Teaching has become an important part of my life at Caltech. I am extremely grateful to Professor Frank Porter for providing me with this opportunity. I am

also grateful to Dr. Virginio de Oliveira Sannibale for showing me the ropes in the freshman lab. Finally, I would like to thank Ms. Virginia Licon and Ms. Donna Driscoll for taking care of all practical and administrative problems.

I dearly thank all of my friends from Russia, Caltech, and CERN. In particular, I thank Meiske and her family for making my stay in Pasadena an unforgettable experience. I am also grateful to Dr. N.Ya. Medvedev who took a genuine interest in my progress.

Last but certainly not least, I thank my mother. This thesis is dedicated to her.

Abstract

In this thesis I study the production of photonic events with missing energy in e^+e^- collisions at the Large Electron-Positron (LEP) Collider. My analysis was based on 619 pb^{-1} of data collected by the L3 detector between 1998 and 2000 at center-of-mass energies $\sqrt{s} = 189 - 208$ GeV, the highest energies ever attained in an e^+e^- collider.

I selected a high-purity sample of 2,022 well-reconstructed single- and multi-photon events with missing energy. I analyzed this sample to measure the cross section of the process $e^+e^- \to \nu\bar{\nu}\gamma(\gamma)$. The average ratio of the measured to expected cross section was found to be

$$\left\langle \frac{\sigma^{meas}_{\nu\bar{\nu}\gamma}}{\sigma^{exp}_{\nu\bar{\nu}\gamma}} \right\rangle = 0.987 \pm 0.022\,(stat) \pm 0.010\,(syst) \pm 0.010\,(theory)\,.$$

The number of light neutrino species was extracted:

$$N_\nu = 2.98 \pm 0.05\,(stat) \pm 0.04\,(syst)\,,$$

and the first direct evidence for the reaction $e^+e^- \to \nu_e\bar{\nu}_e\gamma$ was found. The experimental errors in these results are smaller than those of comparable previous measurements. My selection results are also given in the form of tables, which can be used to test any future models involving photonic signatures at LEP.

These measurements take advantage of the unique photon detection capability of the L3 Experiment. The performance and operation of the L3 electromagnetic calorimeter is discussed in detail, with an emphasis on its calibration and monitoring. In particular, I describe a novel calibration system based on a Radiofrequency Quadrupole accelerator, which allowed me to achieve a calibration precision of 0.5%.

Reactions of the type $e^+e^- \to \gamma(\gamma) + \textit{invisible particles}$ are predicted by a broad range of theories beyond the Standard Model, including Supersymmetry and models

with extra spatial dimensions and anomalous gauge-boson couplings. I found no evidence for such models and derived limits on the corresponding signal cross sections and model parameters. Among others, lower limits between 1.6 TeV and 0.66 TeV were set at the 95% confidence level on the new scale of gravity for the number of extra dimensions between 2 and 6.

Contents

List of Tables

List of Figures

Chapter 1

Introduction and Overview

The Large Electron-Positron (LEP) Collider was the highest-energy e^+e^- collider ever built. From 1989 to 2000, it collided electrons and positrons at center-of-mass energies between 89 GeV and 208 GeV. Data collected by the four LEP detectors allow us to test the Standard Model theory of particle interactions with previously unattainable precision.

In this thesis I study the production of photonic events with missing energy at LEP. My motivation for this study is twofold:

(1) to measure the pair-production of neutrinos in e^+e^- collisions

(2) to search for evidence of physics beyond the Standard Model.

The LEP detectors were effectively transparent to neutrinos since these elementary particles interact with ordinary matter only through the weak force. As a consequence, the neutrino-pair production process could only be studied using events from the reaction $e^+e^- \to \nu\bar{\nu}\gamma(\gamma)$. In this reaction the neutrinos are produced via an exchange of the heavy W and Z bosons (the carriers of the weak force), while the photons are radiated predominantly by the incoming electrons and positrons. The corresponding photonic events necessarily appear to be unbalanced since a sizable fraction of energy is carried away by the undetected neutrinos. I select such events to measure the differential $e^+e^- \to \nu\bar{\nu}\gamma(\gamma)$ cross sections, which in turn allows me to perform a precise measurement of the number of light neutrino species and to study the triple and quartic couplings between the photon and the heavy gauge bosons.

My analysis was based on 619 pb^{-1} of data collected by the L3 detector between 1998 and 2000 at center-of-mass energies $\sqrt{s} = 189 - 208$ GeV, which corresponded to

the highest energy and luminosity LEP runs. Approximately 2,000 photonic events with missing energy found in these data were used in my measurements. It should be noted that the BGO electromagnetic calorimeter of L3 stood prominently as the most accurate photon detector at LEP. Calibrated with a Radiofrequency Quadrupole (RFQ) accelerator, it provided an energy resolution of approximately 1% for photons and electrons with energies above 10 GeV. This made the L3 experiment the ideal place at LEP to study photonic event signatures.[1]

In the second part of my analysis, I use the selected sample of photonic events to search for manifestations of physics beyond the Standard Model. The Standard Model has been extremely successful in describing virtually all phenomena observed in high-energy particle collisions. Nevertheless, it also contains a number of conceptual problems which can be solved only by introducing some *new physics*.

Two of the most promising extensions of the Standard Model, Supersymmetry and models with large extra dimensions, are considered in this thesis. In e^+e^- collisions, these new particle interactions could manifest themselves through an enhanced production of single- or multi-photon events with missing energy in the reactions $e^+e^- \to X\gamma$ and $e^+e^- \to X\gamma\gamma$, respectively. Here, X represents one or more new neutral invisible particles. Different analysis techniques are used depending on the specific reaction in question. In particular, I use the high performance triggers and veto detectors of L3 to select single-photon events with energies as low as 1 GeV, which significantly increases the sensitivity of my searches for signs of extra dimensions.[2]

I have organized this thesis in three parts. In the first part (Chapters 2-3 and Appendix A), I give an overview of the theoretical context of my work. In the second part (Chapters 4-5 and Appendices B and C), I describe the experimental apparatus that I use in my study. Finally, the last part (Chapters 6-8 and Appendices D and E) covers my selection of the photonic events with missing energy as well as the measurements and searches that I perform using this event sample.

[1] The BGO resolution was at least three times as good as the resolutions of the other electromagnetic calorimeters at LEP.

[2] The other LEP experiments have not been able to develop an effective selection for photons with energies below 6 GeV.

Following is a brief outline of each chapter.

Chapter 2 begins with an overview of the Standard Model and its status with an emphasis on the electroweak interactions that are relevant to this thesis. The rest of this chapter and Appendix A are devoted to the theoretical description of the reaction $e^+e^- \to \nu\bar{\nu}\gamma(\gamma)$. In Chapter 3, I briefly describe Supersymmetry and models with large extra dimensions, concentrating on the mechanisms which could lead to an anomalous production of photonic events with missing energy.

Chapter 4 covers the LEP accelerator and the L3 detector in general. In Chapter 5 and Appendices B and C, I describe the calibration and monitoring of the BGO electromagnetic calorimeter. In particular, the RFQ calibration technique is discussed in detail. From 1997 through 2000, I coordinated the RFQ calibration runs, analyzed the RFQ data, and produced the BGO calibration constants that were used in the L3 data reconstruction. I was able to improve the RFQ calibration algorithm, which resulted in a BGO energy resolution of about 1%, the best resolution obtained since the BGO barrel was calibrated in the test beams in 1987-88.[3] The significant increase in the calibration quality and elimination of the resolution tails was crucial for my analysis of single- and multi-photon production at LEP.

In Chapter 6 I discuss the methods that I have used to select my samples of photonic events with missing energy. As part of this work, I have performed original studies of detector hermeticity, trigger efficiency, photon conversion, and cosmic contamination. These studies significantly improved the quality of my selection and reduced the systematic errors. Selection results are further detailed in Appendix D. In Chapter 7 I describe my measurements of the $e^+e^- \to \nu\bar{\nu}\gamma(\gamma)$ cross sections and my work on searches for manifestations of physics beyond the Standard Model. Combinations of my results with those of the other LEP experiments are described in Appendix E. Finally, Chapter 8 summarizes the main results of this thesis and compares them with results from other high-energy physics experiments.

[3]For comparison, calibrations used from 1989 to 1996 provided a resolution of about 2% with significant resolution tails.

Chapter 2

Standard Model and Neutrino Production at LEP

This chapter begins with an overview of the Standard Model of electroweak interactions, concentrating on the areas relevant to the analyses in this thesis. I then describe the production of the single- and multi-photon events with missing energy in e^+e^- collisions via initial-state radiation in the neutrino pair-production process. In Chapter 3, I will also discuss several new physics models whose manifestations can be found using this event signature at the LEP e^+e^- collider.

2.1 The Standard Model

2.1.1 Introduction

The goal of particle physics is to describe the elementary constituents of matter and the interactions among them. This field of physics entered its modern phase at the end of the nineteenth century following a number of fundamental discoveries, including the discovery of the electron, the first particle still considered elementary today, by J.J. Thomson in 1897 [1].

Over the next 70 years our understanding of the particle world advanced by leaps and bounds, culminating in the development of the Standard Model of particle physics. The electroweak theory, developed by S. L. Glashow, A. Salam, and S. Weinberg from 1961 to 1968 provides a unified description of electromagnetic and weak interactions [2]. The problem of mass generation in the gauge theories was illuminated by P.W. Higgs in 1964 [3]. The theory of quantum chromodynamics

Fermions						
Family	Lepton	Electric charge	Mass (MeV)	Quark	Electric charge	Mass (GeV)
1.	ν_e	0	$< 3 \cdot 10^{-6}$	u	2/3	$(1.5 - 4) \times 10^{-3}$
	e	–1	0.511	d	–1/3	$(4 - 8) \times 10^{-3}$
2.	ν_μ	0	< 0.19	c	2/3	1.15 – 1.35
	μ	–1	105.7	s	–1/3	0.08 – 0.13
3.	ν_τ	0	< 18.2	t	2/3	174.3 ± 5.1
	τ	–1	1777	b	–1/3	4.1 – 4.4

Gauge bosons				
Interaction	Symbol	Electric charge	Spin	Mass (GeV)
Electromagnetic	γ	0	1	0
Weak	W	$\pm$ 1	1	80.43 ± 0.04
	Z	0	1	91.188 ± 0.002
Strong	g	0	1	0
Gravity	G	0	2	0

Table 2.1: Fundamental constituents of the Standard Model. Particle masses or mass limits are taken from [6]. Graviton, believed to be the carrier of gravity, is also listed.

describing the strong interaction was introduced in 1973 by H. Fritzsch, M. Gell-Mann, H. Leytwyler, D.J. Gross, and F. Wilczek [4]. The proof of renormalizability of the Standard Model was given by G. 't Hooft in 1971 [5]. These theoretical developments comprise the foundations of the Standard Model as a non-Abelian gauge theory based on the symmetry group $SU(3)_C \times SU(2)_L \times U(1)_Y$, where the $SU(3)_C$ group corresponds to the strong interactions of quantum chromodynamics (QCD) and the $SU(2)_L \times U(1)_Y$ groups correspond to the electroweak interactions.

The fundamental particles of Standard Model are divided into fermions and bosons. The fermions are spin 1/2 particles constituting the matter fields. Every fermion has a matching anti-particle with identical mass and opposite quantum numbers. The

fermions can be subdivided into two groups, those that can interact via the strong force, and those that cannot. The first group is called the quarks and the second the leptons. Both groups contain six particles that can be separated into 3 generations (families), each consisting of two leptons or two quarks. The primary leptons of the three generations are electron, muon, and tau; each has an associated neutrino. The quarks are up, down, charm, strange, top, and bottom. Table 2.1 contains a list of the fermions and their masses. It should be noted that the Standard Model contains no explanation for these 3 generations nor the different masses of the fermions.

The bosons are integral spin particles which mediate the interactions between the fermions. The boson sector of the Standard Model includes the photon, the W and Z bosons, the Higgs, and the gluons (see Table 2.1). The photon mediates the electromagnetic force, the W and Z mediate the weak force, and the gluons mediate the strong force. Gravity is not included in the Standard Model, but it is believed to be mediated by spin-2 graviton. The photons and gluons are presumed to be massless, while the W, Z, and Higgs bosons are massive. The mechanism by which the W and Z bosons acquire masses will be discussed in the next section.

The Standard Model theory has so far stood up to all tests that have been applied to it using particle collisions at the highest possible energies reachable today, as well as precision measurements at lower energies. The intermediate heavy vector bosons, W and Z, were discovered in 1983 and 1984 by the CERN SPS experiments UA1 and UA2, with masses in agreement with the expectations of the Standard Model. The third family of fermions has been completed in 1994 and 2000 with the discovery of the top quark and the tau neutrino by the CDF, DØ [7], and DONuT [8] experiments at Fermilab. Figure 2.1 illustrates the success of the Standard Model in describing various fermion and boson production processes in e^+e^- collisions at LEP. It is, however, widely believed that the Standard Model is not a complete theory and is only a low-energy approximation of a more comprehensive theory which should also incorporate gravity. The status of the Standard Model is discussed in more detail in Section 2.1.3.

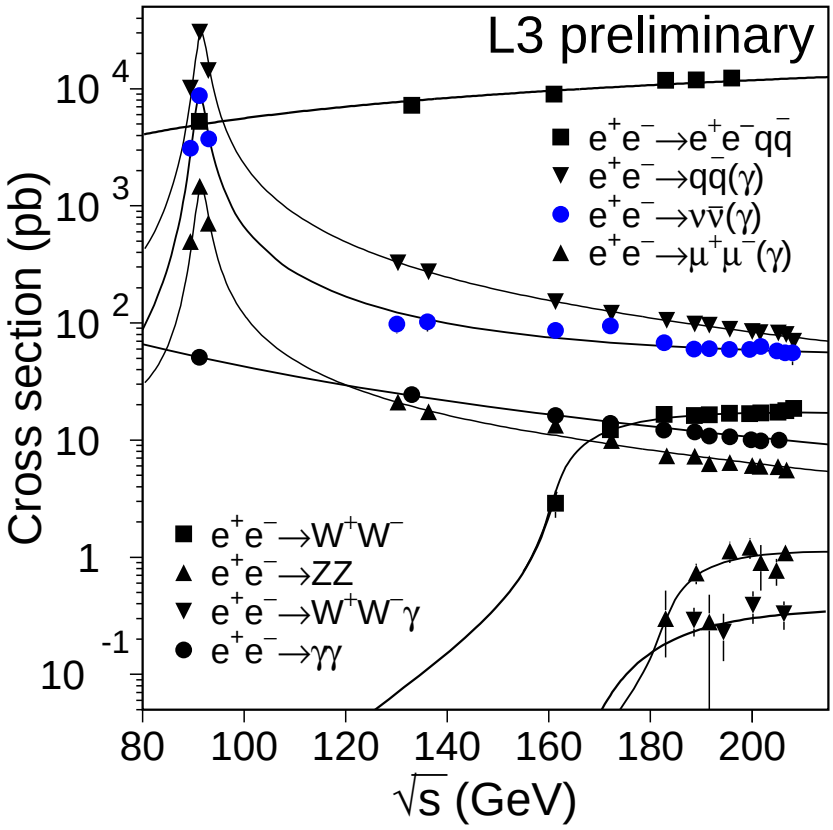

Figure 2.1: Standard Model at LEP: the curves show the Standard Model predictions for the cross-sections of various production processes expected to be observed in e^+e^- collisions at center-of-mass energies ($\sqrt{s}$) ranging from 89 GeV to 208 GeV, while the dots represent the actual measurements performed with the L3 detector at LEP [9].

2.1.2 Electroweak Interactions

This thesis concentrates on the electroweak sector of the Standard Model [2], whose Lagrangian can be written as a sum of four terms:

$$\mathcal{L} = \mathcal{L}_{\text{Fermion}} + \mathcal{L}_{\text{Yang-Mills}} + \mathcal{L}_{\text{Higgs}} + \mathcal{L}_{\text{Yukawa}} \,. \tag{2.1}$$

The Fermion Lagrangian describes the dynamics of the fermions, i.e., their kinetic energy and interactions with the gauge bosons. The Yang-Mills Lagrangian contains the kinetic-energy and self-interaction terms of the gauge fields. The Higgs and Yukawa Lagrangians generate the masses of the gauge bosons and fermions, respectively.

Massless Yang-Mills Theory

The construction of the Standard Model electroweak theory starts with an introduction of a gauge-covariant derivative $\mathcal{D}_\mu$ to ensure the gauge invariance of the Lagrangian:

$$\mathcal{D}_\mu = \partial_\mu + i\, g'^2\, \frac{1}{2}\, B_\mu \cdot Y + i\, g\, \vec{W}_\mu \cdot \vec{T}\,, \tag{2.2}$$

where Y and B are the hypercharge and the corresponding gauge field of the $U(1)_Y$ group, $\vec{T}$ denotes the generators of $SU(2)_L$ group (commonly represented by Pauli matrices), the vector-boson triplet $\vec{W}$ is the $SU(2)_L$ gauge field, and g' and g are the $U(1)_Y$ and $SU(2)_L$ couplings, respectively.

The underlying symmetry is spontaneously broken by introducing a complex Higgs doublet (see the next section), and the physical gauge bosons are obtained through mixing of the neutral B and W^3 gauge fields:

$$\begin{aligned} A &= \sin\theta_{\rm W}\, W^3 + \cos\theta_{\rm W}\, B\,, \\ Z &= \cos\theta_{\rm W}\, W^3 - \sin\theta_{\rm W}\, B\,, \end{aligned} \tag{2.3}$$

where A represents the photon, the carrier of the electromagnetic force, and the Z boson carries the neutral weak current; the weak mixing angle is defined as $\cos\theta_W = g/\sqrt{g'^2 + g^2}$. The charged weak interactions are mediated by the W^+ and W^- bosons, which are defined as

$$W^\pm \;=\; \frac{1}{\sqrt{2}}\left(W^1 \mp i W^2\right). \tag{2.4}$$

Although the physical vacuum does not have the $SU(2)_L \times U(1)_Y$ symmetry, it does have a manifest $U(1)$ symmetry corresponding to a linear combination of generators:

$$Q = T_3 + \frac{Y}{2}\,, \tag{2.5}$$

where Q is the electromagnetic charge, Y is the hypercharge, and T_3 is the weak isospin. The fermions are then placed into left-handed iso-doublets and right-handed iso-singlets characterized by the quantum numbers T_3 and Y (see Table 2.2), where the left-handed and right-handed parts of a generic fermion field ψ are given by $\psi_{L,R} = 1/2(1 \mp \gamma^5)\psi$.

Families			T_3	Y	Q
$\begin{pmatrix} \nu_e \\ e \end{pmatrix}_L$	$\begin{pmatrix} \nu_\mu \\ \mu \end{pmatrix}_L$	$\begin{pmatrix} \nu_\tau \\ \tau \end{pmatrix}_L$	$1/2$	-1	0
			$-1/2$	-1	-1
ν_{eR}	$\nu_{\mu R}$	$\nu_{\tau R}$	0	0	0
e_R	μ_R	τ_R	0	-2	-1
$\begin{pmatrix} u \\ d \end{pmatrix}_L$	$\begin{pmatrix} c \\ s \end{pmatrix}_L$	$\begin{pmatrix} t \\ b \end{pmatrix}_L$	$1/2$	$1/3$	$2/3$
			$-1/2$	$1/3$	$-1/3$
u_R	c_R	t_R	0	$4/3$	$2/3$
d_R	s_R	b_R	0	$-2/3$	$-1/3$

Table 2.2: Fermion quantum numbers. The inclusion of right-handed neutrinos is speculative; they are not part of the Standard Model.

With these postulated representation assignments, the fermion Lagrangian can be written as

$$\mathcal{L}_{\text{Fermion}} = \sum_\psi \overline{\psi}\, i\gamma^\mu \partial_\mu\, \psi + J^\mu_{em}\, A_\mu + J^\mu_{NC}\, Z_\mu + J^{\pm\mu}_{CC}\, W^\pm_\mu\,, \tag{2.6}$$

where the fermionic currents that couple to the gauge-boson fields A, Z, and W are:

$$J^\mu_{em} = \sum_\psi Q_\psi\, \overline{\psi}\, \gamma^\mu \partial_\mu\, \psi\,, \tag{2.7}$$

$$J^\mu_{NC} = \frac{g}{2\cos\theta_{\text{W}}} \sum_\psi \overline{\psi}\, \gamma^\mu (g_V - g_A\gamma_5)\, \psi\,, \tag{2.8}$$

$$J^{\pm\mu}_{CC} = \frac{g}{\sqrt{2}} \sum_\psi \overline{\psi}_L\, \gamma^\mu T^\pm \psi_L\,, \tag{2.9}$$

respectively, and the sums of ψ run though all lepton and quark flavors. The familiar coupling constant of the electromagnetic interaction e is given by $e = g\sin\theta_{\text{W}}$, while the vector and axial-vector parts of the neutral weak current have the couplings $g_V = T_3 - 2\,Q\sin^2\theta_{\text{W}}$ and $g_A = T_3$. It is interesting to note that the weak force does not conserve parity — the W boson interacts only with the left-handed particles (or right-handed antiparticles).

The Yang-Mills Lagrangian can then be written in terms of the field strength

tensors as

$$\mathcal{L}_{\text{Yang-Mills}} = -\frac{1}{4}B^{\mu\nu}B_{\mu\nu} - \frac{1}{4}W_i^{\mu\nu}W^i_{\mu\nu}\,, \tag{2.10}$$

predicting triple and quartic boson couplings. The couplings between the neutral bosons are forbidden and the only allowed triple and quartic boson vertices require at least two charged bosons.

The Higgs Mechanism

The Higgs boson is a spin-0 particle which breaks the $SU(2)_L \times U(1)_Y$ symmetry of the Standard Model by acquiring a vacuum expectation value. The Higgs field is chosen to be a complex doublet, which is the simplest possible non-trivial representation of $SU(2) \times U(1)$, and the Higgs Lagrangian has the form:

$$\mathcal{L}_{\text{Higgs}} = (\mathcal{D}^\mu\Phi)^\dagger(\mathcal{D}_\mu\Phi) - V(\Phi^\dagger\Phi)\,, \tag{2.11}$$

where the potential function V is the $SU(2)_L$ invariant potential of the Higgs field:

$$V(\Phi^\dagger\Phi) = \mu^2\Phi^\dagger\Phi + \lambda(\Phi^\dagger\Phi)^2. \tag{2.12}$$

The potential must increase with $(\Phi^\dagger\Phi)$, hence $\lambda > 0$, while the mass parameter μ^2 can still be negative. In this case the potential has a non-trivial minimum value V_{min} for

$$\Phi^\dagger\Phi = -\frac{\mu^2}{2\lambda} \equiv \frac{v^2}{2} > 0\,, \tag{2.13}$$

where $v/\sqrt{2}$ is the vacuum expectation value of the Higgs field. The $SU(2)_L$ symmetry of the Higgs potential leads to a whole family of Higgs ground states. After choosing a specific one as the vacuum ground state, a gauge rotation allows us to write its expansion as

$$\Phi(x) = \frac{1}{\sqrt{2}}\begin{pmatrix} 0 \\ v + H(x) \end{pmatrix}, \tag{2.14}$$

leaving only one physical Higgs boson $H(x)$. This vacuum expectation breaks the $SU(2) \times U(1)$ symmetry and results in a Lagrangian describing not only a massive Higgs boson but also massive vector fields W and Z:

$$\mathcal{L}_{\text{Higgs}} = \frac{1}{2}\Big[\frac{(g'^2+g^2)\,v^2}{4} Z_\mu Z^\mu + \frac{g^2 v^2}{4}(W_\mu^+ W^{-\mu} + W_\mu^- W^{+\mu}) + (2\mu^2 H^2)\Big] + ... \quad (2.15)$$

It should be noted that the photon field A remains massless. The boson masses are then given by

$$\begin{aligned} M_Z &= \frac{\sqrt{g'^2+g^2}\,v}{2}\,, \\ M_W &= \frac{gv}{2}\,, \\ M_\gamma &= 0\,, \\ M_H &= \sqrt{2}\mu\,. \end{aligned} \quad (2.16)$$

Mass terms for the fermions are introduced via Yukawa couplings of the fermion fields to the doublet Higgs field, and the Yukawa Lagrangian can written as

$$\mathcal{L}_{\text{Yukawa}} = -\frac{v+H}{\sqrt{2}} g_f \bar{f} f\,, \quad (2.17)$$

which immediately gives the fermion masses as $m_f = v g_f/\sqrt{2}$. The remaining Lagrangian terms proportional to H describe the fermion-Higgs interactions with a coupling strength m_f/v. The fermion masses differ by several orders of magnitude (see Table 2.1) and the Standard Model contains no explanation for this effect.

2.1.3 Status of the Standard Model

The Standard Model has had tremendous success in describing the considerable amount of data from all high-energy collider experiments. The LEP Electroweak Working Group combines the most important measurements from the LEP, Tevatron and SLD experiments in a single fit to the Standard Model [10]. Figure 2.2 shows the pull distribution for 18 measurements used in this fit, including the direct measurements of the top quark mass and the masses and widths of the W and Z bosons. For

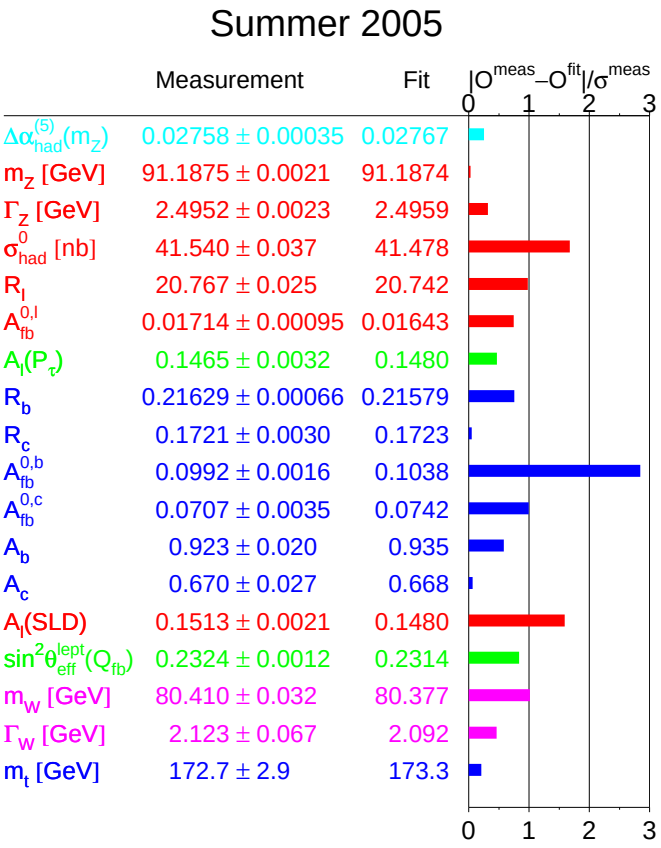

Figure 2.2: Precision electroweak measurements and their pulls, derived from the global fit to the Standard Model (as of Summer 2005).

a given parameter, the pull is defined as the difference between the measured value of this parameter and the best-fit divided by the measurement error (standard deviation). A very good agreement between the fitted and measured parameter values is observed.

The precision measurements of the electroweak parameters depend logarithmically on the Higgs boson mass through radiative corrections. Therefore, the global fit can be used to constrain the Higgs mass in the Standard Model. Figure 2.3 shows the $\Delta\chi^2$ of the fit, which gives the preferred value of the Higgs mass as

$$M_H = 91^{+45}_{-32}\ \text{GeV}, \tag{2.18}$$

which in turn can be translated into an upper limit of $M_H < 186$ GeV at the 95% con-

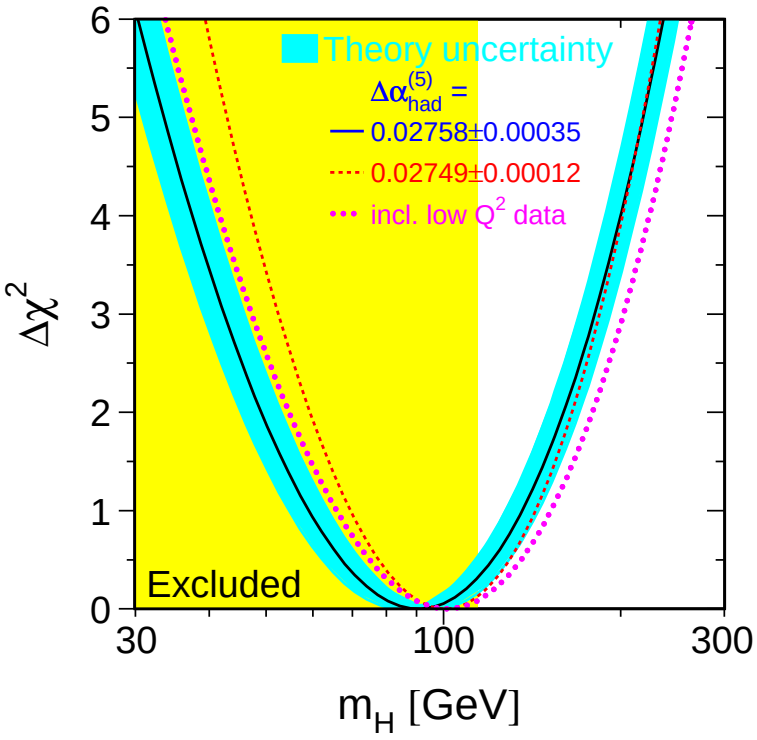

Figure 2.3: $\Delta\chi^2$ of the global fit to the precision electroweak data as a function of the Higgs boson mass (as of Summer 2005). The shaded region on the left corresponds to the limit on the Higgs mass from the direct searches at LEP2.

fidence level [10]. It should be noted that direct searches for Higgs production at LEP lead to the conclusion that the Standard-Model Higgs should be heavier than 114.4 GeV (95% confidence level) [11]. The Higgs discovery is the main goal of the upcoming Large Hadron Collider (LHC) physics program, and the above limits indicate that the Standard Model Higgs is well within the reach of the LHC.

Despite its apparent success, the Standard Model raises many unanswered questions, e.g., it does not explain the large differences in particle masses, why there are three fermion generations, what is the source of CP violation, or how to solve the hierarchy problem of the Higgs mass.

Eventually one would also like to include gravity in a unified theory along with other particle interactions. This brings up another question: why the Planck scale ($M_{\rm Pl} \sim 10^{19}$ GeV) is so much bigger than the electroweak scale ($M_{\rm EW} \sim 10^2$ GeV).

These and other inherent problems of the Standard Model cannot be solved without the introduction of some *new physics* [12]. Two of the most popular extensions of the Standard Model, supersymmetry and models with large extra dimensions, are discussed in the next chapter.

Recently the first clear sign of physics beyond the Standard Model has been found in the form of neutrino oscillations. Experiments using neutrinos generated by cosmic-ray interactions in the atmosphere, by nuclear fusion in the Sun, and by nuclear fission in reactors have established neutrino-flavor oscillations: $\nu_\mu \to \nu_\tau$ and $\nu_e \to \nu_\mu/\nu_\tau$ [13]. As a consequence, the neutrinos should have non-zero masses, which violates one of the Standard Model assumptions. Combining the neutrino oscillation data with direct limits on the neutrino masses (see Table 2.1) yields masses in the sub-eV range [14]. This should not have any noticeable impact on the physics results in this thesis where the neutrinos are assumed to be massless, as expected in the Standard Model.

2.2 Neutrino Production at LEP

Neutrino pair-production accompanied by one or more photons is the only irreducible background for new physics processes involving photons and missing energy in the final state. On the other hand, a study of this process is interesting in itself since it allows one to verify the predictions of the Standard Model and determine the number of light neutrino species. A deviation from the Standard Model value of $N_\nu = 3$ would constitute a clear indication of new physics, e.g., it would suggest the existence of a new fermion generation.

In the Standard Model reaction $e^+e^- \to \nu\bar{\nu}\gamma(\gamma)$, the photons are radiated mainly from the incoming electrons and positrons, a process called *initial-state radiation* (ISR or *bremsstrahlung*).[1] Therefore a precise measurement of this process provides a unique opportunity to test and improve the present understanding of the ISR and other higher-order QED effects in the fermion and boson production in high-energy

[1] Final-state radiation is not allowed because the neutrinos are neutral particles. However, for a small fraction of events, the photon is radiated from the internal W boson propagator.

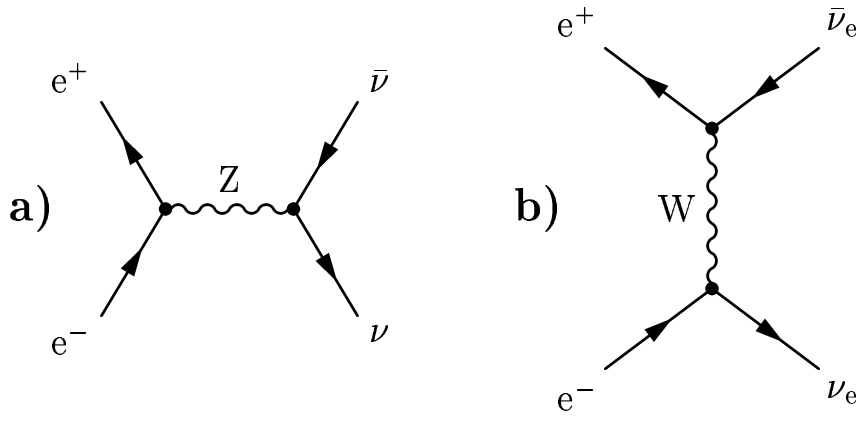

Figure 2.4: Feynman diagrams of the tree-level process $e^+e^- \to \nu\bar{\nu}$. In the s–channel, all three neutrino species are pair-produced via Z exchange a), whereas only electron neutrinos are allowed in the t–channel W exchange b).

e^+e^- collisions. An accurate description of such corrections is required for the precision measurements at LEP[2] and at future high-energy e^+e^- colliders.

2.2.1 The Reaction $e^+e^- \to \nu\bar{\nu}$

In the Standard Model, the reaction $e^+e^- \to \nu_l\bar{\nu}_l$ proceeds through s–channel Z exchange for all three neutrino flavors ($\nu_l = \nu_e, \nu_\mu, \nu_\tau$) and through t–channel W exchange for electron neutrinos only. The lowest order (*Born Approximation*) diagrams of this process are shown in Figure 2.4. Using the Feynman rules, the amplitudes $\mathcal{M}_Z$ and $\mathcal{M}_W$ corresponding to these diagrams can be written as

$$\begin{aligned} \mathcal{M}_{\mathcal{Z}} &= \sum_{l=e,\mu,\tau} \frac{g^2}{2\cos^2\theta_W}(\bar{\nu}_l\gamma_\mu P_L\nu_l)\frac{g^{\mu\sigma} - q_Z^\mu q_Z^\sigma/M_Z^2}{M_Z^2 - q_Z^2}\left[\, g_R\bar{e}\gamma_\sigma P_R e + g_L\bar{e}\gamma_\sigma P_L e\,\right], \\ \mathcal{M}_{\mathcal{W}} &= \frac{g^2}{2}(\bar{e}\gamma_\mu P_L\nu_e)\frac{g^{\mu\sigma} - q_W^\mu q_W^\sigma/M_W^2}{M_W^2 - q_W^2}(\bar{\nu}_e\gamma_\sigma P_L e)\,, \end{aligned} \tag{2.19}$$

where $P_{L,R} = (1 \mp \gamma^5)/2$ denotes the chiral projection operators and $g_R \equiv (g_V - g_A)/2 = \sin^2\theta_W$ and $g_L \equiv (g_V + g_A)/2 = -\frac{1}{2} + \sin^2\theta_W$ are the coupling constants of the right- and left-handed electrons to the Z boson.

[2]For example, the uncertainty on the theoretical description of the initial- and final-state radiation in the reaction $e^+e^- \to W^+W^- \to 4f(\gamma)$ is an important source of systematic errors on the measurement of the W boson mass at LEP [15].

The Born-level cross section is then given by [16]

$$\sigma^0_{e^+e^-\to\nu\bar{\nu}}(s) = \frac{N_\nu G_F^2}{6\pi} M_Z^4 (g_R^2 + g_L^2) \frac{s}{[(s-M_Z^2)^2 + (M_Z\Gamma_Z)^2]}$$
$$- \frac{G_F^2}{\pi} g_L \frac{M_W^2 M_Z^2 (s-M_Z^2)}{(s-M_Z^2)^2 + (M_Z\Gamma_Z)^2} \left[\frac{(s+M_W^2)^2}{s^2} \log\left(\frac{s+M_W^2}{M_W^2}\right) - \frac{M_W^2}{s} - \frac{3}{2} \right]$$
$$+ \frac{G_F^2}{\pi} M_W^2 \left[\frac{s+2M_W^2}{2s} - \frac{M_W^2}{s} \left(\frac{s+M_W^2}{s}\right) \log\left(\frac{s+M_W^2}{M_W^2}\right) \right], \qquad (2.20)$$

where $\sqrt{s}$ is the center-of-mass energy, Γ_Z is the width of the Z boson, and G_F is the Fermi coupling constant ($G_F/\sqrt{2} = g^2/8M_W^2$). The three terms in Equation 2.20 originate from the square of the Z−amplitude, the W−Z interference, and the square of the W−amplitude, respectively. The first term is the only one sensitive to the number of light neutrino species N_ν since only the electron neutrinos can be produced in the t–channel. It should be noted that in the Standard Model, the cross sections of the $\nu_\mu\bar{\nu}_\mu$ and $\nu_\tau\bar{\nu}_\tau$ pair-production can be assumed to be identical since small effects arising from possibly nonzero neutrino masses are undetectable at LEP.

The Born-level cross section of the reaction $e^+e^-\to\nu\bar{\nu}$ is shown in Figure 2.5a.[3] At energies around the Z pole, $\sqrt{s} \simeq 91$ GeV (LEP1 energy range), the $\nu_e\bar{\nu}_e$ and $\nu_\mu\bar{\nu}_\mu$ cross sections are almost the same reaching the maximum value of 3.9 nb, and the t–channel contribution to the $\nu_e\bar{\nu}_e$ cross section amounts to only about 1%. The situation changes at LEP2 energies, $\sqrt{s} \simeq 200$ GeV, where the t–channel contribution clearly dominates, $\sigma_{Born}(\nu_e\bar{\nu}_e) = 40$ pb and $\sigma_{Born}(\nu_\mu\bar{\nu}_\mu) = 1$ pb.

The inclusion of the ISR and other higher-order QED corrections is very important for this process. Figure 2.5b shows the cross section of the reaction $e^+e^-\to\nu\bar{\nu}(\gamma)$,[4] as predicted by the `KKMC` program [17] which takes into account the ISR effects (see Section 2.2.3). Comparing the ISR-corrected and Born-level cross sections, we can see that at LEP2 the inclusion of ISR increases the total $\nu_\mu\bar{\nu}_\mu(\gamma)$ cross section by a factor of seven, $\sigma_{ISR}(\nu_\mu\bar{\nu}_\mu) \simeq 7$ pb. This effect can be easily understood by examin-

[3] Here and in the following, the index l for the different neutrino species is omitted and a sum of all generations is denoted as "$\nu\bar{\nu}$."

[4] The "(γ)" in the formula indicates the possible emission of one or more photons.

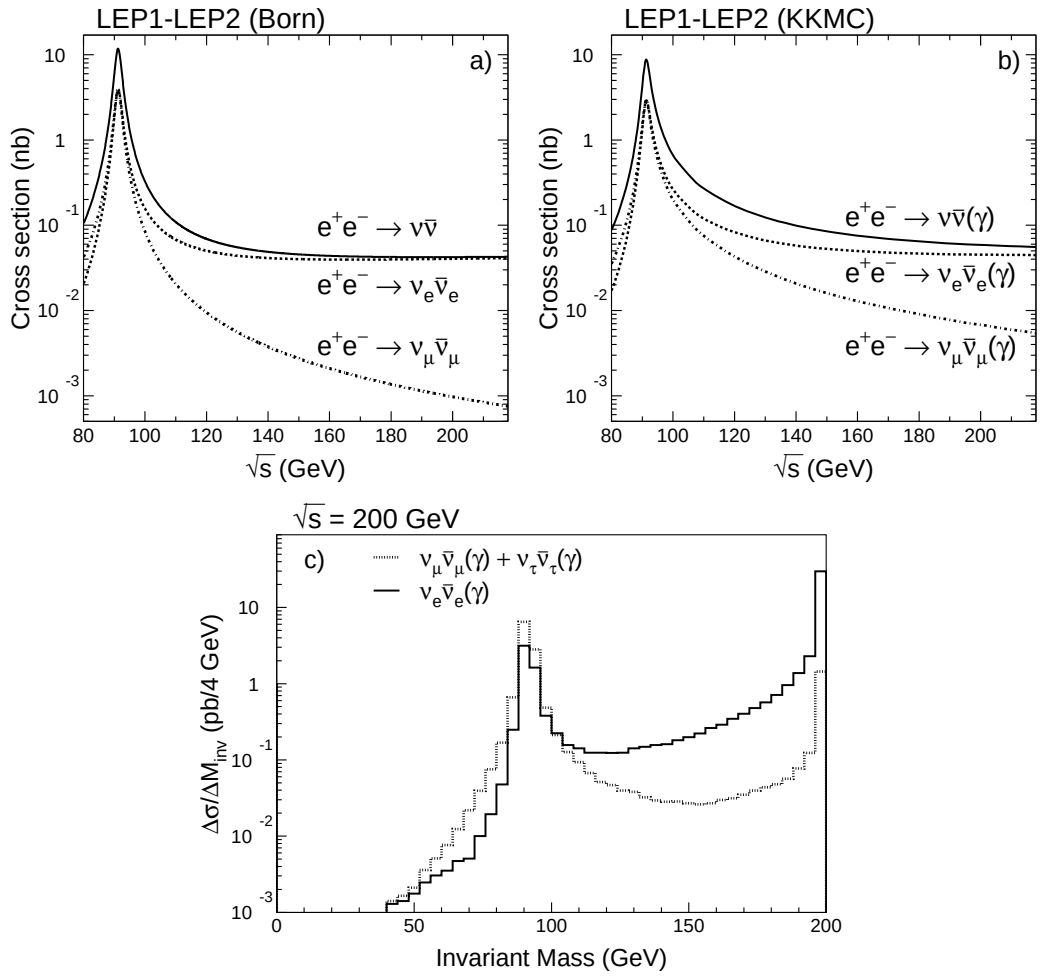

Figure 2.5: Total cross section of the reaction $e^+e^- \to \nu\bar{\nu}(\gamma)$ as a function of the center-of-mass energy a) at Born-level and b) as predicted by the KKMC program. c) The $\nu\bar{\nu}$ invariant mass distribution at $\sqrt{s} = 200$ GeV for an event sample generated with the KKMC program. Contributions from different neutrino species are shown separately.

ing the invariant mass distribution of the $\nu\bar{\nu}$ pairs (see Figure 2.5c). For the muon neutrinos, the majority of generated events have the invariant mass close to the Z mass: $M_{inv}(\nu_\mu\bar{\nu}_\mu) \simeq M_Z$. Thus, the photon emission has the effect of reducing the effective center-of-mass energy from 200 GeV to about 91 GeV, where the Born-level cross section is much higher. The Z bosons in the s–channel are produced predominantly on-shell. This effect, called *the radiative return to the Z*, was observed for all fermion pair-production processes at LEP2. The resulting peak in the two-fermion invariant mass distribution is often referred to as *the Z-return peak*. Figure 2.5c also

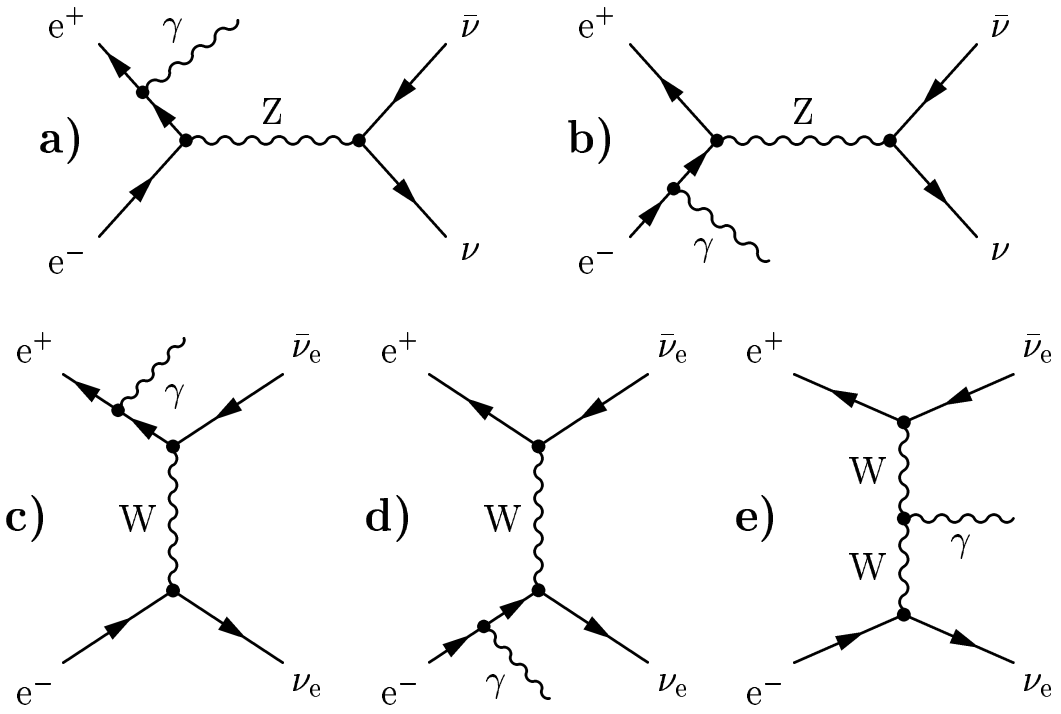

Figure 2.6: Lowest-order Feynman diagrams for the reaction $e^+e^- \rightarrow \nu\bar{\nu}\gamma$.

shows that the electron neutrinos are produced predominantly in the t–channel, where $M_{inv}(\nu_e\bar{\nu}_e) \simeq \sqrt{s}$.

2.2.2 Production of Single- and Multi-Photon Events at LEP

As shown in Figure 2.6, the reaction $e^+e^- \rightarrow \nu\bar{\nu}\gamma$ proceeds mainly via initial state radiation from the incoming electrons and positrons. In addition, a small fraction of photons ($\simeq 0.5\%$) can be emitted in the t–channel W boson fusion (Figure 2.6e) [18]. Since the produced neutrinos are undetectable,[5] such events would lead to the single-photon and missing energy signature. Therefore, the total rate of the initial state radiation as well as the energy and angular distributions of the emitted photons have to be known to a high precision.

A general and simple approach to this problem is to "dress" the Born-level cross

[5]Only a tiny fraction ($\sim 10^{-9}$) of 100 GeV neutrinos would interact with the material of the L3 detector [19].

section of the $\nu\bar{\nu}$ pair production ($\sigma_0(s)$) with a radiator function $H(x_\gamma, \theta_\gamma; s)$ [20]:

$$H = \frac{\alpha}{2\pi}\frac{1}{x_\gamma}\left[2\,\frac{1+(1-x_\gamma)^2}{\sin^2\theta_\gamma + 4m_e^2/s} - x_\gamma^2\right], \tag{2.21}$$

where $x_\gamma = E_\gamma/E_{beam}$, m_e is the electron mass, and α is the QED coupling constant. The differential cross section of the reaction $e^+e^- \to \nu\bar{\nu}\gamma$ can then be evaluated as

$$\frac{d\sigma}{dx_\gamma d\cos\theta_\gamma} = \sigma_0([1 - x_\gamma]\cdot s)\cdot H(x_\gamma, \theta_\gamma; s)\,. \tag{2.22}$$

Examining Equation 2.21, we can see that the differential cross section is expected to peak at low photon energies and polar angles. In addition, Equation 2.22 explains the appearance of the Z-return peak. In the s–channel, the Born-level cross section $\sigma_0(s)$ is very high near the Z pole so that the differential cross section has a maximum for photons with *recoil mass* close to the Z boson mass. The photon recoil mass is defined as the invariant mass recoiling against the photon(s) and is given by

$$M_{\rm rec} = \sqrt{\left(\sqrt{s} - E_\gamma\right)^2 - |\vec{p}_\gamma|^2}\,, \tag{2.23}$$

where $E_\gamma = \sum_i E_{\gamma_i}$ and $\vec{p}_\gamma = \sum_i \vec{p}_{\gamma_i}$ are the total energy and momentum of the photons. For single-photon events, Equation 2.23 simplifies to $M_{\rm rec} = \sqrt{s - 2\sqrt{s}E_\gamma}$. The position of the Z-return peak in the recoil mass distribution is independent of the collision energy. Therefore, instead of using the photon energy variable, the photon recoil mass is usually used.

The radiator function approach is capable of calculating the total cross section of the single-photon production with a precision of about 4% [21]. This level of accuracy is not satisfactory for my analysis. Therefore, I use specially developed Monte Carlo programs to simulate the $e^+e^- \to \nu\bar{\nu}\gamma(\gamma)$ process (see next section). The following differential distributions were obtained using the `KKMC` program.

As discussed in Chapter 6, the main variables used in the selection of single- and multi-photon events were the photon polar angle (θ_γ) and transverse momentum, $P_t^\gamma = E_\gamma \sin\theta_\gamma$. Because the efficiency of the L3 tracker decreased rapidly with polar

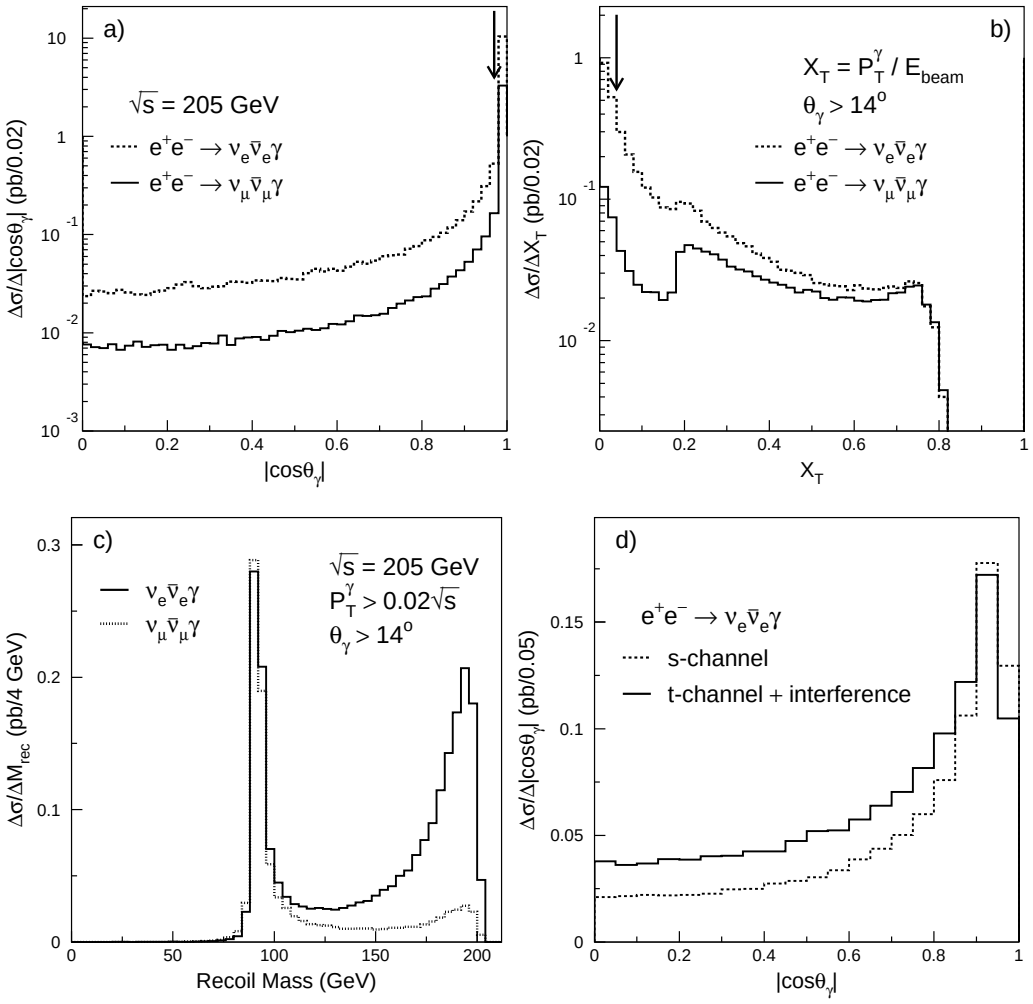

Figure 2.7: Distributions of a) the polar angle and b) the transverse momentum for single-photon events generated with a threshold $E_\gamma > 1$ GeV, at $\sqrt{s} = 205$ GeV. The arrows indicate the "selection" cuts. Distributions of c) the recoil mass and d) the polar angle after the application of these cuts.

angle, a lower cut on the polar angle of the photon had to be applied[6] $14° < \theta_\gamma < 166°$. The main background to this topology stemmed from the radiative Bhabha scattering process, $e^+e^- \to e^+e^-\gamma$, where both electrons were lost in the beam pipe, and only a photon was scattered at a large polar angle. To reject such events, the transverse momentum of the photon was required to be above $0.02\sqrt{s}$. These two "selection" cuts defined the phase space region of my single-photon selection.

As shown in Figure 2.7a, the angular cut rejected about 80% of both the $\nu_\mu\bar{\nu}_\mu\gamma$ and $\nu_e\bar{\nu}_e\gamma$ events. The distribution of the scaled transverse momentum, $x_t = P_t^\gamma / E_{beam}$,

[6]The BGO electromagnetic calorimeter of L3 extended down to $\theta_{min}(\mathrm{BGO}) = 10°$.

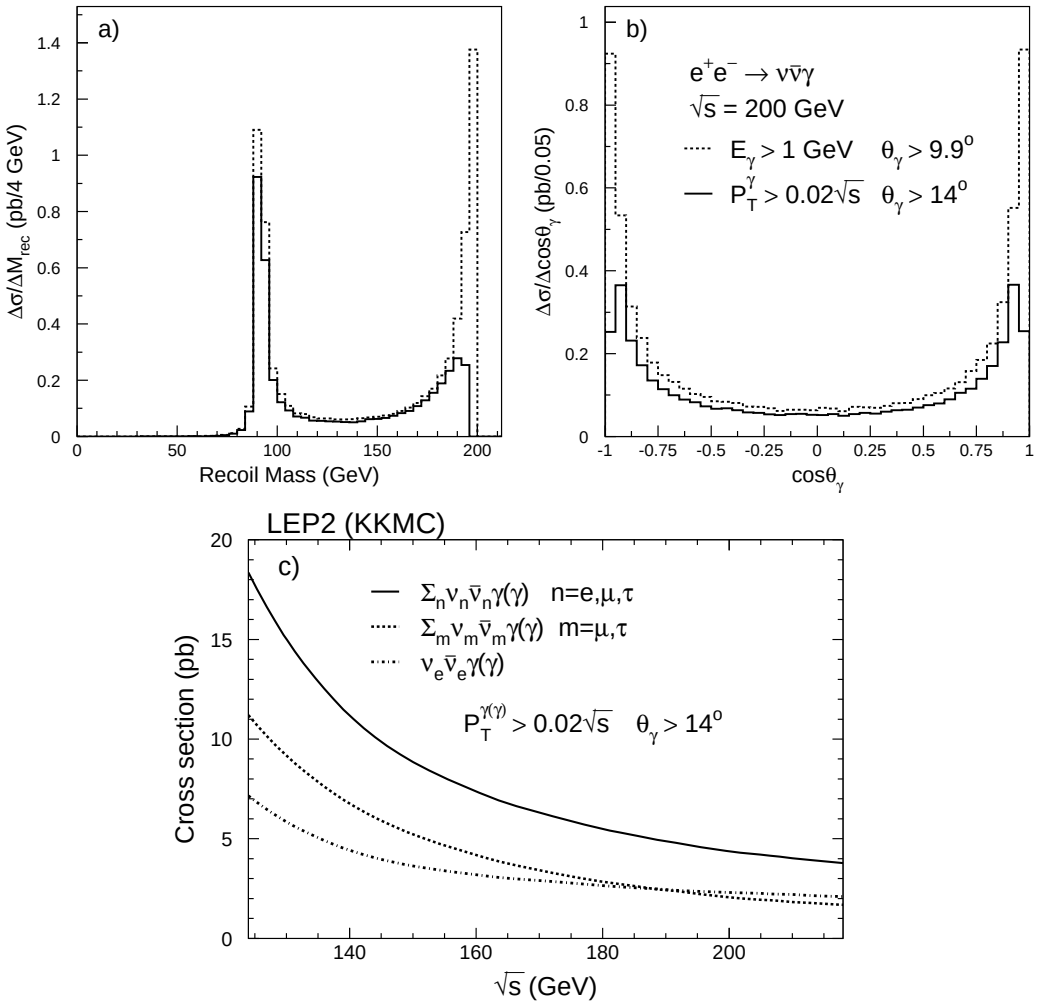

Figure 2.8: Differential cross sections of the reaction $e^+e^- \to \nu\bar{\nu}\gamma$ as functions of a) the recoil mass and b) $\cos\theta_\gamma$, calculated with the KKMC program at $\sqrt{s} = 200$ GeV. c) Total cross section of the reaction $e^+e^- \to \nu\bar{\nu}\gamma(\gamma)$.

after this cut is shown in Figure 2.7b. The visible peak structure at $x_t \simeq 0.02$ comes from the events in the Z-return peak. The cut on the transverse momentum, $P_t^\gamma > 0.02\sqrt{s}$, rejected only about 15% of the $\nu_\mu\bar{\nu}_\mu\gamma$ events and about 40% of the $\nu_e\bar{\nu}_e\gamma$ events.

Figures 2.7c,d show the recoil mass and polar angle distributions of the single-photon events passing these "selection" cuts. While the Z-return peak is present in both the electron- and muon-neutrino radiative spectra, the $\nu_e\bar{\nu}_e\gamma$ production dominates in the region of high recoil masses (low photon energies).

Since the neutrinos escaped detection, one could not distinguish between the $\nu_e\bar{\nu}_e\gamma$

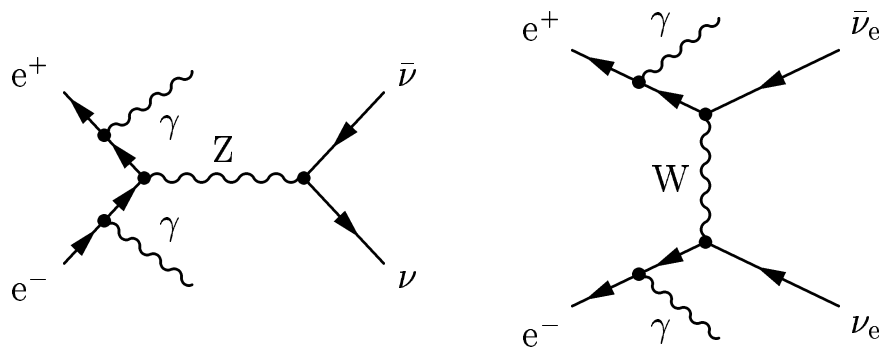

Figure 2.9: Lowest-order Feynman diagrams for the reaction $e^+e^- \rightarrow \nu\bar{\nu}\gamma\gamma$. Only two of the 19 allowed diagrams are shown.

and $\nu_\mu\bar{\nu}_\mu\gamma$ final states. The combined $\nu\bar{\nu}\gamma$ distributions of the photon recoil mass and polar angle are shown in Figures 2.8a,b. For comparison, these figures also show the same distributions obtained after relaxing the "selection" cuts to $E_\gamma > 1$ GeV and $\theta_\gamma > \theta_{min}(\mathrm{BGO}) = 10°$, which roughly corresponds to the energy and angular acceptance of the BGO electromagnetic calorimeter (see Chapters 4 and 5).

The total cross section of the single- and multi-photon production processes is shown in Figure 2.8c, where events with more than one photon with $E_\gamma > 1$ GeV and $\theta_\gamma(180° - \theta_\gamma) > 14°$ are also included. This plot shows that at LEP2 ($\sqrt{s} \simeq 200$ GeV) the radiative production of the electron neutrinos was as large as the combined production of the muon and tau neutrinos, $\sigma(\nu_e\bar{\nu}_e\gamma(\gamma)) \simeq \sigma(\nu_\mu\bar{\nu}_\mu\gamma(\gamma)) + \sigma(\nu_\tau\bar{\nu}_\tau\gamma(\gamma))$.

Multi-Photon Production in the Standard Model

As will be discussed in the next chapter, several supersymmetric processes can lead to the *multi-photon and missing energy* final state via $e^+e^- \rightarrow YY \rightarrow XX\gamma\gamma$, where X and Y are new neutral invisible particles. Therefore, it is interesting to consider the production of multi-photon events in the Standard Model, $e^+e^- \rightarrow \nu\bar{\nu}\gamma\gamma(\gamma)$.

This process corresponds to a total of 6 Feynman diagrams for the $\nu_\mu\bar{\nu}_\mu\gamma\gamma$ production and 19 Feynman diagrams for the $\nu_e\bar{\nu}_e\gamma\gamma$ production. These diagrams correspond to all possible combinations of two photons emitted from the incoming electron and positron as well as from the W boson propagator in the t–channel. As an example, two of such Feynman diagrams are shown in Figure 2.9.

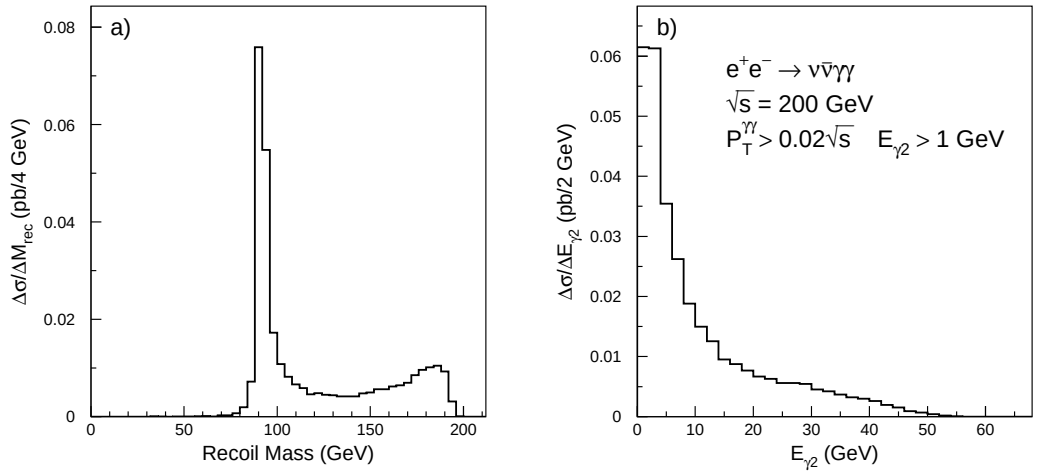

Figure 2.10: Differential cross sections of the $e^+e^- \to \nu\bar{\nu}\gamma\gamma$ process as functions of a) the recoil mass and b) the energy of the second photon, calculated with the KKMC program at $\sqrt{s} = 200$ GeV.

A multi-photon and missing energy event is defined as having at least two photons with $E_\gamma > 1$ GeV and $\theta_\gamma(180^\circ - \theta_\gamma) > 14^\circ$. In addition, the transverse momentum of the multi-photon system should satisfy $P_t^{\gamma\gamma} > 0.02\sqrt{s}$. Figure 2.10 shows the differential cross sections of this reaction as functions of the recoil mass and the energy of the second most energetic photon (E_{γ_2}). While the recoil mass distribution has the familiar feature of the Z-return peak, the E_{γ_2} spectrum is dominated by soft photons, exhibiting the behavior expected from Equations 2.21 and 2.22. At LEP2, the total cross section of the $e^+e^- \to \nu\bar{\nu}\gamma\gamma$ process was about 15 times smaller than that of the $e^+e^- \to \nu\bar{\nu}\gamma$ process.

2.2.3 Monte Carlo Event Generators

In order to estimate the efficiency of the $e^+e^- \to \nu\bar{\nu}\gamma(\gamma)$ event reconstruction and selection, I rely on Monte Carlo (MC) simulations. I also use MC programs to calculate the expected rate of the single- and multi-photon production in the Standard Model and to estimate systematic errors caused by uncertainties in the theoretical modelling of these processes.

During the final years of the LEP2 program, from 1998 to 2000, the four LEP experiments collected about 2.5 fb^{-1} of data at $\sqrt{s} = 189 - 208$ GeV. The statistical

error of the corresponding $\nu\bar{\nu}\gamma(\gamma)$ cross section measurement is expected to be below 2%. Thus, the expected cross section have to be known with a relative precision of at least 1%, and the corresponding differential distributions have to be simulated with a similar level of accuracy.

Up to the year 2000, most of the LEP experiments had used the `KORALZ` MC event generator [22]. It was originally written to simulate the $\tau\bar{\tau}$ pair-production and decay at energies near the Z pole (LEP1) and was later extended to include the $\nu\bar{\nu}\gamma(\gamma)$ process. The `KORALZ` generator did not use the exact cross section of the tree-level reaction $e^+e^- \to \nu\bar{\nu}\gamma$ so that contributions from the t–channel W exchange diagrams were added using rather simple approximations [23]. This resulted in a systematic uncertainty of about 4% on the single-photon cross section, while for the multi-photon final states the systematic uncertainty could be as high as 10% [24].

In 2000, the `KORALZ` event generator was replaced by a more advanced and precise MC program, `KKMC` [17]. Initially, it could be used to simulate any fermion pair-production processes, $e^+e^- \to f\bar{f}(\gamma)$, except for Bhabha scattering and neutrino pair-production. The $\nu\bar{\nu}\gamma(\gamma)$ production process was later incorporated in this program and a further-improved version was released in September 2002 as `KKMC v4.19`. This version of the `KKMC` generator was the main source of single- and multi-photon Monte Carlo events for my analyses.

The `KKMC` program includes the complete $\mathcal{O}(\alpha^2)$ calculations for the reaction $e^+e^- \to \nu\bar{\nu}\, n\gamma$ with $n = 1, 2$, including contributions from diagrams with the emission of one real and one virtual photon. The higher-order ISR and other QED corrections are calculated using the YFS-inspired Coherent Exclusive Exponentiation scheme [25], as discussed in Section A.3. The complete $\mathcal{O}(\alpha)$ electroweak corrections with higher-order extensions are implemented using the `DIZET` library [26].

The systematic errors are estimated to be about 0.8%, 1.3%, and 5% for the $\nu_\mu\bar{\nu}_\mu\gamma$, $\nu_e\bar{\nu}_e\gamma$, and $\nu\bar{\nu}\gamma\gamma$ production processes, respectively [24]. Thus, the `KKMC` program achieved the goal of a one percent precision on the total cross section of the $e^+e^- \to \nu\bar{\nu}\gamma(\gamma)$ process.

An independent cross check is provided by the `NUNUGPV` event generator [27]. It

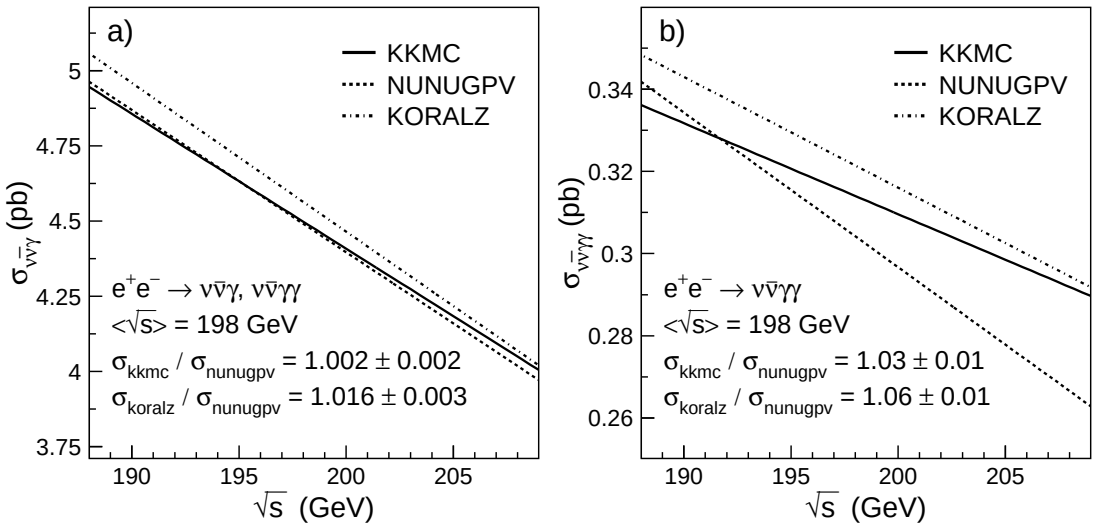

Figure 2.11: Total cross sections a) of the combined single- and multi-photon production process and b) of the multi-photon production process, as predicted by the KKMC, NUNUGPV, and KORALZ event generators.

includes the exact matrix elements for the reactions $e^+e^- \to \nu\bar{\nu}\, n\gamma$, with $n = 1, 2, 3$. The ISR and other higher-order QED corrections are calculated using the Structure Function techniques (see Section A.2). The main limitation of the NUNUGPV program is the absence of the exact $\mathcal{O}(\alpha)$ electroweak corrections, which results in a precision of 1–2% for the simulation of the single-photon production process [28]. In addition, contrary to the KKMC generator, the NUNUGPV program cannot be used for the inclusive reaction $e^+e^- \to \nu\bar{\nu}(\gamma)$. The main advantage of the NUNUGPV is its ability to simulate the single- and multi-photon production processes in the presence of anomalous triple and quartic gauge-boson couplings. Therefore, I will use this program in my search for anomalous boson couplings.

Figure 2.11 shows a comparison between the KKMC, NUNUGPV, and KORALZ event generators in the energy range studied in this thesis, $\sqrt{s} = 189 - 208$ GeV. The cross section curves predicted by the KKMC and NUNUGPV show an excellent agreement, well within the expected theoretical precision. A clear improvement over the accuracy level of the KORALZ is also observed.

The specific algorithms used in the KKMC and NUNUGPV Monte Carlo programs are described in more detail in Appendix A.

Chapter 3

Supersymmetry and Models with Large Extra Dimensions

The Standard Model is in very good agreement with all confirmed experimental data from high-energy colliders. Despite its remarkable success, the Standard Model contains several conceptual problems and raises a number of open questions (see Section 2.1.3 of the previous chapter). Therefore, the majority of particle physicists believe that there is a theory which extends the Standard Model to higher energies and improves our understanding of the particle world.

In this chapter, I describe two of the most interesting extensions of the Standard Model, Supersymmetry and models with large extra dimensions. In particular, I will concentrate on how these theories could lead to an anomalous production of photonic events with missing energy. I will also discuss the search strategies for such signals at LEP.

3.1 Supersymmetry

3.1.1 Introduction

In 1928, Paul Dirac incorporated the symmetries of the Lorentz group into quantum mechanics [29]. As a natural consequence, he found that each known particle had to have a partner – an antiparticle. Matter-antimatter symmetry was not revealed until experimental tools were developed to detect positrons in cosmic rays [30]. In a similar manner, Supersymmetry (SUSY) predicts partner particles for all known particles [31]. The basic idea of SUSY models is the existence of fermionic charges

that relate bosons to fermions:

$$\hat{Q}|\text{fermion}>=|\text{boson}> \qquad \hat{Q}|\text{boson}>=|\text{fermion}>, \tag{3.1}$$

which in turn means that each Standard Model particle should have a SUSY *superpartner*. The new SUSY particles are then combined with their partner Standard Model particles into *supermultiplets*. Two particles of a supermultiplet have the same quantum numbers and couplings but differ by 1/2 unit of spin. For example, the superpartners of quarks and leptons are scalar particles called *squarks* and *sleptons* (for more details see Section 3.1.2).

Supersymmetry has become the dominant framework for formulating physics beyond the Standard Model. Perhaps the most compelling argument for the existence of Supersymmetry is that this is the last still undiscovered symmetry consistent with the relativistic quantum theory [32]. Furthermore, SUSY realizations near the electroweak scale (i.e., below or near 1 TeV) can be used to cure several of the shortcomings of the Standard Model, as I discuss below.

Hierarchy Problem

The main theoretical reason to expect SUSY at an accessible energy scale is provided by the *hierarchy* or *naturalness* problem of the Higgs mass. In the Standard Model, quantum loop corrections to the Higgs mass [33], illustrated by the one-loop diagrams in Figure 3.1a, are each quadratically divergent:

$$\delta M_H^2 \;=\; \mathcal{O}\left(\frac{g_2^2}{16\pi^2}\right)\int^{\Lambda} d^4k\frac{1}{k^2} \;=\; \mathcal{O}\left(\frac{\alpha}{\pi}\right)\Lambda^2\,, \tag{3.2}$$

where the cutoff Λ represents the scale where new physics beyond the Standard Model appears. If we assume that the Standard Model is valid all the way up to the Planck mass $M_{\rm P} \sim 10^{19}$ GeV, where gravity is expected to become as strong as other particle interactions, then the quantum corrections of Equation 3.2 will be 36 orders of magnitude greater than the physical values of $M_H \sim 100$ GeV [34]. In principle, this

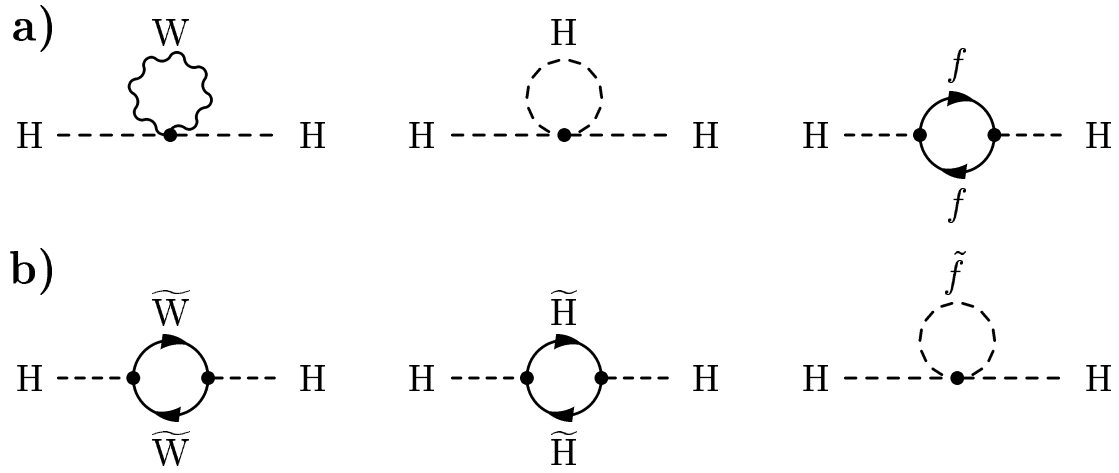

Figure 3.1: a) One-loop quantum corrections to M_H^2 in the Standard Model and b) the additional corrections in Supersymmetry.

is not a problem from the mathematical point of view in renormalization theory: one could postulate the tree-level value of the Higgs mass to be very large so that it would (almost) completely cancel the loop corrections and give us the correct physical value of M_H. However, this mechanism appears to be rather unnatural and one would prefer to keep the quantum corrections of the same order as the physical value of the Higgs mass.

This is possible in a supersymmetric theory, in which there are equal numbers of bosons (b) and fermions (f) with identical couplings. Since the contributions from the bosonic and fermionic loops have opposite signs (see Figure 3.1), the residual one-loop corrections become:

$$\delta M_H^2 = -\left(\frac{g_f^2}{16\pi^2}\right)\left(\Lambda^2 + m_f^2\right) + \left(\frac{g_b^2}{16\pi^2}\right)\left(\Lambda^2 + m_b^2\right) = \mathcal{O}\left(\frac{\alpha}{4\pi}\right)\left|m_b^2 - m_f^2\right|, \quad (3.3)$$

which is smaller than M_H^2 if the supersymmetric partners have similar masses:

$$\left|m_b^2 - m_f^2\right| \leq 1 \text{ TeV}^2. \quad (3.4)$$

This means that in order to keep the naturalness argument valid, masses of supersymmetric partner particles should be not much larger than 1 TeV.

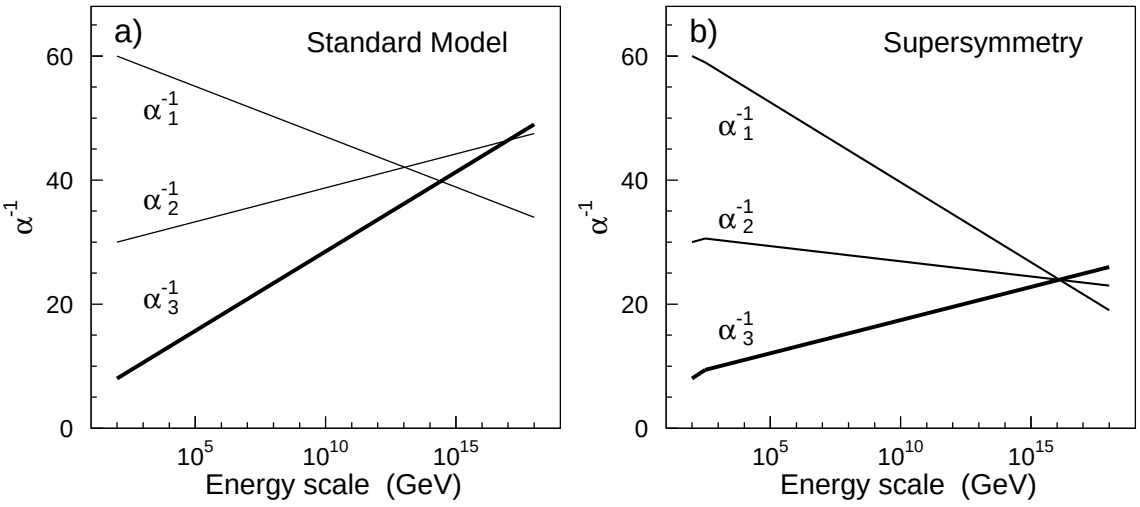

Figure 3.2: Evolution of the $SU(3)_C \times SU(2)_L \times U(1)_Y$ gauge couplings to high energy scales in the Standard Model a) and in Supersymmetry b).

Gauge Unification in SUSY

Another appealing feature of Supersymmetry at the weak scale is related to the effect it has on the running of the gauge couplings. In grand unification theories (GUTs), one assumes that there exists a unification of QCD and the electroweak sector of the Standard Model. In other words, the three inverse coupling constants ($1/\alpha_1$, $1/\alpha_2$, $1/\alpha_3$) of the electromagnetic, weak, and strong interactions converge and become equal at the unification energy scale. The coupling constants depend on the energy scale Q through loop corrections to the corresponding vertices and gauge bosons propagators [35], where the loops are generated by all particles with masses smaller than Q. Therefore, the evolution of the coupling constants is sensitive to the particle content of the theory.

In the Standard Model, the three couplings tend to approach each other at high energies, but fail to coincide at a single point, as shown in Figure 3.2a. However, the evolution graph will be changed if there exists Supersymmetry on the TeV scale. The loop corrections from the new SUSY particles start contributing above the energy scale $M_{\rm SUSY} \sim 1$ TeV, which produces a kink in the evolution of the coupling con-

stants.[1] Figure 3.2b shows that in this case the grand unification is indeed allowed and occurs at the unification scale of $U_{\mathrm{SUSY}} \sim 10^{16}$ GeV.

R–Parity

Supersymmetry opens the possibility of Lagrangian terms which explicitly violate lepton (L) and baryon (B) number conservation. However, if SUSY is realized on the TeV scale, then such $B-$ and $L-$violating interactions are severely restricted by the experimental measurements. For example, no evidence for fast proton decay has been observed, and the current lower bound on the proton lifetime is $\tau > 2.1 \times 10^{29}$ years at the 90% confidence level [6].

In order to forbid the lepton- and baryon-number violating terms, a new symmetry is introduced: *R–parity* [36]. For a particle of spin S, the R–parity is defined as

$$\mathrm{R} \;=\; (-1)^{3(B-L)+2S}. \tag{3.5}$$

This is a multiplicative quantum number, and all particles of the Standard Model have R–parity $+1$, while their superpartners (*sparticles*) have R–parity -1. The conservation of R–parity in scattering and decay processes has a crucial impact on the supersymmetric phenomenology:

- Sparticles can only be produced in pairs.
- Heavier sparticles decay into lighter ones.
- The lightest sparticle (LSP) is stable because it has no allowed decay modes.

Throughout this thesis the R–parity is assumed to be conserved.

The LSP must be neutral and colorless since there are stringent cosmological bounds on the existence of light stable particles which are electrically charged or strongly interacting [37]. As a consequence, the LSP in R–parity conserving SUSY models interacts with ordinary matter only by the exchange of a heavy virtual SUSY

[1] The masses of SUSY particles are assumed to be below or near M_{SUSY}.

particle and cannot be detected at collider experiments (much like a neutrino) [38]. Thus, a generic collider signature for R–parity conserving Supersymmetry is missing transverse momentum from the escaping LSPs.

Moreover, in such SUSY theories the LSP is a primary candidate for the non-baryonic dark matter, *Cold Dark Matter* [39], which is required in the current models of cosmology and galaxy formation [40]. Recent results from the WMAP experiment [41] suggest that more than 80% of the matter in our Universe consists of cold dark matter. Further aspects of the non-baryonic and supersymmetric dark matter can be found in Reference [42].

3.1.2 The Minimal Supersymmetric Standard Model

The simplest supersymmetric extension of the Standard Model is called the Minimal Supersymmetric Standard Model (MSSM). The particle spectrum of the MSSM consists of the Standard Model particles and their superpartners. In addition, the MSSM contains an extra Higgs doublet, giving a total of two doublets with hypercharge $Y = \pm 1$. In this way, flavor changing neutral currents[2] are avoided at tree level since the $Y = -1$ and $Y = +1$ doublets couple only to the "up"–type and "down"–type quarks (and charged leptons), respectively [44]. The particle content of the MSSM is listed in Table 3.1.

If supersymmetry was an exact symmetry of nature, then the Standard Model particles and their superpartners would be degenerate in mass and the sparticles would have been discovered long time ago. Thus, it is clear that a realistic SUSY theory must contain *supersymmetry breaking*. The most general way to introduce supersymmetry breaking is to add to the Lagrangian explicit *soft*[3] SUSY-breaking terms consistent with the symmetries of the Standard Model. The effective Lagrangian of the MSSM

[2] In the Standard Model with only one Higgs doublet, tree-level flavor changing neutral currents are automatically absent because the same operations that diagonalize the mass matrix automatically diagonalize the Higgs-fermion couplings [43].

[3] These interactions are referred to as soft because they do not re-introduce the quadratic divergences which motivated the introduction of Supersymmetry in the first place [45].

Particles	Supersymmetric partners			
	Weak interaction eigenstates		Mass eigenstates	
$l = \mathrm{e}, \mu, \tau$	$\tilde{l}_\mathrm{L}$, $\tilde{l}_\mathrm{R}$	Sleptons	$\tilde{l}_1, \tilde{l}_2$	
ν_l	$\tilde{\nu}_l$	Sneutrinos	$\tilde{\nu}_l$	
q = u, c, t / d, s, b	$\tilde{\mathrm{q}}_\mathrm{L}$, $\tilde{\mathrm{q}}_\mathrm{R}$	Squarks	$\tilde{\mathrm{q}}_1, \tilde{\mathrm{q}}_2$	
g	$\tilde{\mathrm{g}}$	Gluino	$\tilde{\mathrm{g}}$	
$\mathrm{W}^\pm$	$\widetilde{\mathrm{W}}^\pm$	Wino	$\tilde{\chi}^\pm_{1,2}$	Charginos
$\mathrm{H}^\pm$	$\widetilde{\mathrm{H}}^\pm$	Higgsinos		
γ	$\tilde{\gamma}$	Photino	$\tilde{\chi}^0_{1\ldots4}$	Neutralinos
Z	$\widetilde{\mathrm{Z}}$	Zino		
h, H, A	$\widetilde{\mathrm{H}}_{1,2}$	Higgsinos		
G	$\widetilde{\mathrm{G}}$	Gravitino	$\widetilde{\mathrm{G}}$	

Table 3.1: Particle content of the MSSM.

can then be written as a sum of SUSY-preserving and SUSY-breaking parts:

$$\mathcal{L} = \mathcal{L}_{SUSY} + \mathcal{L}_{soft}. \tag{3.6}$$

The resulting theory has more than 100 additional parameters which were not present in the Standard Model. The number of such parameters can be significantly reduced by making explicit assumptions about the nature of the supersymmetry breaking, as discussed in detail in Section 3.1.3.

Higgs in Supersymmetry

The extended Higgs sector of the MSSM contains two doublets. One of the doublets couples exclusively to "down"-type quarks and charged leptons and has a vacuum expectation value v_d, while the other couples only to "up"-type particles with a vacuum expectation value of v_u [43]. The squared sum of the their vacuum expectation

values is connected to the W boson mass through

$$v_d^2 + v_u^2 = v^2 = 4M_W^2/g^2 \simeq (246 \text{ GeV})^2, \tag{3.7}$$

while their ratio, traditionally written as

$$\tan\beta = \frac{v_u}{v_d}, \tag{3.8}$$

is a free parameter of the model. After the electroweak symmetry breaking, five physical Higgs particles remain in this model: a charged Higgs boson pair ($H^{\pm}$), two CP–even neutral Higgs bosons (h and H with $M_h \leq M_H$), and one CP–odd neutral Higgs boson (A). At tree level, the whole Higgs-sector is determined by two parameters, typically taken to be $\tan\beta$ and M_A [43].

It should be also noted that, at tree level, the MSSM predicts that the lightest neutral Higgs boson (h) should not be heavier than the Z boson, $M_h \leq M_Z$ [46]. However, this upper bound is somewhat weakened if one includes the quantum loop corrections. Current calculations yield $M_h \lesssim 130$ GeV [47], which implies that the MSSM Higgs boson should be observed at the LHC.

Neutralinos and Charginos

As a result of supersymmetry breaking, SUSY particles with the same quantum numbers are allowed to mix in a manner analogous to the mixing of the B and W^3 fields due to the electroweak symmetry breaking in the Standard Model (see Section 2.1.2). In particular, the superpartners of the Higgs and electroweak gauge bosons, higgsinos and gauginos, can mix with each other. The neutral higgsinos ($\widetilde{\mathrm{H}}_1$ and $\widetilde{\mathrm{H}}_2$) and the neutral gauginos ($\widetilde{\mathrm{B}}$ and $\widetilde{\mathrm{W}}^3$) combine to form four neutral mass eigenstates called neutralinos, $\tilde{\chi}^0_{1\ldots4}$. The charged higgsinos ($\widetilde{\mathrm{H}}^+$ and $\widetilde{\mathrm{H}}^-$) and the charged winos ($\widetilde{\mathrm{W}}^+$ and $\widetilde{\mathrm{W}}^-$) mix to form four charged eigenstates called charginos, $\tilde{\chi}^{\pm}_{1,2}$ (see Table 3.1). By convention these are labeled in ascending order with $m_{\tilde{\chi}^0_1} < m_{\tilde{\chi}^0_2} < m_{\tilde{\chi}^0_3} < m_{\tilde{\chi}^0_4}$ and $m_{\tilde{\chi}^{\pm}_1} < m_{\tilde{\chi}^{\pm}_2}$.

This mixing can be expressed using the following three parameters: M_1 and M_2 which correspond to the bino and wino mass terms in the SUSY-breaking part of Lagrangian $\mathcal{L}_{soft}$, and the Higgs mixing parameter μ. The physical chargino and neutralino masses can then be obtained by diagonalizing the mass mixing matrices

$$\mathcal{M}_{\tilde{\chi}^{\pm}} = \begin{pmatrix} M_2 & \sqrt{2}\mathrm{M_W}\sin\beta \\ \sqrt{2}\mathrm{M_W}\cos\beta & \mu \end{pmatrix} \tag{3.9}$$

for charginos and

$$\mathcal{M}_{\tilde{\chi}^0} = \begin{pmatrix} M_1 & 0 & -\mathrm{M_Z}\, s_\theta \cos\beta & \mathrm{M_Z}\, s_\theta \sin\beta \\ 0 & M_2 & \mathrm{M_Z}\, c_\theta \cos\beta & -\mathrm{M_Z}\, c_\theta \sin\beta \\ -\mathrm{M_Z}\, s_\theta \cos\beta & \mathrm{M_Z}\, c_\theta \cos\beta & 0 & -\mu \\ \mathrm{M_Z}\, s_\theta \sin\beta & -\mathrm{M_Z}\, c_\theta \sin\beta & -\mu & 0 \end{pmatrix} \tag{3.10}$$

for neutralinos, where $s_\theta \equiv \sin\theta_\mathrm{W}$, $c_\theta \equiv \cos\theta_\mathrm{W}$, and the mass matrix for neutralinos is given in the gauge-eigenstate basis ($\tilde{\mathrm{B}}$,$\widetilde{\mathrm{W}}^3$,$\tilde{\mathrm{H}}_1$,$\tilde{\mathrm{H}}_2$) [48]. In general, the neutralino mass eigenstates do not correspond to a photino (a fermion partner of the photon) or a zino (a fermion partner of the Z boson), but are complicated mixtures of these states. The photino is a mass eigenstate only if $M_1 = M_2$. Physics involving the neutralinos therefore depends on M_1, M_2, μ, and $\tan\beta$ parameters.

In order to reduce the number of free parameters in the theory, a frequently used approach is to assume that the gaugino masses also unify at the GUT scale. In this case, the effective gaugino mass parameters are related to each other through:

$$M_1 = \frac{5}{3}\tan^2\theta_\mathrm{W}\, M_2\,, \qquad M_3 \equiv m_{\tilde{\mathrm{g}}} = \frac{\alpha_\mathrm{s}}{\alpha_\mathrm{em}}\sin^2\theta_\mathrm{W}\, M_2\,, \tag{3.11}$$

where M_3 is the mass parameter associated with $SU(3)_C$, $m_{\tilde{\mathrm{g}}}$ is the gluino mass, and M_1 and M_2 enter the neutralino and chargino mass matrices. Substituting the following parameter values $\alpha_S = 0.118$, $\alpha = 1/128$, and $\sin^2\theta_W = 0.23$, one finds

$$M_3 : M_2 : M_1 \approx 7 : 2 : 1 \tag{3.12}$$

at the electroweak scale. In particular, this means that the gluino should be much heavier than the lighter neutralinos and charginos [38].

Sfermions

The supersymmetric partners of the quarks and leptons are scalar bosons called squarks, charged sleptons, and sneutrinos. For a given fermion f, there are two supersymmetric partners $\tilde{f}_{\rm L}$ and $\tilde{f}_{\rm R}$, the superpartners for the two helicity states (left and right-handed) of this fermion.[4] In general, $\tilde{f}_{\rm L}$ and $\tilde{f}_{\rm R}$ are not mass eigenstates since they are allowed to mix. However, the strength of this mixing is proportional to the mass of the corresponding Standard Model partner and, hence, the mixing is expected to be negligibly small for the first two generations of sparticles. Only for the third generation is a substantially large mixing possible. In this case, the squark and slepton mass eigenstates are generically called $\tilde{f}_1$ and $\tilde{f}_2$.

3.1.3 Supersymmetry Breaking

As mentioned in the previous section, supersymmetry must be a broken symmetry. According to the Goldstone theorem [49], spontaneous breaking of any global symmetry gives rise to a massless Nambu-Goldstone mode with the same quantum numbers as the broken symmetry generator. In the case of supersymmetry, the broken generator is the fermionic charge Q and the Nambu-Goldstone particle must be a massless neutral fermion called the *goldstino*. The goldstino would then be the LSP and could play a role in SUSY phenomenology [50].

However, no satisfactory models of global supersymmetry breaking exist. Thus, the supersymmetry must be made a local symmetry. In this case, the goldstino is absorbed by the gravitino, the spin–3/2 superpartner of the graviton, which also acts as a gauge field [51]. The gravitino participates in the supersymmetric version of the

[4] There is no $\tilde{\nu}_{\rm R}$ in the MSSM.

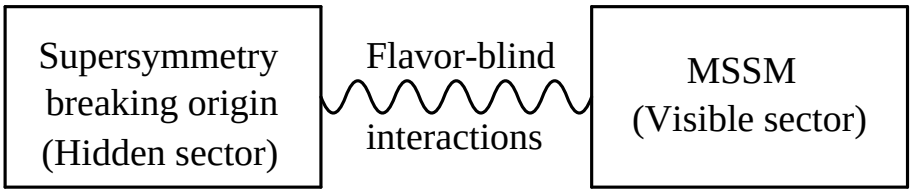

Figure 3.3: The presumed schematic structure of the supersymmetry breaking.

Higgs mechanism and acquires a non-zero mass

$$m_{\widetilde{\mathrm{G}}} \sim \frac{F}{M_{\mathrm{Pl}}}, \tag{3.13}$$

where $\sqrt{F}$ is the characteristic scale of the local supersymmetry breaking and M_{Pl} is the Planck mass [38].

Thus far no one has succeeded in crafting an acceptable model in which the supersymmetry breaking arises solely due to interactions between the MSSM particles. This problem is usually addressed by extending the MSSM to a new theory which holds two distinct sectors: a "hidden" sector built of particles with no direct couplings to the Standard Model gauge group and a "visible" sector containing the particles of the MSSM. There should be no tree-level interactions between particles of the visible and hidden sectors. It is assumed that supersymmetry breaking occurs in the hidden sector and is transmitted to the visible sector of the MSSM by some mechanism, as shown in Figure 3.3. Two theoretical scenarios have been examined in detail: *gravity-mediated* and *gauge-mediated* supersymmetry breaking.

Gravity-mediated SUSY Breaking

In the gravity-mediated SUSY breaking scenario (SUGRA), the mediating interactions between the hidden and visible sectors are assumed to be of gravitational nature [52, 53]. More precisely, they are assumed to be associated with some new physics, which includes gravity and enters at the Planck scale. In such models, the SUSY breaking scale is predicted to be of the order of 10^{11} GeV. The gravitino mass is then expected to be comparable to the masses of the MSSM sparticles, while its

couplings are of gravitational strength. Hence, it follows that the gravitino would not play any role in collider physics.

In the minimal SUGRA model,[5] the scalar quarks and leptons are assumed to have the same mass and the same trilinear couplings at the GUT scale [52]. With these universality conditions, the whole sparticle spectrum is determined by only five free parameters: M_2, μ, and $\tan\beta$, described in the previous section; the common scalar mass at the GUT scale m_0; and the common Higgs-sfermion-sfermion trilinear interaction parameter A at the GUT scale [54]. In R–parity conserving SUGRA models, the LSP is typically taken to be the lightest neutralino.

Gauge-mediated SUSY Breaking

In the gauge-mediated supersymmetry breaking scenario (GMSB), the supersymmetry breaking is assumed to be communicated to the visible sector by the ordinary electroweak and QCD gauge interactions The SUSY breaking again occurs in the hidden sector, however the splitting of masses in the MSSM sector is generated at some lower energy scale, in the "messenger sector," which contains pairs of heavy messenger quarks and leptons [55, 56]. The direct coupling of messengers to the hidden sector generates a supersymmetry breaking spectrum in the messenger sector. Gauge interactions then mediate supersymmetry breaking needed in the observable sector. In this scenario, the supersymmetry breaking scale $\sqrt{F}$ is expected to be between about 10 TeV and 100 TeV, and the gravitino mass is typically in the eV to keV range. The couplings of the gravitino to the other MSSM particles can become strong enough to let the gravitino play an important role in collider experiments.

Since the GMSB scenario can naturally lead to photonic signatures at LEP, let us discuss the MSSM spectrum in such models. The whole mass spectrum of the MSSM can be described by five free parameters of the model plus the gravitino mass [57]. The free GMSB parameters are the supersymmetry breaking scale in the messenger sector Λ, the messenger mass M_m, the messenger index N_m (an integer), $\tan\beta$, and sign(μ), where μ is the Higgs mixing parameter. Several examples of the MSSM

[5] The minimal SUGRA model is sometimes referred to as mSUGRA or constrained MSSM.

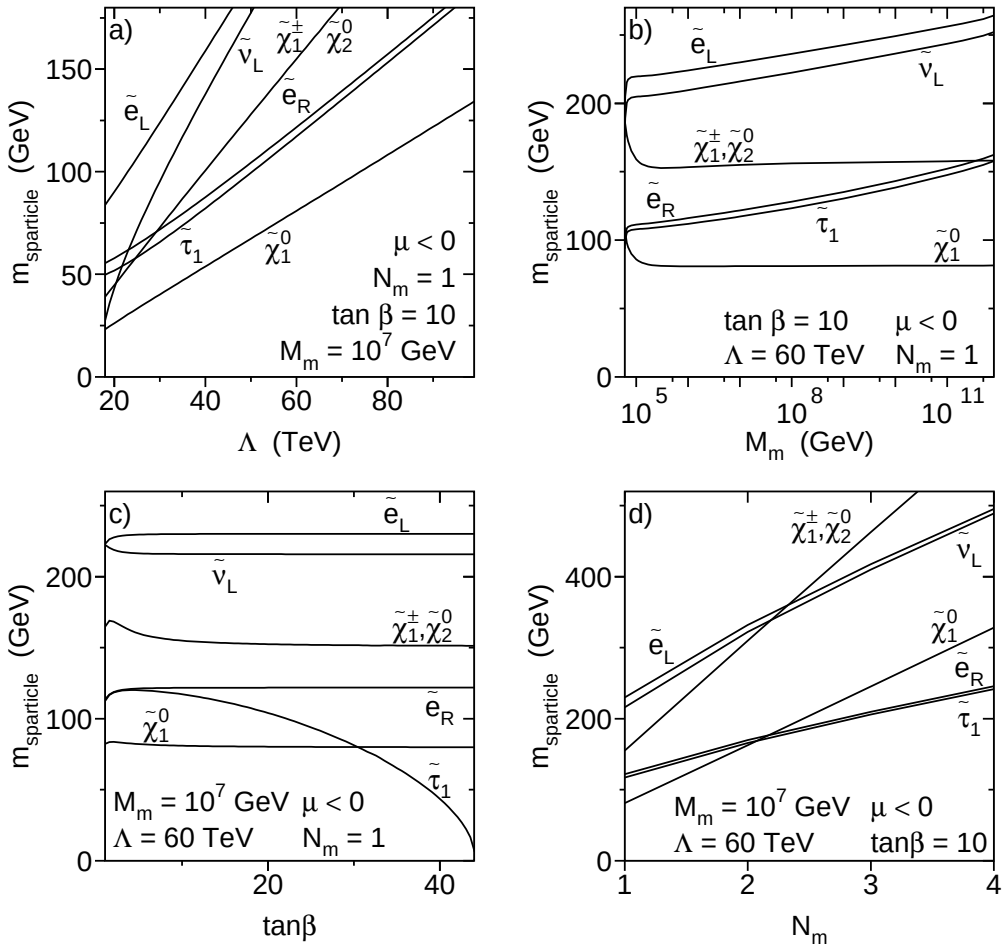

Figure 3.4: The masses of the sleptons and lightest gauginos as functions of the GMSB parameters Λ, M_m, $\tan\beta$, and N_m [58]. The values of the fixed parameters are indicated on the plots.

mass spectra are shown in Figure 3.4 for a broad range of the GMSB parameters, as calculated with the `ISASUSY` program [59]. A hierarchy between strongly interacting and weakly interacting particles holds throughout the whole parameter space keeping squarks much heavier than sleptons and the lightest gauginos.

The gravitino is always the LSP in the GMSB theories, while the next-to-lightest supersymmetric particle (NLSP) can either be the lightest neutralino $\tilde{\chi}_1^0$ or the lightest stau $\tilde{\tau}_1$ depending on the values of N_m, M_m, and $\tan\beta$ (see Figure 3.4). In this thesis, I will consider only the $\tilde{\chi}_1^0$ NLSP scenario because only such scenario could lead to an anomalous production of photonic events with missing energy at LEP.

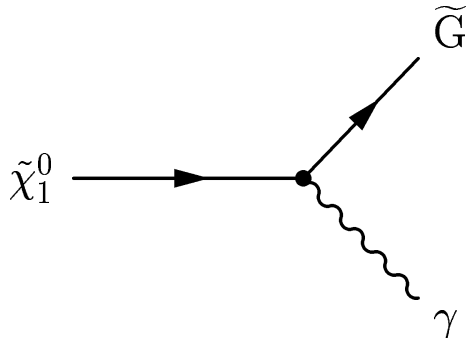

Figure 3.5: Feynman graph for the two-body neutralino decay $\tilde{\chi}_1^0 \to \gamma\tilde{\mathrm{G}}$.

The lightest neutralino is in general a mixture of the superpartners of the electroweak gauge and Higgs bosons, which can be conveniently parameterized as

$$\tilde{\chi}_1^0 = \sum_{i=1}^{4} N_i \psi_i^0 \,, \tag{3.14}$$

where $\psi^0 = (\tilde{\mathrm{B}}, \widetilde{\mathrm{W}}^3, \tilde{\mathrm{H}}_1, \tilde{\mathrm{H}}_2)$ is the gauge-eigenstate basis. In most cases of GMSB models, the lightest neutralino is almost pure bino,[6] $N_1 \simeq 1$, and decays predominantly into a gravitino and a photon, $\tilde{\chi}_1^0 \to \gamma\tilde{\mathrm{G}}$ (see Figure 3.5) [56]. The corresponding decay width is given by [60]

$$\Gamma(\tilde{\chi}_1^0 \to \gamma\tilde{\mathrm{G}}) = \frac{\kappa_\gamma}{48\pi} \frac{m_{\tilde{\chi}_1^0}^5}{m_{\mathrm{Pl}}^2 m_{\tilde{\mathrm{G}}}^2} \,, \tag{3.15}$$

where $\kappa_\gamma = |N_1 \cos\theta_{\mathrm{W}} + N_2 \sin\theta_{\mathrm{W}}|^2$ gives the photino component of the neutralino and $m_{\mathrm{Pl}} = M_{\mathrm{Pl}}/\sqrt{8\pi} \approx 2.4 \cdot 10^{18}$ GeV is the reduced Planck mass. The Planck-scale suppression $m_{\tilde{\chi}_1^0}^2/m_{\mathrm{Pl}}^2$ is compensated by the factor $m_{\tilde{\chi}_1^0}^2/m_{\tilde{\mathrm{G}}}^2$, which gives a sizable decay width. In the rest frame of the decaying neutralino, the photons and gravitinos are produced isotropically with an energy equal to $m_{\tilde{\chi}_1^0}/2$ (for kinematic purposes the gravitino mass can be ignored).

It should be noted that sufficiently heavy neutralinos can also decay into a Z boson

[6] Bino is the superpartner of B, the gauge boson of the $U(1)_Y$ group of the Standard Model.

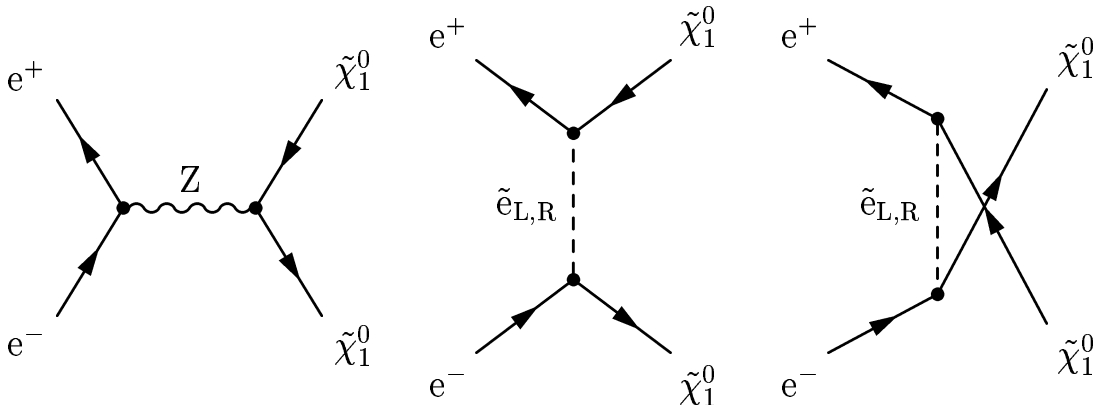

Figure 3.6: Feynman diagrams for the neutralino pair-production at LEP.

and a gravitino. However, this decay mode is strongly suppressed:

$$\frac{\Gamma(\tilde{\chi}_1^0 \to \mathrm{Z}\tilde{\mathrm{G}})}{\Gamma(\tilde{\chi}_1^0 \to \gamma\tilde{\mathrm{G}})} = \frac{\kappa_\mathrm{Z}}{\kappa_\gamma}\left(1 - \frac{M_Z^2}{m_{\tilde{\chi}_1^0}^2}\right)^4 , \tag{3.16}$$

where $\kappa_\mathrm{Z} = |N_{11}\sin\theta_\mathrm{W} + N_{12}\cos\theta_\mathrm{W}|^2 + \frac{1}{2}|N_{13}\cos\beta - N_{14}\sin\beta|^2$. If the neutralino is pure bino, $\kappa_\mathrm{Z}/\kappa_\gamma \simeq 0.3$. Complete expressions for the neutralino decay rates into three-body final states ($\tilde{\chi}_1^0 \to \tilde{\mathrm{G}} f \bar{f}$) can be found in Reference [61].

3.2 Single- and Multi-Photon Signatures in SUSY

Different SUSY models may lead to different single- or multi-photon with missing energy signatures. In this section, I will describe the possible signal topologies, discuss my motivation for searching for such signals at LEP, and outline the search strategies that I will later use in Chapter 7.

3.2.1 Neutralino Production in GMSB

Neutralinos can be pair-produced in $\mathrm{e^+e^-}$ collisions by Z exchange in the s–channel or by scalar electron exchange in the t– and u–channels [62]. The Feynman diagrams of this process are shown in Figure 3.6. As discussed in the previous section, I consider

the GMSB scenario where the massless (for kinematic purposes) gravitino is the LSP and the lightest neutralino is the NLSP and almost pure bino. Since only the higgsino components of the neutralino directly couple to the Z boson, the s–channel contribution is negligible. The cross section of this reaction is an incoherent sum of contributions from the right- and left-handed selectron exchange diagrams[7] and is given by [64]

$$\begin{aligned}\frac{d\sigma}{d\cos\theta} &= \sum_{i=\tilde{e}_R,\tilde{e}_L} \frac{\beta^3}{s}\frac{\pi\alpha Y_i^4}{2\cos^4\theta_W} \times \Big[\frac{1-\cos^2\theta}{(1+\Delta M_i)^2-\beta^2\cos^2\theta} \\ &\quad + \frac{2\Delta M_i^2\cos^2\theta}{[(1+\Delta M_i^2)^2-\beta^2\cos^2\theta]^2}\Big], \end{aligned} \tag{3.17}$$

where $\sqrt{s}$ is the center-of-mass energy, θ is the polar angle, $\beta = \sqrt{1-4m^2_{\tilde{\chi}^0_1}/s}$ is the neutralino velocity in the laboratory frame, $\Delta M_i = 2\cdot(m_i^2 - m^2_{\tilde{\chi}^0_1})/s$, and Y_i is the hypercharge of the right- and left-selectrons ($Y_{\tilde{e}_R} = -2$ and $Y_{\tilde{e}_L} = -1$). Because the selectron hypercharge is to the fourth power and the left-selectron is usually heavier than the right-selectron, it is clear that the dominant contributions come from the $\tilde{e}_R$ exchange.

For given values of the neutralino mass and center-of-mass energy, the production cross section depends only on the selectron mass. In GMSB models, the ratio $m_{\tilde{e}_R}/m_{\tilde{\chi}^0_1}$ cannot become larger than about 1.5 [65]. Thus, the $e^+e^- \to \tilde{\chi}^0_1\tilde{\chi}^0_1$ cross section cannot be smaller than a certain minimum value. Figure 3.7 shows the maximum and minimum cross section values as a function of the neutralino mass. This cross section range was obtained with the following scan over the GMSB parameter space:

$$\begin{aligned} 10\text{ TeV} \le\ & \Lambda && \le 100\text{ TeV} \\ \Lambda/0.9 \le\ & M_m && \le \Lambda/0.01 \\ & N_m && = 1,2,3,4 \\ 1 \le\ & \tan\beta && \le 60 \\ & \operatorname{sign}\mu && = \pm, \end{aligned} \tag{3.18}$$

[7] The two selectrons $\tilde{e}_R$ and $\tilde{e}_L$ do not mix, and the interference between the right and left-handed selectron exchange diagrams is suppressed by a factor of $\mathcal{O}(m_e/m_{\tilde{e}})$ and hence is negligible [63].

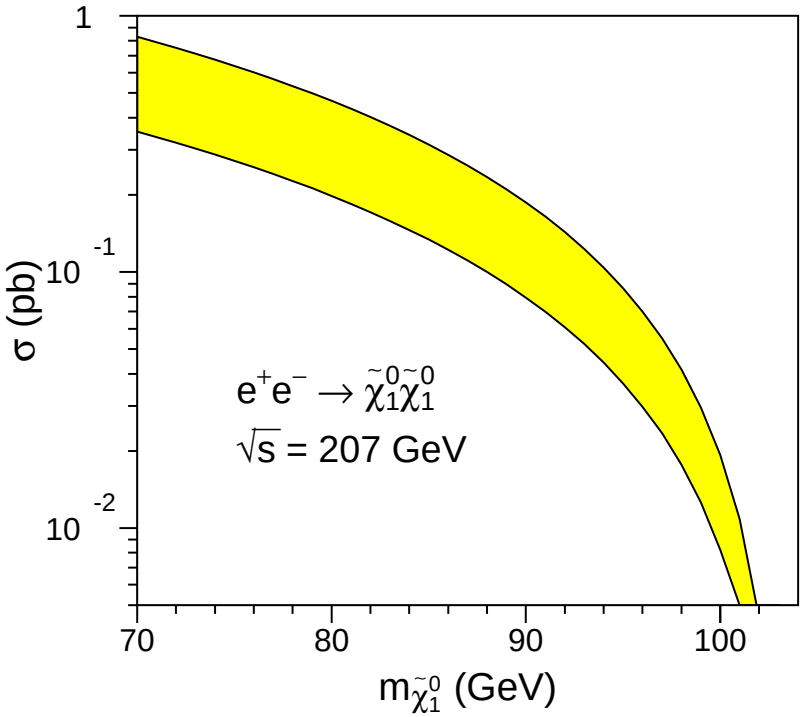

Figure 3.7: Cross section range for the reaction $e^+e^- \to \tilde{\chi}_1^0\tilde{\chi}_1^0$ at $\sqrt{s}$ = 207 GeV, as a function of the mass of the lightest neutralino in GMSB models.

where the parameter ranges that I used were defined in Reference [65]. Sparticle masses and couplings are calculated from the GMSB model parameters using the `ISASUSY` program [59], which has been interfaced to the `SUSYGEN` Monte Carlo generator [66] to derive the neutralino pair-production cross section, including initial-state radiation. Figure 3.7 shows that for any values of the GMSB parameters, the reaction $e^+e^- \to \tilde{\chi}_1^0\tilde{\chi}_1^0$ has a sizable cross section almost up to the kinematic limit of $m_{\tilde{\chi}_1^0} = \sqrt{s}/2$.

As discussed in the previous section, the produced neutralinos decay predominantly into a gravitino and a photon. Because the gravitinos would escape undetected, the reaction $e^+e^- \to \tilde{\chi}_1^0\tilde{\chi}_1^0 \to \tilde{G}\tilde{G}\gamma\gamma$ would lead to two photons and missing energy in the final state. Each of the neutralinos is produced with an energy equal to the beam energy, $E_{\tilde{\chi}_1^0} = \sqrt{s}/2$, and decays isotropically. Thus, the photon energies

have a flat distribution in the range $E_{\min} < E_{\gamma_1}, E_{\gamma_2} < E_{\max}$ with

$$E_{\max,\min} = \frac{1}{4}\left(\sqrt{s} \pm \sqrt{s - 4m^2_{\tilde{\chi}^0_1}}\right) . \tag{3.19}$$

In order to investigate the kinematic distributions of the final-state photons, I used the SUSYGEN program to generate samples of 300,000 MC events for three different values of the neutralino mass: $m_{\tilde{\chi}^0_1} = 55, 75, 95$ GeV. The event samples were generated at $\sqrt{s} = 200$ GeV which corresponded to the typical center-of-mass energy of LEP2. Figures 3.8a,c show that the photon energy spectrum is indeed flat. The corresponding distributions of the polar angle ($\cos\theta_\gamma$) and the recoil mass are shown in Figures 3.8b,d, where the event recoil mass was defined in Section 2.2.2, Equation 2.23. The distribution of the photon polar angle is also almost flat.[8]

In this search channel, the main background comes from the Standard Model process $e^+e^- \to \nu\bar{\nu}\gamma\gamma$ (see Section 2.2.2). However, by comparing Figures 3.8 and 2.10 one can see that the kinematic distributions of the signal are very different from those of the background. In particular, the energy of the second photon is expected to be much higher for the signal than for the background. Moreover, the photons from the reaction $e^+e^- \to \nu\bar{\nu}\gamma\gamma$ are expected to be produced predominantly at low polar angles. Thus, an almost complete suppression of the background can be achieved with quite loose cuts on the E_{γ_2} and $\cos\theta_\gamma$ variables.

It should be noted that for certain values of the GMSB parameters the neutralino decay length can become non-negligible. The probability that a neutralino with energy $\sqrt{s}/2$ will travel a distance $\leq x$ in the laboratory frame before decaying is given by

$$P(x) = 1 - \exp(-x/L) . \tag{3.20}$$

[8] The neutralino production angle is not severely peaked (see Equation 3.17), and the decay $\tilde{\chi}^0_1 \to \tilde{G}\gamma$ is isotropic. Hence, the photon polar angle in the laboratory frame has a distribution very close to isotropic.

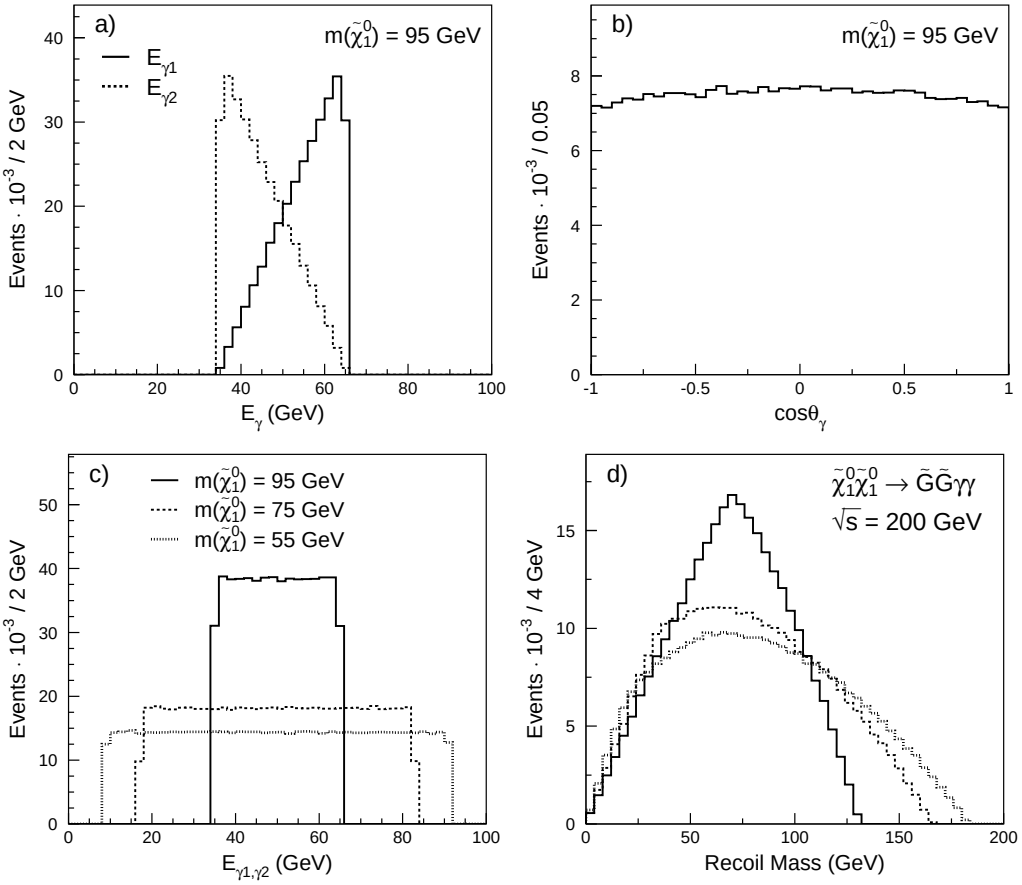

Figure 3.8: Kinematic distributions for the reaction $e^+e^- \to \tilde{\chi}_1^0\tilde{\chi}_1^0 \to \tilde{G}\tilde{G}\gamma\gamma$ at $\sqrt{s} = 200$ GeV, with arbitrary normalization. The distributions of a) $E_{\gamma_1}, E_{\gamma_2}$ and b) $\cos\theta_\gamma$ are shown for $m_{\tilde{\chi}_1^0} = 95$ GeV. Also shown are c) the photon energy and d) the recoil mass spectra, for various values of $m_{\tilde{\chi}_1^0}$.

The decay length L can be calculated using Equation 3.15 and expressed as [60]

$$L \;=\; 1.76 \cdot 10^{-3}\,(\kappa_\gamma)^{-1} \left(\frac{s}{4m^2_{\tilde{\chi}_1^0}} - 1\right)^{1/2} \left(\frac{100\ \text{GeV}}{m_{\tilde{\chi}_1^0}}\right)^5 \left(\frac{m_{\tilde{\mathrm{G}}}}{1\ \text{eV}}\right)^2 \text{cm}\,, \tag{3.21}$$

where, due to the dominantly bino nature of the neutralino, $(\kappa_\gamma)^{-1} \simeq 1.3$. For instance, for $\sqrt{s} = 200$ GeV, $m_{\tilde{\chi}_1^0} = 80$ GeV, and $m_{\tilde{\mathrm{G}}} = 200$ eV the neutralino decay length is approximately 2 m. In this case, the majority the neutralinos would decay inside the detector, away from the beam vertex.

As I will show in Chapter 7, the efficiency of the usual multi-photon selection drops significantly for decay lengths larger than about 10 cm. In order to investigate

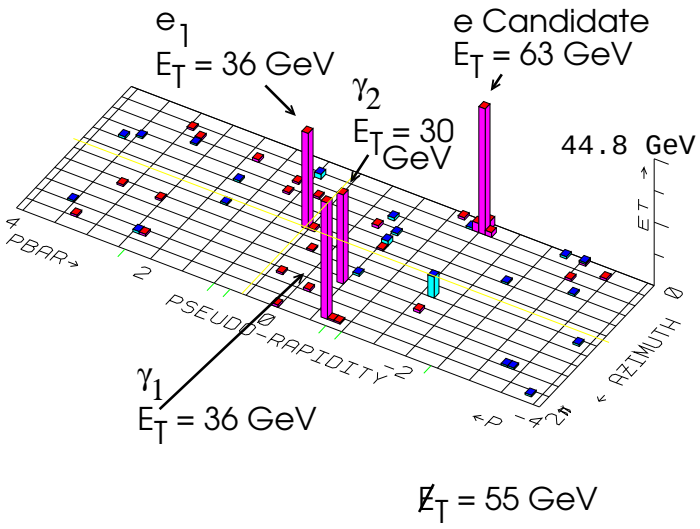

Figure 3.9: The ee$\gamma\gamma$ event observed by the CDF experiment [67].

the region of intermediate decay lengths, $0.1\,\mathrm{m} \lesssim L \lesssim 100\,\mathrm{m}$, I developed a new event selection which was able to identify *non-pointing* photons, i.e., photons not originating from the primary event vertex.

3.2.2 The CDF Event

In 1995, the CDF experiment at the Tevatron $p\bar{p}$ collider observed an event with two high-energy electrons, two high-energy photons, and a large amount of missing transverse energy (see Figure 3.9) [67]. There is no obvious explanation for this event in the Standard Model. The only Standard Model process able to produce such ee$\gamma\gamma$ events consists of the WW$\gamma\gamma$ production, where each W boson decays into an electron and a neutrino. However, the event rate from this process is expected to be very low and has been estimated by the CDF collaboration to be $(1 \pm 1) \cdot 10^{-6}$ events in their data sample corresponding to $85\,\mathrm{pb}^{-1}$ [67].

As a consequence, this unusual event generated a lot of interest among particle theorists, resulting in a publication of dozens of papers with various interpretations in models with physics beyond the Standard Model. In particular, this event has brought wide attention to photonic signatures in SUSY.

In GMSB models, this event is a candidate for the process $q\bar{q} \rightarrow \tilde{e}_R^+\tilde{e}_R^-$ with subsequent decays $\tilde{e}_R^\pm \rightarrow e^\pm \tilde{\chi}_1^0$ and $\tilde{\chi}_1^0 \rightarrow \tilde{G}\,\gamma$, where the neutralinos and gravitinos escape detection.[9] Regions kinematically allowed for the CDF event correspond to 85 GeV $< m_{\tilde{e}_R} <$ 135 GeV and 50 GeV $< m_{\tilde{\chi}_1^0} <$ 100 GeV [68]. This means that the reaction $e^+e^- \rightarrow \tilde{\chi}_1^0\tilde{\chi}_1^0 \rightarrow \tilde{G}\tilde{G}\gamma\gamma$ could provide an excellent opportunity for SUSY discovery at LEP. This reaction was examined in the previous section.

The CDF event has also been interpreted in neutralino LSP models [69]. Again, the selectron pair-production in $q\bar{q}$ collisions can be the origin of this event, with the selectrons decaying into an electron and a $\tilde{\chi}_2^0$, and the $\tilde{\chi}_2^0$ then decaying radiatively to $\tilde{\chi}_1^0$. Within this framework, the event can only be accommodated in models with relaxed GUT boundary conditions for the gaugino mass parameters (see Equation 3.11). If this is the explanation for the CDF event, the best possibility for SUSY discovery at LEP is the reaction $e^+e^- \rightarrow \tilde{\chi}_2^0\tilde{\chi}_2^0 \rightarrow \tilde{\chi}_1^0\tilde{\chi}_1^0\gamma\gamma$. This reaction is examined in the next section.

In conclusion, searches for photonic events from the neutralino-pair production at LEP were highly motivated by the above interpretations of the CDF event.

3.2.3 Neutralino Production in SUGRA

In SUGRA models, the appearance of photonic final states with missing energy is possible only in the scenario where the R–parity is conserved, the next-to-lightest neutralino $\tilde{\chi}_2^0$ is the NLSP, and the lightest neutralino $\tilde{\chi}_1^0$ is the LSP. Moreover, the radiative decay $\tilde{\chi}_2^0 \rightarrow \tilde{\chi}_1^0\gamma$ should be the dominant decay mode. This decay mode is usually suppressed since it is a one-loop process (see Figure 3.10). In most SUSY scenarios, the next-to-lightest neutralino decays predominantly via $\tilde{\chi}_2^0 \rightarrow \tilde{\chi}_1^0 f\bar{f}$ through an exchange of a virtual sfermion or a Z boson.

As discussed in Section 3.1.2, the neutralinos are in general a superposition of the neutral gauginos and higgsinos. The couplings of sfermions to neutralinos involve only the gaugino component, while the Z boson couples only to the higgsino

[9] Chargino production also provides a possible explanation: $q\bar{q} \rightarrow \tilde{\chi}_1^+\tilde{\chi}_1^-$ with the decays $\tilde{\chi}_1^\pm \rightarrow e^\pm\,\nu_e\,\tilde{\chi}_1^0$ and $\tilde{\chi}_1^0 \rightarrow \tilde{G}\,\gamma$.

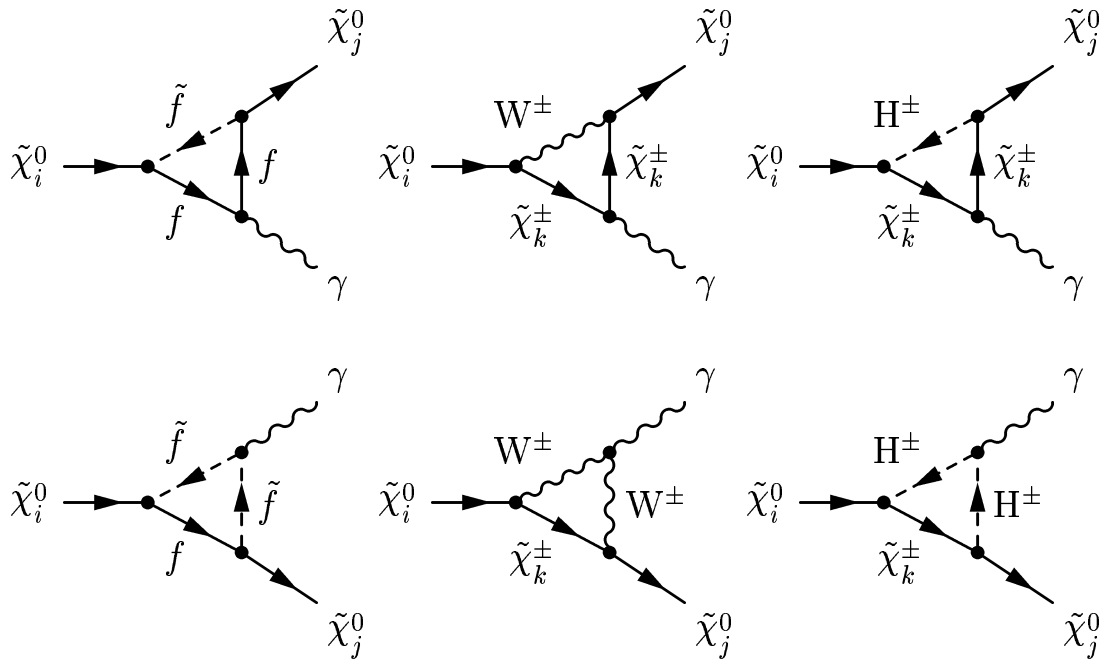

Figure 3.10: Feynman graphs for the radiative neutralino decay $\tilde{\chi}^0_2 \to \tilde{\chi}^0_1\gamma$.

component [70]. Hence, the tree-level decays $\tilde{\chi}^0_2 \to \tilde{\chi}^0_1 f\bar{f}$ require either simultaneous gaugino components in both neutralinos for the sfermion exchange process or simultaneous higgsino components for the Z exchange process. The above condition is not needed for the radiative decay, where both the gaugino and the higgsino components of neutralinos may be involved (apart from the two graphs on the left-hand side of Figure 3.10). Therefore, whenever the lightest neutralino is mainly higgsino and the next-to-lightest neutralino is mainly gaugino, the tree level $\tilde{\chi}^0_2$ width for the direct three-body decay is reduced and the radiative decay $\tilde{\chi}^0_2 \to \tilde{\chi}^0_1\gamma$ is enhanced.

It should be noted that this scenario is allowed only in a limited region of the MSSM parameter space [70]. However, it is favored by the SUGRA interpretation of the CDF event [69]. In particular, this scenario implies that the next-to-lightest neutralino is almost pure photino, $\tilde{\chi}^0_2 \simeq \tilde{\gamma}$, and the lightest neutralino is almost pure higgsino, $\tilde{\chi}^0_1 \simeq \tilde{\mathrm{H}}_b$, where $\tilde{\mathrm{H}}_b = \sin\beta\,\tilde{\mathrm{H}}_1 + \cos\beta\,\tilde{\mathrm{H}}_2$. In this case, the radiative decay $\tilde{\chi}^0_2 \to \tilde{\chi}^0_1\gamma$ is expected to have a branching ratio of almost 100%.

In this SUGRA scenario, the pair-production of neutralinos $\mathrm{e^+e^-} \to \tilde{\chi}^0_2\tilde{\chi}^0_2$ with a

subsequent decay $\tilde{\chi}_2^0 \to \tilde{\chi}_1^0\gamma$ leads to events with two photons and missing energy (due to the escaping neutralinos). The production mechanism and event topology are very similar to those of the GMSB process $e^+e^- \to \tilde{\chi}_1^0\tilde{\chi}_1^0 \to \tilde{G}\tilde{G}\gamma\gamma$, which was described in Section 3.2.1. Again, the dominant contributions come from the t– and u–channel $\tilde{e}_{R,L}$ exchange diagrams, and the radiative decay of the neutralino is isotropic in its rest frame. For a given center-of-mass energy, the $e^+e^- \to \tilde{\chi}_2^0\tilde{\chi}_2^0$ cross section depends only on the neutralino and selectron masses and is given by [63]

$$\frac{d\sigma}{d\cos\theta} = \sum_{i=\tilde{e}_R,\tilde{e}_L} \frac{\pi\alpha^2 s\beta^3}{4}\Big[\Big(\Delta M_i^2 + \frac{s}{2}\Big)^2 - \frac{s^2\beta^2}{4}\cos^2\theta\Big]^{-2} \times \Big[\frac{s^2\beta^2}{4}\cos^4\theta - s\Big[2\Big(\Delta M_i^2 + \frac{s}{2}\Big) - m_{\tilde{\chi}_2^0}^2 - \frac{s}{4}\Big]\cos^2\theta + \Big(\Delta M_i^2 + \frac{s}{2}\Big)^2\Big(1+\cos^2\theta\Big)\Big], \quad (3.22)$$

where $\sqrt{s}$ is the center-of-mass energy, θ is the polar angle, $\beta = \sqrt{1 - 4m_{\tilde{\chi}_2^0}^2/s}$ is the neutralino velocity in the laboratory frame, and $\Delta M_i = m_i^2 - m_{\tilde{\chi}_2^0}^2$. The pair-produced neutralinos are photino-like so that their couplings to the left- and right-selectrons are identical. This means that for $m_{\tilde{e}_R} = m_{\tilde{e}_L}$, the contributions from the $\tilde{e}_R$ and $\tilde{e}_L$ exchange diagrams are the same.

The photon energy and angular distributions have the same flat shape as the distributions from the GMSB reaction $e^+e^- \to \tilde{\chi}_1^0\tilde{\chi}_1^0$ (see Figure 3.8). However, in this case the lightest neutralino cannot be assumed to be massless, so that the expression for the kinematically allowed range of the photon energy needs to modified as

$$E_{\max,\min} = \frac{E_{\tilde{\chi}_2^0}}{2}\left(1 \pm \sqrt{1 - \frac{m_{\tilde{\chi}_2^0}^2}{E_{\tilde{\chi}_2^0}^2}}\right)\frac{m_{\tilde{\chi}_2^0}^2 - m_{\tilde{\chi}_1^0}^2}{m_{\tilde{\chi}_2^0}^2}, \quad (3.23)$$

where $E_{\tilde{\chi}_2^0} = \sqrt{s}/2$. Because the event topologies for the SUGRA and GMSB processes ($e^+e^- \to \tilde{\chi}_2^0\tilde{\chi}_2^0$ and $\tilde{\chi}_1^0\tilde{\chi}_1^0$) are essentially the same, for this signal I will use the same search strategy that I described in Section 3.2.1.

Neutralino production in SUGRA can also lead to a single-photon event topology via the reaction $e^+e^- \to \tilde{\chi}_2^0\tilde{\chi}_1^0$ with a subsequent decay $\tilde{\chi}_2^0 \to \tilde{\chi}_1^0\gamma$ [62]. However, for the photino-like $\tilde{\chi}_2^0$ and higgsino-like $\tilde{\chi}_1^0$, the cross section for this process is expected

to be extremely low [64]. Nevertheless, I will search for this reaction in the context of the model-independent search $e^+e^- \rightarrow XY \rightarrow YY\gamma$, where X and Y are new neutral invisible particles. As above, the photon energy and angular distributions are flat, and the kinematically allowed range of the photon energy is given by Equation 3.23, where the neutralino energy is $E_{\tilde{\chi}_2^0} = (s + m^2_{\tilde{\chi}_2^0} - m^2_{\tilde{\chi}_1^0})/(2\sqrt{s})$.

3.2.4 The Reactions $e^+e^- \rightarrow \tilde{\chi}_1^0\widetilde{G}$ and $e^+e^- \rightarrow \widetilde{G}\widetilde{G}\gamma$

In Section 3.1.3 I discussed models with gauge-mediated supersymmetry breaking, where the LSP is the gravitino with a mass in the eV to keV range. Such light gravitinos can also arise in other SUSY models.

Even without any assumptions about the mechanism of supersymmetry breaking, the mass of the gravitino would still be coupled to the scale of local supersymmetry breaking by Equation 3.13. When the scale of local supersymmetry breaking is decoupled from the breaking of global supersymmetry, as in no-scale supergravity models [71], the gravitino can become *superlight* (10^{-6} eV $\lesssim m_{\widetilde{G}} \lesssim 10^{-4}$ eV) and can be produced not only in decays of SUSY particles but also directly, either in pairs [72] or associated with a neutralino [68, 73]. The process $e^+e^- \rightarrow \tilde{\chi}_1^0\tilde{\chi}_1^0 \rightarrow \widetilde{G}\widetilde{G}\gamma\gamma$ can also be interpreted [74] in terms of the MSSM model parameters M_2, μ and $\tan\beta$, which were introduced in Section 3.1.2.

No-scale supergravity becomes especially predictive in a model with flipped SU(5) gauge symmetry [75], where only one free parameter is needed to determine the whole mass spectrum of the MSSM except the gravitino mass [68]. This model was proposed by Lopez, Nanopoulos, and Zichichi, and is traditionally referred to as the LNZ model. Figure 3.11 shows that in the LNZ model the lightest neutralino is usually the NLSP. Phenomenologically, this model is the same as the neutralino LSP scenario in GMSB except that the gravitino mass is several orders of magnitude smaller and the neutralino always decays at the event vertex.

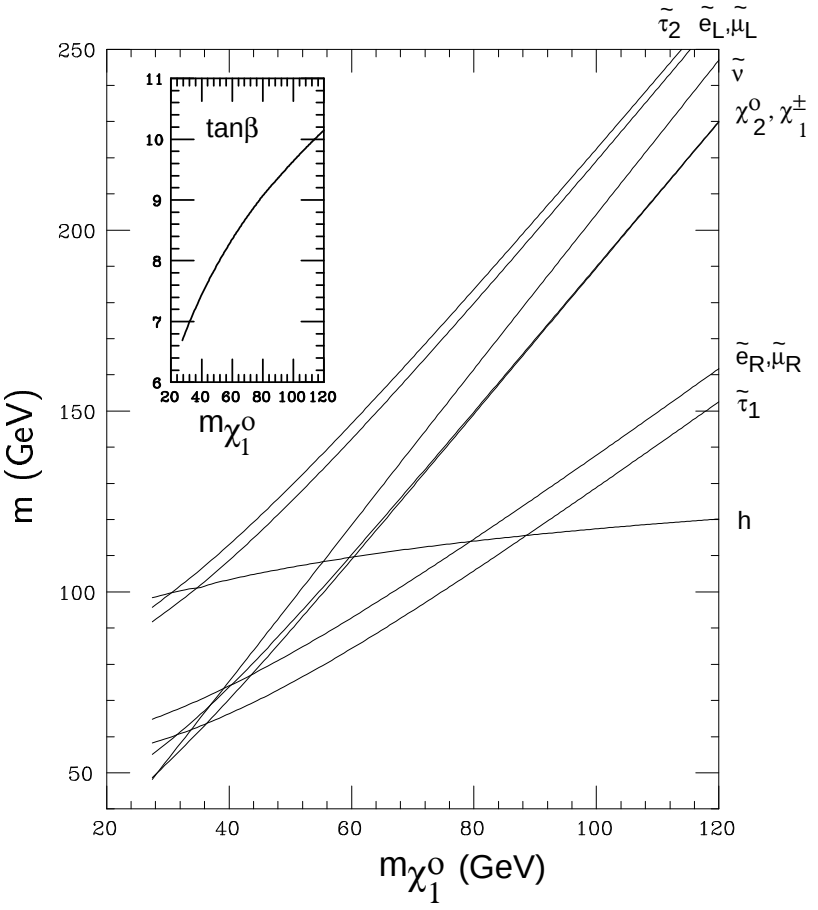

Figure 3.11: Masses of the lighter MSSM particles in the LNZ model versus the neutralino mass. The inset shows the variation of $\tan\beta$ with $m_{\tilde{\chi}^0_1}$ [68].

$\tilde{\chi}^0_1\widetilde{G}$ Production

The reaction $e^+e^- \to \tilde{\chi}^0_1\tilde{G} \to \tilde{G}\tilde{G}\gamma$ would lead to events with a single photon and missing energy in the final state. The Feynman diagrams of this process are shown in Figure 3.12. This reaction is expected have a sizable event rate at LEP2 only for very light gravitinos, $m_{\tilde{G}} \lesssim 10^{-4}$ eV, since its cross section scales as the inverse of the gravitino mass squared [73]. Thus, this process does not play a role in GMSB models where the gravitino is much heavier (see Section 3.1.3).

Due to the bino-like nature of the neutralino, the radiative decay $\tilde{\chi}^0_1 \to \tilde{G}\gamma$ is always the dominant decay mode. However, if the neutralino is heavier than the Z boson, the contribution of the decay into the Z needs to be taken into account. For

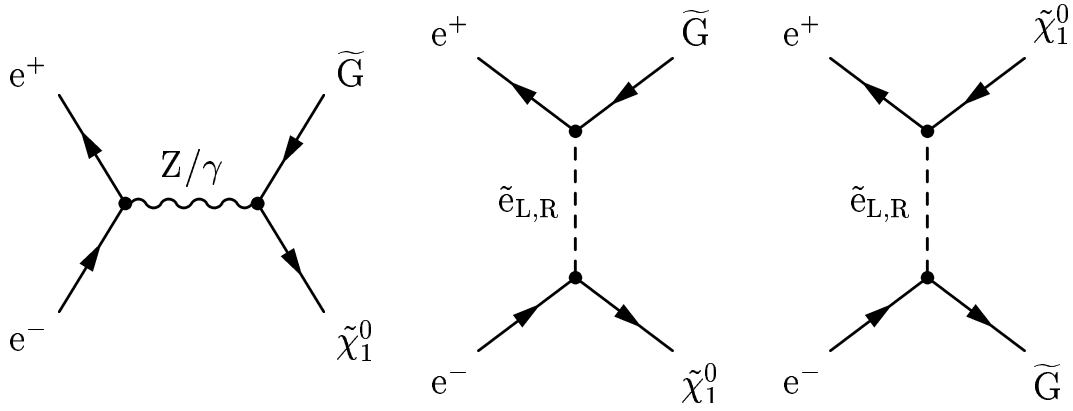

Figure 3.12: Feynman diagrams for the reaction $e^+e^- \to \tilde{\chi}_1^0\tilde{G}$.

instance, if $m_{\tilde{\chi}_1^0} = 200$ GeV, the branching ratio of the decay $\tilde{\chi}_1^0 \to \tilde{G}Z$ is equal to about 10% (see Equations 3.15 and 3.16).

In order to investigate the kinematic distributions of this process, I used samples of 300,000 MC events generated with the `SUSYGEN` program for two different values of the neutralino mass, $m_{\tilde{\chi}_1^0} = 150, 180$ GeV, at $\sqrt{s} = 200$ GeV, which corresponded to the typical center-of-mass energy of LEP2. Figure 3.13 shows that the resulting distributions of the photon energy and the cosine of the polar angle are again almost flat, where the kinematically allowed range for the photon energy is given by

$$\frac{m_{\tilde{\chi}_1^0}^2}{2\sqrt{s}} < E_\gamma < \frac{\sqrt{s}}{2}\,. \tag{3.24}$$

In this search channel, the principal background comes from the Standard Model process $e^+e^- \to \nu\bar{\nu}\gamma$ (see Section 2.2.2) whose differential cross sections are also shown in Figure 3.13. The kinematic distributions of the signal are very different from those of the background. For a large fraction of signal events, the photon energy is expected above the Z-return peak of the reaction $e^+e^- \to \nu\bar{\nu}\gamma$, where the Standard Model background is expected to be very low. Thus, a clean separation of the signal from the background can be achieved by an appropriate lower cut on the photon energy.

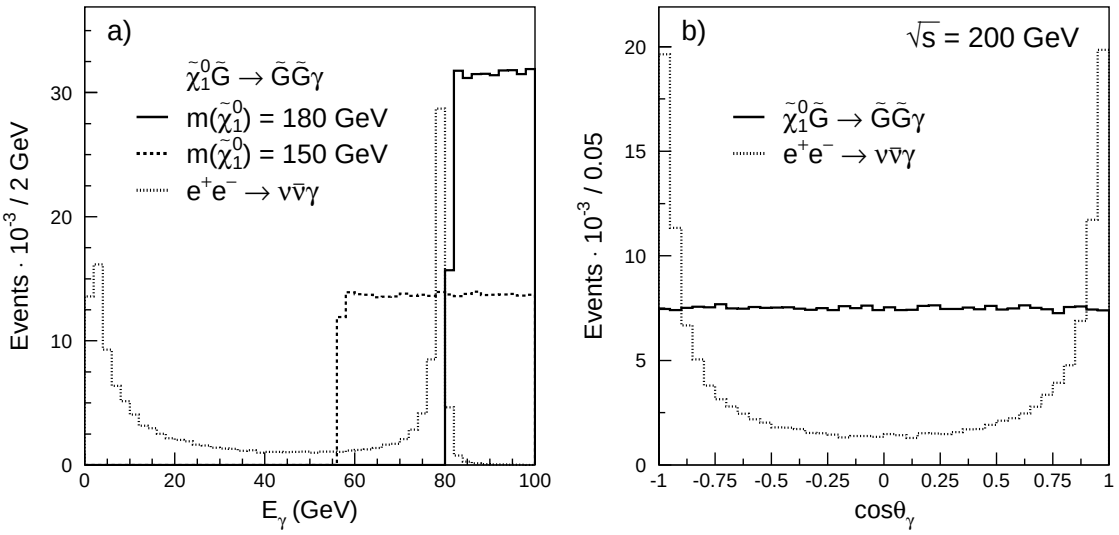

Figure 3.13: Distributions of a) the photon energy and b) the photon polar angle for the reaction $e^+e^- \to \tilde{\chi}_1^0\tilde{G} \to \tilde{G}\tilde{G}\gamma$ at $\sqrt{s} = 200$ GeV. Also shown are the corresponding distributions for the dominant background process $e^+e^- \to \nu\bar{\nu}\gamma$ with arbitrary normalization.

Gravitino Pair-Production

If the masses of all other SUSY particles are greater than the center-of-mass energy available at LEP, then the superlight gravitinos could still be detected via the reaction $e^+e^- \to \tilde{G}\tilde{G}\gamma$ [72, 76]. This process proceeds predominantly via initial-state radiation in the gravitino pair-production process, and its differential cross section is given by [72]

$$\frac{d^2\sigma}{dx_\gamma\, d\cos\theta_\gamma} = \left(\frac{\alpha {G_N}^2}{45}\right) \frac{s^3}{{m_{\tilde{G}}}^4}\, f(x_\gamma, \theta_\gamma)\,, \tag{3.25}$$

where G_N is the gravitational constant, $m_{\tilde{G}}$ is the gravitino mass, x_γ is the photon scaled energy $(E_\gamma/E_{\rm beam})$, θ_γ is the polar angle, and

$$f(x,\theta) = 2(1-x)^2 \left[\frac{(1-x)(2-2x+x^2)}{x\sin^2\theta} + \frac{x(-6+6x+x^2)}{16} - \frac{x^3\sin^2\theta}{32}\right]. \tag{3.26}$$

The production cross section depends only on one SUSY parameter – the gravitino mass. The photon energy spectrum is expected to be soft, as shown in Figure 3.14. Unfortunately, the dominant background process $e^+e^- \to \nu\bar{\nu}\gamma$ also proceeds via initial-

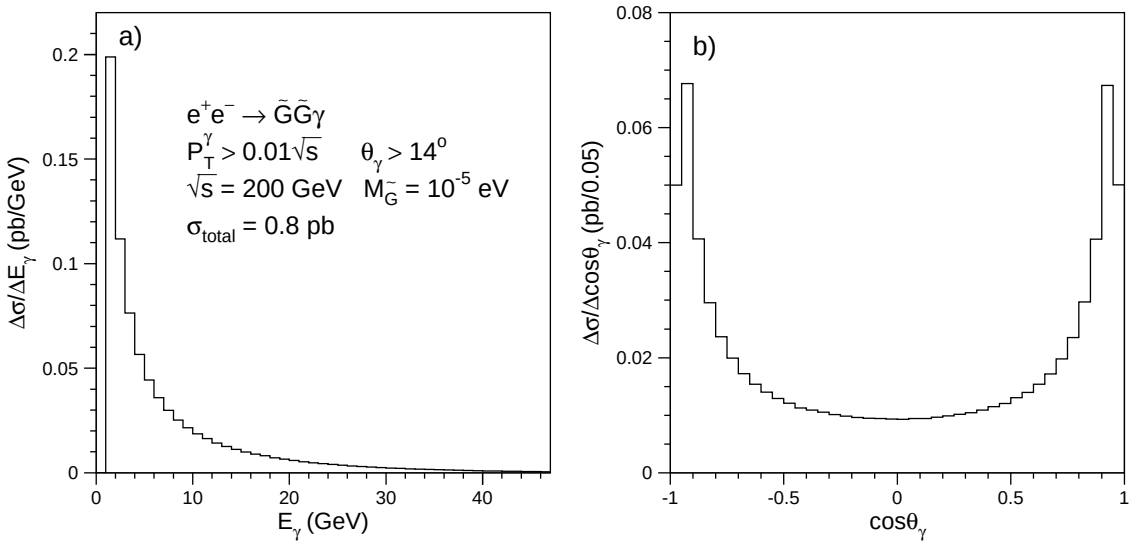

Figure 3.14: Differential cross sections of the reaction $e^+e^- \to \tilde{G}\tilde{G}\gamma$ as functions of a) the photon energy and b) $\cos\theta_\gamma$, calculated for $\sqrt{s} = 200$ GeV and $m_{\tilde{G}} = 10^{-5}$ eV.

state radiation, and its kinematic distributions are expected to be similar to those of the signal[10] (see Figures 2.8 and 2.7 in Section 2.2.2). Therefore, a clean separation of the signal from the background is not possible for this search channel.

3.2.5 Summary

In this section I briefly summarize the photonic SUSY signatures and the corresponding theoretical models. Common to all scenarios I considered are the requirements that the R–parity is conserved and that the lightest supersymmetric particle is colorless and electrically neutral (see Section 3.1). Two distinct signatures are investigated: events with a single photon plus missing energy and events with two photons plus missing energy in the final state. Several SUSY models predict processes that could lead to such signals at LEP.

Three SUSY processes could yield the single-photon signature: $\tilde{\chi}_1^0\tilde{\chi}_2^0$ production in SUGRA models where the neutralino is the LSP (see Section 3.2.3) and $\tilde{\chi}_1^0\tilde{G}$ and $\tilde{G}\tilde{G}\gamma$ production in models with superlight gravitinos, such as no-scale SUGRA

[10] The differential cross section of the signal does not have the Z-return peak.

Signature	Process	Decay	Model
$\gamma + E_{\mathrm{miss}}$	$\tilde{\chi}_1^0\tilde{\chi}_2^0$	$\tilde{\chi}_2^0 \to \tilde{\chi}_1^0\gamma$	SUGRA [62]
	$\tilde{\chi}_1^0\tilde{\mathrm{G}}$	$\tilde{\chi}_1^0 \to \tilde{\mathrm{G}}\gamma$	no-scale SUGRA, LNZ [68, 73]
	$\tilde{\mathrm{G}}\tilde{\mathrm{G}}\gamma$	—	no-scale SUGRA [72]
$\gamma\gamma + E_{\mathrm{miss}}$	$\tilde{\chi}_2^0\tilde{\chi}_2^0$	$\tilde{\chi}_2^0 \to \tilde{\chi}_1^0\gamma$	SUGRA [62]
	$\tilde{\chi}_1^0\tilde{\chi}_1^0$	$\tilde{\chi}_1^0 \to \tilde{\mathrm{G}}\gamma$	GMSB [65]
			no-scale SUGRA [73]

Table 3.2: Summary of the single- and multi-photon signatures in SUSY.

(see Section 3.2.4). The $\tilde{\chi}_1^0\tilde{\mathrm{G}}$ process can also be interpreted in the framework of the LNZ model, which is a more restrictive no-scale SUGRA model. An additional requirement needs to be imposed for the $\tilde{\mathrm{G}}\tilde{\mathrm{G}}\gamma$ process — all other SUSY particles have to be heavier than the center-of-mass energy [72].

The two-photon signature can arise from two similar reactions: $\tilde{\chi}_2^0\tilde{\chi}_2^0$ production in neutralino LSP models (see Section 3.2.3) and $\tilde{\chi}_1^0\tilde{\chi}_1^0$ production in gravitino LSP models (see Section 3.2.1). Searches for both these reactions at LEP are highly motivated by supersymmetric interpretations of the unusual event observed by the CDF experiment (see Section 3.2.2). The first process can be discussed in terms of the SUGRA model parameters introduced in Section 3.1.3. The second process is predicted by GMSB and no-scale SUGRA models (Sections 3.1.3 and 3.2.4). In GMSB models, the lightest neutralino can have a macroscopic decay length, which requires a special selection for photons not originating from the primary event vertex.

The photonic signatures and the corresponding SUSY processes and models are summarized in Table 3.2. The Standard Model background for these final-state topologies comes from the neutrino pair-production process accompanied by one or more photons from initial-state radiation, $\mathrm{e^+e^-} \to \nu\bar{\nu}\gamma(\gamma)$. Usually this background process can be almost completely suppressed using simple cuts on the photon energy and polar angle (see Sections 3.2.1 and 3.2.4). The only exception is the reaction $\mathrm{e^+e^-} \to \tilde{\mathrm{G}}\tilde{\mathrm{G}}\gamma$, where the signal cannot be separated from the Standard Model background.

3.3 Models with Large Extra Dimensions

The large disparity between the weak scale ($M_{\text{weak}} \sim 10^2$ GeV) and the traditional scale of gravity given by the Planck scale ($M_{\text{Pl}} \sim 10^{19}$ GeV) is considered to be one of the major theoretical problems in elementary particle physics. The origin of this large gap, as well as its stability under quantum corrections, demands explanation. This is known as the *hierarchy problem* of the Standard Model. The hierarchy problem can be successfully cured by introducing supersymmetry at the weak scale, as described in Section 3.1. Below I discuss another class of theories that are capable of addressing the hierarchy problem, models with *large extra dimensions* [77].

These models assume that the Standard Model fields, including ourselves, are confined to a four-dimensional hypersurface (brane) inside the full space-time (bulk), whereas the gravitational fields are also allowed to propagate in n extra spatial dimensions. We currently have almost no knowledge of gravity at distances less than about a millimeter since direct tests of Newton's law are based on torsion-balance experiments that are mechanically limited [78, 79]. Hence, it is conceivable that gravity may behave differently at small scales.

However, Newton's law must be reproduced at large distances so that gravity must behave as if there were only three spatial dimensions for $r \gtrsim 1\,\text{mm}$. In the ADD scenario[11] this is achieved by compactifying the extra dimensions on circles, where the geometry of these dimensions is flat and the topology is that of a torus.

The fundamental gravitational scale M_D is then related to the Planck scale through

$$M_{\text{Pl}}^2 \sim M_D^{2+n} R^n, \tag{3.27}$$

where R is the radius of the extra dimensions. Thus, the fundamental scale of gravity can be lowered to the TeV range while the size of the compactified extra dimensions can be as large as a millimeter. The radius of the compactified extra dimensions (R) can be expressed as a function of the parameters M_D and n. Assuming compactifi-

[11] This scenario was originally proposed by Arkani-Hamed, Dimopoulos, and Dvali in 1998 [77].

cation on a torus, this relationship is given by [80]

$$G_N^{-1} = 8\pi R^n M_D^{n+2}, \tag{3.28}$$

where G_N^{-1} is Newton's constant of gravitation. The case of one extra spatial dimension is thus ruled out since for $M_D \sim$ TeV, it would alter Newton's law at distances comparable to the size of the solar system.

Extra spatial dimensions could manifest themselves at present and future colliders in a variety of ways [78]. In particular, in e^+e^- collisions they could lead to the single-photon and missing energy signature in processes involving production of gravitons and branons. Below I give a brief description of these processes.

3.3.1 Graviton-Photon Production

In the framework of large extra dimensions, gravitational fields propagating in the bulk can be expressed as a series of states known as a Kaluza-Klein tower. For an observer trapped on the brane, these graviton modes appear as massive spin-2 neutral particles (G) that can couple to the Standard Model fields on the brane. As a result, real gravitons can be produced in e^+e^- collisions through the direct emission of a graviton and a photon, $e^+e^- \rightarrow \gamma G$ [80, 81]. The produced graviton behaves as if it was a massive, stable, and non-interaction particle and thus appears as missing energy in the detector. As shown in Figure 3.15, this process is expected to proceed through s–channel photon exchange, t–channel electron exchange, and four-particle contact interactions [81].

The differential cross section of this process depends on both the M_D and n [80]:

$$\frac{d^2\sigma\,(e^+e^- \rightarrow \gamma G)}{dx_\gamma\, d\cos\theta_\gamma} = \frac{\alpha}{32s}\frac{\pi^{n/2}}{\Gamma(n/2)}\left(\frac{\sqrt{s}}{M_D}\right)^{n+2} f(x_\gamma, \cos\theta_\gamma)\,, \tag{3.29}$$

where x_γ is the ratio of the photon energy to the beam energy, θ_γ is the polar angle

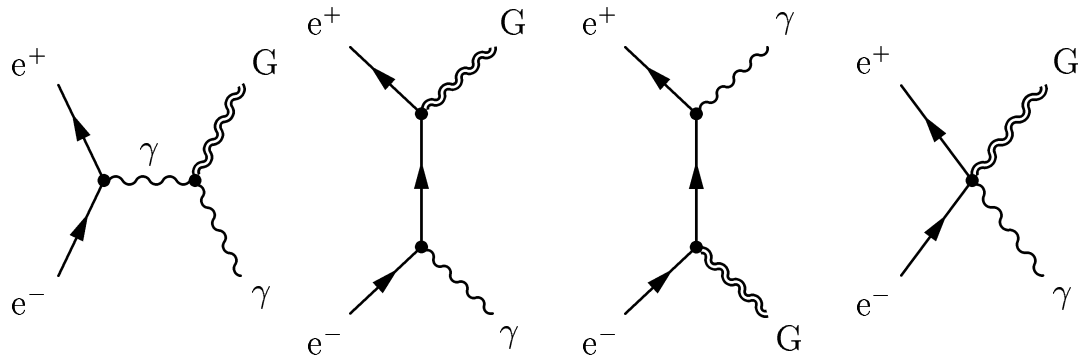

Figure 3.15: The lowest-order Feynman diagrams for the emission of a real graviton and a photon.

of the photon, α is the QED coupling, and the function $f(x, y)$ is given by

$$f(x,y) \;=\; \frac{2(1-x)^{\frac{n}{2}-1}}{x(1-y^2)}\left[(2-x)^2(1-x+x^2) - 3y^2x^2(1-x) - y^4x^4\right]. \qquad (3.30)$$

Figure 3.16 shows that the differential cross section increases rapidly at low photon energies and polar angles, where it scales as $(E_\gamma \sin^2\theta_\gamma)^{-1}$. The principal Standard Model background for this reaction comes from the process $e^+e^- \to \nu\bar{\nu}\gamma$, whose cross section also behaves as $\sim (E_\gamma \sin^2\theta_\gamma)^{-1}$ in the region of low E_γ and θ_γ (see Section A.1). Therefore, the graviton-photon signal cannot be separated from the $\nu\bar{\nu}\gamma$ background and can only be detected as an excess of events with one soft photon.

3.3.2 Branon Pair-Production in e^+e^- Collisions

A different theoretical scenario may also be considered. In this approach, the three-dimensional brane is treated as an additional physical body in the theory with its own dynamics. This may lead to the appearance of additional degrees of freedom corresponding to brane fluctuations along the extra-space dimensions, which would manifest themselves as new stable particles called *branons* ($\tilde{\pi}$) [82]. Their dynamics are determined by an effective theory with couplings of the same order as the brane tension (f). It should be noted that branons are natural dark-matter candidates [83] (see the discussion on dark-matter in Section 3.1).

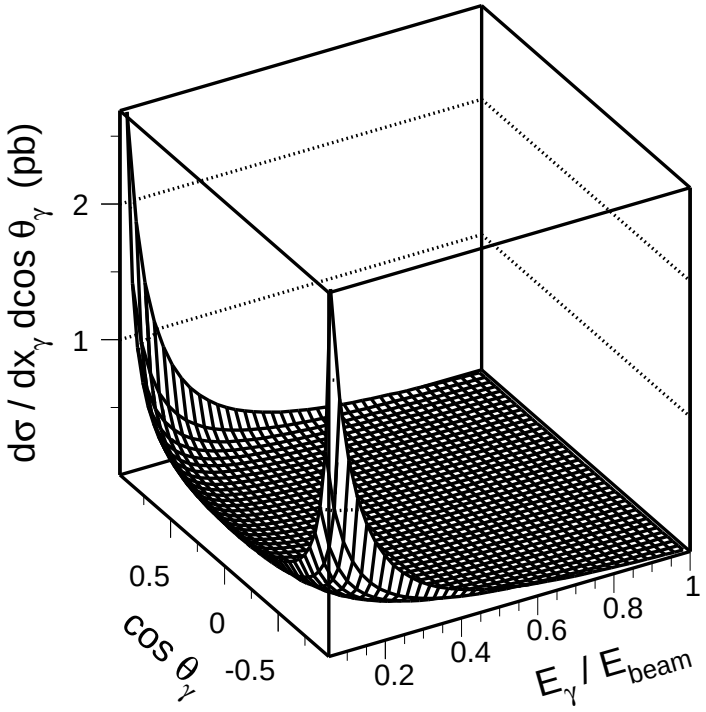

Figure 3.16: Differential cross section of the $e^+e^- \to \gamma G$ process, computed for $n = 2$, $M_D = 1.5$ TeV, and $\sqrt{s} = 207$ GeV.

Branons couple to the Standard Model particles in pairs and can be detected in e^+e^- collisions via the reaction $e^+e^- \to \tilde{\pi}\tilde{\pi}\gamma$. The Feynman diagrams of this process are shown in Figure 3.17. The final-state branons do not interact in the detector and are hence invisible. Thus, the experimental signature of the branon-photon production is the presence of a single photon together with missing energy. The differential cross section of this process is given by [84]

$$\frac{d^2\sigma\,(e^+e^- \to \tilde{\pi}\tilde{\pi}\gamma)}{dx_\gamma\, d\cos\theta_\gamma} = \frac{a_0 \alpha s}{f^8 \pi^2} \left(s(1-x_\gamma) - 4M^2\right)^2 \sqrt{1 - \frac{4M^2}{s(1-x_\gamma)}} \times \left[x_\gamma(3 - 3x_\gamma + 2x_\gamma^2) - x_\gamma^3 \sin^2\theta_\gamma + \frac{2(1-x_\gamma)(1+(1-x_\gamma)^2)}{x_\gamma \sin^2\theta_\gamma}\right], \tag{3.31}$$

where f is the brane tension, M is the branon mass,[12] $a_0 \equiv 1/61440$, and x_γ and θ_γ are the scaled energy and the polar angle of the photon ($x_\gamma = E_\gamma / E_{beam}$). The

[12]For simplicity, I consider a scenario with only one light branon species of mass M.

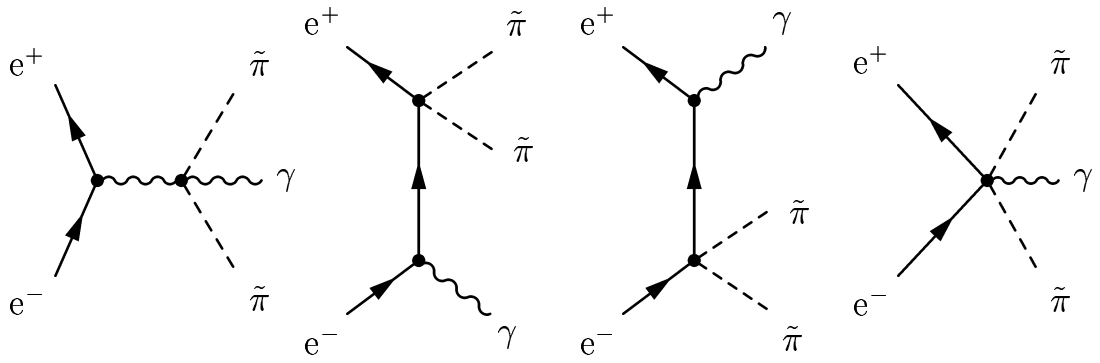

Figure 3.17: Feynman diagrams for the reaction $e^+e^- \to \tilde{\pi}\tilde{\pi}\gamma$.

kinematic properties of this signal are similar to those of the graviton-photon emission $e^+e^- \to \gamma G$, which was described in the previous section.

Searches for gravitons and branons are in a sense complementary [85]. If the brane tension is above the effective scale of gravity, $f \gg M_D$, the first evidence for extra dimensions would be the discovery of gravitons, giving information about the gravity scale and the number of extra spatial dimensions. If the brane tension is below the gravity scale, $f \ll M_D$, then the first signal of extra dimensions would be the discovery of branons, allowing a measurement of the brane tension scale, the number of branon species, and their masses [84].

Chapter 4

The L3 Detector at LEP

The work described in this thesis was based on data collected by the L3 detector at the LEP e^+e^- accelerator. This chapter gives an overview of these experimental facilities, with an accent on the elements important for my physics analyses.

4.1 The LEP Collider

The Large Electron-Positron (LEP) collider [86] was designed to provide electron-positron collisions at center-of-mass energies up to about 200 GeV. It was the largest synchrotron accelerator in the world, with the main ring tunnel having a circumference of 26.67 km. The tunnel crosses the French-Swiss border near Geneva and lies between 40 and 150 m below the surface. It is composed of eight 2.9 km long arcs and eight straight sections extending 210 m on either side of the eight collision points. The four LEP experiments, L3 [87], ALEPH [88], OPAL [89], and DELPHI [90] were installed in the large experimental halls built around even-numbered collision points. The layout of the LEP ring is shown in Figure 4.1.

4.1.1 LEP Injector Chain

Before entering the LEP ring, the electrons and positrons passed through a complex system of injectors. The injector chain started with a 200 MeV electron linac. Its intense electron beam was used to produce positrons in a tungsten target. The positrons emerging from the target and electrons produced by a nearby gun were accelerated to 600 MeV by another linac. The linacs operated at 100 Hz and delivered

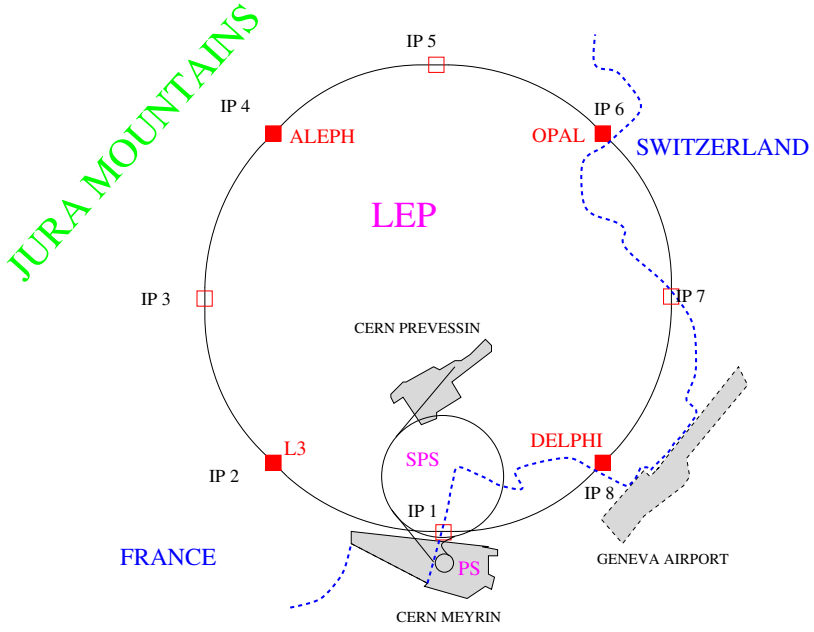

Figure 4.1: The LEP collider at CERN. The eight collision points are denoted as IP1-IP8.

the beam pulses which were then stored in eight bunches in the electron-positron accumulator ring (EPA). From the EPA, electrons and positrons were transferred to the next accelerator, the CERN Proton Synchrotron (PS), where they were accelerated to 3.5 GeV. The final element in the chain was the CERN Super Proton Synchrotron (SPS), which delivered the beams to LEP at an energy of 22 GeV. Figure 4.2 gives an overview of the LEP injector chain which is described in [91].

The advantage of building LEP at CERN was the possibility to include the already existing PS and SPS synchrotrons in the LEP injector chain. The PS is by far the oldest accelerator in use at CERN. It was built in 1959 and has a circumference of 630 m. The SPS was built in 1976 and has a circumference of 6.9 km. This accelerator allowed the breakthrough discovery of the W and Z bosons in 1983 by the UA1 and UA2 collaborations [92, 93]. Both the PS and SPS can accelerate not only electrons, but also protons and heavy ions. Moreover, the SPS was able to simultaneously operate as a LEP injector and produce stable 450 GeV proton beams for the fixed-

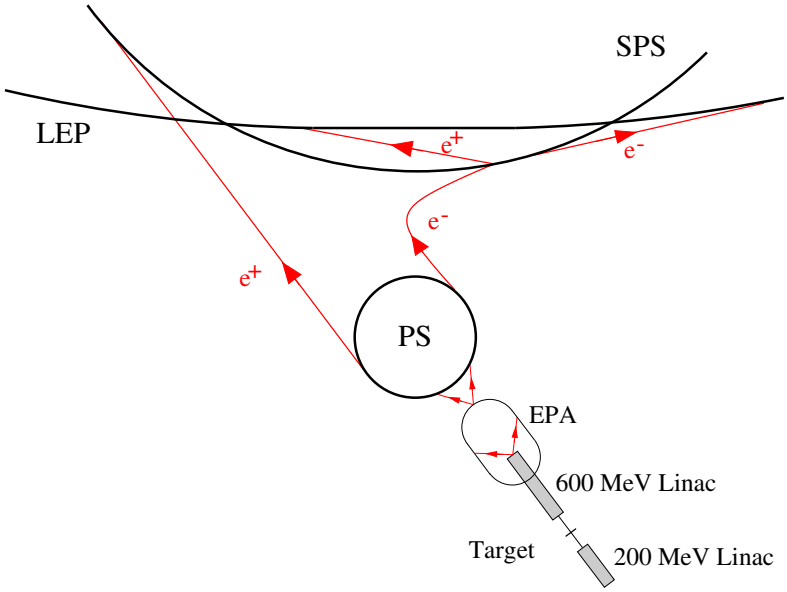

Figure 4.2: Layout of the LEP injector chain (dimensions not to scale).

target experiments. The Large Hadron Collider (LHC)[1] will soon replace LEP in its underground tunnel. However, due to their versatility, the PS and SPS synchrotrons will not be dismantled. Both of them will be used to inject proton and Pb ion beams into the LHC [94].

4.1.2 LEP Physics Program

Contrary to the fast-cycling PS and SPS, the LEP collider had a slow repetition rate. Each operation cycle, referred to as a *fill*, started by preparing the machine for injection at 22 GeV. Electrons and positrons were injected in parallel for 10-30 minutes. As soon as the filling process was finished, radio-frequency cavities accelerated the beams to the target energy at a rate of about 125 MeVs^{-1}. As electrons passed through a cell of a conducting (or superconducting) cavity, the electric fields within the cavity were timed to oscillate in the direction of acceleration. A corresponding timing was also present for the positrons, which counter-circulated in the same beam

[1]The LHC will be a proton-proton collider with a maximum center-of-mass energy of 14 TeV. It should either discover the Higgs Boson or disprove the existence of the Standard Model Higgs sector.

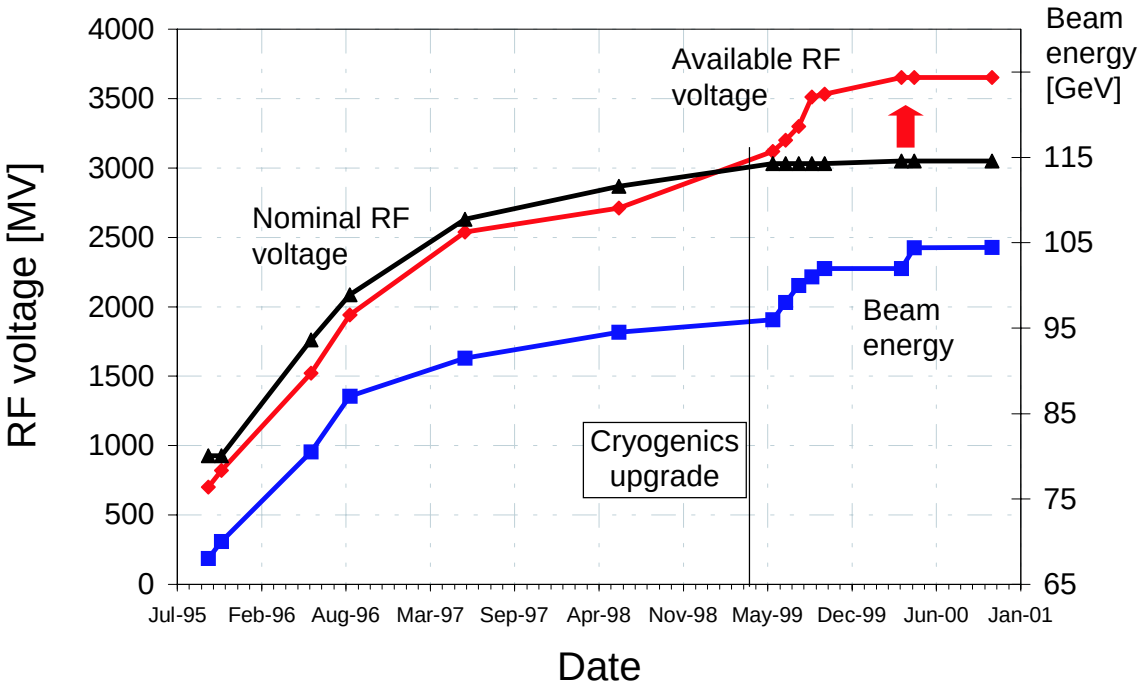

Figure 4.3: Time evolution of the LEP beam energy, the nominal (with the design accelerating gradient of 6 MV/m) and the available circumferential RF voltage.

pipe. A total of about 5400 magnets were used to focus and bend the beams into the required orbit.

LEP began operation in 1989. The LEP run from 1989 to 1995 was dedicated to precision studies of the Z boson properties. This period is referred to as LEP1. Electron-positron collisions were provided at several well-determined center-of-mass energies around the Z resonance, and the four LEP experiments collected 15.5 million Z decays into quarks plus 1.7 million leptonic Z decays. The most impressive result of the LEP1 physics program is the 2×10^{-5} accuracy on the Z boson mass measurement [95].

Starting in 1996 LEP began running at higher energies. Its center-of-mass energy gradually increased from about 90 GeV at LEP1 to almost 210 GeV in 2000, the last year of the LEP program. Attaining such high center-of-mass energies came with the high price tag of synchrotron radiation, emitted by electrons and positrons under

circular acceleration in LEP. The energy loss per particle per turn due to synchrotron radiation was given by [96]

$$\Delta \mathrm{E[eV]} \simeq 8.85 \times 10^4 \, \frac{\mathrm{E}^4[\mathrm{GeV}]}{\rho[\mathrm{m}]} \,, \tag{4.1}$$

where E was the beam energy and ρ was the average bending radius (3100 m for LEP). For a center-of-mass energy of 209 GeV, about 3.2% of the beam energy was lost per turn [97]. Thus, the maximum beam energy was limited by the available accelerating voltage provided by the RF cavities. The available accelerating voltage was increased in two ways:

- **Installation of additional RF cavities.** Between 1995 and 1999 most of the originally installed copper cavities were removed and replaced by the superconducting ones. The resulting voltage increase is shown by the graph "Nominal RF voltage" in Figure 4.3.

- **Increase of the accelerating gradient.** Until 1999, the accelerating gradient in the superconducting cavities was close to its design value of 6 MV/m [96]. After the cryogenics upgrade in 1999 it was continually improved to a maximum value of 7.5 MV/m [96] in 2000 (see Figure 4.3).

At the end of LEP its RF system consisted of 288 super-conducting cavities and 56 original copper cavities and provided more than 3.5 GV of accelerating voltage per turn.

The operation of the RF system could be disrupted by RF trips.[2] One RF trip would cause a reduction of about 100 MV in the available accelerating voltage. During the recovery time the maximum LEP beam energy was then reduced by about 0.8 GeV. The mean time between trips in 2000 was about 14 minutes, and the recovery time per trip was about 2-3 minutes. The average length of a fill at a given

[2]RF trips occurred on a statistical basis and were mainly produced by field emission, which could lead to local heating of cavity walls and a sharp rise in the pressure of the helium bath [97]. One trip would usually disrupt only one klystron at a time, leading to a temporary loss of eight superconducting cavities.

center-of-mass energy depended on the rate of the RF trips and the available RF margin, which was given by the difference between the maximum available RF voltage and the RF voltage required to sustain the beams at this center-of-mass energy. It was possible to operate LEP at an energy lower than the maximum one and still keep the beams during RF trips. However, at the maximum beam energy (without any RF margin) the average physics coast lasted only 14 minutes, whereas the fill set-up time was about 60 minutes. Operation at the maximum energy would be quite inefficient, and the luminosity production rate would be severely reduced. To achieve the highest effective beam energy and maintain an acceptable luminosity production level, a special ramping strategy (*mini-ramp strategy*) was implemented in the year 2000 [96]. A physics fill was started at a lower energy (2 RF trips margin), then ramped in collision to a medium energy (1 RF trip margin), and finished at the maximum beam energy (no margin). The balance between the effective energy and luminosity production rate was constantly optimized to achieve a maximum Higgs discovery potential.

The mini-ramp strategy employed in 2000 and the gradual increase of the accelerating gradient in 1999 resulted in a wide scatter of the LEP center-of-mass energies during the last two years of the LEP2 phase. Figure 4.4 shows the integrated luminosity collected by the L3 experiment during each year of the LEP2 program.[3] The data analyzed in this thesis was taken during 1998-2000, when L3 collected about 627 pb^{-1} at center-of-mass energies between 189 GeV and 208 GeV. The highest peak luminosity of about 1.2×10^{32} $\mathrm{cm}^{-2}\mathrm{s}^{-1}$ was achieved in 1999, corresponding to the average beam current of 5.5 mA (in two times 4 bunches).

LEP Beam Energy Measurement

The most important LEP operating parameter for physics studies is beam energy. At LEP1, the resonant depolarization method [98] was used to determine the beam energy to a precision of about 5 MeV [99]. The method utilized the Sokolov-Ternov effect [100] that leads to self-polarization of the beams parallel (and antiparallel) to

[3]The LEP2 phase officially started in 1996 when L3 collected about 20 pb^{-1} in the 160-170 GeV center-of-mass energy range.

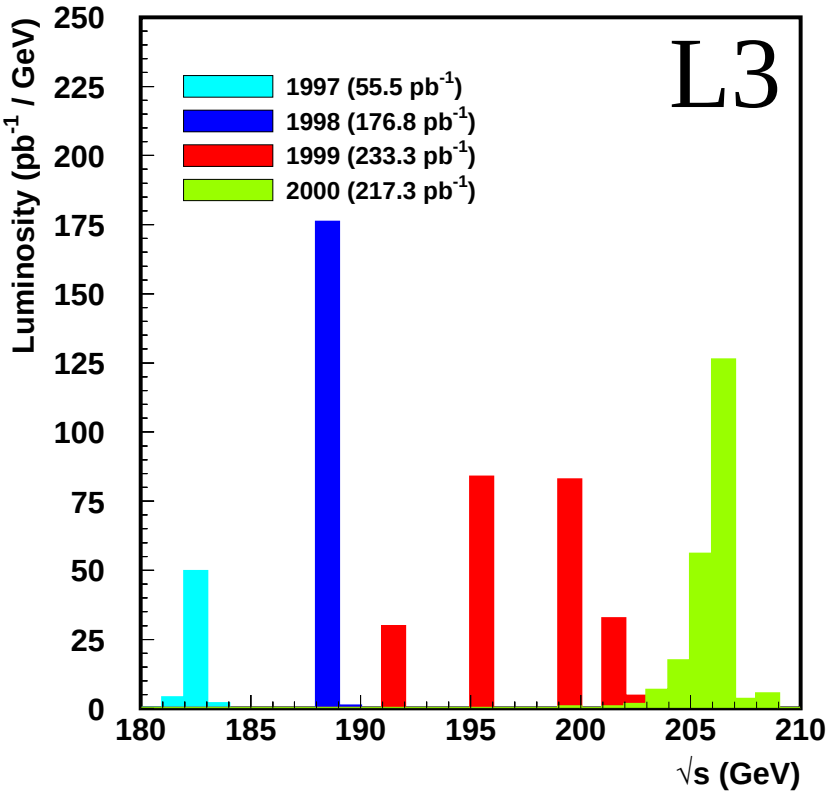

Figure 4.4: Integrated luminosity recorded by L3.

the magnetic bending field due to synchrotron radiation emission.

The precession frequency of the polarization vector was measured by inducing a resonant depolarization of the beam with a radial oscillating field from a coil. If the perturbation from the radial field was in phase with the spin precession, then the spin rotations about the direction of the perturbation field caused the spins of the particles to partially flip. About 10^4 turns or one second were needed to destroy the transverse polarization. The precession frequency was proportional to the electron's energy; thus one could extract the average beam energy by measuring the frequency of the perturbation field corresponding to the resonant depolarization.

Unfortunately, depolarizing effects due to magnetic field imperfections increased sharply with the beam energy. Thus, the method of resonant depolarization was impossible to use at beam energies above around 60 GeV. At LEP2, nuclear magnetic resonance (NMR) probes inserted in 16 of LEP dipole magnets were used to monitor

the magnetic field for a relative beam energy measurement. The probes were calibrated at lower energy using the resonant depolarization method. The uncertainty of the extrapolation to the actual LEP2 beam energies proved to be the leading error on the energy measurement.

In order to check the validity of the NMR-extrapolation method and to reduce the systematic error, a special magnetic spectrometer [101] was installed in 1999. The idea was to measure the beam trajectory before and after a special dipole magnet of known integrated field, thereby directly determining the beam energy during physics running at LEP2. Good agreement between the magnetic spectrometer and NMR-extrapolation methods was observed [102], and the total error on the LEP beam energy was estimated [103] to be about 11 MeV (or $\simeq$0.01%) and 20 MeV (0.02%) for the data taken in 1998-1999 and in 2000, respectively.[4]

4.2 The L3 Detector

The L3 detector was designed to reconstruct and identify particles produced in e^+e^- interactions and provide accurate measurements of both particle momenta and energies. Compared to the other three detectors at LEP, L3 emphasized precise energy measurements of electrons, photons, and muons. The majority of the detectors installed at particle colliders, including the L3 detector, may be described as a series of cylindrical, concentric subdetectors arranged around the beam pipe with the interaction point at the center and a set of endcap subdetectors covering the ends of the cylinders. The layout of the L3 detector is depicted in Figure 4.5.

Particles produced at the interaction point and traveling outwards through the L3 detector first encountered a set of two tracking subdetectors designed primarily to give information on the trajectories of charged particles (tracks). Since a surrounding coil provided a strong magnetic field inside the entire detector, the curvature of the track yielded the particle momentum. The particles then reached a high-density calorimeter

[4] The significant increase in uncertainty for 2000 was associated with a special magnetic field configuration, which was used in that year in order to boost the beam energy.

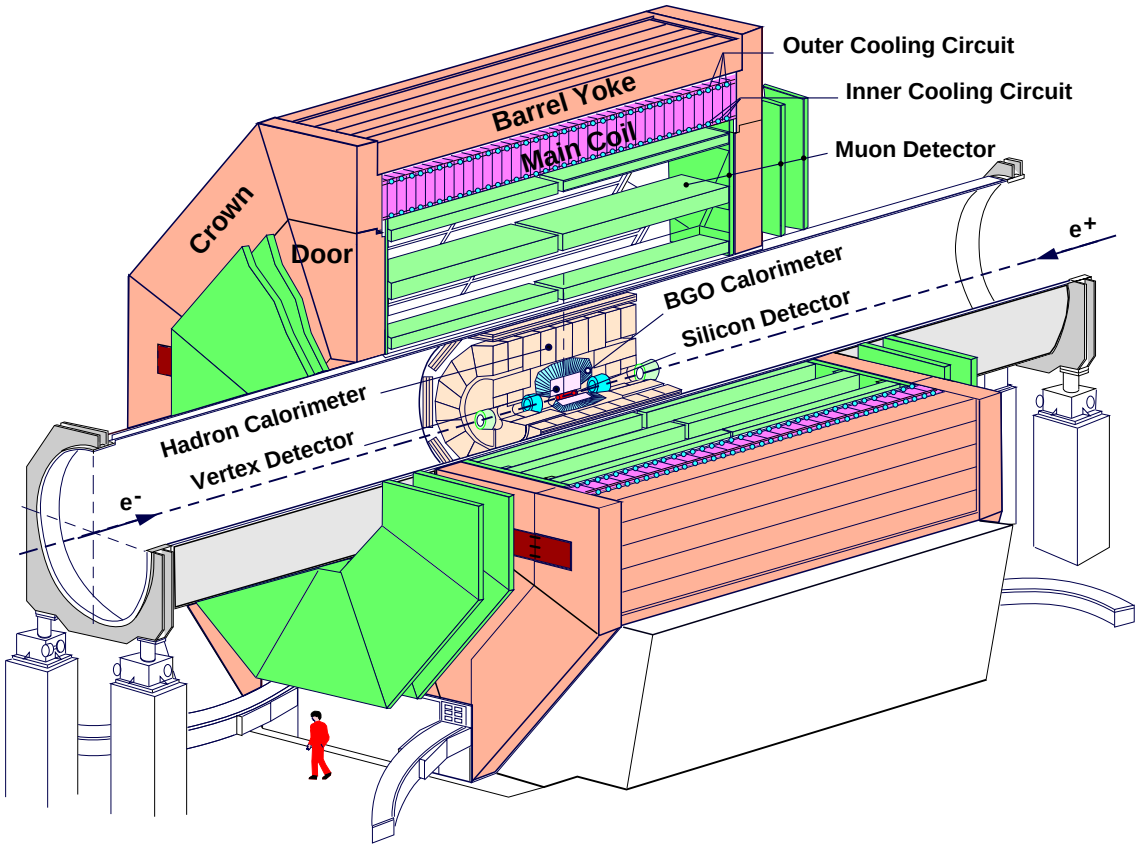

Figure 4.5: Perspective cut-away view of the L3 detector, showing the location of the subdetectors, the support tube and the magnet.

arrangement designed to help identify them and/or evaluate their energies. Any particles that managed to pass through the calorimeters entered the muon chambers designed to tag (identify) muons and measure their momenta. The tracking system and calorimeters were contained in a steel tube, which also supported the muon chambers and maintained the alignment of the subdetectors. Figure 4.6 shows a side view of the inner L3 detector.

The Cartesian (x,y,z) coordinate system used within L3 has its origin at the interaction point, which is also the geometrical center of the detector. The z-axis runs parallel to the beam-pipe in the electron beam direction. The x-axis points towards the center of LEP, while the y-axis points vertically upwards. A cylindrical coordinate system is also used with the origin and z-axis coinciding with those of the Cartesian

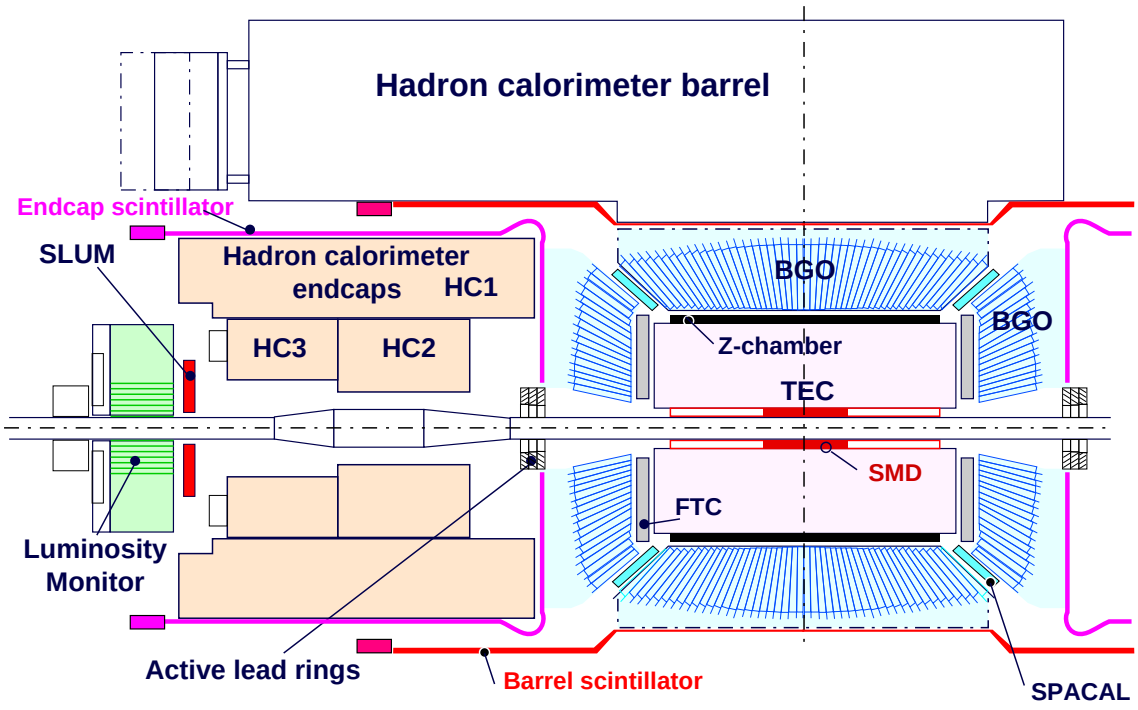

Figure 4.6: A schematic representation of the inner components of the L3 detector. In addition to the tracking system (TEC, SMD, and FTC) and the calorimeters, also shown are the active lead rings, the luminosity monitor, and the scintillators.

system. The planes $\phi = 0°$ and $\phi = 90°$ contain the x-axis and y-axis, respectively, with $r = \sqrt{x^2 + y^2}$. In addition, it is often useful to refer to the polar angle θ with respect to the z-axis.

A detailed description of the L3 detector is given in [87]. It should be noted that L3 had been undergoing constant modification[5] during the LEP1 and the beginning of the LEP2 phase. This analysis, however, is only concerned with the data-taking period of 1998-2000, when the detector configuration remained unchanged. The most important subdetector for the analysis presented in this thesis was the electromagnetic calorimeter since it provided a precise measurement of photon energies and flight directions. Nevertheless, all other L3 subdetectors were relevant to the selection of the single- and multi-photon events. They were used to reject background events

[5]Only the original components of the L3 detector are covered in [87]. References to papers describing the detector upgrades will be given when needed.

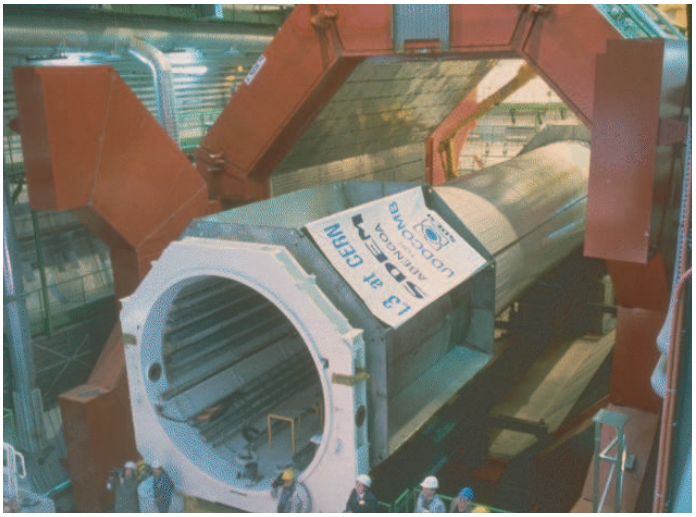

Figure 4.7: The Magnet and Support Tube during their installation at L3. The doors of the magnet are open and the support tube has been positioned along the center of the magnet.

from other Standard Model processes and from cosmic rays. The description of the L3 subdetectors follows.

4.2.1 The Magnet

A large magnet with a relatively low field was chosen in order to optimize the muon momentum resolution, which improved linearly with the field but quadratically with the lever arm. The magnet is composed of a water-cooled solenoid coil, a soft iron yoke, and two steel endcaps that provide support for the yoke. The magnet has an outside radius of 7.9 m, an inside radius of 5.9 m, and is 11.9 m in length. The total weight of the L3 magnet is 7800 tons.[6]

The magnet (see Figure 4.7) surrounded the entire L3 detector[7] providing a 0.5 T field parallel to the beam axis. The magnetic field was mapped inside the support tube with Hall probes and outside with about 1000 magnetoresistors and 5 NMR probes.

[6]The L3 magnet was included in the 1997 Guinness Book of Records as the World's Largest Electromagnet.

[7]Except for a part of the forward-backward muon spectrometer.

It is interesting to note that the L3 magnet is the only part of the L3 detector which will be used for the LHC program. The ALICE experiment [104] is currently being built inside the L3 magnet to study lead-ion as well as proton-proton collisions at the LHC.

4.2.2 Central Tracking Detectors

The central tracking system was used to identify charged particles and to measure their trajectories (tracks). It included a Time Expansion Chamber (TEC) and a Silicon Microvertex Detector (SMD). Additional measurements of the z-coordinate were obtained from the Z-chamber and the Forward Tracking Chambers (FTC) (Figure 4.6). Due to the limited space available inside the electromagnetic calorimeter, the TEC had only a modest lever arm of 31.7 cm, and as pointed out previously, the L3 magnetic field was relatively weak.

The design goal of TEC was to identify the charge of 50 GeV particles at 95% confidence level. That target was met by choosing a drift chamber design in which a relatively large low-field drift region was separated from a high-field amplification region by two planes of grounded wires. Charged particles traversing the gas volume of TEC caused ionization of the gas atoms. The ionization electrons would then drift to the anode wires (Figure 4.8), and the drift times of these electrons could be used to reconstruct the track position. The drift times were precisely determined by measuring the centroids of the arrival time distributions collected by each anode wire. A drift velocity of about 6 μm/ns was attained in the low-field region, whereas in the amplification region it was about 50 μm/ns [105]. The drift velocity was precisely determined *in situ* using a gas test chamber and was kept constant within 0.1% [106].

The TEC was composed of two concentric cylindrical drift chambers, divided into 12 inner and 24 outer sectors. Each sector had a central anode plane and was separated from its neighbouring sectors by cathode planes. The TEC wires were arranged parallel to the z-axis so that the coordinate measurement was made in the bending plane. The inner (outer) sectors contained 8 (54) anode wires each.

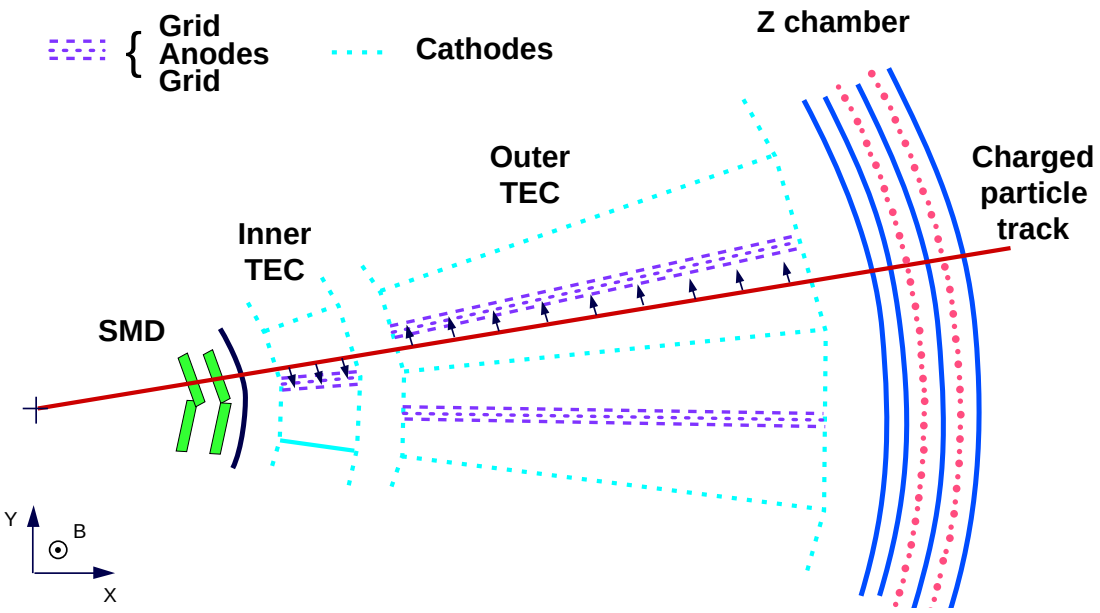

Figure 4.8: A charged particle produced within the beam pipe would first cross the SMD, then the TEC, and finally the Z-Chamber before hitting the calorimetry. The geometry of a TEC sector is shown in detail.

A detailed $r\phi$ view of the L3 tracking system is shown in Figure 4.8. The sensitive region in which the traversing tracks could be measured by all 62 anode wires was $44^\circ < \theta < 136^\circ$. Particles with $\theta(180^\circ - \theta) < 10^\circ$ could not be detected by the TEC.

The expansion of the drift time provided detectable time differences between hits from neighbouring tracks. Typically hits separated by 500 μm were reconstructed individually. The excellent double track resolution proved to be useful in the selection of converted photons. This will be discussed in more detail in Chapter 6, Section 6.3.4.

The z-coordinate of a track was measured by the Z-chamber, which consisted of two proportional wire chambers surrounding the cylindrical outer surface of TEC. It was read out by cathode strips tilted with respect to the z-axis and covering the angular region of $45^\circ < \theta < 135^\circ$. The spatial resolution of the Z-chamber was about 300 μm. In the forward region the FTC was used to measure the x-y coordinates of a track at fixed z. These proportional chambers were located between the TEC and electromagnetic calorimeter endcaps and covered polar angles $12^\circ < \theta(180^\circ - \theta) < 34^\circ$.

The SMD [107] consisted of two radial layers of double-sided silicon strip detectors located at distances of 6 cm and 8 cm from the beam axis and covering polar angles $22^\circ < \theta < 158^\circ$. It provided ϕ and z measurements with approximately 10 μm accuracy. The SMD significantly improved the momentum and vertex resolution of the tracking system by providing two additional points close to the interaction point for each reconstructed track.

The combined TEC-SMD transverse momentum resolution at large polar angles ($\theta > 45^\circ$) was $\sigma(1/P_T) = 0.015$ GeV^{-1}. The angular resolution was found to be $\sigma_\phi = 0.6$ mrad and $\sigma_\theta = 3.4$ mrad.

4.2.3 Electromagnetic Calorimeter

The physics analysis that I present in this thesis relied heavily on the electromagnetic calorimeter (ECAL) of the L3 detector. In this section I describe the construction principle, the geometry, and the readout chain of the ECAL. This discussion will be continued in the next chapter, where I will describe its particle reconstruction algorithm as well as its calibration and monitoring.

The L3 ECAL was designed to provide excellent energy and spatial resolution for photons and electrons over a wide energy range, from 100 MeV to 100 GeV. As I will discuss in Section 5.6, it was precisely calibrated using an RFQ accelerator and its energy resolution was measured to be: $\sigma(E)/E = 3.2\,\%/\sqrt{E} \oplus 0.9\,\%$ (E in GeV). The L3 ECAL was a total absorption calorimeter made of 10,734 bismuth germanium oxide (BGO) crystals. The crystals pointed directly towards the L3 interaction point and were arranged to form two symmetrical half-barrels surrounding the TEC and two endcaps mounted behind the FTC. The geometry of the BGO calorimeter is illustrated in Figure 4.9.

Electromagnetic Showers in the BGO Crystals

At energies above 100 MeV, electrons and positrons traversing dense matter lose their energy primarily through the bremsstrahlung process [6], radiating photons as a result

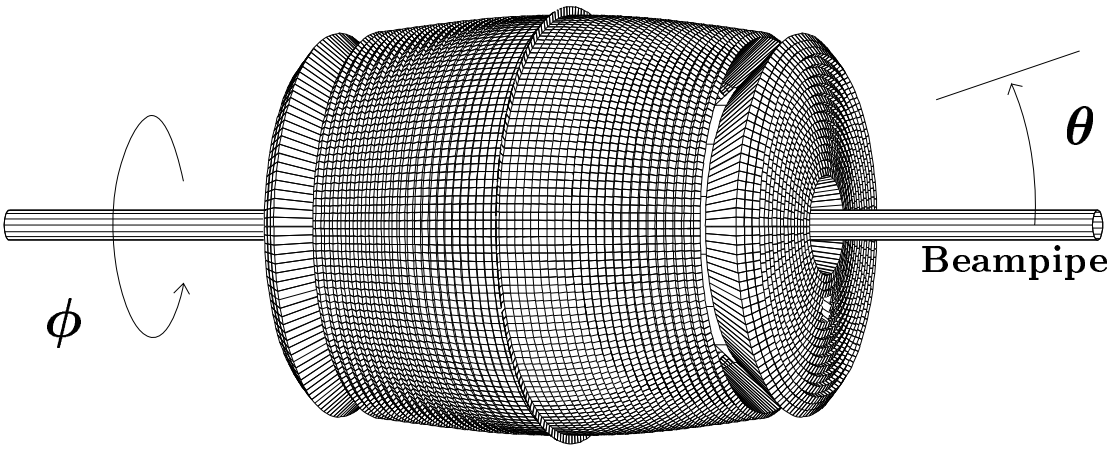

Figure 4.9: The BGO electromagnetic calorimeter.

of the Coulomb interaction with the electric fields of the atomic nuclei:

$$e^{\pm}(N) \rightarrow e^{\pm} + \gamma\,,$$

where (N) represents the interaction with the Coulomb field of the nucleus. Similarly, photons with energies greater than 10 MeV interact with the matter predominantly through the process of electron-positron pair production:

$$\gamma(N) \rightarrow e^{+} + e^{-}.$$

Both pair production and bremsstrahlung processes produce secondary photons and electrons which can also interact with the material. The resulting chain reaction is called an *electromagnetic shower* [6]. As the shower develops, the energy of its constituents decreases and other energy loss processes start to contribute. Eventually, the energy of all particles produced in the shower is absorbed by the showering material. Since high-energy photons and electrons generate the same chain reactions originating from different initial interactions, they produce showers that are virtually indistinguishable.[8] The physics of electromagnetic showers and calorimeters is described in detail in [108].

[8]Contrary to electrons, high energy photons traveled, on average, 1.5 cm before converting into an $e^{+} + e^{-}$ pair [108]. However, this difference in the shower maximum position could not be detected since the BGO calorimeter had no longitudinal segmentation.

To describe the shower development in a material-independent way, units of *radiation length* and *Molière radius* are frequently used. The numerical values of these two units depend only on the showering material. The radiation length (X_0) is defined as a distance over which a high energy (E > 1 GeV) electron loses approximately 63% (i.e., $1 - e^{-1}$) of its energy. The Molière radius (R_M) describes the lateral shower profile, where approximately 90% of the shower is typically contained in a cylinder of radius R_M around the shower axis. The BGO inorganic crystal scintillator was chosen to be used in L3 because of its very short radiation length and Molière radius, $X_0 = 1.12$ cm and $R_M = 2.4$ cm, and because of its high scintillation light yield. The high stopping power of the BGO translated into the compactness of the calorimeter, which was important due to limited space available inside the support tube.

In a BGO crystal, the passage of low-energy electrons and positrons (E $\leq$ 10 MeV) through the crystal lattice causes short-lived excitations in the system of lattice electrons. The decay of lattice excitations produces scintillation photons with a wavelength spectrum peaked at about 480 nm (green light). The amount of the scintillation light is proportional to the deposited energy ($\simeq 2.8 \times 10^3\ \gamma$/MeV). Since the BGO crystals are optically transparent, the scintillation light can be detected and used to compute the energy of the electromagnetic shower.

The Geometry of the Electromagnetic Calorimeter

The BGO crystals of the L3 electromagnetic calorimeter had a truncated pyramidal shape (Figure 4.10) with a front surface of $\simeq 2 \times 2\,cm^2$, a rear surface of $\simeq 3 \times 3\,cm^2$, and a depth of about 21.5 radiation lengths (24 cm). To minimize the mechanical stress, each crystal was housed in its own cell of a carbon fiber support structure. The walls between the crystals were about 0.2 mm thick. The dead material of the walls together with the clearances represented about 2.1% of the solid angle coverage of the ECAL.

The crystals were aligned with their axes pointing to the interaction point, but with a slight tilt to reduce the number of particles escaping detection in the gaps between the crystals.

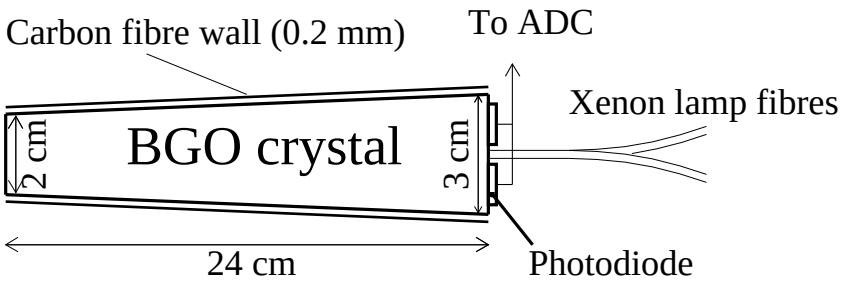

Figure 4.10: A BGO crystal.

The BGO calorimeter consisted of the following four large crystal arrays.

- **Two half-barrels.** Each half-barrel contained 3840 crystals that were arranged in a 160×24 matrix in the $\phi - \theta$ plane. The combined total angular coverage of the BGO barrel was $42.3° < \theta < 137.7°$. The 160 ϕ-slices of 24 crystals were tilted by about 0.6° to aim at a position 5 mm away from the interaction point.

- **Two endcaps.** Each endcap was made of 1527 crystals arranged into six large rings. Each of the large rings was made of three crystals in θ-coordinate (three individual $\theta -$ rings), except for the inner one which contained only two $\theta -$ rings. The number of crystals in ϕ varied from 48 in the inner ring to 128 in the outer ring.[9] Nine crystals were taken out from each endcap at $\phi \simeq 270°$ and $\theta(180° - \theta) \simeq 16°$ to create a hole for the beam pipe of the RFQ calibration system, which will be described in Chapter 5. The endcaps were installed in 1991. Unfortunately, the construction of the central tracking system required more space than was originally foreseen. Therefore the endcaps had to be displaced by a distance of about ± 13 cm along the z-axis and covered $9.9° < \theta(180° - \theta) < 36.8°$. This configuration induced a θ-tilt of $2.1° - 5.4°$ with respect to the nominal direction to the interaction point. The tilt in ϕ was 0.6°, the same as for the crystals in the barrel.

[9] The exact numerical values for the six large rings were 48, 64, 80, 96, 112, and 128.

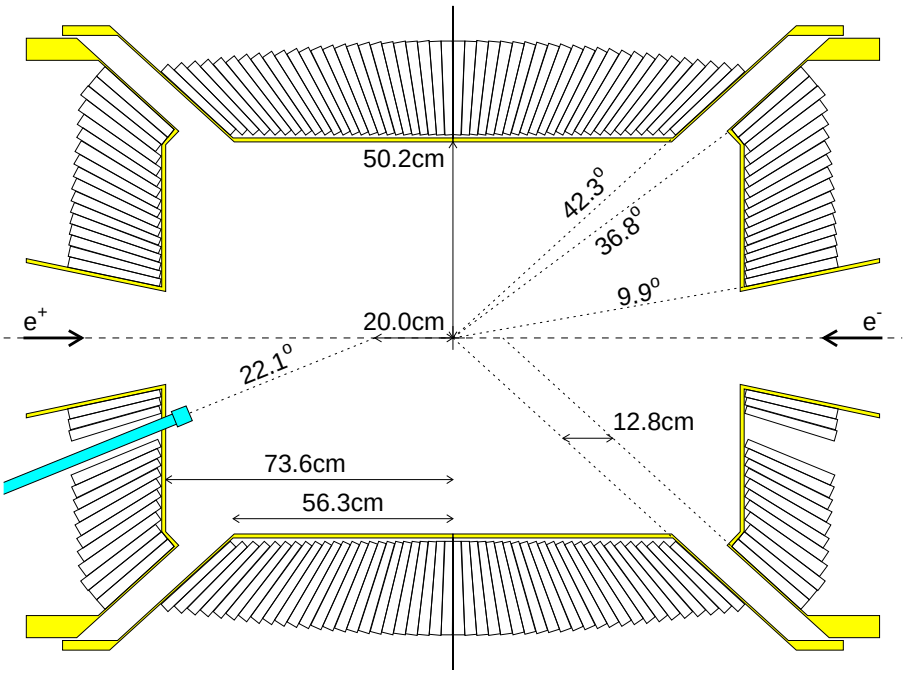

Figure 4.11: A side view of the L3 electromagnetic calorimeter in the vertical $y-z$ plane. The beam pipe in the bottom left corner is part of the RFQ calibration system developed by the Caltech L3 group.

Figure 4.11 shows a cross section of the BGO calorimeter in the vertical $y-z$ plane. The dimensions of the calorimeter are also shown. Due to the angular interval between the barrel and the endcaps, the solid angle coverage of the BGO was about 92.1% of 4π steradians.

The BGO Readout System

Achieving good linearity and energy resolution required a nearly uniform light collection efficiency. The light flux collected at the rear face of a polished BGO crystal decreased strongly (up to 50%) with the distance from the front face. After coating the crystals with a 40-50 μm thick layer of high reflectivity white paint, the maximum variations in the collected light flux as a function of the distance from the front face were only about 5%.[10]

[10] The variations in the crystal light yield were measured using cosmic muons and were required to be less than 10% for all accepted BGO crystals [109].

To detect the BGO scintillation light a pair of silicon photodiodes were glued to a rear surface of each crystal (Figure 4.10). There were two reasons to choose photodiodes over conventional photomultiplier tubes: 1) photodiodes were not sensitive to the L3 magnetic field; 2) they took very little space. The photodiodes had a sensitive area of 1.5 cm^2 each and were read out as a single unit. Their quantum efficiency was about 70% at 480 nm, resulting in a charge deposition of about 0.2 fC (1200 electrons) per MeV of the shower energy. After preamplification and shaping, the signal from each individual crystal was split into three separate signals which were then processed by the first-level trigger and by two independent pulse-height analyses optimized for small (*low energy chain*) and large (*high energy chain*) signal amplitudes. The low energy chain was amplified by a factor of 32 with respect to the high energy chain, after which the two chains were processed identically.

The signal in each chain was first integrated and then stored in a sample and hold circuit. The stored signal was further amplified in two stages, each with a gain of four, resulting in a total of six levels of amplification for the two chains. A specifically designed analog to digital converter (ADC) was then used to digitize the collected signal of each crystal. The *floating-point* design of the BGO ADCs utilized an accurate 12-bit ADC with a 220 μs conversion time to cover 21 bits of effective dynamic range with six different amplifications[11] [110].

The first step of the digitization was to choose the level of amplification (or gain) that provided the largest unsaturated signal. When the input signal for a particular amplification approached the maximum voltage of the 12-bit ADC, the next lower amplification was used for the digitization. This design resulted in a 12-bit digitization, which together with the 9-bit (1:512) selectable gain corresponded to the effective 21-bit dynamic range. A digitization accuracy of at least 0.1% was achieved for the BGO signals above 100 MeV. The actual dynamic range extended from about 1 MeV up to 200 GeV. The energy equivalent of the transition between different gains depended on gain calibrations, pedestals, and energy calibrations. The distribution of the transition energies is plotted in Figure 4.12.

[11] The six signal amplifications corresponded to approximately 1, 2^2, 2^4, 2^5, 2^7, and 2^9.

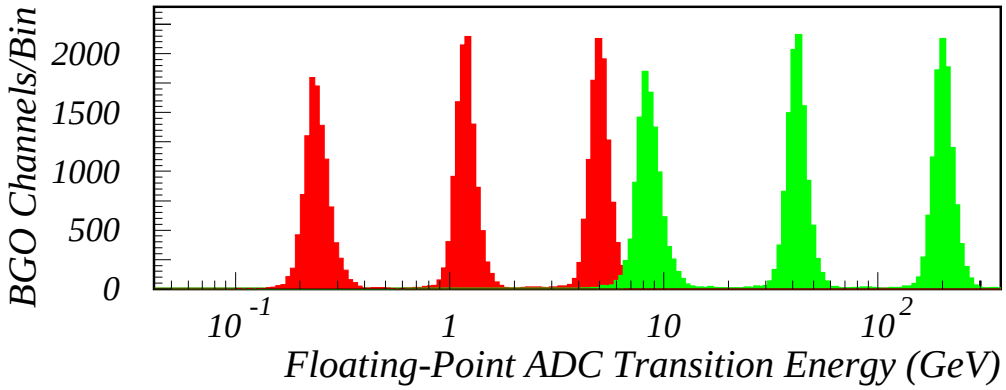

Figure 4.12: The distribution of transition energies of all BGO ADCs. The three peaks on the left correspond to the low energy channel, the peaks on the right correspond to the high energy channel.

Performance of the BGO Calorimeter

High intrinsic resolution, precise calibration, and a relatively low amount of material between the crystals and the interaction point were the main factors that made the BGO[12] the best electromagnetic calorimeter at LEP2. Its energy resolution, $\sigma(E)/E$, was better than 2% for electrons and photons with energies above 5 GeV. The linearity of the BGO response in the energy range of 1-100 GeV proved to be better than 1%.

To compare the electromagnetic calorimeters of the four LEP experiments, it is convenient to compare their measured energy resolutions for 45 GeV electrons and positrons.[13] The energy resolution of the L3 BGO for such electrons was approximately 1.0%, whereas the resolutions of the ALEPH, OPAL, and DELPHI (HPC) calorimeters were about 3.5% [111], 4.0% [112], and 6.5% [113], respectively.

The energy reconstruction algorithm of the BGO, its calibration and monitoring, as well as its performance will be described in detail in Chapter 5.

[12]In L3 the BGO electromagnetic calorimeter is most often referred to as simply the BGO.

[13]The reasoning behind the choice of the 45 GeV electrons will be explained in Chapter 5, Section 5.6.2. In addition, 45 GeV corresponds to approximately the middle point of the energy range 1-100 GeV, the region of interest for the analysis described in this thesis.

Gap Filler

In 1996, the gaps between the BGO barrel and the endcaps were equipped with *ECAL GAP filler* (EGAP) [114]. The EGAP counters consisted of 48 bricks of lead with a set of scintillating fibers embedded inside each brick. Its energy resolution for 45 GeV electrons was expected to be about 4.0%, significantly worse than that of the BGO. In 1998, a dedicated study of the EGAP performance *in situ* was carried out using Bhabha scattering events, $e^+e^- \to e^+e^-$. The selected events were required to have two back-to-back TEC tracks pointing in the direction of EGAP. The study showed that about 10% of such electrons passed undetected, much more than was expected from an early simulation of the EGAP response [115]. Because of this large detection inefficiency, I did not use the EGAP to identify and measure photons.[14]

4.2.4 Scintillation Counters

The L3 scintillation counter system [116] was composed of 30 barrel counters and 2×16 endcap counters. As shown in Figure 4.6, the counters were located between the BGO and hadron calorimeters and covered polar angles of $11.5° < \theta < 168.5°$. The scintillators were designed for a precision measurement of the relative timing of charged particles traversing the detector. The timing resolution was about 0.8 ns in the barrel and 1.9 ns in the endcaps. The scintillation counters were indispensable for the rejection of the background from out-of-time cosmic rays.

4.2.5 Hadron Calorimeter

Hadronic showers develop in a similar manner to electromagnetic ones, but are more complex as they involve both the electromagnetic and the strong interactions. The shower dimensions are governed by the nuclear interaction length of the absorber medium, which is defined as an average distance a high-energy hadron has to travel inside that medium before a nuclear interaction occurs [108]. The BGO calorimeter

[14] The EGAP was never used in any of the L3 analyses requiring precise measurement of photons or electrons.

corresponded to only about one nuclear interaction length and, obviously, could not be used to stop and measure hadrons. The hadron calorimeter (HCAL) was built for this purpose.

The HCAL surrounded the BGO calorimeter and was made of depleted uranium and brass absorber plates interleaved with proportional wire chambers. Its barrel covered the central region $35^\circ < \theta < 145^\circ$, while the endcaps covered $5.5^\circ < \theta(180^\circ - \theta) < 35^\circ$. The hadron calorimeter covered approximately 99.5% of the full solid angle of 4π steradians. The L3 HCAL is depicted in Figure 4.13.

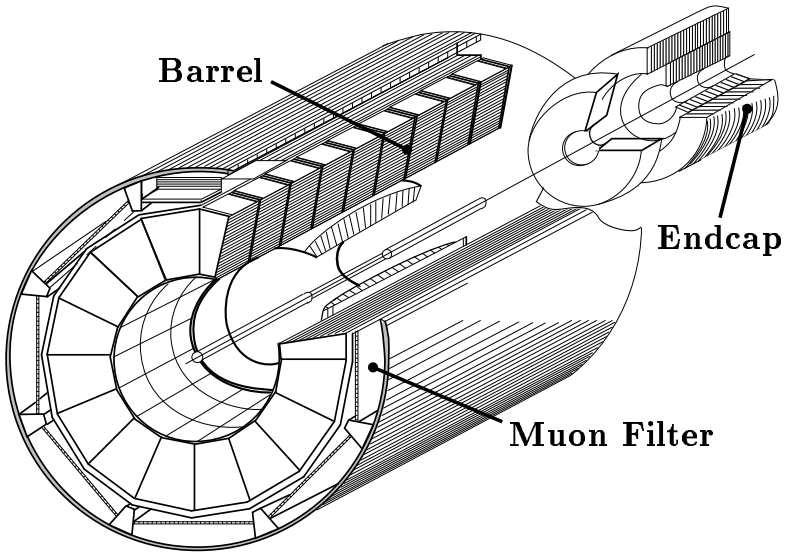

Figure 4.13: A perspective view of the hadron calorimeter and the muon filter.

The barrel had a modular structure consisting of 9 rings in θ of 16 modules in ϕ each. Each module was composed of radially stacked alternating layers of 5 mm thick depleted uranium absorber and 5.6 mm thick brass wire chambers. The modules in the middle three rings contained 58 layers of chambers each, while the modules in the other six rings contained 53 layers. Successive chambers were aligned with wires perpendicular to each other. The wires were then grouped into towers with the following readout segmentation: $\Delta\phi \simeq 2.5^\circ$, $\Delta z \simeq 6cm$, and $\Delta r \simeq 8cm$. The total number of readout channels was 23,040. Viewed from the interaction point, the HCAL barrel represented 3.5-5.5 nuclear interaction lengths. The high granularity of the

barrel was successfully used in my search for long-lived neutralinos (see Chapter 7). Prior to their installation in L3, the HCAL modules were tested in test beams. The measured energy resolution for hadrons was found to be: $\sigma(E)/E = (55/\sqrt{E} + 5)\%$ [87].

The HCAL endcaps were each divided into 6 modules making up 3 rings. Viewed from the interaction point, the endcaps represented 6-7 nuclear interaction lengths.

Muon Filter

The muon filter was designed to ensure that hadronic showers were contained inside the support tube. In addition, the muon filter protected the muon chambers from the uranium noise of HCAL. The muon filter was mounted on the inside wall of the support tube and provided another nuclear interaction length behind the HCAL barrel. It was divided into eight identical octants (Figure 4.13), each made of six layers of 10 mm thick brass absorber plates, interleaved with five layers of proportional chambers, and followed by five 15 mm thick absorber plates matching the circular shape of the support tube. The material of the support tube contributed an additional 0.5 nuclear interaction lengths.

Each octant was 4 m long, 1.4 m wide and contained 78 proportional chambers. The proportional chambers were aligned parallel to the z-axis. The segment of the muon track passing through an octant was determined with a precision better than 1.5 mm in the $r\phi$ plane [117]. The overall chamber efficiency measured using test beams was about 97% [87]. The muon filter was used in my search for long-lived neutralinos to reject the background from cosmic rays, as discussed in Chapter 7.

4.2.6 Muon Spectrometer

The barrel muon chamber system (MUCH) consisted of three layers of drift chambers arranged in eight octants. The MUCH was located between the support tube and the magnet, as shown Figure 4.5, and covered the angular range $43^\circ < \theta < 137^\circ$. Each octant contained three layers of *P-chambers* measuring the $r\phi$ coordinates and two

Z-chambers (located in the inner and outer layers) measuring the z-coordinate of the muon track. The momentum resolution $\sigma(P_T)/P_T$ for 45 GeV muons was found to be about 4.0% [118].

The forward-backward muon chambers (endcaps) extended the angular coverage of the muon spectrometer down to $\theta > 22^\circ$ with respect to the beam axis. Both endcaps consisted of three layers of drift chambers mounted on the 90 cm thick magnet doors, and the momentum resolution of the endcaps was limited by multiple scattering in the magnet doors. Depending on the muon polar angle, it varied from 12% to 32% for 45 GeV muons [118].

The muon spectrometer was used in my single-photon selection to identify and reject cosmic ray events.

4.2.7 Active Lead Rings

The *Active Lead Rings* detector (ALR) played an important role in the analysis presented in this thesis. I used the ALR to tag radiative Bhabha scattering events, $e^+e^- \to e^+e^-\gamma$. Not only was this reaction the dominant source of background, but the selected sample of radiative Bhabha events was also used for several important detector checks as will be discussed in Chapter 6.

The ALR [119] was composed of two identical detectors covering polar angles $3.9^\circ < \theta(180^\circ - \theta) < 8.7^\circ$. The detectors were situated between the BGO and the HCAL about one meter away from the interaction point in $+z$ and $-z$ directions (see Figure 4.6). Originally installed to protect the inner tracker from beam-related background, the ALR was upgraded in 1995 to improve its resolution and reliability. Each detector consisted of seven 18.5 mm thick lead rings interleaved with five scintillator rings which were segmented in θ and ϕ. Figure 4.14 shows the structure of the ALR and the segmentation of the scintillator layers. An energy resolution of 15% was obtained for a selected sample of 45 GeV Bhabha electrons. The same Bhabha sample was used to check the angular resolutions. They were measured to be 0.2° in θ and 2° in ϕ [120].

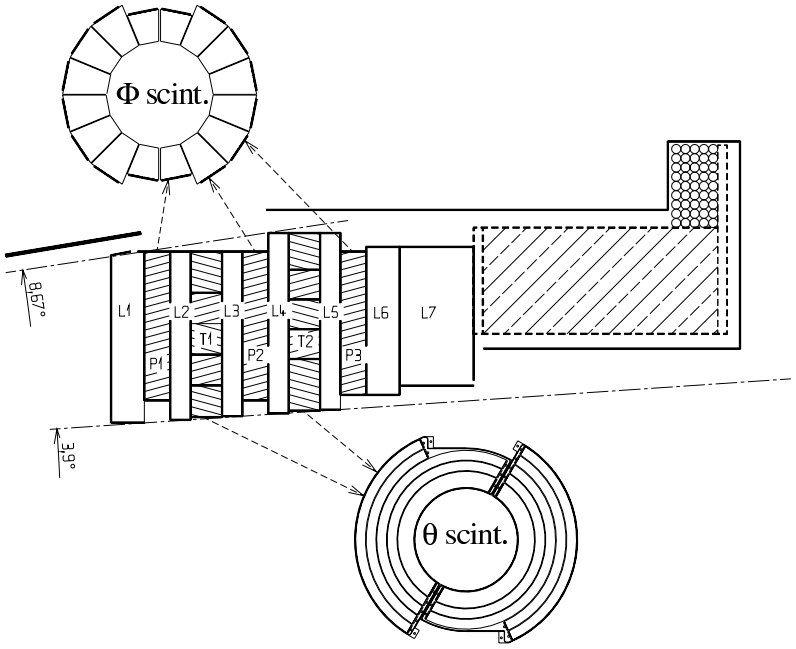

Figure 4.14: A side view of one of the two L3 ALR detectors. The segmentation scheme of the scintillator layers is also shown. The interaction point is located about one meter to the left (not shown on the plot).

4.2.8 Luminosity Monitors

The majority of the Standard Model measurements and searches for new physics at L3 require an accurate knowledge of the LEP luminosity. Bhabha scattering at low polar angles is generally used as a tool to measure luminosity at e^+e^- colliders. The differential cross section ($d\sigma/d\Omega$) of this process can be calculated theoretically to a very high precision ($\simeq 0.1\%$) [121] and grows as $1/\theta^4$. Using a sample of $N_{e^+e^-}$ selected Bhabha events, the luminosity can be derived from

$$\mathcal{L} = \frac{N_{e^+e^-}}{\sigma_{e^+e^-}\varepsilon}, \tag{4.2}$$

where ε is the selection efficiency and $\sigma_{e^+e^-}$ is the accepted cross section.

The L3 luminosity detector [122] consisted of a BGO calorimeter (LUMI) and a silicon tracker (SLUM), installed in front of the LUMI. As shown in Figure 4.6, the detectors were installed at a distance of 2.7 m from the interaction point, covering

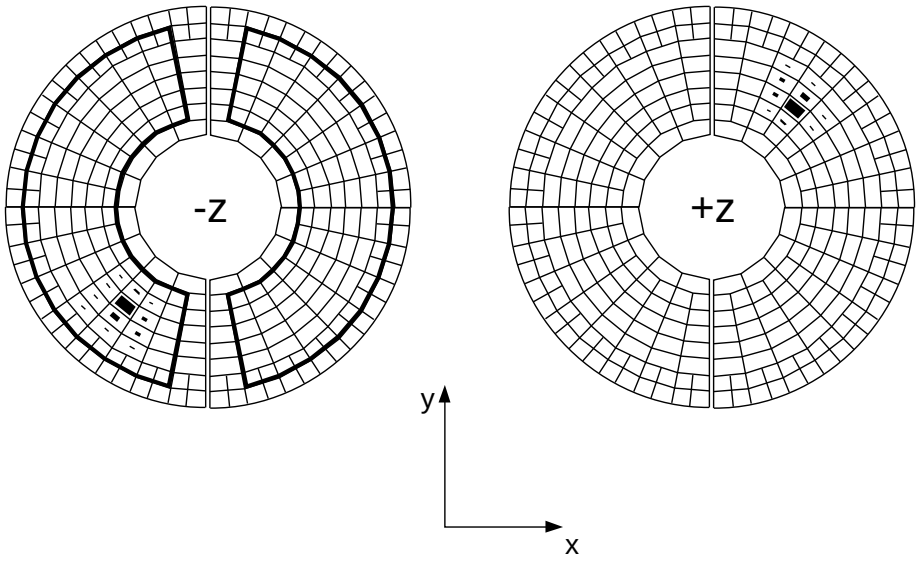

Figure 4.15: A Bhabha event observed in the LUMI. The sizes of the black areas are proportional to the energy deposited in each crystal. The contour on the left-hand side indicates the fiducial volume used for the luminosity measurement.

the angular range $1.4^\circ < \theta(180^\circ - \theta) < 3.9^\circ$. Each of the two LUMI calorimeters contained 304 BGO crystals (see Figure 4.15) and had an energy resolution of 2%. The SLUM was installed in 1993 to improve the angular resolution of the system.

The precision of the luminosity measurement by L3 was dominated by systematic uncertainties and was about 0.2% for the data sets I used.

4.2.9 L3 Trigger System

The LEP beam crossing frequency was about 45 kHz, while the L3 data acquisition system could not cope with rates in excess of about 10 Hz. The L3 trigger system [123] was designed to act as a filter that would decide whether an "interesting" e^+e^- event took place. This system rejected background processes (e.g., beam gas or cosmic ray events) and detector noise signals while maintaining a high efficiency for recording interesting physics processes.

Triggering at L3 was performed in three steps (levels) of increasing complexity.

The level 1 trigger consisted of five independent triggers which used signals from different L3 subdetectors. In case of a positive decision the detector data was digitized and stored within 500 μs in multi-event buffers. During that time interval the L3 readout system would not accept any new input and all further data taking would be blocked ("dead time"). The "dead time" at LEP2 was typically about 7% [124]. Negative trigger decisions did not affect the L3 readout chain since the electronics were cleared before the next beam crossing. The level 1 trigger accepted events at a rate of 15-20 Hz. Events with a coincidence of at least two level 1 triggers were automatically accepted by L3 and were written on tape.

The level 2 trigger worked in parallel with the level one trigger and used the same information. However, as it had more time available, it could use more complex algorithms. It accepted events on the basis of a more detailed calorimetric and track analysis and the matching between tracks and hits in calorimeters and in scintillators. The level 2 trigger rate was between 10 and 15 Hz. The accepted events were then forwarded to the level 3 trigger.

The level 3 made its decision using fully digitized signals from all subdetectors. The accurate digital data with its higher resolution and granularity allowed tighter cuts and thresholds to be applied, compared to the lower level triggers. The final L3 event rate written on tape was about 3-6 Hz.

Energy Trigger

The energy trigger was one of the level 1 subtriggers and processed signals from the BGO calorimeter.[15] It was the only trigger that could accept single photon events and was of special importance to my analysis. As described in Section 4.2.3, the preamplifier output of each BGO crystal was available to the trigger. To reduce the number of channels in the readout, the signals from the barrel calorimeter were grouped into *blocks* of 30 crystals each. The barrel was divided into 32 azimuthal (ϕ) and 8 polar (θ) segments, resulting in a total of 256 blocks. In a similar manner,

[15]It also handled signals from the HCAL and the luminosity monitor. However, those were not relevant to the single-photon selection.

the BGO endcaps were also divided into segments giving an additional 256 channels. Analog signals from the 512 channels formed the input to the energy trigger. Each of these channels was digitized by a system of Fast Encoding and Readout ADC (FERA) modules. The FERA system used the charge collected by the readout photodiodes during a 2 μs gate, in contrast to the 11 μs gate of the BGO "complete" readout.

The energy trigger employed several algorithms to reject the background and noise events. The most notable among them were the following:

- **The total energy trigger.** The total energy measured in the BGO was required to be greater than about 30 GeV.

- **The BGO cluster trigger.** This algorithm performed a search for clusters in the BGO. For a positive decision, at least one cluster with energy above approximately 5 GeV had to be present.

- **The single photon trigger (barrel only).** This trigger was developed specifically to accept single-photon events in the BGO barrel. It required a single, isolated BGO cluster with an energy above about 80% of the total energy measured by the BGO [125]. The threshold of this trigger was set as low as possible, at approximately 0.9 GeV.

In summary, the L3 trigger acceptance for single-photon events was limited to the region of $E_\gamma \geq 0.9$ GeV (barrel) and $E_\gamma \geq 5$ GeV (endcaps), where E_γ is the photon energy. The performance of the energy trigger will be discussed in Chapter 6 (Section 6.3.2).

4.2.10 Detector Reconstruction and Simulation in L3

For each event accepted by the trigger system, an *event record* was written on tape. It consisted of "raw" digitized data from all L3 subdetectors. The off-line event reconstruction followed several steps. First, the raw data was read and decoded. Next, the reconstruction for signals from each subdetector was performed. For example, the energy deposited in each BGO crystal was calculated from the electronic pulse

measured by the readout system. Finally, a common software package was used to group individual detector hits into meaningful objects, such as calorimetric clusters or tracks in TEC and muon chambers. The obtained information was stored on disk and was available to the L3 community for further analysis.

The Detector Simulation

In order to compare results from data with various theoretical predictions, the detector response to any particular process is calculated. The complexity of the detector makes it impossible to perform such calculations analytically. Instead, various Monte Carlo techniques are used to simulate the detector response [126].

Monte Carlo simulation of the L3 detector proceeds via two steps. The first step is to create *event lists* using a Monte Carlo generator corresponding to a theoretical description of any given interaction process. The event lists contain the four-momenta of the generated particles, their decay lengths and vertices of creation, the expected production cross section, and other information. Event generators used in L3 form a common library, and their output is standardized to simplify further analysis procedures. Different event generators are written using different coding techniques and, sometimes, even different programming languages. The conversion of a new generator as provided by its authors to the standard L3 format is usually the responsibility of an L3 physicist interested in using this generator in his or her analysis. Such conversion generally involves rewriting large parts of code and is not an easy task.

The second step of the simulation consists in propagating the generated particles through a detailed representation of the L3 detector, which simulates energy loss, scattering, and showering of particles in the detector materials. This program was written using the `GEANT3` detector description and simulation tool [127]. The same program is used to simulate the response of each active detector element to particles passing through it. Detector imperfections (such as dead or noisy channels in the calorimeters, disconnected TEC sectors, etc.) are also taken into account.

After the "full" detector simulation, the generated events are stored on disk and can be compared directly with the L3 data events.

Chapter 5

The RFQ Calibration

The L3 detector was built with a specific purpose: to look for manifestations of new physics using precision measurements of photons and leptons [128]. The L3 BGO calorimeter stood prominently as the most accurate photon detector at LEP (see Section 4.2.3 p. 80). For example, L3 was the only experiment to observe the χ_{c1} meson at LEP via the reaction $\mathrm{Z} \to \chi_{c1} + \mathrm{X},\ \chi_{c1} \to J/\Psi\,\gamma,\ J/\Psi \to \mathrm{e^+e^-}, \mu^+\mu^-$ [129]. The resulting measurement of the branching fraction $\mathrm{Br}(\mathrm{Z} \to \chi_{c1} + \mathrm{X})$ is still the most accurate available.

In Section 4.2.3 I summarized the construction principle, the geometry, and the readout chain of the BGO calorimeter. In this chapter, I describe its calibration and monitoring as well as its particle reconstruction algorithm. In particular, the RFQ calibration technique, which provided the most precise calibration at LEP, is discussed in detail.

5.1 Particle Reconstruction in the BGO

The BGO calorimeter was designed to measure the energy and direction of the showers produced by particles traversing the BGO crystals. The shower shape parameters can be used to classify such particles as either particles producing electromagnetic showers (electrons, positrons or photons), particles producing minimum ionizing signals (mostly muons), or particles with mainly hadronic interactions.

The design of the BGO was optimized for photons and electrons which could be precisely reconstructed as they generated compact electromagnetic showers with little shape variation. Such showers were almost fully contained in the BGO material.

The rear-end leakage was determined to be below 2% even for 45 GeV electrons (see Section 6.3.6). Hadrons lost their energy in the BGO through ionization and nuclear interactions, developing showers with larger fluctuations and significant leakage (the BGO material represented only one nuclear interaction length). Relativistic muons did not interact strongly with the BGO material and produced small signals,[1] which were a slowly varying function of the muon energy [6].

The first step of the particle reconstruction algorithm was to convert a raw ADC signal of each BGO crystal into a corresponding energy value. The transformation for a crystal k is given by

$$E_k = C_k \cdot (A_k - P_k), \tag{5.1}$$

where

- E_k is the energy deposited in this crystal
- C_k is the calibration constant for this crystal
- A_k is the ADC signal
- P_k is the ADC pedestal.

The pedestals for all channels were updated on a daily basis and were obtained using a special type of calibration runs (*BASE* runs), which were performed between LEP fills. In contrast, the calibration constants were usually determined twice each year — before and after the LEP annual run.

The second stage of the particle reconstruction algorithm involved building a map of all individual energy depositions to localize showers in the BGO. Crystals with significant energy depositions were grouped into clusters, defined as a set of adjacent crystals with an energy of more than 10 MeV per crystal. Then, in each cluster local maxima (*bump crystals*) were identified and the remaining crystals were attached to the bump crystals to form *BGO bumps*. Bump crystals were required to have energy greater than 40 MeV and be more energetic than the 8 neighboring crystals in the

[1] Multi-GeV muons traversing the full length of the crystal deposited on average between 200 and 250 MeV [108].

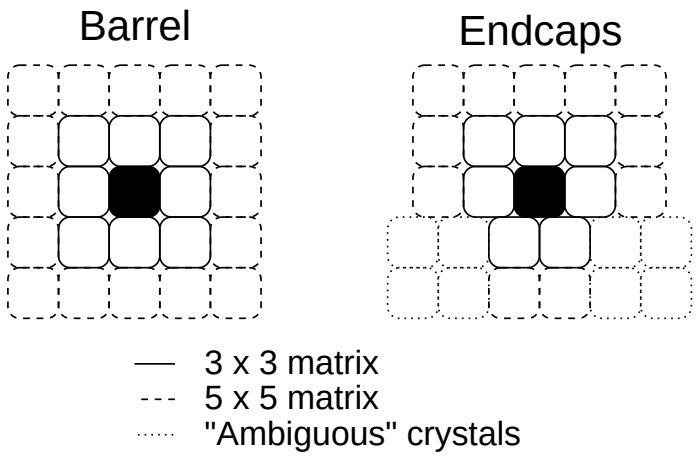

Figure 5.1: Crystals forming 3×3 and 5×5 matrices in the barrel and in the endcaps.

3×3 matrix. The non-bump crystals were assigned to the nearest bump crystal in the same cluster. If a crystal was equidistant to two bump crystals, it was assigned to the most energetic one.

Each BGO bump was assumed to correspond to a particle traversing the calorimeter, and the energy of such particle was calculated using the following quantities:

$$S_1 \equiv E_1 \ , \qquad S_9 \equiv \sum_{3\times3} E_i \ , \qquad S_{25} \equiv \sum_{5\times5} E_i \ ,$$

where E_1 is the energy of the bump crystal and the sums range over crystals in the 3×3 and 5×5 matrices centered on the bump crystal. The layout of these matrices is shown in Figure 5.1. In the endcap regions where crystals were not aligned in ϕ across different θ-rings, some care had to be taken in creating the 3×3 and 5×5 matrices. A special algorithm was implemented to extend the $n \times n$ matrix in the following way. For each new θ-ring the middle crystal was chosen to be the one with ϕ closest the ϕ-position of the central crystal. When two crystals had the same $\Delta\phi$, the one with the highest energy was chosen as the middle one of this θ-ring.

During the R&D tests, prior to and during the construction of the BGO calorimeter, extensive studies of the electromagnetic shower development and containment in the BGO crystals were performed using both beam tests and MC simulations [130].

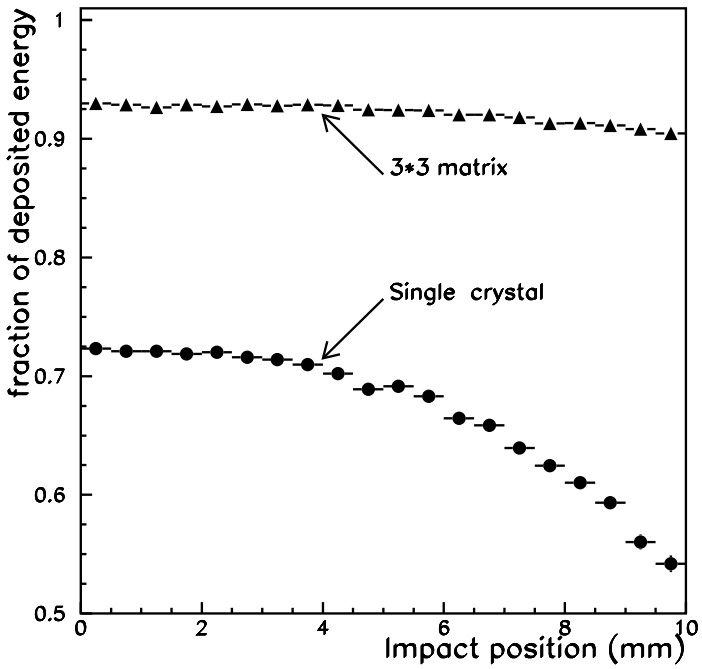

Figure 5.2: The fraction of the shower energy deposited in the central crystal and in the 3×3 crystal matrix as a function of the distance from the impact point to the crystal center [131].

On average, electromagnetic showers from electrons incident on the crystal axis would deposit about 75% of energy in the central crystal and about 94% and 97% of energy in the 3×3 and 5×5 matrices, respectively. A first approximation of the shower energy can therefore be obtained using S_9 or S_{25} energy sums scaled by an appropriate constant factor.

The lateral energy loss due to the finite crystal size and the gaps between the crystals depends on the impact point position. Therefore the shower profile also depends on the position of the impact with respect to the crystal center. Figure 5.2 shows this dependence for the fractional energies S_1/E_{shower} and S_9/E_{shower} as determined during the beam tests[2] [131]. It was noticed that the lateral energy leakage was correlated with the ratio S_1/S_9, and a *corrected sum-of-nine* energy was defined as

$$S_9^c = \frac{S_9}{c_1(\theta) \cdot S_1/S_9 + c_2(\theta)}, \tag{5.2}$$

[2]The test beam studies are described in the next section.

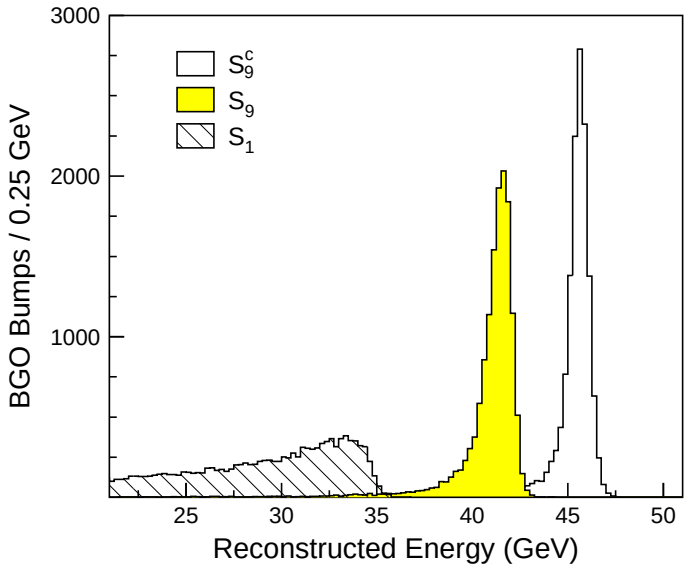

Figure 5.3: Distributions of the energy quantities S_1, S_9 and S_9^c reconstructed for the 45.6 GeV Bhabha electrons.

where the parameters $c_1(\theta)$ and $c_2(\theta)$ are θ-dependent coefficients. They were chosen to satisfy $\langle S_9^c \rangle \simeq E_{incident}$, where $E_{incident}$ was the energy of the incident beam of electrons. Numerically, c_1 is 0.1231 and c_2 is 0.8222 for the barrel, while in the endcaps $c_1 = 0.065 + F_1(\theta)$ and $c_2 = 0.865 + F_2(\theta)$. $F_1(\theta)$ and $F_2(\theta)$ are θ-dependent functions of the order of a few percent. Figure 5.3 shows the distributions of S_1, S_9, and S_9^c for 45.6 GeV electrons selected using the Bhabha scattering process, $e^+e^- \rightarrow e^+e^-$. One can see that S_9^c provides a clear improvement in the energy resolution.

In a similar fashion, a *corrected sum-of-25* (S_{25}^c) can be constructed using quantities S_1 and S_{25}. Because the electromagnetic showers are almost fully contained in the 3×3 crystal matrix, the S_{25}^c variable gives the same energy resolution as S_9^c for showers with $E_{shower} > 50$ GeV. For showers with smaller energy depositions, the use of S_9^c is preferred since this quantity is less affected by the BGO electronic noise and the (possible) presence of dead channels in the crystal matrices. However, the S_{25}^c quantity proved to be very useful in distinguishing between electromagnetic showers and showers originating from hadrons and cosmic rays (as discussed in the next chapter).

To reconstruct the impact point of the incident particles, the following procedure is used. First, the center-of-gravity of the bump is calculated using the the energy depositions in the 3×3 crystal matrix and the actual positions of the crystal front faces θ_i and ϕ_i:

$$\Theta_{cog} = \frac{\sum_{i=1}^{9} \theta_i E_i}{S_9} \qquad \Phi_{cog} = \frac{\sum_{i=1}^{9} \phi_i E_i}{S_9} \; .$$

The center-of-gravity is displaced from the true impact point due to the granularity of the calorimeter. Because the bump crystal has a very large weight in this sum, the center-of-gravity is always shifted to the center of the bump crystal. This effect can be taken into account using a correction function determined in beam tests, where the beam position could be measured with proportional chambers placed in front of the crystal matrix. The correction function is given by

$$x_{impact} = \alpha \tan \beta x_{cog} + \gamma x_{cog} \qquad y_{impact} = \alpha \tan \beta y_{cog} + \gamma y_{cog} \; ,$$

where x and y are given in the local Cartesian coordinate system with the center of bump crystal at the origin, and $\alpha = 6.0288$ mm, $\beta = 0.53$ mm^{-1}, and $\gamma = 0.215$. This procedure was proven to work very well for electromagnetic bumps in the energy range studied in this thesis [132].

5.2 Test Beam Studies

In 1987-88, prior to their installation in L3, both BGO half-barrels and a part of the endcaps were extensively studied [131] in the X3 beam line of the CERN super proton synchrotron (SPS).[3] Electron beams at four energies, 2, 10, 20, and 50 GeV, were used. One half-barrel was also tested using a 180 MeV electron beam extracted from the LEP injector Linac. The half-barrels were installed on a rotating table so that each crystal could be calibrated individually. A position accuracy of less than 1 mm was achieved, and the angle between the beam and longitudinal axis of the crystal was determined to be less than 5 mrad.

[3] The SPS was also a part of the LEP injector chain, which was described in detail in Section 4.1.1.

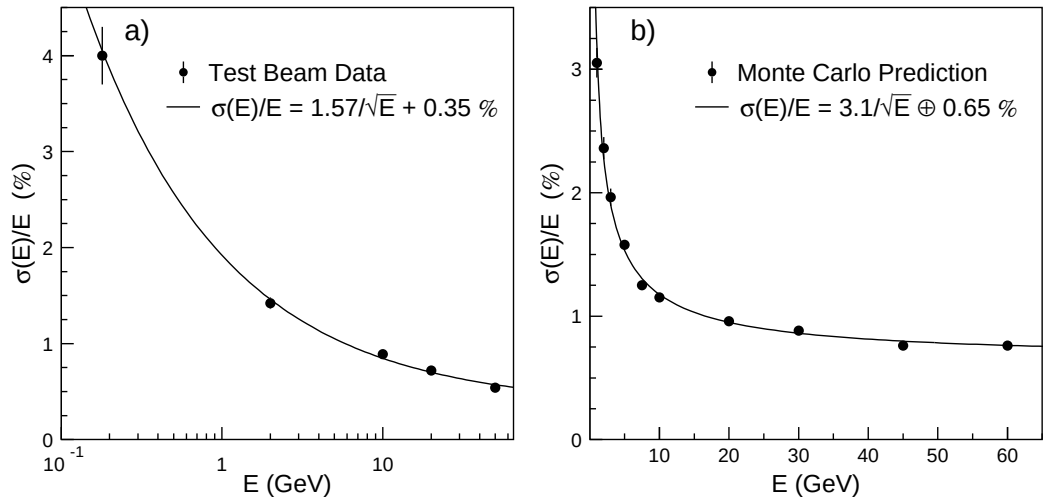

Figure 5.4: BGO energy resolution curves from a) test beam precalibration and b) Monte Carlo simulations.

The test beam studies were conducted to achieve the following objectives: to study the shower profile characteristics,[4] to calibrate each BGO crystal, and to measure the energy and angular resolutions of the calorimeter. About 800 events per crystal were collected, and the calibration constants were determined with an accuracy of 0.5%. Since the crystals were calibrated in the final configuration and with the final readout electronics, the obtained calibration constants were actually used at the beginning of the LEP physics program.

For each value of the beam energy, the overall energy resolution in the barrel was estimated by fitting the combined shower energy distributions of all crystals. After subtracting contributions from the calibration and beam energy errors, the BGO energy resolution was parametrized as

$$\frac{\sigma_E}{E}(\text{Test beam}) = \frac{1.6 \pm 0.1\ \%}{\sqrt{E}} + 0.35 \pm 0.05\ \%\ (E \text{ in GeV}). \tag{5.3}$$

The test beam measurements and the fitted resolution curve are shown in Figure 5.4a.

The energy resolution can also be studied using large samples of electrons gener-

[4] The results of the shower development studies were already used in the previous section.

ated using the *ideal* L3 Monte Carlo program. This program simulates the electromagnetic shower development in the BGO under the assumption of perfectly known calibration constants. The obtained energy resolution as a function of shower energy, shown in Figure 5.4b, is best fitted with[5]

$$\frac{\sigma_E}{E}(\mathrm{MC}) = \frac{3.1 \pm 0.1\ \%}{\sqrt{E}} \oplus 0.65 \pm 0.03\ \%\ (E \text{ in GeV})\,, \tag{5.4}$$

where the first term is expected to be mainly due to photostatistics fluctuations and the second term comes from shower containment limitations and calorimeter non-uniformities [133].

Naively, one would expect this resolution function to be in agreement with the one obtained with the test beams. However, one can see that this is not the case. For example, for 45 GeV showers the BGO energy resolution obtained using Monte Carlo simulation is expected to be about 0.9%, which is much worse than the 0.5% resolution obtained with the test beam. Moreover, the *in situ* energy resolution at the beginning of the LEP1 physics program was measured to be about 1.4% [134]. The reason for this discrepancy is the difference between the bump selection criteria used in the test beam precalibration and *in situ* at LEP. Only bumps with an impact point within 5 mm from the crystal center, $R_{impact} < 5$ mm, were selected in test beams studies. This very severe cut was not applied in the analysis of LEP data, as it would reject about 80% of electromagnetic showers.

In order to verify that this is indeed the cause of the discrepancy, I used a sample of about 6,600 Bhabha electrons with an energy of about 103 GeVwhich I selected in high energy data collected by L3 in the year 2000.[6] Figure 5.2 shows that the quantity S_1 decreases faster with increasing R_{impact} as compared to the quantity S_9. Thus, the ratio S_1/S_9 can be used to estimate R_{impact} and, as shown in Reference [135], the cut on the impact position applied in the test beam studies is equivalent to $S_1/S_9 > 0.8$ The distribution of S_1/S_9 for data and Monte Carlo is shown in Figure 5.5a, and the

[5]The symbol "$\oplus$" denotes the quadratic sum.

[6]The selection of Bhabha events is described in detail in Section 5.6.2.

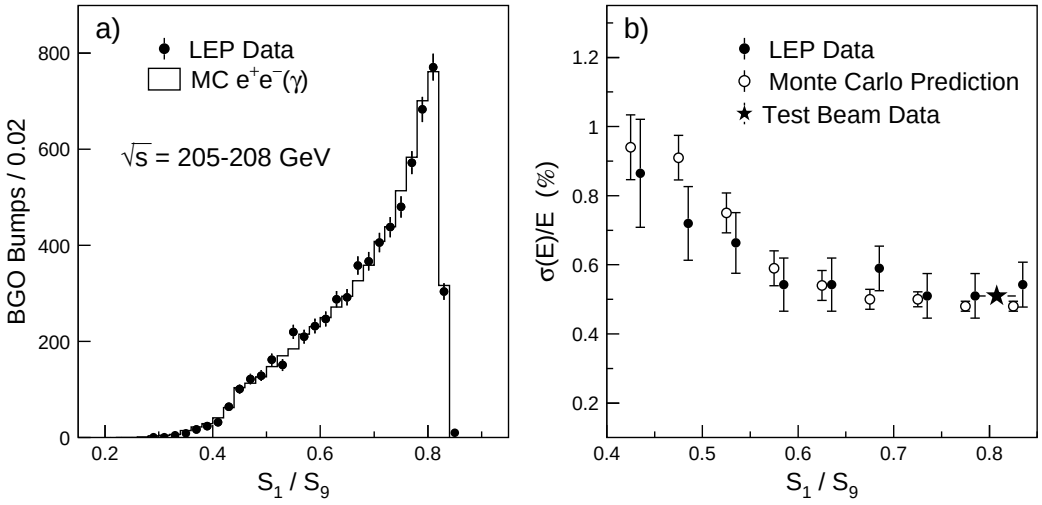

Figure 5.5: a) Distribution of S_1/S_9 for 103 GeV electrons. b) BGO energy resolution as a function of S_1/S_9 derived from LEP data, Monte Carlo simulation, and test beam studies. For clarity, the data points are slightly displaced horizontally.

obtained BGO energy resolution[7] as a function of S_1/S_9 is plotted in Figure 5.5b. A good agreement between measurements with LEP data and Monte Carlo predictions is observed. It is also important to note that for bumps with $S_1/S_9 > 0.8$, the resolution given by Monte Carlo simulation agrees well with the resolution measured in the test beam precalibration. Therefore, it can be concluded that the energy dependence of the BGO intrinsic resolution is better described by Equation 5.4. The validity of this equation is further confirmed in Section 5.6.2.

5.3 Monitoring of the BGO Calorimeter

In this section, I describe several techniques and systems used to monitor the BGO calorimeter at LEP. These include the temperature control and monitoring systems, the Xenon calibration system, and the detection of dead BGO channels. I also discuss problems with the BGO calibration at the beginning of the LEP2 phase and the need for a more precise calibration.

[7] The resolution measurement procedure is explained in Section C.1.

5.3.1 Temperature Control and Monitoring

The BGO light yield is temperature dependent; it decreases with increasing temperature with a coefficient of $-1.55\%/^{\circ}$C. Therefore, in order to achieve the designed energy resolution it was necessary to carefully control and monitor the BGO temperature. The temperature control was provided by active thermal shields consisting of brass screens to which copper pipes carrying a silicone-based coolant were soldered. These shields were used to dissipate the heat generated by preamplifiers and first-level boards (2 W per channel) and to prevent heat transfer from the BGO to the neighboring subdetectors.

Year	Barrel RB24		Barrel RB26		Endcap RB24		Endcap RB26	
	T_{front}	T_{back}	T_{front}	T_{back}	T_{front}	T_{back}	T_{front}	T_{back}
1998	17.11	16.94	16.97	16.94	17.49	17.50	16.98	17.49
1999	17.02	16.88	16.99	17.01	17.39	17.39	16.89	17.49
2000	17.01	16.89	16.90	16.91	17.28	17.31	16.92	17.39

Table 5.1: Mean temperatures (in °C) of the front and back surfaces of the four BGO subdetectors. The results are given as the annual averages for each year during the period 1998-2000.

The temperature monitoring was performed using 1792 2AD590 sensors (1280 in the barrel and 2×256 in the endcaps) with a reading accuracy of 0.1°C. They were positioned on the front and rear faces of one in every 12 BGO crystals. The temperature sensor data was digitized and read out in the same as way as the crystal light output data. The annual average front and back temperatures of the four BGO subdetectors are given in Table 5.1 for the period 1998-2000. This table shows that the average BGO temperature was about 17°C and its variations from year to year were below 0.1°C. It also shows that the average temperature gradient between the front and back surfaces was maintained to be at most a few tenths of a degree.

The BGO temperature was usually measured once a day, and the temperature map for the front and rear faces of the entire calorimeter was computed by fitting the sensor data to the Laplace's equation for heat transfer, $\nabla^2 T(\vec{r}) = 0$. The distributions of the front BGO temperature from a typical fit in 2000 are shown in Figures 5.6a

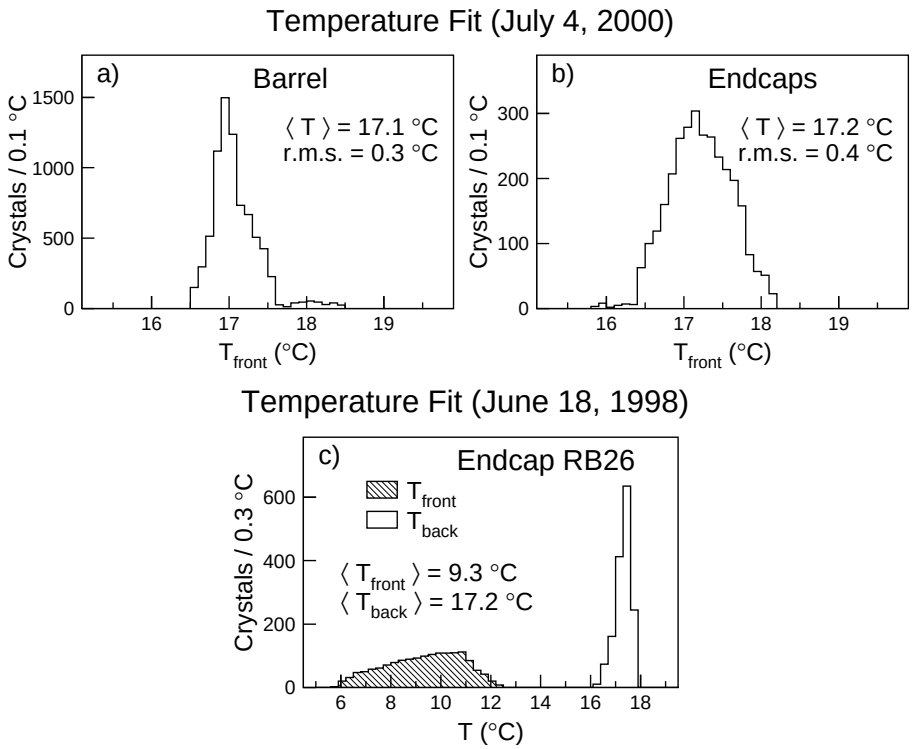

Figure 5.6: Distribution of the front BGO temperature, (a) in the barrel and (b) in the endcaps, from a typical temperature fit in 2000. (c) Distributions of the front and back BGO temperatures of the RB26 endcap from a typical "bad" temperature fit in 1998.

and 5.6b for the barrel and the endcaps, respectively. The energy reconstructed in a BGO crystal, as given by Equation 5.1, should then be multiplied by a temperature correction factor which is given by

$$C_T = 1 + 0.0155 \cdot (T_{max} - T_0), \quad T_{max} = T_{front} + \eta(E) \cdot \ (T_{back} - T_{front}), \qquad (5.5)$$

where T_0 is the reference temperature (chosen to be 18°C), T_{max} is the temperature at the location of shower maximum, T_{front} and T_{back} are the temperatures of the front and back crystal surfaces, and $\eta(E)$ denotes the longitudinal position of the shower maximum relative to the crystal length. The relative shower depth is energy dependent, and the reference values of $\eta(E)$ were determined to be $\eta(2\ \text{GeV}) = 0.21$, $\eta(10\ \text{GeV}) = 0.27$, and $\eta(50\ \text{GeV}) = 0.33$ [131].

The fit uncertainty on the surface temperatures of a given BGO crystal was esti-

mated to be 0.3°C [136]. The relative error on the temperature correction factor for the shower energy measurement can be then calculated from Equations 5.2 and 5.5 and is equal to about 0.5%. The actual uncertainty contributing to the BGO energy resolution may be slightly higher due to the aging of the temperature sensors.[8] It was estimated that during the LEP2 phase (1996-2000), 5-10% of the temperature sensors were either dead or provided unreliable data.

The number of such sensors was particularly high on the front side of the RB26 endcap,[9] where it led to the problem of so-called "bad" temperature fits. Figure 5.6c shows distributions of the front and back temperatures from a "bad" fit in 1998. As can be seen from this figure, the average back temperature is close to the expected value of about 17°C, whereas the front temperatures are given to be in the range of 6-12°C. This significant difference between the front and back temperatures was caused by several front sensors which produced unphysically low temperature readings.[10] In total, "bad" temperature fits affected about 6% of L3 data in 1997-1998, which gave rise to a clear secondary peak at $E_{shower}/E_{beam} \approx 0.85$ in the energy distribution for Bhabha electrons reconstructed in the RB26 endcap. I first noticed this effect in 1998 when I was selecting Bhabha events to test the RFQ calibration of the BGO calorimeter. I then carried out a study of the reliability of the BGO temperature monitoring and corrected the "bad" fits in the L3 database. During 1998-2000 I was responsible for monitoring the performance of the BGO temperature control system.

5.3.2 Dead Crystals

During the twelve years of BGO calorimeter operation at LEP, a certain number of readout channels started to malfunction and did not provide reliable readings. The appearance of such channels, which were usually referred to as *dead crystals*, was caused by malfunctioning photodiodes or preamplifiers and not by problems with the BGO crystals themselves. Since the BGO calorimeter was not accessible at LEP, the

[8] The study of the temperature fit uncertainty was performed in 1994 [136].
[9] The two halves of the L3 detector are traditionally referred to as RB26 and RB24.
[10] For instance, several "bad" fits produced sub-zero temperatures.

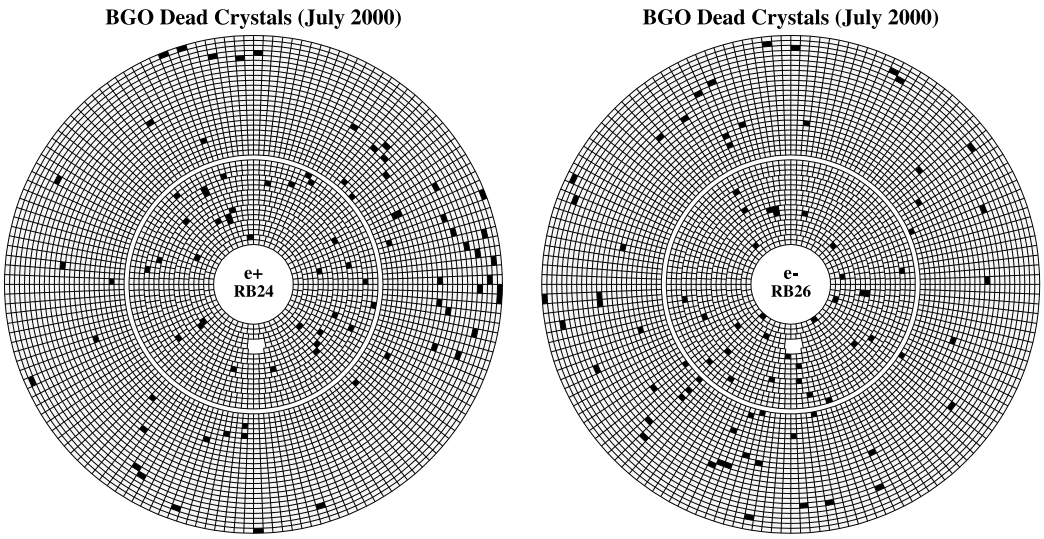

Figure 5.7: Distributions of the dead channels for the two sides of the BGO calorimeter. The dead crystals are shown as black squares and the inner and outer rings represent the endcaps and half-barrels, respectively.

readout electronics could not be repaired and the dead crystals had to be dropped from the standard BGO reconstruction.

The number of dead crystals was almost constant during the LEP2 phase and amounted to about 1.5% of the total BGO channels (about 100 channels in the barrel and 60 channels in the endcaps) [137]. The majority of the dead crystals were identified online with Xenon flashlamps, as described in the next section. The remaining dead crystals were detected offline using large samples of events with high multiplicity hadronic jets. Such events provided azimuthally-independent irradiation of the BGO calorimeter and the malfunctioning channels could be identified as deviations in the crystal occupancy distributions of the individual BGO θ-rings [135]. An additional class of dead channels was found during the first RFQ calibration in 1997. While investigating the problem of hard resolution tails, I found that the long tail, above $E_{shower}/E_{beam} = 1.1$, of the Bhabha energy distribution was caused to a large extent by about 20 crystals with mismeasured pedestals,[11] which were then also discarded from the BGO reconstruction.

[11] This problem was caused by a bug in the pedestal measurement algorithm, which had been overlooked at LEP1.

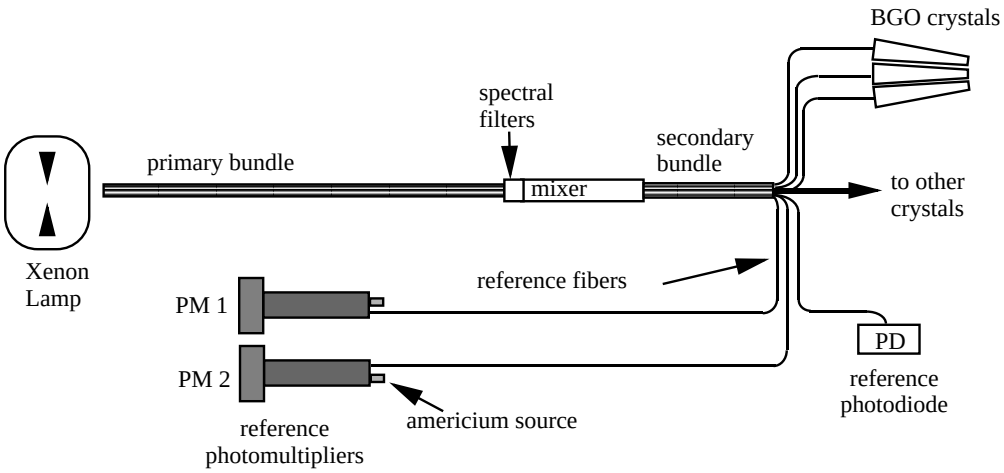

Figure 5.8: Schematic diagram of the Xenon monitoring system.

Figure 5.7 shows that the dead crystals were almost uniformly distributed and did not form dead regions in the BGO. To compensate for the energy loss caused by the BGO dead crystals, I developed a special algorithm, described in detail in Section C.2. This algorithm proved to be useful for both the RFQ calibration and the reconstruction of the electromagnetic showers.

5.3.3 Xenon Monitoring System

BGO light collection efficiency and electronics gain variations were monitored *in situ* with a Xenon flasher system [138, 139]. The system consisted of 32 Xenon lamps which generated light flashes with a spectrum tuned to match the spectrum of the BGO scintillation light. Light from each lamp was first transported to light mixers using bundles of optical fibers (*primary fiber bundles*) and then to the individual crystals using secondary fiber bundles (see Figure 5.8). The intensity of light from each mixer was measured with two reference photomultipliers, which were in turn monitored using γ rays from a radioactive ^{241}Am source. Both low and high gain electronics channels were studied using light pulses of different intensity, equivalent to about 1.1 GeV and 30 GeV.

Xenon calibration runs were performed on a daily basis and were very useful for

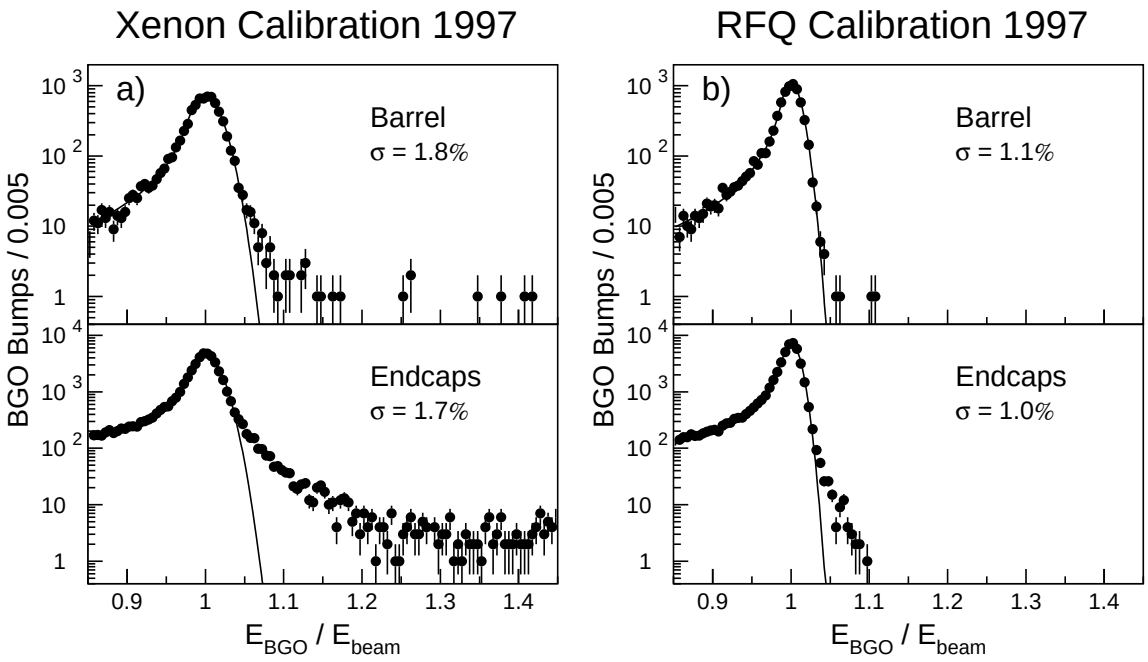

Figure 5.9: Energy distributions of Bhabha electrons selected in 1997 L3 data and reconstructed using a) Xenon and b) RFQ calibrations. The obtained BGO energy resolutions are shown on the plots.

monitoring the channel by channel BGO performance[12] and for studying the aging of the BGO [140]. Prior to 1997, the Xenon system was also used for the BGO calibration. The intercalibration of the BGO crystals was obtained using Xenon light flashes, while the absolute normalization was provided by Bhabha electrons. Energy resolutions of about 1.4% were achieved [134]. At the beginning of the LEP2 phase, the precision of the Xenon calibration started to deteriorate due to a significant decrease in the available Bhabha statistics.[13] In 1997 the BGO energy resolution obtained using Xenon calibration was about 1.8% with significant resolution tails,[14] as shown in Figure 5.9a. The test beam precalibration clearly showed that with an adequate calibration, the BGO calorimeter was capable of providing a sub-percent energy resolution. The goal of decreasing the calibration errors was achieved by the

[12] As described in the previous section.

[13] The cross section of the Bhabha scattering process was much lower at LEP2 than at LEP1.

[14] About 1.5% of Bhabha electrons in the endcaps and 0.7% in the barrel were reconstructed with $E_{shower}/E_{beam} > 1.1$.

RFQ calibration system, designed and built by the Caltech L3 group. Figure 5.9 shows a comparison between the Xenon calibration and the first successful RFQ calibration. The RFQ calibration system and method are described in the following sections.

5.4 RFQ Calibration Concept

In high-energy physics experiments, the task of calorimeter calibration is usually performed in two consecutive steps: 1) relative channel-to-channel calibration (*intercalibration*) and 2) adjustment of the absolute energy scale of the calorimeter (*absolute calibration*). At e^+e^- colliders, Bhabha scattering produces electrons with energy close to the beam energy and is widely used for the absolute calibration of electromagnetic calorimeters. In rare cases such as CLEO-II at CESR [141], the Bhabha production rate can be so high that no prior intercalibration is required. However, most often an intercalibration with a dedicated calibration system is necessary. For L3 at LEP2, the rate of useful Bhabha events in the BGO barrel was very low (2-3 Bhabha showers per crystal per year), and a rapid, reliable, and precise intercalibration of the BGO was of utmost importance. The Xenon monitoring system (see the previous section) was not able to intercalibrate the BGO calorimeter with the required 1% precision,[15] and a new intercalibration system was clearly needed.

Electromagnetic calorimeters are often intercalibrated with γ-rays from radioactive sources (e.g., at CUSB [142], Crystal Ball [143], and BaBar [144]). Unfortunately, the maximum photon energy easily available from a long-lived radioactive source is the 2.6 MeV line of ^{228}Th, which was much too close to the pedestal at L3 [145]. Cosmic rays can also be used as a calibration tool (e.g., at KLOE [146] and BELLE [147]). However, this technique was proven to be impractical for L3 since the required intercalibration precision of 1% could be achieved only after several months of dedicated running [148]. In order to solve the problem of the BGO intercalibration, the Caltech L3 group developed a novel calibration system based on a Radiofrequency Quadrupole

[15] The Xenon system was not able to directly test the scintillation mechanism of the BGO crystals. In addition, it was impossible to unfold the BGO aging from the aging of the optical fibers which were used to bring the light from Xenon flashlamps to the individual BGO crystals.

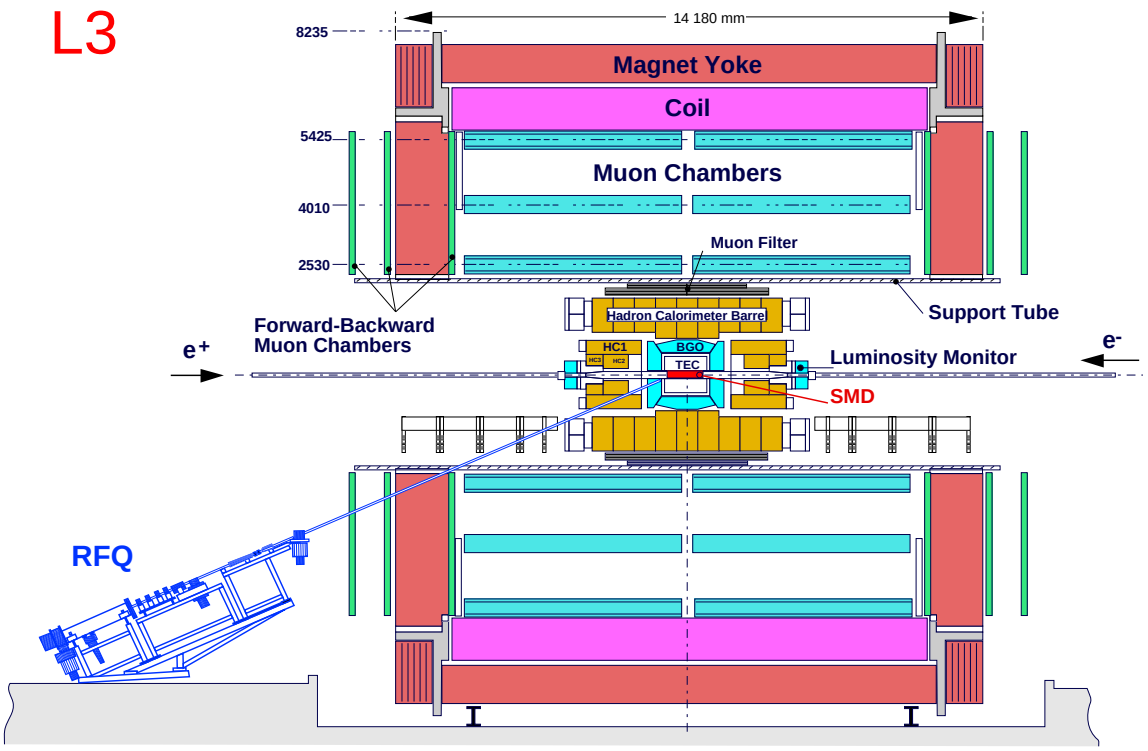

Figure 5.10: Side view of the RFQ system installed in L3.

(RFQ) accelerator. The principle behind the system was to bombard a lithium target, permanently installed inside the BGO calorimeter, with a pulsed H^- beam from the RFQ accelerator. After focusing and steering, the beam was neutralized to allow it to pass undisturbed through the L3 magnetic field. Radiative capture of protons

$$p + {}^{7}_{3}\mathrm{Li} \rightarrow {}^{8*}_{4}\mathrm{Be} \rightarrow {}^{8}_{4}\mathrm{Be} + \gamma$$

produced a monochromatic flux of 17.6 MeV photons, which was used to simultaneously calibrate the entire BGO calorimeter on a crystal-by-crystal basis [149]. This particular nuclear reaction was chosen because it provides the highest photon energy attainable with non-cryogenic targets [145]. Figure 5.10 shows the installation of the RFQ system in the L3 detector.

5.5 The RFQ Calibration System

The RFQ calibration system was conceived and developed by the Caltech L3 group in 1984-1991 [150]. In 1992, it was installed in the L3 cavern and the inaugural *in situ* RFQ run was performed in 1993. After a major maintenance and upgrade of the system during the 1994-95 LEP shutdown, two successful high-statistics calibration runs were performed in 1995 giving the first RFQ calibration of the BGO [151].

The Crystal Ball experiment was the first to employ an accelerator (a Van de Graaf) as a calibration tool [143, 152]. However, the L3 RFQ calibration system was substantially more advanced as it was designed to provide a much higher beam intensity[16] and to be permanently installed in the detector. The last feature was essential given the size and complexity of L3 and required the use of an H^- ion beam coupled with a beam neutralizer. In addition, it imposed severe restrictions on the size of the system and on the designs of the RFQ beam pipe and target.

The RFQ calibration system consisted of the following components:

- A 30 keV RF-driven (2 MHz) volume H^- ion source with a maximum output current of 7.5 mA.
- A low-energy beam transport.
- A 1.85 MeV RFQ (425 MHz) accelerator, with a maximum output beam current of 35 mA.
- A high-energy beam transport comprising focusing and steering magnets.
- A beam neutralizer ($H^- \rightarrow H^0 + e^-$) consisting of a 1 m long N_2 gas cell, at a typical pressure of $5 \cdot 10^{-4}$ Torr, with a maximum neutralization efficiency of 55%.
- A 10 m long beam pipe, equipped with a star-cell ion pump (20 LPS) and a non-evaporable getter ribbon pump (3 LPS).

[16] The Crystal Ball experiment mainly used the nuclear reaction ${}^{19}_{9}\mathrm{F}(\mathrm{p},\alpha)\,{}^{16*}_{8}\mathrm{O}$ which has an order of magnitude larger cross section than the reaction ${}^{7}_{3}\mathrm{Li}(\mathrm{p},\gamma)\,{}^{8}_{4}\mathrm{Be}$ used in the L3 RFQ calibration [153]. Moreover, the BGO calorimeter had about 10 times more crystals than the NaI(Tl) main detector of the Crystal Ball.

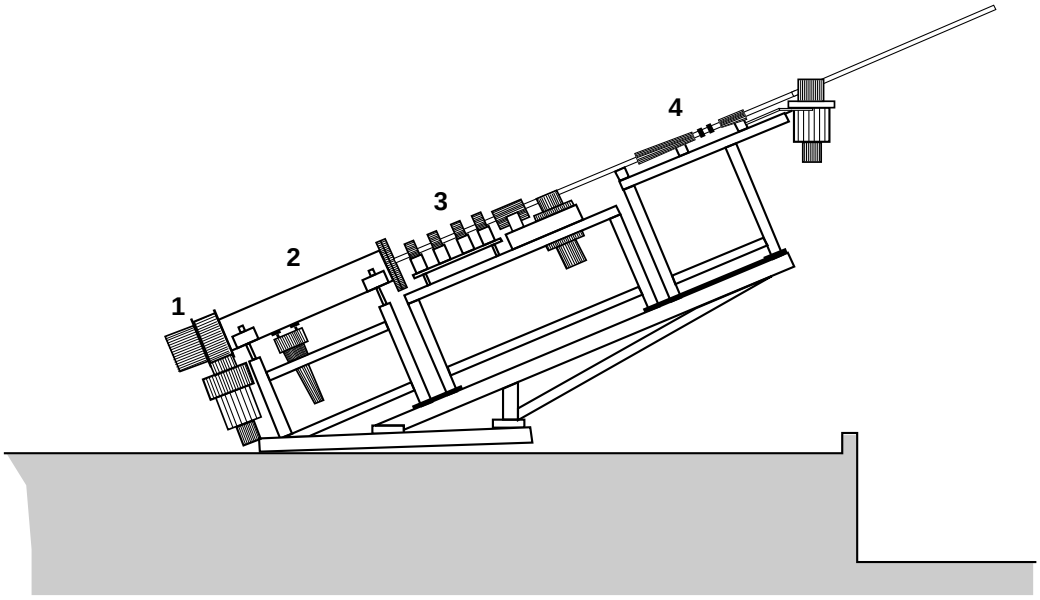

Figure 5.11: Schematic drawing of the RFQ system: 1) ion source; 2) RFQ accelerator; 3) steering and focusing magnets; 4) beam neutralizer.

- A water cooled LiH target, mechanically sealed with a thin Mo foil and mounted at the end of the beam pipe.
- Data acquisition and readout systems.

In order to protect the low energy ion beam from the fringe field of the L3 magnet, the RFQ accelerator, ion source, and neutralizer were enclosed inside a magnetic shield made of 15 mm thick mild-steel plates. A general view of the RFQ system is shown in Figure 5.11, and a detailed description of the RFQ system components can be found in Appendix B.

The RFQ calibration system proved to be reliable and robust. From 1995 to 2000, a total of nine RFQ calibration runs were performed, collecting a total of about 100 million triggers. Only one of the scheduled runs (Fall 1998) had to be canceled due to a malfunction in the ion source. The last calibration run performed in September 2000 showed no evidence of aging of the RFQ system hardware.

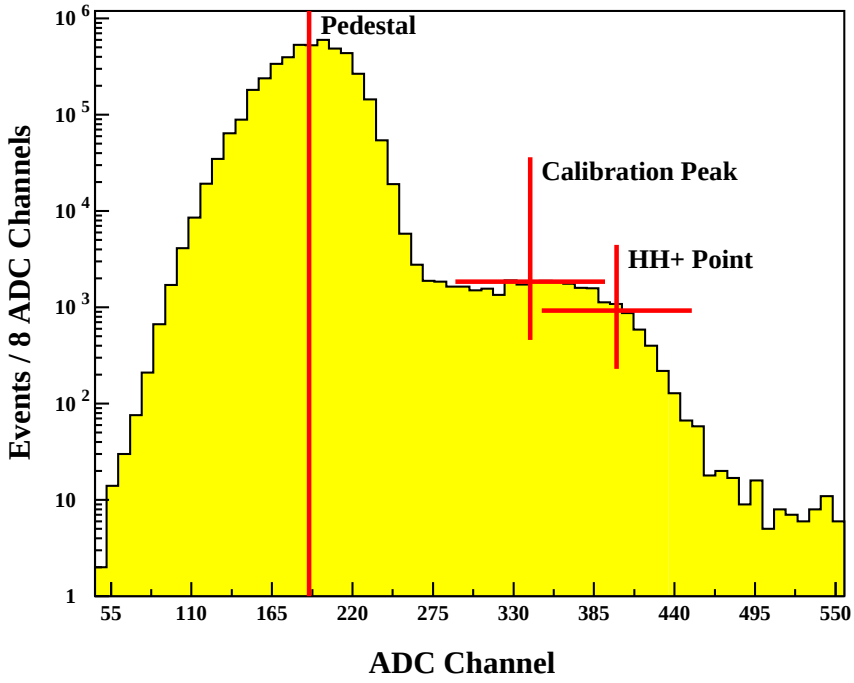

Figure 5.12: Typical energy spectrum of the photons produced by the RFQ system. Also shown is the definition of the HH^+ calibration point.

5.6 BGO Calibration

In this section I describe the methods that I developed and used to calibrate the BGO calorimeter using both the RFQ and LEP data. I also present the calibration results and briefly discuss how the RFQ experience can be used in calibrating the CMS electromagnetic calorimeter at the LHC.

5.6.1 Intercalibration with the RFQ System

The RFQ calibration runs were taken twice a year, before and after the annual LEP data taking run. Each RFQ run took three to five days to complete and, with an average DAQ rate of 80 Hz, produced about 10 million calibration triggers (beam pulses on target). As described in Section 5.4, the RFQ calibration was performed using 17.6 MeV photons produced by the radiative capture reaction $^{7}_{3}\mathrm{Li}(\mathrm{p},\gamma)\,^{8}_{4}\mathrm{Be}$. A typical photon energy spectrum recorded by a BGO crystal is shown in Figure 5.12.

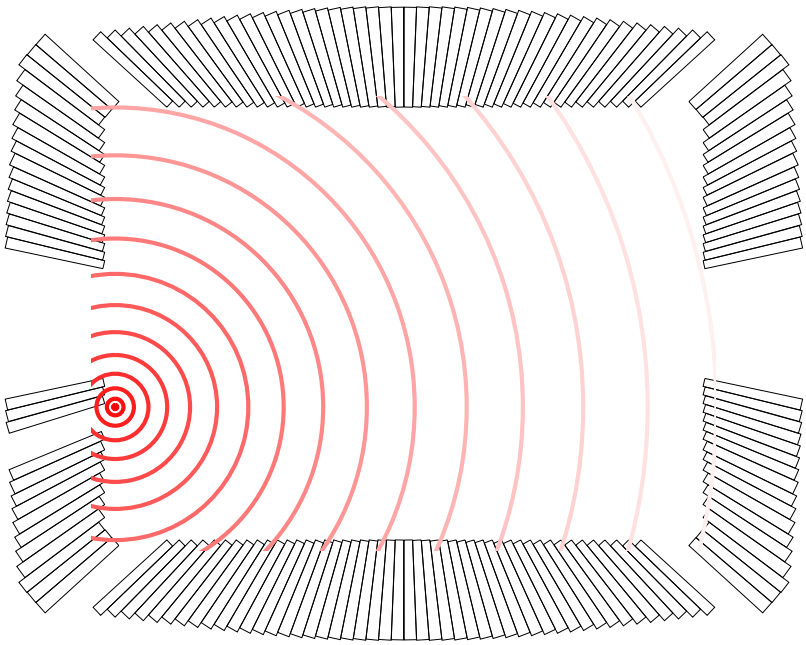

Figure 5.13: Side view of the BGO calorimeter with concentric circles representing the photon flux originating at the RFQ target.

The calibration constants were then derived as

$$\text{Calibration Constant}(\text{keV/ADC Count}) = \frac{E_{\text{HH}^+}}{\text{HH}^+ - \text{Pedestal}}, \tag{5.6}$$

where E_{HH^+} was assumed to be equal to 17.6 MeV and the "HH^+" edge was the specific feature used for calibration and defined as the point half-way below and to the right of the calibration signal peak (see Figure 5.12). Figure 5.13 shows that the RFQ target was significantly off-center with respect to the BGO calorimeter. As a result, the incident photon angle and the amount of material in front varied from crystal to crystal. Previous studies[17] had shown that while the HH^+ point was the least sensitive to these systematic effects, the induced variations in the actual values of E_{HH^+} could be as high as 2-3% [150, 155]. These geometrical effects were corrected for by the absolute calibration with Bhabha events, as described in the next section.

The position of the HH^+ point was found using a simple *moving window* algorithm.

[17]Including Monte Carlo studies [150, 154] and beam tests with a Van de Graaf at Caltech [150] and with an RFQ at AccSys Technology [150, 155].

The procedure started with finding the maximum of the signal peak by defining three adjacent windows and assuming that the spectrum was parabolic in the windowed region. The windows were slid along until the estimated maximum was found within the windowed region. The maximum was then computed as a weighted average of the values obtained by varying the window sizes from 16 to 48 ADC counts. After the maximum was found, the HH^+point was obtained with a similar method which used two adjacent windows and assumed that the spectrum was linear in the windowed region. Another method of finding the HH^+ point by using a cubic spline fit had also been tested and gave similar results [150].

Calibration Results

The rate of calibration photons per crystal was characterized by the *photon occupancy*, defined as the fraction of triggers with energy deposition in one crystal larger than 14 MeV. Because of the off-center location of the RFQ target, the occupancy differed from crystal to crystal and was significantly higher for the RB24 half of the BGO calorimeter (the side closer to the RFQ target). Figure 5.14 shows the photon occupancy for the calibration run performed in September 2000. The typical crystal occupancy was about 0.008% for the near side (RB24) and about 0.004% for the far side (RB26).

As discussed in Section B.5, a veto scheme was implemented to reject photons not contained in a single crystal. Because of this, the highest calibration efficiency was achieved when the average occupancy was about 1-2% [149]. The intensity of the calibration photon flux was below this optimum level mainly because the ion source was not capable of delivering a sufficiently high H^- current (see Section B.1.1).

The BGO temperature was monitored during the RFQ runs and the calibration constants derived from Equation 5.6 were corrected to the reference temperature of 18°C using Equation 5.5. Calibration constants obtained from the September 2000 RFQ run are shown in Figure 5.15, and the typical calibration constant value is about 90 keV/ADC Count. Comparing Figures 5.14 and 5.15, one can see that contrary to the distribution of the crystal occupancy, the spatial distribution of the calibration

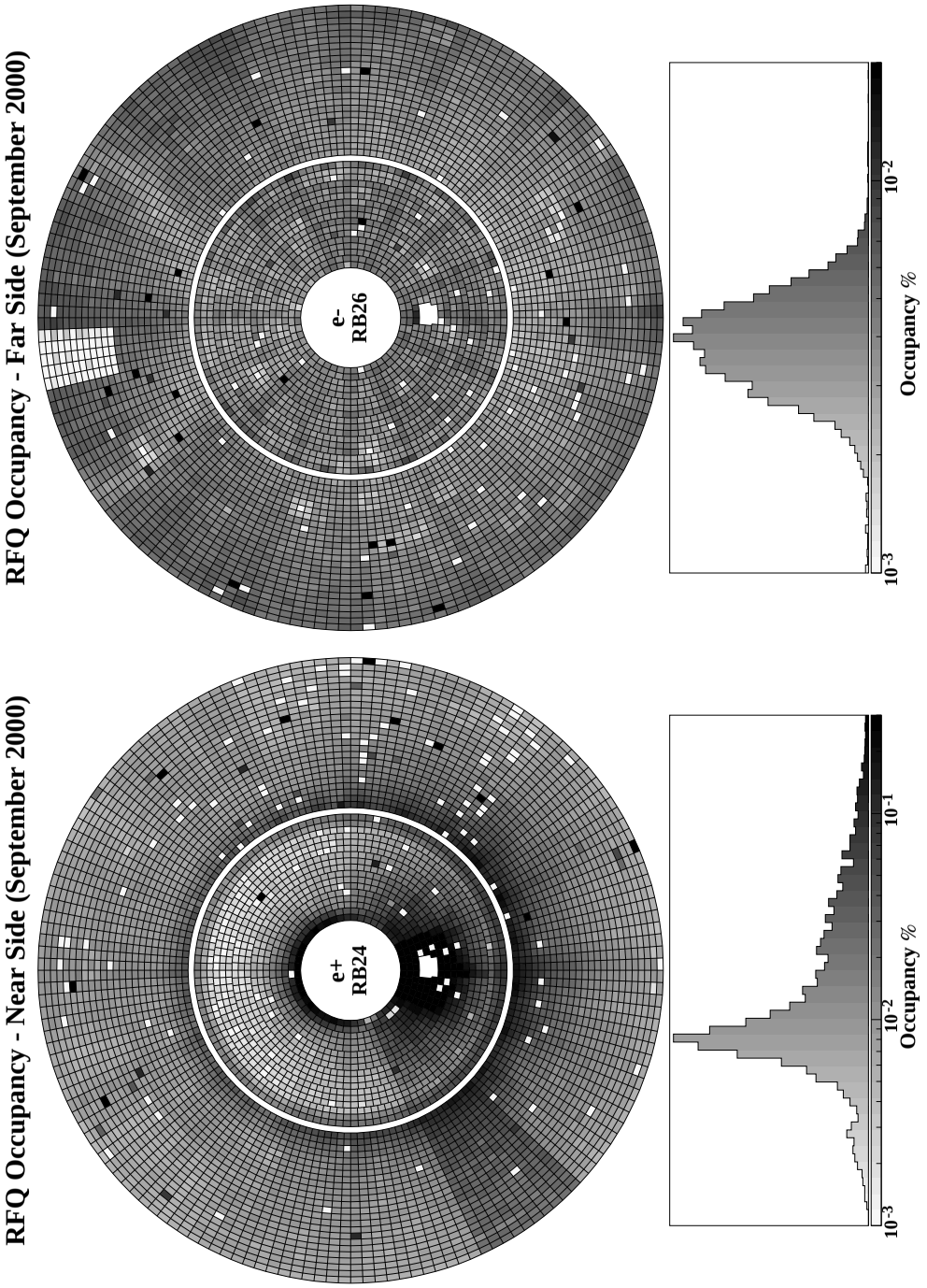

Figure 5.14: Crystal occupancy for the September 2000 RFQ run. The inner and outer rings represent the endcaps and half-barrels, respectively. The holes in the endcaps are for the RFQ beam pipe.

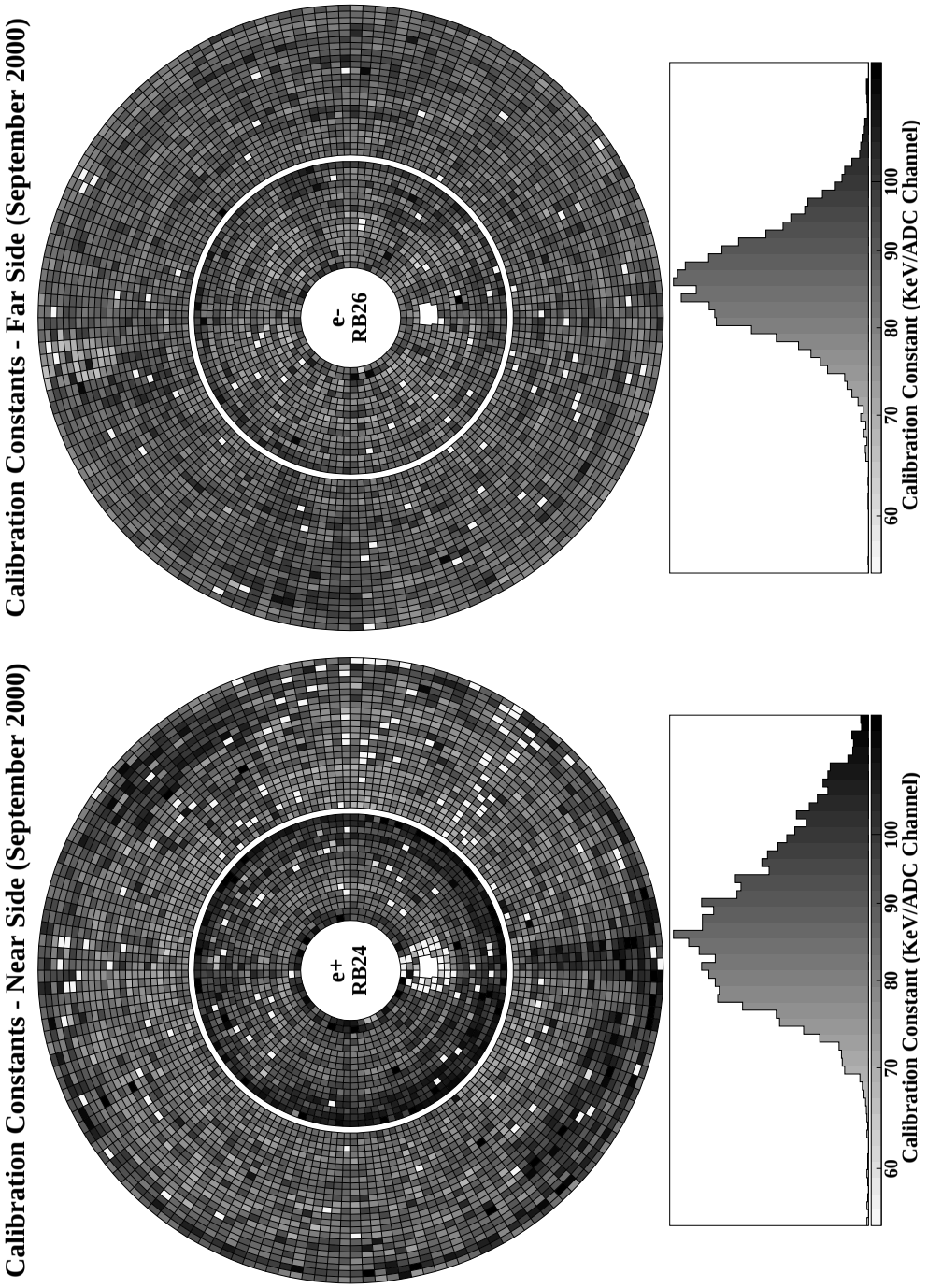

Figure 5.15: Calibration constants from the September 2000 RFQ run. The inner and outer rings represent the endcaps and half-barrels, respectively. The holes in the endcaps are for the RFQ beam pipe.

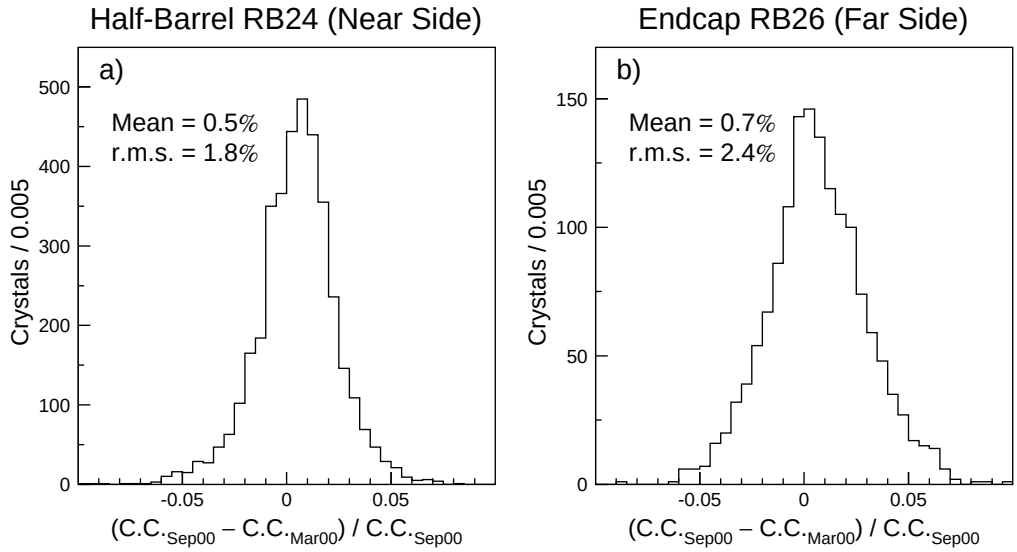

Figure 5.16: Relative difference between the two sets of calibration constants derived from the March and September 2000 RFQ runs. Shown are the distributions for the near side barrel and far side endcap.

constants was relatively uniform across the BGO and unaffected by various systematic effects such as the off-center location of the RFQ target and electronic noise in the readout segments of the BGO calorimeter.

The statistical precision of the intercalibration can be estimated by plotting the relative difference between constants obtained from two independent runs, as shown in Figure 5.16 for the two runs taken in the year 2000. The RMS width of this distribution shows that the statistical uncertainty on the RFQ calibration constants[18] was about 1% for all four parts of the calorimeter.[19] The non-zero shift in the average constant value is consistent with the aging of the BGO response (see Section C.3).

However, the total error of the RFQ calibration was dominated by the systematic uncertainties, as can be seen from Figure 5.17, which shows the energy distribution of Bhabha electrons reconstructed using a set of the RFQ calibration constants. The overall precision of the intercalibration was determined to be about 2% in the barrel

[18]Calibration constants from the semiannual RFQ runs were usually averaged, and the obtained set of constants was used as a starting point for the annual absolute calibration of the BGO.

[19]It should be also noted that this estimate is consistent with the values obtained from an early test at AccSys Technology [150] and from the first *in situ* RFQ calibration runs at L3 [151].

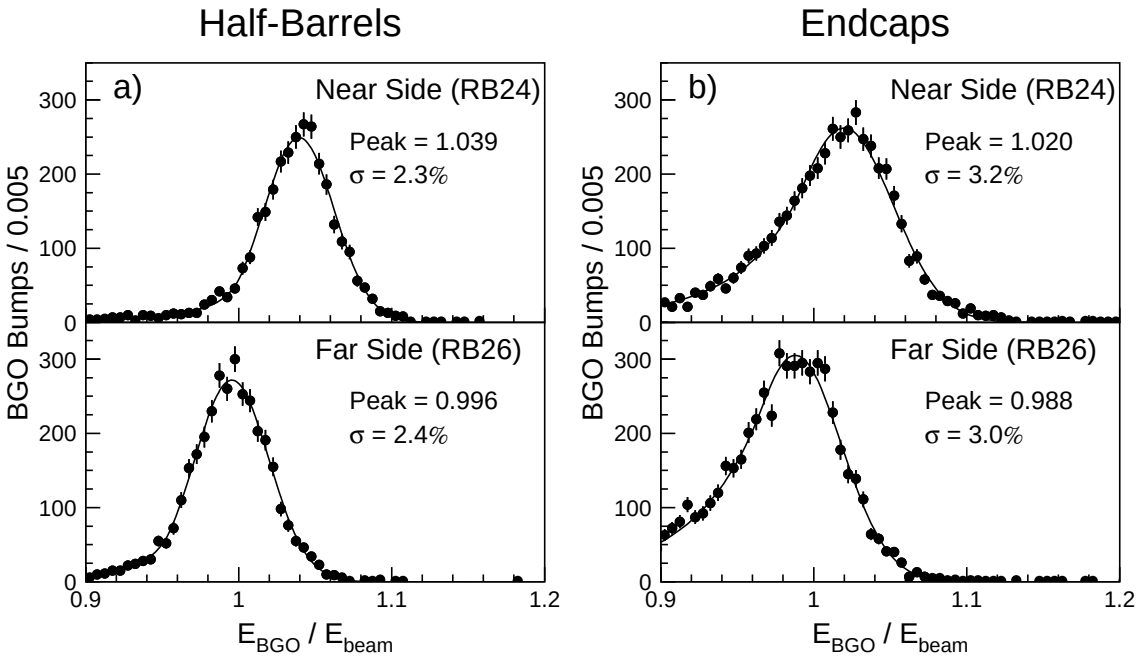

Figure 5.17: Energy spectra of Bhabha electrons reconstructed using a set of the RFQ intercalibration constants, a) in the barrel and b) in the endcaps. The peak positions and resolutions are indicated on the plots.

and 3% in the endcaps. The quality of the intercalibration was worse in the endcaps due to the more complicated geometrical effects. The RFQ target was located very close to the surface of the near side endcap (RB24), producing significant variations in the photon incident angle. For the far side endcap (RB26), the propagation of the calibration photon flux was perturbed by the TEC end-flange, a 5 cm thick aluminum plate.

In addition to the geometrical effects, the calibration precision was affected by the nonlinearity of the BGO response, as we had to extrapolate from the 17 MeV energy scale of the calibration up to the $\mathcal{O}$(10 GeV) scale of physics at LEP. Figure 5.17 shows that the geometrical effects also induced a noticeable shift (1-2% depending on the subdetector) in the absolute scale of the RFQ calibration. However, the above systematic effects were time-independent and thus could be easily corrected for using Bhabha electrons, as described in the next section.

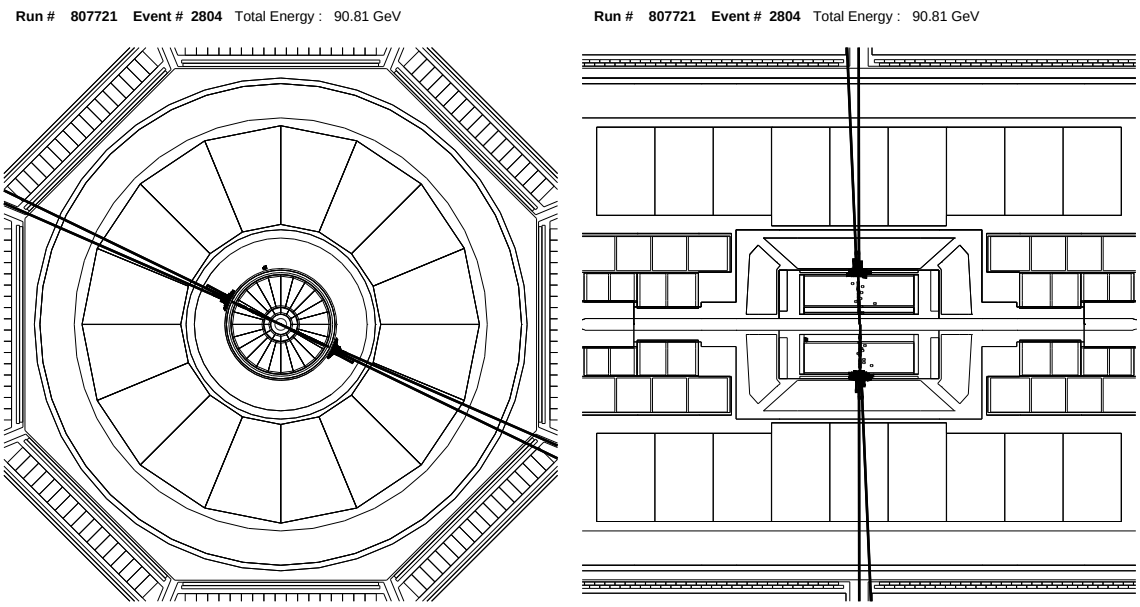

Figure 5.18: A typical back-to-back Bhabha scattering event recorded by the L3 detector at $\sqrt{s} = 91.2$ GeV and displayed in the $x - y$ and $x - z$ planes. Tracks reconstructed in the TEC are shown as back-to-back lines originating near the primary vertex. Energy deposits in the BGO crystals are shown as towers whose height is proportional to the crystal energy.

5.6.2 Absolute Calibration with Bhabha Events

Selection of Bhabha Events

The Bhabha scattering process, $e^+e^- \to e^+e^-(\gamma)$, is widely used in calibration of electromagnetic calorimeters because it produces events with back-to-back electrons whose energy is kinematically constrained to be close to the beam energy, which is usually known to a very high precision ($0.01 - 0.02\%$ at LEP). A typical back-to-back Bhabha event recorded by the L3 detector in April 2000 is shown in Figure 5.18. Therefore, the first step of the absolute calibration was to select a sample of such Bhabha events. The selection criteria that I used are listed below:

Fiducial volume

$42^\circ < \theta_{1,2} < 138^\circ$ (barrel) and $10^\circ < \theta_{1,2}(180^\circ - \theta_{1,2}) < 37^\circ$ (endcaps), where θ_1 and θ_2 denote the polar angles of the two most energetic bumps. This cut ensured that the most energetic bumps were both in the BGO barrel or both in the endcaps.

Shower energies $E_1 > 0.8 \cdot E_{beam}$ and $E_2 > 0.5 \cdot E_{beam}$,
where E_1 and E_2 were the energies of the two most energetic bumps and E_{beam} was the beam energy. This cut rejected most of the $e^+e^- \to \tau^+\tau^-$ background.

Acollinearity $\zeta < 5°$,
where ζ was the acollinearity angle between the two most energetic bumps.[20] This was the most important cut of the selection as it rejected most of the radiative Bhabha events, $e^+e^- \to e^+e^-\gamma$, and ensured that the selected events contained only back-to-back showers. Without this cut, as much as 20% of the Bhabha events were expected to include at least one electron with energy below $0.9 \cdot E_{beam}$ since a significant fraction of energy could be carried away by initial and final state photon radiation.

Transverse shower profile $S_9^c/S_{25}^c > 0.94$.
This requirement was widely used in L3 to reject showers originating from hadrons and cosmic rays. It ensured that both BGO bumps had the shower profile consistent with the one expected for an electron or a photon. More than 99% of Bhabha showers were expected to pass this cut.

Longitudinal shower profile $E_{\mathrm{HCAL}}/E_{\mathrm{BGO}} < 0.08$,
where E_{BGO} was the bump energy as measured by the BGO and E_{HCAL} was defined as a sum of energies of the HCAL clusters in a 10° cone around the bump direction. This requirement rejected showers with significant leakage into the hadron calorimeter. More than 98% of Bhabha showers were expected to pass this cut. The performance of these shower-shape cuts will be discussed in more detail in Section 6.3.1 of Chapter 6.

No other significant activity in the detector $E_{vis} - E_{\mathrm{BGO}} < 5$ GeV and $E_3 < 0.3$ GeV,
where $E_{vis} - E_{\mathrm{BGO}}$ gave the energy not assigned to the identified BGO bumps and E_3 was the energy of the third most energetic shower in the BGO, if any.

This selection is similar to the BGO-based Bhabha selection which was widely used at LEP1 [151]. Since no information from the tracking system of L3 was used,

[20] About 20% of the showers were either near the calorimeter edges or had a dead channel in the 3×3 matrix around the bump crystal. For events with at least one such shower, the acollinearity cut was relaxed to 8°.

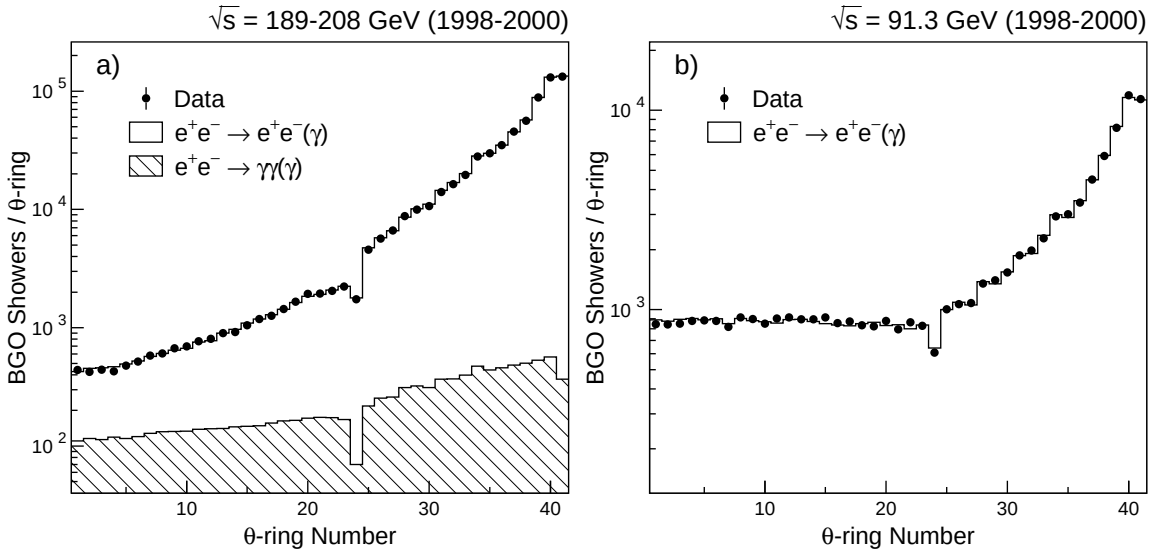

Figure 5.19: θ-ring distribution of the back-to-back showers used in the absolute calibration of the BGO. Shown are the distributions for the samples selected in 1998-2000 at a) $\sqrt{s} = 189 - 208$ GeV and b) $\sqrt{s} = 91.3$ GeV. Here the θ-ring number refers to the location of the central crystal of the electromagnetic shower.

events from the collinear photon (di-photon) production process, $e^+e^- \to \gamma\gamma(\gamma)$, were also accepted. At Born level, this is a well-understood QED process with a cross section significantly smaller than that of the Bhabha scattering.

Figure 5.19a shows the θ-ring[21] distribution for events selected in 625 pb^{-1} of data collected by L3 during 1998-2000 at $\sqrt{s} = 189-208$ GeV. Also shown are the expected distributions for the Bhabha scattering and collinear photon production, which are obtained using the `BHWIDE` [156] and `GGG` [157] Monte Carlo generators, respectively. Good agreement between data and Monte Carlo predictions was observed. The number of selected events increased sharply with the θ-ring number and was much higher in the endcap region ($N_{\theta-\mathrm{ring}} > 24$). This was because at LEP2 energies the Bhabha scattering proceeded predominantly through the t-channel electron exchange so that its differential cross section rose steeply at low polar angles.

However, in the BGO barrel the production cross section at high center-of-mass

[21] As described in Section 4.2.3, each BGO half-barrel and endcap consisted of 24 and 17 individual θ-rings, respectively (see Figures 4.9 and 4.11).

energies was rather small: at $\sqrt{s} = 200$ GeV $\sigma_{e^+e^-} = 22$ pb and $\sigma_{\gamma\gamma} = 4$ pb [135, 158]. To increase the calibration statistics, I also used data from *Z-peak* LEP runs.

During each year of the LEP2 program, 15-20 days were dedicated to LEP runs at the Z peak, $\sqrt{s} = 91.3$ GeV, and the collected samples of two-fermion events were used to calibrate the LEP detectors.[22] At the Z peak, the Bhabha scattering reaction was dominated by the s-channel Z exchange, and its production cross section in the barrel region was significantly higher: $\sigma_{e^+e^-(\gamma)} \simeq 1$ nb [151]. During 1998-2000, the L3 detector recorded a total of 11.1 pb^{-1} of data at $\sqrt{s} = 91.3$ GeV. The corresponding θ-ring distribution of the selected Bhabha showers is shown in Figure 5.19b.

Combining the two selected samples gave a total of about 50,000 and 850,000 calibration showers for the BGO barrel and endcaps, respectively. In order to improve the calibration precision in the barrel, I also selected a sample of about 20,000 Bhabha events using 30.1 pb^{-1} of data collected in 1995 at or near the Z resonance. It should be noted that the back-to-back Bhabha and di-photon events could be used not only for the absolute calibration of the BGO, but also for the studies of the BGO aging and non-linearity, as described in Appendix C.

Iterative Calibration Algorithm

After the event samples had been selected, the absolute calibration scale could be set using an iterative calibration algorithm which exploited the fact that the showers in the selected back-to-back e^+e^- and $\gamma\gamma$ events were kinematically constrained to have an energy close to the beam energy. The calibration constant for a given crystal was obtained as follows [159]:

$$\mathcal{C}_N(n_\theta, n_\phi, n_z) = \mathcal{C}_{N-1}(n_\theta, n_\phi, n_z) \cdot \frac{1}{\sum_{i=1}^{n_{bumps}} w_i} \sum_{i=1}^{n_{bumps}} \frac{E_{beam}}{E_i} w_i \,, \tag{5.7}$$

where

1. N was the iteration step number.

[22] The $\mu^+\mu^-$ events were used to calibrate the muon chambers and the charged particle trackers, the $q\bar{q}$ events provided the jet energy scale, and the Bhabha scattering events were used to calibrate the trackers and electromagnetic calorimeters.

2. $\mathcal{C}(n_\theta, n_\phi, n_z)$ was the calibration constant.

3. n_θ, n_ϕ, and n_z were the coordinates of the crystal — n_θ was the θ-ring number, n_ϕ gave the ϕ-coordinate, and $n_z = 1, 2$ corresponded to the two halves of the BGO calorimeter (RB24 and RB26).

4. n_{bumps} was the number of the selected BGO bumps containing this crystal in the 3×3 crystal matrix centered on the crystal with the maximum energy deposition.

5. E_{beam} was the beam energy.

6. E_i was the energy (corrected sum-of-nine) of the ith bump computed using the raw ADC signals and the calibration constants from the previous iteration step, $\{\mathcal{C}_{N-1}\}$, according to Equations 5.1 and 5.2.

7. w_i was the weight assigned to the ith event for the crystal, which I chose to be equal to the ratio of the energy deposited in the crystal to the total energy deposited in the 3×3 crystal matrix, where these energy quantities were also computed using the calibration constants $\{\mathcal{C}_{N-1}\}$ and the raw ADC signals.

The initial set of constants, $\{\mathcal{C}_0^{\mathrm{RFQ}}\}$, was provided by the RFQ intercalibration.[23] Since the available Bhabha statistics was limited and the precision of the RFQ intercalibration was quite high, five or six iteration steps were usually sufficient to reach the maximum calibration precision, and no significant improvement could be obtained by increasing the number of iterations.

To further reject radiative Bhabha events, only bumps with an energy above $0.95 \cdot E_{beam}$ were used in the calibration. In addition, to minimize systematic effects from the BGO non-linearity and electronic noise, a BGO bump was not used ($w_i = 0$) if the energy deposited in the crystal in question was below 2 GeV.

For the endcaps where the Bhabha statistics was relatively high, only events selected in L3 data from the two most recent years were used in the calibration. For the

[23] The RFQ constants for the four BGO subdetectors were first multiplied by four different constant factors to correct for the overall shift induced by the geometrical effects, i.e., to bring the overall normalization of the Bhabha peaks in Figure 5.17 to one.

barrel, the entire available sample of the back-to-back events from LEP2 (1998-2000) had to be used. Moreover, Bhabha events from the 1995 data sample were used to correct for the geometrical systematic effects in the following way. First, a set of the calibration constants, $\{\mathcal{C}^{95}\}$, was obtained using Equation 5.7, where the starting set of constants, $\{\mathcal{C}_0^{\mathrm{RFQ95}}\}$, was provided by the two RFQ calibration runs taken in 1995.[24] A set of correction factors was then calculated as

$$\{\mathcal{F}_{\mathrm{corr}}\} = \frac{\{\mathcal{C}^{95}\}}{\{\mathcal{C}_0^{\mathrm{RFQ95}}\}}\,. \tag{5.8}$$

The correction factors were applied to the barrel intercalibration constants before running the iterative procedure on the selected LEP2 Bhabha sample. This procedure was found to improve the calibration precision because the majority of the systematic errors on the RFQ intercalibration constants were time-independent, as discussed in Section 5.6.1.

The absolute calibration was performed with data collected during the last three year of the LEP2 program (1998-2000) at center-of-mass energies ranging from 91 GeV to 208 GeV. Therefore, additional correction factors had to be applied to take into account the aging and energy non-linearity of the BGO response. These correction factors were determined by complementary studies of the BGO performance, described in Appendix C, Sections C.3 and C.4.

About 20% of the BGO showers were either near the calorimeter edges or had a dead channel in the 3×3 matrix. Such showers were also included in the selected Bhabha samples in order to calibrate the edge crystals and crystals adjacent to the dead channels. The resulting shower energy mismeasurement had to be estimated and corrected for on an event-by-event basis. A detailed description of this procedure is given in Appendix C, Section C.4.

In the L3 BGO, a multi-GeV electromagnetic shower would typically spread over the 3×3 crystal matrix and was reconstructed using energy depositions in all nine

[24] It is interesting to note that the derived set of the calibration constants, $\{\mathcal{C}^{95}\}$, provided a better energy resolution than the "official" BGO calibration used in the reconstruction of the 1995 L3 data (1.3% *vs.* 1.8%).

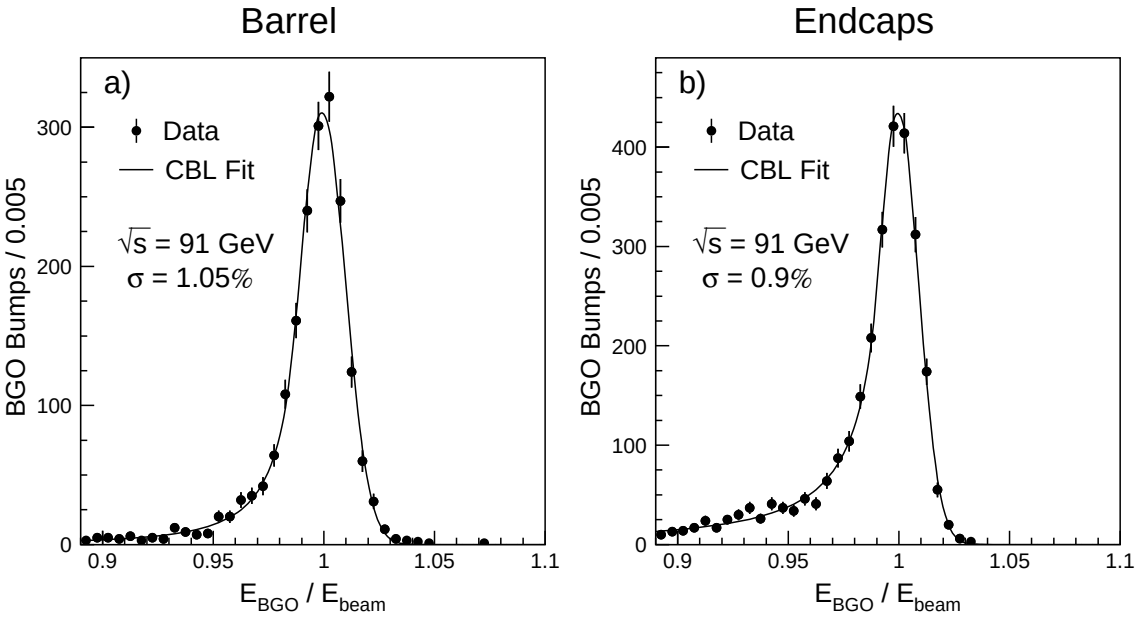

Figure 5.20: Energy spectrum of the unbiased Bhabha sample selected in the L3 Z-peak data collected in 2000 at $\sqrt{s} = 91.3$ GeV a) for the BGO barrel and b) for the BGO endcaps. The peak positions and resolutions are indicated on the plots.

crystals of the matrix. The iterative calibration algorithm that I developed took this effect into account, thus providing a clear advantage over the algorithms used in the 1987-88 beam tests and at LEP1, which calibrated only the central crystal of the shower [131, 139]. At the same time, this algorithm was robust — all 11,000 crystals of the calorimeter could be calibrated in less than an hour (using a 1 GHz Linux box). In addition, it provided a straightforward way to correct for the non-linearity and aging of the calorimeter response.

5.6.3 Calibration Results

BGO Energy Resolution

An unbiased measurement of the BGO energy resolution was performed with Bhabha events not included in the sample used for the absolute calibration.[25] Figure 5.20 shows that for 45 GeV electrons, the achieved energy resolution was 1.05% in the

[25]Each year, a third of the Bhabha events from the Z-peak calibration runs were used to test the calibration precision.

Source of uncertainty	Magnitude of uncertainty [%]	
	Barrel	Endcaps
"Intrinsic" resolution	0.80 ± 0.03	0.71 ± 0.03
Temperature fit	0.45 ± 0.15	0.45 ± 0.15
RFQ calibration	0.52 ± 0.16	0.38 ± 0.21
BGO energy resolution	1.05 ± 0.04	0.92 ± 0.04

Table 5.2: Factors contributing to the relative BGO energy resolution (in %) for 45.6 GeV electrons.

barrel and 0.9% in endcaps. The peak position and resolution were obtained by fitting the spectrum to a lineshape function which was first used by the Crystal Ball experiment and is referred to as "CBL Fit" on the plot. This was done to take into account the peak distortion and the low-energy tail induced by the initial state radiation (for more details see Section C.1).

Other factors contributing the energy resolution were the intrinsic resolution of the calorimeter and the temperature measurement errors, as discussed in Sections 5.2 and 5.3.1, respectively. The calibration error could then be evaluated by subtracting these factors in quadrature, and was found to be 0.5% for the BGO barrel and 0.4% for the BGO endcaps, i.e., about three times smaller compared to that at LEP1 and at the beginning of LEP2. Table 5.2 summarizes the sources of uncertainty contributing to the BGO energy resolution for 45 GeV electrons. One can see that contrary to the case of LEP1, at LEP2 the calibration error was no longer the dominant source of uncertainty on the energy measurement for multi-GeV electrons and photons.

In addition to the improvement in the BGO resolution, the *RFQ+Bhabha* calibration also eliminated the problem of the high-energy resolution tails, as can be seen by comparing Figures 5.9a and 5.20. This was crucial for many L3 analyses at LEP2, including the one presented in this thesis.

For the BGO barrel, the energy resolution as a function of shower energy was derived by adjusting the constant term in the expression for the BGO intrinsic resolution given by Equation 5.4. This procedure was justified because both the calibration and

temperature fit errors were energy-independent and, thus, contributed only to the constant term. The obtained resolution function was

$$\frac{\sigma_E}{E}(\text{barrel}) = \frac{3.1 \pm 0.3\ \%}{\sqrt{E}} \oplus 0.9 \pm 0.1\ \%\ (E \text{ in GeV})\,, \tag{5.9}$$

where the errors were estimated using the measured widths of the Bhabha peak (see Table 5.2) and the π^0 and η mass peaks, which were reconstructed as discussed below. In a similar fashion, the energy resolution for the endcaps was found to be:

$$\frac{\sigma_E}{E}(\text{endcaps}) = \frac{3.3 \pm 0.3\ \%}{\sqrt{E}} \oplus 0.8 \pm 0.1\ \%\ (E \text{ in GeV})\,. \tag{5.10}$$

The angular resolution of the BGO was also studied and the obtained resolution functions are summarized in Appendix C, Section C.5.

The validity of these equations for lower energies was verified using a sample of π^0 mesons selected in hadronic events ($e^+e^- \to q\bar{q}$) from the 1999 Z-peak calibration data. The π^0 mesons decay predominantly into two photons, $\pi^0 \to \gamma\gamma$. Therefore the event selection required two photons with energies above 1 GeV and 0.3 GeV for the most and least energetic photons, respectively [160]. The $\gamma\gamma$ invariant mass distribution for such two photon combinations is shown in Figure 5.21a. The obtained π^0 mass resolution of $\sigma_{DATA}(\pi^0) = 8.0 \pm 0.2$ MeV was well reproduced by the Monte Carlo simulation which gave $\sigma_{MC}(\pi^0) = 7.8 \pm 0.1$ MeV [161].

In the same way, the η resonance could also be measured in its two-photon decay mode. Figure 5.21b shows the η mass distribution reconstructed using the hadronic Z-decays at LEP1 [162]. Here both photons were required to have an energy above 0.5 GeV, and the typical photon momentum was harder than the momentum of the photons from π^0 decays. A Gaussian fit to the η peak gave a width of $\sigma_{DATA}(\eta) = 16.1 \pm 0.6$ MeV, in good agreement with the Monte Carlo prediction of $\sigma_{MC}(\eta) = 16.3 \pm 0.2$ MeV.

Similar studies performed using L3 data collected during 1994-2000 also showed a good agreement between the data and Monte Carlo simulations [161, 163]. It can

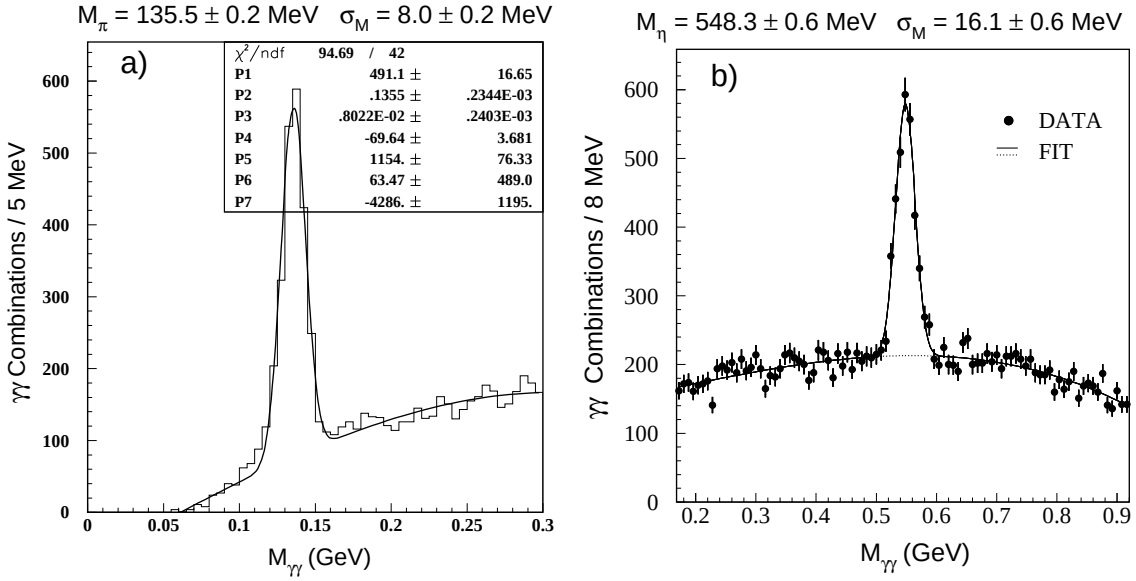

Figure 5.21: The $\gamma\gamma$ invariant mass distributions showing a) the π^0 mass peak measured using hadronic events from the 1999 Z-peak calibration data [160], and b) the η mass peak measured using the LEP1 data [162]. The peak positions and widths are indicated on the plots.

be therefore concluded that Equations 5.9 and 5.10 adequately describe the BGO energy resolution down to $E_\gamma \simeq 1$ GeV, i.e., for the entire energy range studied in this thesis.[26]

The absolute calibration of the BGO was performed mainly with electrons, while the subject of this thesis consists of studying single- and multi-photon events. As discussed in Section 4.2.3, electromagnetic showers produced by multi-GeV photons and electrons developed in a similar fashion, and the BGO response was expected to be essentially the same for both types of showers. This was also confirmed by the Monte Carlo simulations of the detector response.

As a cross check, I compared the BGO resolution for 100 GeV photons and electrons using back-to-back Bhabha and di-photon events selected in the high-energy data collected in 2000 at $\sqrt{s} = 205 - 208$ GeV. The main event selection criteria that I used are listed in the previous section. An additional cut requiring two charged tracks matching with the BGO bumps was applied for the $e^+e^- \to e^+e^-$ candidates,

[26] A more accurate resolution function for sub-GeV showers can be found in Reference [110].

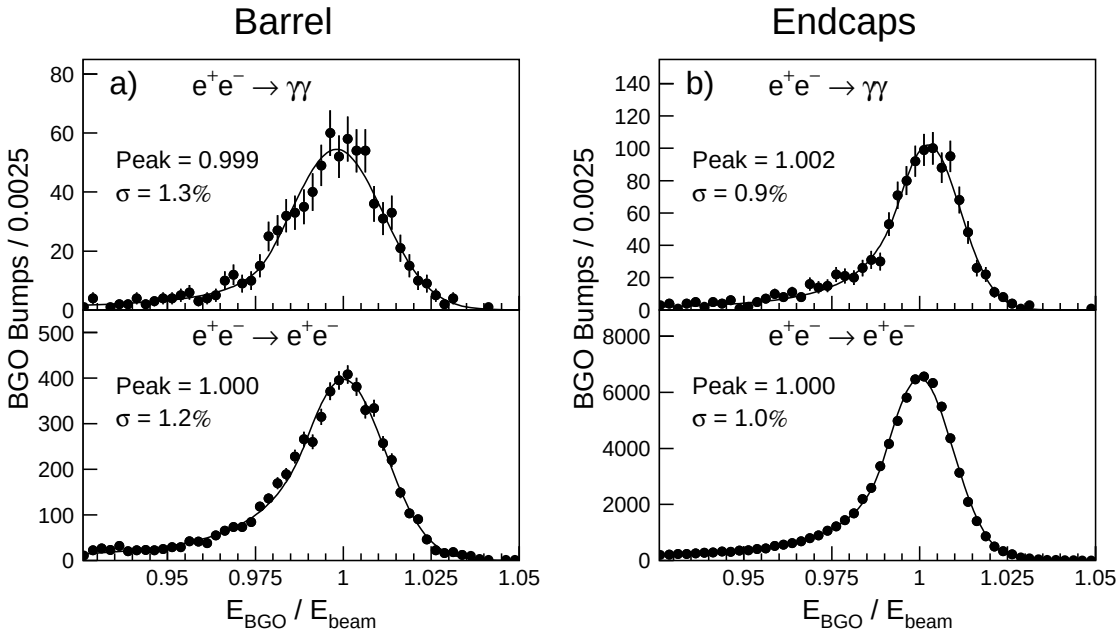

Figure 5.22: Energy spectra of the back-to-back Bhabha and di-photon events selected in the 2000 data collected at $\sqrt{s} = 205 - 208$ GeV a) for the BGO barrel and b) for the BGO endcaps. The peak positions and resolutions are indicated on the plots. For the di-photon spectra, the statistical errors on the peak positions and widths are about 0.001 and 0.1%, respectively.

while the $e^+e^- \to \gamma\gamma$ events were selected by requiring no significant activity in the TEC. To avoid biases, I used calibration constants from the year 1999.[27]

As shown in Figure 5.22, the peak positions and widths for the electron and photon energy spectra were statistically compatible, indicating that the calibration procedure did not introduce any significant systematic bias in the BGO response to multi-GeV photons. It should be noted that since the shower energies were reconstructed using the 1999 calibration constants, the measured values of the BGO resolution were slightly worse than predicted by Equations 5.9 and 5.10.

Calibration of the CMS Electromagnetic Calorimeter

The electromagnetic calorimeter of the CMS detector at the LHC will consist of 77,200 lead tungstate crystals and has a design goal of measuring electrons and photons

[27] The 1999 calibration constants were multiplied by constant factors to take into account the BGO aging.

with an energy resolution of better than 1% over a large energy range. Such a high resolution will be needed to maximize the sensitivity to the Higgs boson[28] in the two-photon decay channel, $H \to \gamma\gamma$ [164].

Achieving a precise *in situ* calibration is the key to maintaining the calorimeter resolution at the design level. The experience gained in calibrating the L3 BGO calorimeter at LEP has already proved to be very useful for the development of the calibration strategy at CMS. The example of L3 shows that achieving a $\sim 0.5\%$ calibration precision in a challenging physics environment is feasible. However, it also shows that the calorimeter calibration is not an easy task and that without an adequate preparation, it may take several years to develop necessary calibration tools and methods. To avoid repeating the mistakes of L3, four CMS teams, including the Caltech team, are conducting considerable research in this area.

The calibration of the CMS ECAL will also be performed in two stages. The intercalibration will be carried out using a laser-based monitoring system, built by the Caltech group [165]. While the absolute calibration is expected to be achieved using physics events from the $W \to e\nu$, $Z \to e^+e^-$, and $\eta(\pi^0) \to \gamma\gamma$ processes [166, 167].

In the CMS ECAL, a multi-GeV electromagnetic shower will not be contained in a single crystal and a 5×5 crystal array will be used to reconstruct its energy and position in a manner similar to the one used for the BGO bumps (see Section 5.1). Thus, a special calibration algorithm is needed to take this effect into account. To address this problem, the CMS groups working on the absolute calibration of the ECAL are now using the L3 iterative calibration algorithm that I developed. Not only is this algorithm simple and robust, but studies have also shown that it performs as well as a more complex calibration algorithm based on the Householder method for solving linear equations [166].

[28]The Higgs discovery is the main goal of the LHC program and $H \to \gamma\gamma$ is one of the most promising decay channels.

Conclusion

During 1997-2000, the L3 BGO calorimeter was successfully calibrated with the RFQ calibration system and Bhabha events. A calibration precision of about 0.5% was achieved and the BGO design goal of 1% energy resolution was reached for the first time since the 1987-88 beam tests. The RFQ calibration was used in the L3 data reconstruction and was shown to significantly improve the quality of several physics analyses, including the one presented in this thesis.

The experience gained in calibrating the L3 BGO at LEP is now successfully used for the calibration of the CMS lead tungstate calorimeter. Complementary studies of the BGO performance, including the studies of the BGO non-linearity and aging are presented in Appendix C.

Chapter 6

Selection of Photonic Events with Missing Energy

In this chapter I present the methods that I have used to select and reconstruct photonic events with missing energy. I also describe how I suppressed background contributions and took into account various detector effects.

In the Standard Model of the electroweak interactions, single- or multi-photon events with missing energy could only be produced via the reaction $e^+e^- \to \nu\bar{\nu}\gamma(\gamma)$, as described in Chapter 2, Section 2.2. Such events were reconstructed using the precisely calibrated BGO electromagnetic calorimeter (see the previous chapter). However, in order to maximize the selection efficiency and minimize systematic errors, I used all other main subdetectors of L3 to perform studies of several detector effects and physics processes. I describe this work in more detail in the following sections. This work included studies of the forward calorimeters, BGO trigger efficiency and hermeticity, photon conversion, and detector noise. Also addressed are the problems of background suppression and cosmic contamination.

At the end of this chapter and in Appendix D, I describe the selected event samples and the corresponding selection efficiencies. In the next chapter I will use these data to measure the neutrino production at LEP and to search for manifestations of physics beyond the Standard Model.

6.1 Data and Monte Carlo Samples

Data collected by the L3 detector at LEP in the years from 1998 through 2000 were considered. They corresponded to the highest energy and luminosity LEP runs taken

Year	$\sqrt{s}$ (GeV)	Named as	$\mathcal{L}$ (pb^{-1})
1998	188.6	189	176.0
1999	191.6	192	29.5
	195.5	196	83.9
	199.5	200	81.3
	201.7	202	34.8
2000	202.5−205.5	205	74.8
	205.5−207.2	207	130.2
	207.2−209.2	208	8.6

Table 6.1: Center-of-mass energies, naming conventions, and corresponding integrated luminosities for the L3 data used in my analysis.

at center-of-mass energies $\sqrt{s} = 188.6 - 209.2$ GeV. Each year an integrated luminosity of approximately 200 pb^{-1} was collected, giving a total of 627 pb^{-1}. A detailed description of LEP performance was given in Chapter 4, Section 4.1.2.

Severe malfunctioning of the detector components crucial for my analysis could have a very large effect on the characteristics and rate of accepted events. Moreover, such time-dependent hardware problems were difficult to incorporate in the detector simulation. Therefore, to reduce systematic uncertainties related to the performance of the detector, I rejected both data and Monte Carlo events in the runs during which any of the main L3 subdetectors,[1] the energy trigger, and the global data acquisition system were not operating normally. As a result, the integrated luminosity I used in my analysis was reduced by about 1.3%, giving a total of about 619 pb^{-1}. The LEP data were divided into eight subsets according to the center-of-mass energy. The corresponding integrated luminosities and the naming conventions are listed in Table 6.1.

I rely on Monte Carlo simulations to optimize my selection cuts and to estimate the effects of my event reconstruction and the purity and efficiency of my selection. While modern Monte Carlo programs are extremely detailed and accurate, they are

[1] The main subdetectors of L3 did not include the muon filter and the VSAT.

not perfect. Therefore, any opportunity to double check a measurement or correction depending on the Monte Carlo simulations was exploited. The Monte Carlo generators that I used to simulate the relevant Standard Model processes are listed below.

The production of the photonic events with missing energy via initial-state radiation in the neutrino pair-production process, $e^+e^- \to \nu\bar{\nu}\gamma(\gamma)$, was simulated using the `KKMC` [17] and `NUNUGPV` [27] MC generators. They were studied in Chapter 2 Section 2.2.3 and described in detail in Appendix A.

The large-angle (back-to-back) Bhabha scattering process and the di-photon production process, $e^+e^- \to \gamma\gamma(\gamma)$, were simulated using the `BHWIDE` [156] and `GGG` [157] programs, respectively. I have already used these two generators in my studies of the BGO performance (see Section 5.6.2 of Chapter 5). In this chapter, I use events from these processes to study the efficiency of my event selection. In addition, the di-photon production process constituted the dominant source of background for the multi-photon channel.

The small-angle Bhabha scattering process, $e^+e^- \to e^+e^-\gamma(\gamma)$, was simulated using the `TEEGG` MC generator [168]. In this process, one or more particles were scattered at very low polar angles and typically escaped undetected along the beam pipe. This reaction could result in three event topologies according to the type of particles scattered at large polar angles: single-photon, single-electron, and electron-photon.[2] The single-photon Bhabha events constituted the main source of background for the single-photon channel. The single-electron events, where only one electron[3] was seen in the BGO, allowed me to study the trigger and scintillator efficiency as well as the performance of the forward calorimeters. It should be noted that the cross section of the single-electron process was more than ten times higher than the cross section of the single-photon and electron-photon radiative Bhabha scattering processes combined (see Table 6.2).

The four-fermion production processes $e^+e^- \to e^+e^-\nu\bar{\nu}(\gamma)$ and $e^+e^- \to e^\pm\ell^\mp\nu_e\nu_\ell(\gamma)$

[2]The small-angle Bhabha scattering process, where the electron or positron is not detected, is also known as Compton scattering. It has recently been measured by L3 [171].

[3]Unless otherwise stated, in this chapter the word "electron" is used for both electrons and positrons.

$e^+e^- \to$	MC Generator	σ(pb)	Events	Phase-Space Cuts
$\nu\bar{\nu}(\gamma)$	KKMC [17]	57.52	540K	—
$\nu\bar{\nu}\gamma(\gamma)$	NUNUGPV [27]	13.09	200K	$E_{\gamma_1} > 0.8$ GeV $\theta_{\gamma_1} > 1.35°$
$e^+e^-(\gamma)$	BHWIDE [156]	1,286	599K	$\theta_{e_{1,2}} > 8°$
$e^+e^-\gamma(\gamma)$	TEEGG [168]	174.3	120K	$E_\gamma > 0.9$ GeV $\theta_\gamma > 13.5°$ $\theta_{e_{1,2}} < 11°$
		3,027	425K	$E_{e_2} > 0.9$ GeV $\theta_{e_2} > 13.5°$ $\theta_{\gamma,e_1} < 11°$
		95.9	70K	$E_{\gamma,e_2} > 0.1$ GeV $\theta_{\gamma,e_2} > 10°$ $\theta_{e_1} < 5°$
$\gamma\gamma(\gamma)$	GGG [157]	18.3	75K	$\theta_{\gamma_{1,2}} > 5°$
$e^+e^-\nu\bar{\nu}$	EXCALIBUR [169]	0.50	20K	$\theta_{e_1} > 5.1°$
$e^\pm\ell^\mp\nu_e\nu_\ell$		1.09	40K	$\ell = \mu, \tau$
$e^+e^-e^+e^-$	DIAG36 [170]	705	600K	$m_{e_3e_4} > 3.1$ GeV $\theta_{e_{3,4}} > 10°$
$\tau^+\tau^-(\gamma)$	KORALZ [22]	6.8	15K	—

Table 6.2: Standard Model processes, Monte Carlo programs, cross sections within the indicated kinematic regions and the size of the corresponding event samples. All events were generated at $\sqrt{s} = 207$ GeV. The three lines for the radiative Bhabha process correspond to the single-photon, single-electron, and electron-photon event topologies, respectively.

were simulated using the EXCALIBUR MC generator [169]. These processes also provided an important source of background for my selection. Finally, the reactions $e^+e^- \to e^+e^-e^+e^-(\gamma)$ and $e^+e^- \to \tau^+\tau^-(\gamma)$ were simulated using the DIAG36 [170] and KORALZ [22] programs, respectively.

The Monte Carlo programs that I used are summarized in Table 6.2, which lists the production cross sections, the size of the corresponding event samples, and the phase-space cuts used during the event generation.

The L3 detector response was simulated using the GEANT program [127], which described effects of energy loss, multiple scattering, and showering in the detector. Time-dependent detector inefficiencies,[4] as monitored during the data taking period, were included in the simulation. It should be noted that during the last three years of the LEP program (1998-2000), the configuration and performance of the L3 detector were very stable. In particular, the number and the location of the dead channels, the

[4] Such detector inefficiencies included the position of the dead or noisy channels in the calorimeters and the location of the disconnected sectors in the TEC and muon chambers.

accuracy of the subdetector calibrations, and the trigger thresholds remained essentially unchanged. Therefore, in most of my detector studies, I regarded these three years as a single data-taking period.[5] Additional cross checks showed no significant year-to-year variation in the selection efficiency related to the detector effects.

6.2 Event Topologies

Electrons and photons were reconstructed using the BGO electromagnetic calorimeter,[6] whose barrel and endcaps subtended the polar angle ranges $43^\circ < \theta < 137^\circ$ and $10^\circ < \theta(180^\circ - \theta) < 37^\circ$, respectively. In order to discriminate between photons and electrons, I used information from the tracking chamber (TEC) whose efficiency decreased rapidly at low polar angles. Therefore, I applied an additional cut on the photon polar angle, $14^\circ < \theta < 166^\circ$.

The main background came from radiative Bhabha scattering, $e^+e^- \rightarrow e^+e^-\gamma$, where both electrons were lost in the beam pipe, and only a photon was scattered at a large polar angle. Such events could be rejected by requiring the transverse momentum of the photon to be above $0.02\sqrt{s}$, as shown in Figure 6.1. This cut ensured that at least one of the scattered electrons could be detected by the forward calorimeters.

The single- and multi-photon events were triggered by the BGO energy triggers, as described in Section 4.2.9. In the barrel and endcap regions, the thresholds of these triggers were set at about 1.5 GeV and 7 GeV, respectively.

The above conditions determined the three event topologies that I considered in my analysis:

- **Single-photon events:** a photon with $14^\circ < \theta_\gamma < 166^\circ$ and $P_t^\gamma > 0.02\sqrt{s}$. There should be no other photon with $E_\gamma > 1$ GeV.

- **Multi-photon events:** at least two photons with $E_\gamma > 1$ GeV, with the most energetic in the region $14^\circ < \theta_\gamma < 166^\circ$ and the other in the region

[5] This approach was used in the majority of the L3 analyses at LEP2.

[6] The performance and the calibration of the BGO calorimeter were described in detail in Chapter 4, Section 4.2.3 and in Chapter 5.

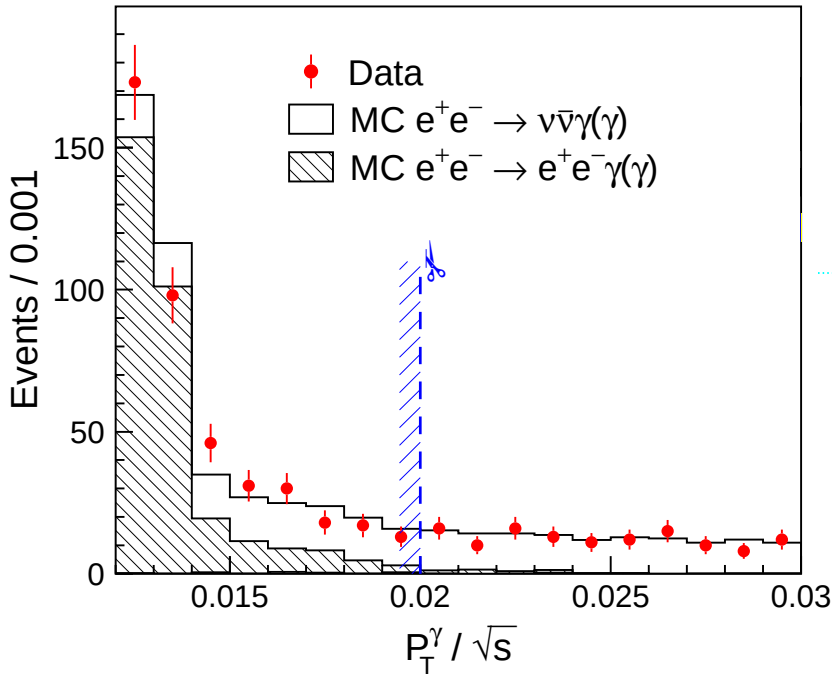

Figure 6.1: Transverse momentum distribution for the single-photon events after all other selection cuts have been applied. The dashed line indicates the position of the cut $P_t^\gamma > 0.02\sqrt{s}$. Only the region of interest is shown.

$12° < \theta_\gamma < 168°$. The transverse momentum of the multi-photon system should satisfy $P_t^{\gamma\gamma} > 0.02\sqrt{s}$.

- **Soft-photon events:** a photon in the barrel region ($43° < \theta_\gamma < 137°$) with $0.008\sqrt{s} < P_t^\gamma < 0.02\sqrt{s}$. There should be no other photon with $E_\gamma > 1$ GeV.

The selected sample of the single- and multi-photon events was dominated by events from the process $e^+e^- \to \nu\bar{\nu}\gamma(\gamma)$. Thus, it could be used to study the cross section of this process and to measure the number of light neutrino species. In the next chapter I will also use this event sample to search for manifestations of Physics beyond the Standard Model, such as extra dimensions, Supersymmetry, and anomalous boson couplings.

In the region of the soft-photon event topology, most of the selected events were expected to be due to the small-angle Bhabha scattering process, $e^+e^- \to e^+e^-\gamma(\gamma)$. The inclusion of the soft-photon sample significantly increased the sensitivity of my

searches for extra dimensions and pair-produced gravitinos.

For a large fraction of the single- and multi-photon events, emission of the ISR photons reduced the effective center-of-mass energy of the e^+e^- pair to the Z resonance, as described in Section 2.2.2. This phenomenon is called the *radiative return to the Z*. Thus, the distribution of the recoil mass to the photon system ($M_{\rm rec}$) was expected to peak around the Z mass. Since this effect did not depend on the value of $\sqrt{s}$, instead of using the photon energy variable I usually used the photon recoil mass, defined as

$$M_{\rm rec} \;=\; \sqrt{\left(\sqrt{s}-E_\gamma\right)^2-|\vec{p}_\gamma|^2}\,, \tag{6.1}$$

where $E_\gamma = \sum_i E_{\gamma_i}$ and $\vec{p}_\gamma = \sum_i \vec{p}_{\gamma_i}$ are the total energy and momentum of the photons. For the single-photon topology, Equation 6.1 becomes $M_{\rm rec} = \sqrt{s-2\sqrt{s}E_\gamma}$.

6.3 Single-Photon Selection

The selection of the $e^+e^-\to\nu\bar{\nu}\gamma(\gamma)$ candidates aimed at identifying events with 1) one neutral electromagnetic energy deposit in the BGO calorimeter and 2) no other activity in the detector apart from what was consistent with noise. Below I describe the basic cuts of the single-photon selection and give a brief outline of the following sections in which these cuts and their performance will be discussed in more detail.

Photon candidates were required to have an energy greater than 1 GeV, and the shape of their energy deposition had to be consistent with an electromagnetic shower. This was ensured by a dedicated shower-shape analysis which is described in the next section. As defined in the previous section, the single-photon events were required to contain only one photon candidate with $14^\circ < \theta_\gamma < 166^\circ$ and $P_t^\gamma > 0.02\sqrt{s}$.

The single-photon events were triggered by the BGO trigger system, whose efficiency as a function of the shower energy is studied in Section 6.3.2.

The visible energy not assigned to the identified photon had to be less than 10 GeV, and the energy measured in the EGAP and HCAL calorimeters had to be less than 7 GeV each. There must be at most one ECAL cluster (bump) with an energy

above 50 MeV not identified as a photon. Each BGO endcap had a hole at $\phi \simeq 270^\circ$ and $\theta(180^\circ - \theta) \simeq 16^\circ$, which was required for the passage of the RFQ beam pipe (see Section 4.2.3). In order to eliminate the related background from mismeasured di-photon events, I rejected single-photon events with a photon in the region opposite to an RFQ hole.

To suppress background from the radiative Bhabha scattering process, events with a transverse momentum less than 15 GeV were rejected if an energy cluster was observed in the forward calorimeters with an acoplanarity[7] with the photon candidate less than 30°. Furthermore, if a photon was detected with an acoplanarity less than 15° with a hadron calorimeter cluster, the energy of that cluster had to be less than 3 GeV. The efficiency of these cuts is discussed in Section 6.3.3.

Electron candidates were removed by requiring that no charged track reconstructed in the central tracking system (TEC) matched the ECAL cluster. The probability of photon conversion in the beam pipe and in the silicon microvertex detector was about 5% in the barrel region and increased rapidly at low polar angles, reaching about 20% at $\theta \simeq 20^\circ$. This effect is studied in Section 6.3.4.

The cosmic ray background was rejected using a set of dedicated anti-cosmic cuts, as described in Section 6.3.5. Finally, the problems of the BGO shower leakage and of the detector noise are studied in Sections 6.3.6 and 6.3.7, respectively. The selection results are presented in Section 6.3.8 and in Appendix D.

A typical single-photon event recorded by the L3 detector is shown in Figure 6.2. The recoil mass of this photon was measured to be consistent with the Z mass, $M_{\rm rec} = 92.6$ GeV. The cluster in the HCAL behind the BGO bump indicates a minor leakage of the electromagnetic shower into the hadron calorimeter. This figure also shows two additional low-energy deposits, in the opposite endcap of the HCAL and in the EGAP calorimeter. These two clusters were most probably faked by the detector noise.

[7] Acoplanarity is defined as the complement of the angle between the projections in the plane perpendicular to the beam axis.

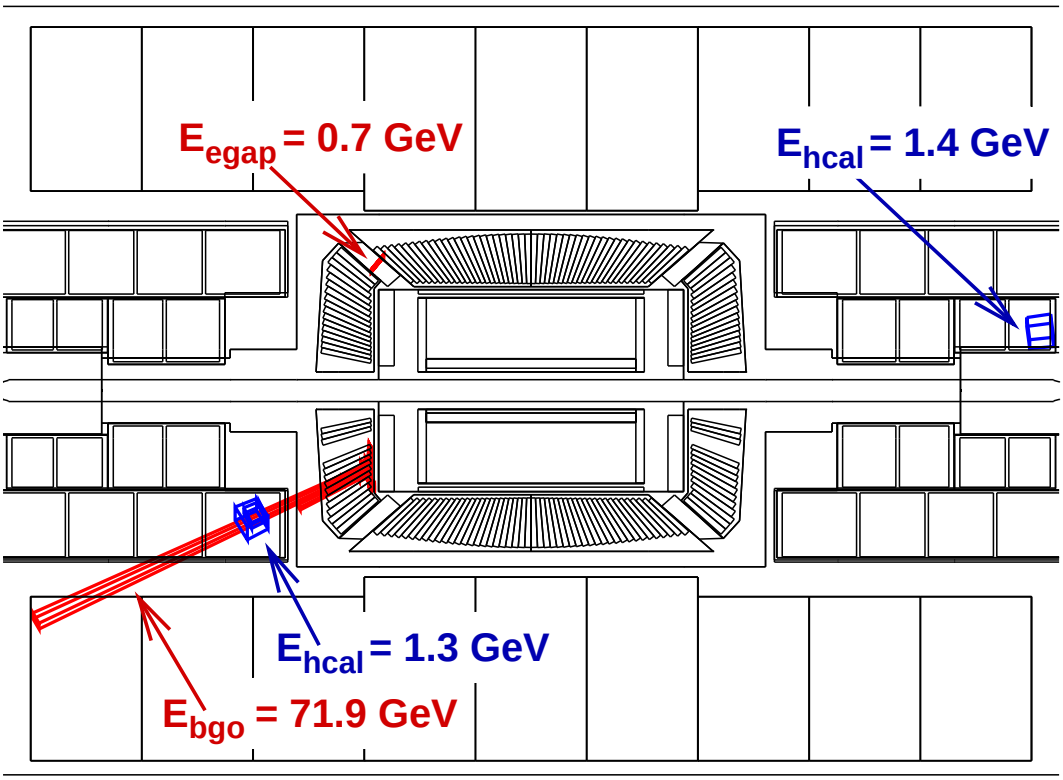

Figure 6.2: A typical single-photon event recorded by the L3 detector and displayed in the $y - z$ plane. This event was recorded in 1998 data at $\sqrt{s} = 189$ GeV.

6.3.1 Shower-Shape Analysis

In order to ensure that the BGO shower of the photon candidate was consistent with an electromagnetic shower, I applied a set of cuts based on the measured shower profile. These *shower-shape* cuts not only ensured that the accepted photon showers were well measured in the BGO but also suppressed a large fraction of background due to cosmic rays and mismeasured events from other Standard Model processes.

The pattern of individual crystal energies in a BGO bump provides a transverse sampling of the shower that developed when a particle passed through the electromagnetic calorimeter (see Section 5.1). In the case of electrons and photons, the resulting shower had a transverse profile that did not depend strongly on the particle energy in the range $E \simeq 1 - 100$ GeV [172]. This transverse profile was characterized by two

quantities, S_9^c/S_{25}^c and shower roundness, which are defined below. The longitudinal profile of the shower could be characterized by the ratio of energy deposited in the hadron calorimeter behind the BGO bump and the bump energy as measured by the BGO, $E_{\rm HCAL}/E_{\rm BGO}$.

In addition, about 20% of the selected showers were either near the calorimeter edges or had a dead channel in their 3×3 matrices (see Section 5.3.2). The resulting mismeasurement of the lateral shower profile was taken into account by relaxing the values of the cuts on shower roundness and S_9^c/S_{25}^c variable.

The S_9^c/S_{25}^c variable was defined as the ratio of the corrected sums of energies deposited in the 3×3 and 5×5 matrices centered on the bump crystal, where the individual S_9^c and S_{25}^c variables were defined by Equation 5.2 in Section 5.1. The electromagnetic BGO showers were almost fully contained in the 3×3 crystal matrix, and, in the case of electrons and photons, this ratio was expected to be close to one. Thus, I required that S_9^c/S_{25}^c should be greater than 0.94. It should be noted that this or similar cut values were widely used in L3 to reject showers originating from hadrons and cosmic rays. For showers with dead or missing crystals, this cut was relaxed to $S_9^c/S_{25}^c > 0.92$.

Photon candidates with significant leakage into the hadron calorimeter were rejected by requiring $E_{\rm HCAL}/E_{\rm BGO} < 0.2$, where $E_{\rm BGO}$ was the bump energy as measured by the BGO and $E_{\rm HCAL}$ was defined as a sum of energies of the HCAL clusters in a 10° cone around the photon direction. The longitudinal shower leakage also affected the BGO energy resolution. This problem is addressed in Section 6.3.6.

To further suppress events from cosmic rays, I used another quantity called shower roundness. It is defined as the ratio of the smallest and largest eigenvalues of the following tensor:

$$F^{\mu\nu} = \sum_i E_i x_i^\mu x_i^\nu \,, \tag{6.2}$$

where E_i is energy of the ith crystal, x_i^μ and x_i^ν are given in the local Cartesian coordinate system with the center of bump crystal at the origin, and the summation is performed over all crystals in the BGO bump [173]. The shower roundness can

be interpreted as the ratio of the minor and major axes of an ellipse describing the transverse profile of the shower. For electrons and photons produced at the interaction point of L3, the transverse shower profiles were expected to have a circular shape, i.e., their shower roundness was expected to be close to one. On the contrary, BGO showers in cosmic ray events usually had small values of roundness since such showers corresponded to photons radiated by cosmic muons, and most of the cosmic muons traversed the BGO calorimeter at a significant angle with respect to the crystal axis. Thus, I required that the measured shower roundness should be greater than 0.4. For showers with dead or missing crystals, the value of this cut was relaxed to 0.2.

The efficiency of the shower-shape selection was measured using large samples of di-photon, back-to-back Bhabha, and single-electron Bhabha events which were selected in the 1998-2000 data. The agreement between data and Monte Carlo simulations was checked using the large samples of MC events from the corresponding Standard Model processes. These three Standard Model processes were chosen because they provided very distinct and clean signatures so that little or no contamination was expected from hadronic events or cosmic rays.

The di-photon and back-to-back Bhabha events were selected using the same selection criteria[8] as the ones described in Section 5.6.2, where I discussed the absolute calibration of the BGO calorimeter using Bhabha events. The di-photon subsample was further selected by requiring no significant activity in the TEC. In the high-energy LEP runs at $\sqrt{s} = 189 - 208$ GeV, I selected samples of about 3,400 and 130,000 di-photon and back-to-back Bhabha events, respectively. In addition, I selected about 30,000 Bhabha events in the calibration data at the Z peak, $\sqrt{s} = 91.3$ GeV. Figure 6.3 shows the distributions of the shower-shape variables for the Bhabha events selected in the Z-peak data. While the distributions of the S_9^c/S_{25}^c and roundness variables demonstrated a good agreement between data and Monte Carlo, the $E_{\rm HCAL}/E_{\rm BGO}$ distributions indicated that the detector simulation underestimated the longitudinal shower leakage.

[8]Except that I did not apply any cuts on the shower shape. In addition, I only used showers with a polar angle $\theta_{shower} > 14°$, i.e., in the fiducial angular region of my photonic selections.

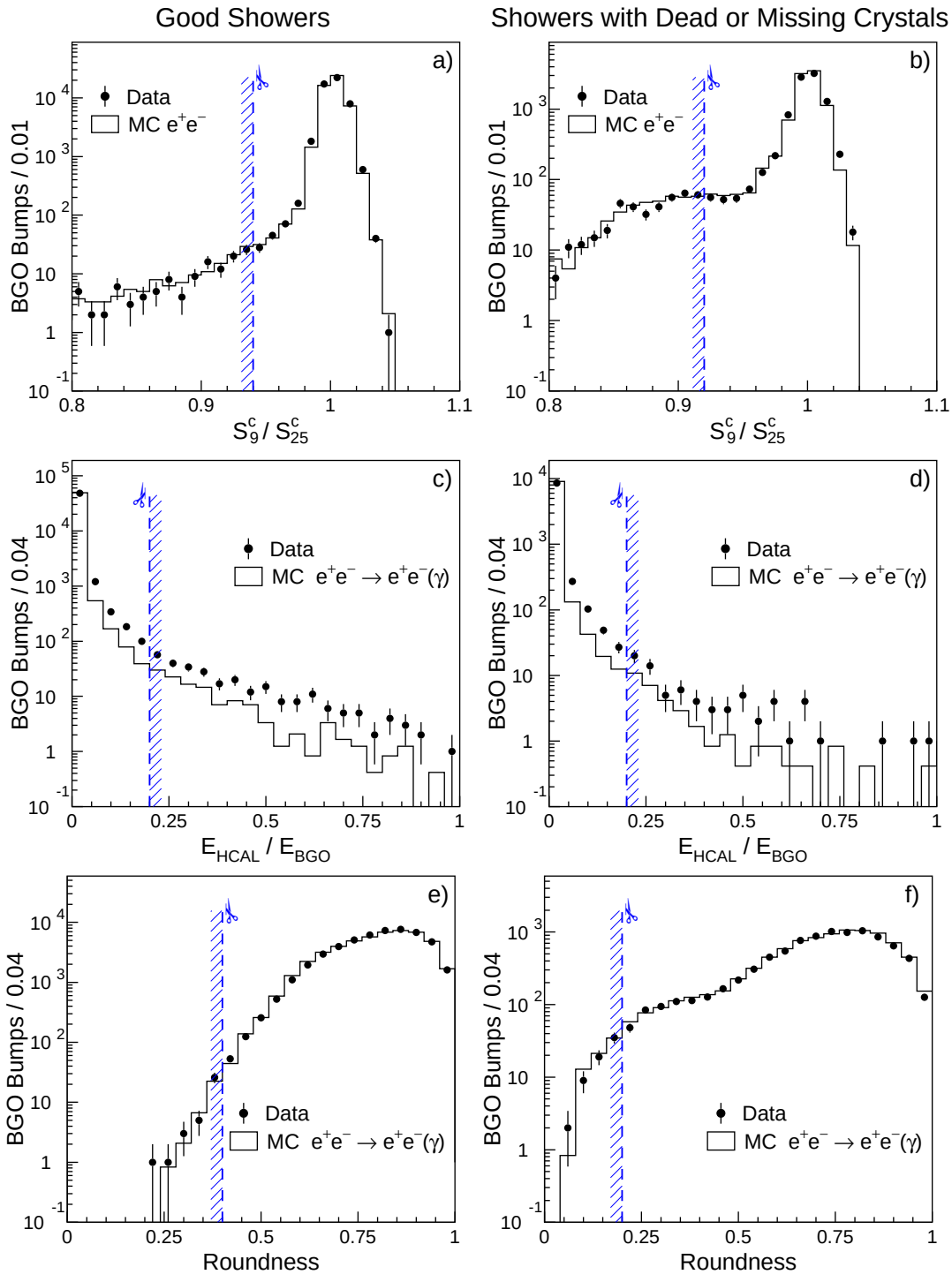

Figure 6.3: Distributions of a,b) S_9^c/S_{25}^c, c,d) $E_{\mathrm{HCAL}}/E_{\mathrm{BGO}}$, and e,f) shower roundness for Bhabha events from the 1998-2000 Z-peak calibration data, after all other shower-shape cuts have been applied (barrel and endcaps combined). The dashed lines indicate the values of the cuts. The distributions for the good bumps and for the bumps with a dead crystal or near the detector edges are shown on the left and right side, respectively.

As I defined in the previous section, the single-electron events were radiative Bhabha scattering events where one electron and a photon had a very low polar angle and only a low energy electron was scattered at a large polar angle. Such events were selected by requiring a single shower in the BGO with a matching track in the TEC and a matching cluster in the forward calorimeters. The polar angle of the single-electron candidate was required to be above 14°, which corresponded to the fiducial region of my photonic selections. The energy of the matching cluster had to be greater than 50 GeV and its acoplanarity with the single-electron candidate less than 10°. There should have been no other activity in the detector apart from what was consistent with noise. The selected events must also satisfy the anti-cosmic cuts defined in Section 6.3.5. To study the efficiency of the shower-shape selection, only showers with an energy $E_{\rm BGO} = 7.5 - 12.5$ GeV were chosen. In total, I selected about 85,000 such single-electron events.

The large statistics back-to-back and single-electron Bhabha samples allowed a precise measurement of the shower-shape selection efficiency for electrons with energies $E_{\rm BGO} \simeq 10, 45$, and 100 GeV. This was important because the energy of the single-photon showers varied between about 5 and 90 GeV, with an average value of $< E_\gamma > = 54$ GeV. In addition, the di-photon sample provided a direct comparison between the showers originating from electrons and photons.

The obtained values of the shower-shape selection efficiency are quoted in Table 6.3. It shows that for all shower energies and types, the efficiency was slightly higher for the MC simulation. This effect was explained by the inaccurate simulation of the longitudinal shower leakage (see Figures 6.3c,d) and was corrected by scaling down the numbers of expected events by a common factor of approximately -0.3%. After this correction, a good agreement between the data and the Monte Carlo simulations was observed. It should be noted that the selection performance was almost the same for the showers in the barrel and in the endcaps. In addition, the selection efficiency for the photon showers was found to be only about 0.2% smaller than that for the electron showers (at 100 GeV). This result was also in good agreement with the predictions of the Monte Carlo simulation. In the case of 45 GeV electrons, the

Production Process and Average Particle Energy		Efficiency of the Shower-Shape Selection [%]		
		Good Bumps		Bumps with Dead or Missing Crystals
		Barrel	Endcaps	
Bhabha Scattering $E_e = 100$ GeV	Data	99.36 ± 0.05	99.13 ± 0.02	94.8 ± 0.1
	MC	99.54 ± 0.03	99.47 ± 0.01	95.3 ± 0.1
Di-Photon $E_\gamma = 100$ GeV	Data	98.92 ± 0.20	99.17 ± 0.16	95.2 ± 0.6
	MC	99.38 ± 0.05	99.32 ± 0.05	95.9 ± 0.2
Bhabha Scattering $E_e = 45$ GeV	Data	99.16 ± 0.07	99.01 ± 0.06	94.3 ± 0.2
	MC	99.45 ± 0.03	99.36 ± 0.03	94.7 ± 0.1
Single Electron $E_e = 10$ GeV	Data	97.94 ± 0.11	98.11 ± 0.06	93.4 ± 0.2
	MC	98.40 ± 0.07	98.23 ± 0.04	93.5 ± 0.1

Table 6.3: Efficiency of the shower-shape selection as measured for different shower energies and types.

efficiency of the shower-shape selection was measured to be about 99.1% for the good showers and 94.3% for the showers with a dead crystal or near the detector edges.

6.3.2 Trigger Efficiency

A good understanding of the trigger performance was required for a precise measurement of the single- and multi-photon production. In this section I describe a study of the trigger efficiency that I performed using Bhabha scattering events.

Events with only photons in the final state could be triggered only by the BGO energy triggers which were described in detail in Section 4.2.9. These triggers included the single-photon (barrel only), the BGO cluster, and the total energy triggers with thresholds at about 1.5, 7, and 30 GeV, respectively.

Near the threshold, the performance of the BGO triggers could be monitored using a dedicated, independent trigger called single-electron trigger [173]. This trigger required a coincidence between a cluster in one of the luminosity monitors and a track in the TEC. Thus, it could be used to select an independent sample of single-electron Bhabha events (as follows from its name). The efficiency of the single-electron trigger

had been measured to be 98.5% [173].

The basic selection of single-electron Bhabha events was described in the previous section. In addition, such events were required to be triggered by the single-electron trigger. The energy of the single-electron showers was required to be above 1 GeV in the BGO barrel and 5 GeV in the endcaps. Furthermore, there had to be no other bump in the BGO with an energy above 0.5 GeV. In 1998-2000 data, I selected a total of about 76,000 and 27,000 single-electron events in the BGO barrel and endcaps, respectively. The corresponding energy spectra are shown in Figures 6.4a,c.

These independently triggered single-electron events could then be used to measure the efficiency of the BGO triggers by checking whether or not these triggers were also activated. Figures 6.4b,d show the obtained BGO trigger efficiency as a function of the shower energy together with the corresponding Monte Carlo prediction. In the barrel it rises sharply at the energy threshold of the single-photon trigger and reaches a plateau mainly determined by the efficiency of the corresponding trigger algorithm. With increasing energy additional triggers became active, resulting in a second threshold rise and a final plateau at about 8 GeV in the barrel and 10 GeV in the endcaps.

The trigger efficiencies in the plateau regions were determined by fitting the obtained efficiency curves to a straight line. In the case of the barrel, a fit in the plateau region $E_{\mathrm{BGO}} = 8 - 16$ GeV gave a value of $93.1 \pm 0.6\%$ for the data and $94.5 \pm 0.2\%$ for the Monte Carlo prediction. In the case of the endcaps, I fitted the plateau region $E_{\mathrm{BGO}} = 10 - 25$ GeV, and the corresponding efficiencies were determined to be $95.7 \pm 0.4\%$ and $97.5 \pm 0.1\%$ for the data and Monte Carlo, respectively. These measurements were in good agreement with the results of an earlier study performed using 1998-1999 data [120].

The main contribution to the trigger inefficiency was due to the presence of inactive trigger channels. About 4.7% of the trigger channels in the barrel and 2% of the channels in the endcaps were flagged as inactive, both during the data taking and during the detector simulations. The location of the inactive channels was well known and stable during the considered period of 1998-2000. No significant time-dependent

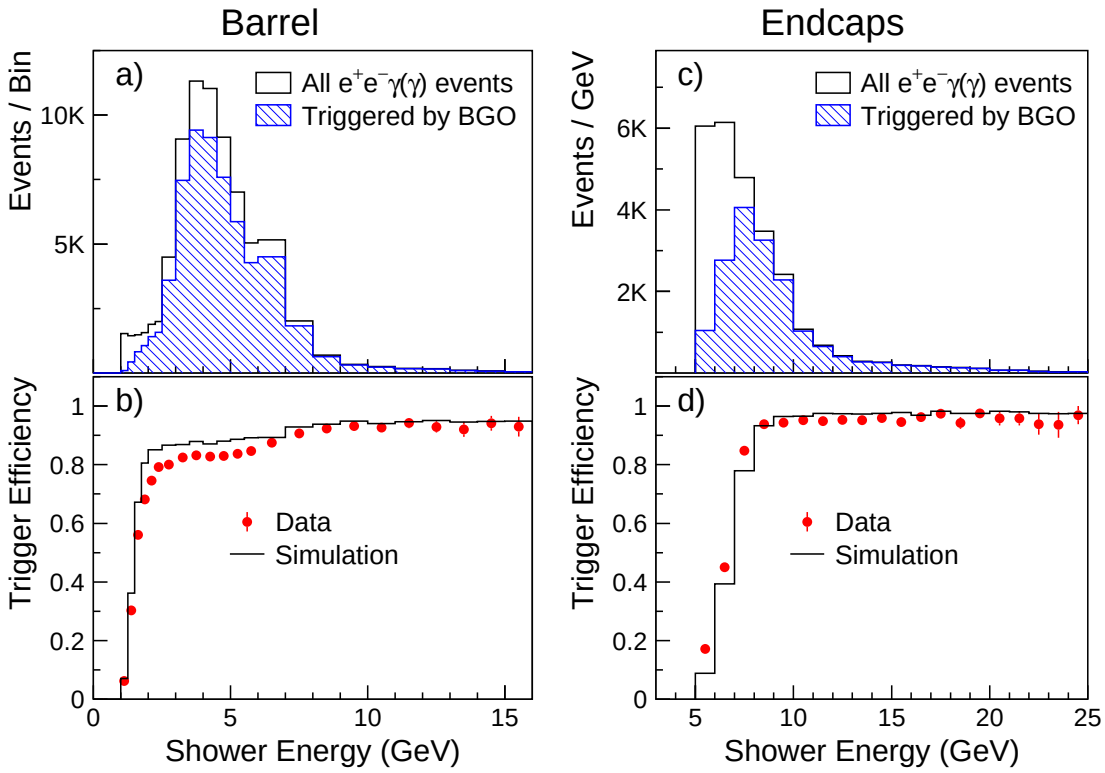

Figure 6.4: Energy spectra of the single-electron events a) in the barrel and c) in the endcaps. Trigger efficiency curves as a function of the shower energy b) for the BGO barrel and d) for the BGO endcaps.

variations in the measured trigger efficiency were found.

Additional factors causing trigger inefficiency included detector noise and finite ADC resolution. These effects were not taken into account during the simulation of the detector response [173]. As demonstrated above, the Monte Carlo simulation overestimated the trigger efficiency in the plateau regions by about 1.5%, both for the barrel and the endcaps. Moreover, for showers with energies near the trigger thresholds, the relative difference between data and Monte Carlo was energy-dependent and could be as high as 20%, as shown in Figures 6.4b,d. As a result, the trigger efficiency in the simulation had to be adjusted to eliminate this discrepancy between data and Monte Carlo.

The measured efficiency curves could not be directly applied to the Monte Carlo simulation of the $e^+e^- \to \nu\bar{\nu}\gamma$ process since its differential cross section differed from

that of the single-electron Bhabha scattering. Therefore, I computed the efficiency curves separately for each of the four $|\cos\theta|$ slices[9] in the barrel and in the endcaps so that the applied correction factors depended on both the shower energy and polar angle.

Figures 6.4a,c show that the cross section of single-electron production decreased rapidly with the single-electron energy. Therefore, I performed a complementary study of the trigger performance at high energies using back-to-back Bhabha events. Such Bhabha events could be independently triggered by the TEC trigger, whose efficiency was found to be about 97% [135]. To measure the efficiency of the BGO triggers, I selected a subsample of such events from the Bhabha sample obtained using the calibration data at the Z peak (see the previous section). With these events, the BGO trigger efficiency was measured to be $99.57 \pm 0.07\%$ in the barrel and $99.72 \pm 0.04\%$ in the endcaps. After applying the correction factors derived using the single-electron events, the corresponding trigger efficiencies for the MC simulation were found to be $99.63 \pm 0.04\%$ and $99.74 \pm 0.03\%$. Good agreement between data and Monte Carlo was observed. In addition, these measurements are consistent with the results of a similar study described in Reference [135].

6.3.3 Background Rejection

The single-photon topology of the radiative Bhabha scattering process, $e^+e^- \to e^+e^-\gamma$, was by far the most copious source of background in my selection of single-photon events. In this process, the incoming electrons were scattered at low polar angle (typically with energies close to the beam energy) and only the radiated photon was detected in the BGO. Such events are referred to as single-photon Bhabha events.

The lower cut on the photon transverse momentum, $P_t^\gamma > 0.02\sqrt{s}$, ensured that at least one of the two electrons was scattered at a significant angle with respect to the beam axis so that it could be detected in the forward calorimeters. As a result, this source of background could be almost completely suppressed by the veto cuts that I

[9] The granularity of the BGO trigger system was described in Section 4.2.9.

describe below. Since the differential cross section of the radiative Bhabha scattering peaked at low values of P_t^γ [168], I applied tighter cuts in the region of low transverse momentum.

For single-photon candidates with a transverse momentum less than 15 GeV, I required that no energy cluster be observed in the forward calorimeters with an acoplanarity with the photon candidate less than 30° (the definition of the acoplanarity was given in footnote 7 on p. 138). As described in Sections 4.2.7 and 4.2.8, the forward calorimeters of L3 covered the polar angle range of $1.4° < \theta(180° - \theta) < 8.7°$ and consisted of the active lead rings (ALR) and the luminosity monitors (LUMI). The upper cuts on the energy of such clusters were set at $E_{\rm ALR} < 0.1$ GeV and $E_{\rm LUMI} < 1$ GeV.

To minimize the inefficiencies caused by the detector noise, this cut was relaxed to $E_{\rm ALR,LUMI} < 60$ GeV for single-photon candidates with $P_t^\gamma > 15$ GeV. This did not increase the background contamination since in radiative Bhabha events with such high values of P_t^γ at least one of the electrons was expected to be scattered into a region covered by the BGO or HCAL endcaps. Such events were rejected by the veto cuts on energy depositions in the HCAL and the BGO.

Figures 6.5a,b show the distributions of energies deposited in the LUMI and ALR calorimeters for single-photon candidates with $P_t^\gamma < 15$ GeV before the corresponding cuts were applied. In total, I selected 9,506 such events in data with about 9,362.3 expected from Monte Carlo. Only about 5% of the MC expectation was due to the genuine single-photon production process, $\mathrm{e^+e^-} \to \nu\bar{\nu}\gamma$.

Figures 6.5c demonstrates that radiative Bhabha events with a cluster in the LUMI calorimeter could be almost completely suppressed by applying a veto cut $E_{\rm LUMI} < 1$ GeV. In the case of the ALR energy spectrum, a large fraction of events had $E_{\rm ALR} < 5$ GeV, as shown in Figure 6.5d. For such events I applied a tighter cut $E_{\rm ALR} < 0.1$ GeV.

The origin of this effect can be understood by reconstructing the polar angle of the electron scattered into the ALR (θ_{tag}). Because the second electron was almost always scattered parallel to the beam axis, the θ_{tag} angle could be estimated using only the energy and polar angle of the photon detected in the BGO. The exact formula

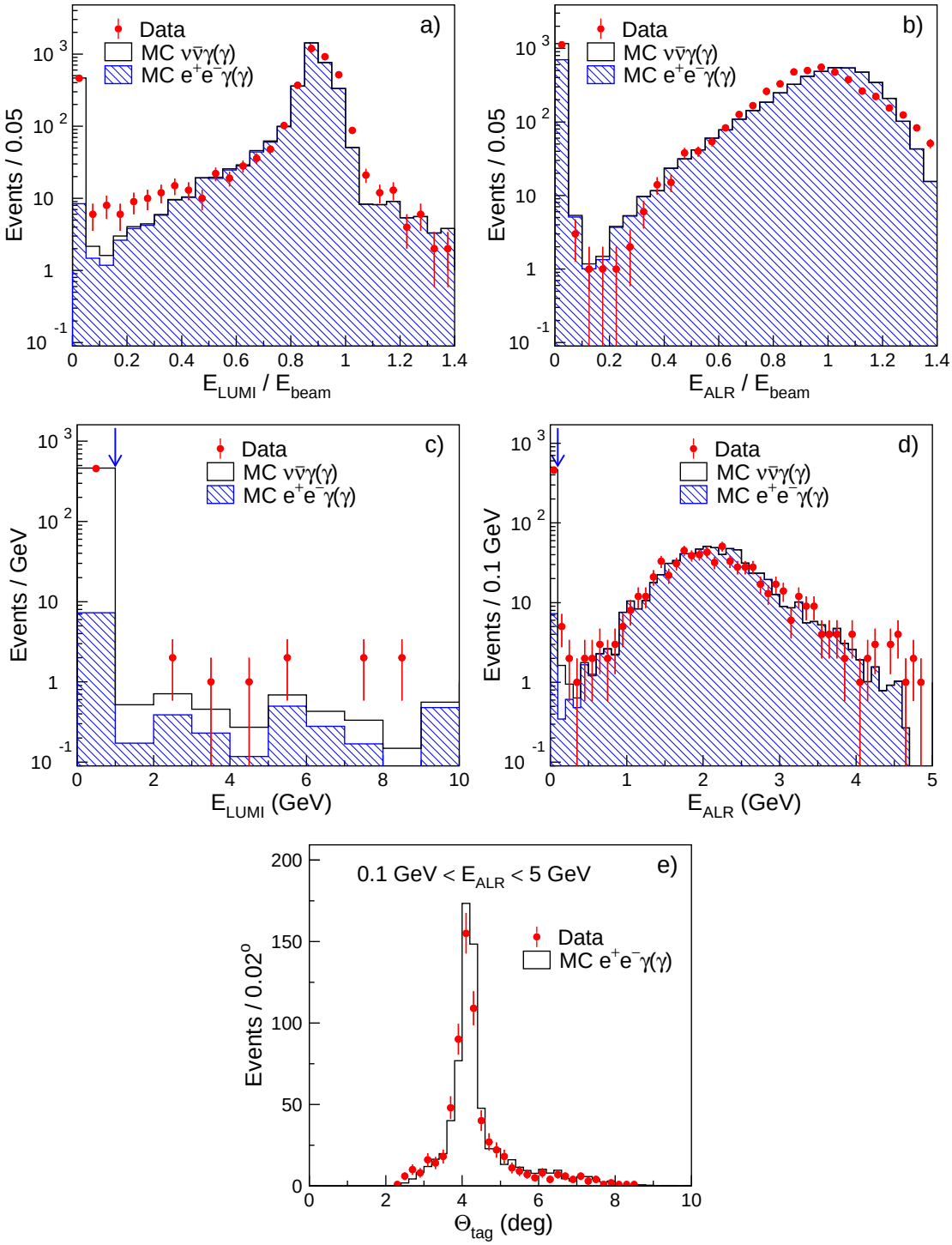

Figure 6.5: Distributions of the energies measured a) in the LUMI and b) in the ALR forward calorimeters scaled to the beam energy before the corresponding veto cuts are applied. Energy measured c) in the LUMI and d) in the ALR calorimeters for the regions of interest $E_{\mathrm{LUMI}} < 10$ GeV and $E_{\mathrm{ALR}} < 5$ GeV, respectively. The arrows indicate the values of the cuts. e) Distribution of the θ_{tag} angle for events with $0.1 < E_{\mathrm{ALR}} < 5$ GeV.

will be quoted in the following. Figure 6.5e shows the distribution of the θ_{tag} angle reconstructed for single-photon candidates with $0.1 < E_{\rm ALR} < 5$ GeV. A clear peak at $\theta_{tag} \simeq 4^\circ$ was observed which corresponded to the region of the lower edge of the ALR calorimeter. Figure 6.5e also shows that this effect was well reproduced in simulations of the detector response.

Tagging Efficiency of the Forward Calorimeters

In order to cross check the veto efficiency of the above cuts, I selected a sample of single-electron events. I applied the same cuts as for the selection of the single-electron sample used in the trigger studies (see the previous section). However, only events in the BGO barrel and triggered by the BGO triggers were accepted. In addition I did not require a matching cluster in the forward calorimeters. In order to suppress background from cosmic rays, the TEC track matched to the BGO shower had to pass certain quality criteria.[10]

The single-electron Bhabha events were previously defined as events in which only one electron was observed in the BGO, and the second electron and the radiated photon were scattered at low polar angles. In most of the such events, one of the two particles (electron or photon) was scattered at a very small polar angle and could be assumed to be parallel to the beam axis, as schematically shown in Figure 6.6.

Under this assumption, the polar angle of the particle scattered at a low, but non-negligible, polar angle can be calculated as

$$\cos\theta_{tag} = \frac{a^2-1}{a^2+1}\,, \text{ with } a = \frac{2\,E_{\rm beam}}{E_{bgo}\,\sin\theta_{bgo}} - \frac{1+\cos\theta_{bgo}}{\sin\theta_{bgo}}\,, \tag{6.3}$$

where E_{bgo} and θ_{bgo} are the energy and polar angle of the electron observed in the BGO calorimeter. In the phase-space region of the single-photon topology, $\theta > 14^\circ$ and $P_t > 0.02\sqrt{s}$, the θ_{tag} angle is constrained to be above about 2.3°.

For my study of the tagging efficiency, I selected a subsample of about 80,000

[10] These quality criteria were: transverse momentum of the track greater than 100 MeV; its distance of closest approach to the interaction point (DCA) less than 10 mm; the number of used wire hits more than 14; the number of wires between the first and last hit at least 15.

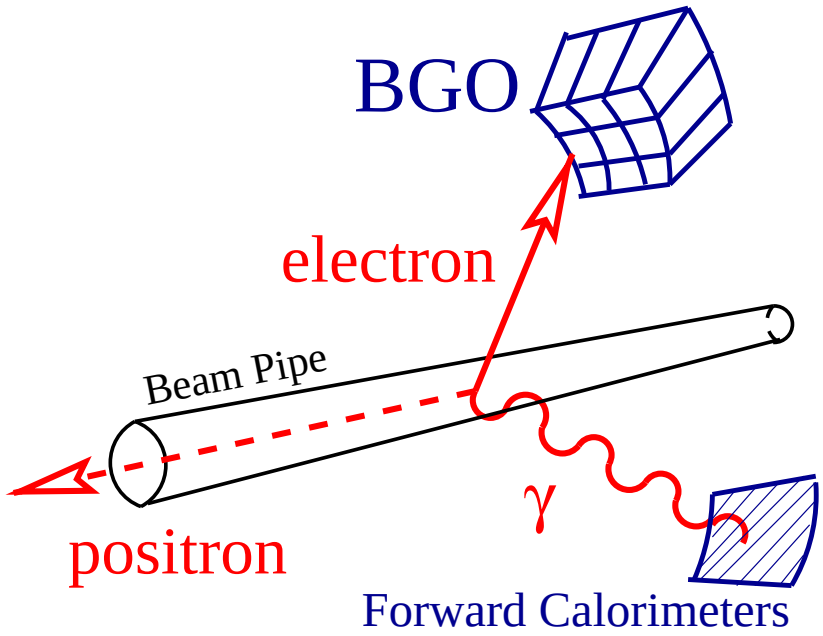

Figure 6.6: Schematic diagram of a single-electron event tagged by one the forward calorimeters.

single-electron events with $1.4^\circ < \theta_{tag}(180^\circ - \theta_{tag}) < 7.5^\circ$. The corresponding θ_{tag} distribution is shown in Figure 6.7a. The tagging efficiency of the forward calorimeters was then calculated as a ratio of the number of events not passing the veto cuts to the total number of single-electron events. The veto cuts on the energy in LUMI and ALR were the same as the ones used in the single-photon selection (see above).

Figure 6.7b compares the obtained veto efficiency as a function of the θ_{tag} angle with the Monte Carlo prediction. In the region of θ_{tag} values compatible with the single-photon event topology, $2.3^\circ < \theta_{tag}(180^\circ - \theta_{tag}) < 7.5^\circ$, the veto efficiency was measured to be $\varepsilon_{veto} = 99.74 \pm 0.03\%$ for the data and $\varepsilon_{veto} = 99.77 \pm 0.02\%$ for the simulation.

I also used the θ_{tag} variable to remove background due to inactive sectors in the HCAL endcaps, where particles escaped undetected. These sectors were located in the azimuthal angle intervals of 82° – 96° and 262° – 276°. In my event selection, the HCAL endcaps were used as veto detectors only in a small gap between the ALR and the BGO endcaps ($8.7^\circ < \theta < 10^\circ$). Therefore, both the single-photon and the

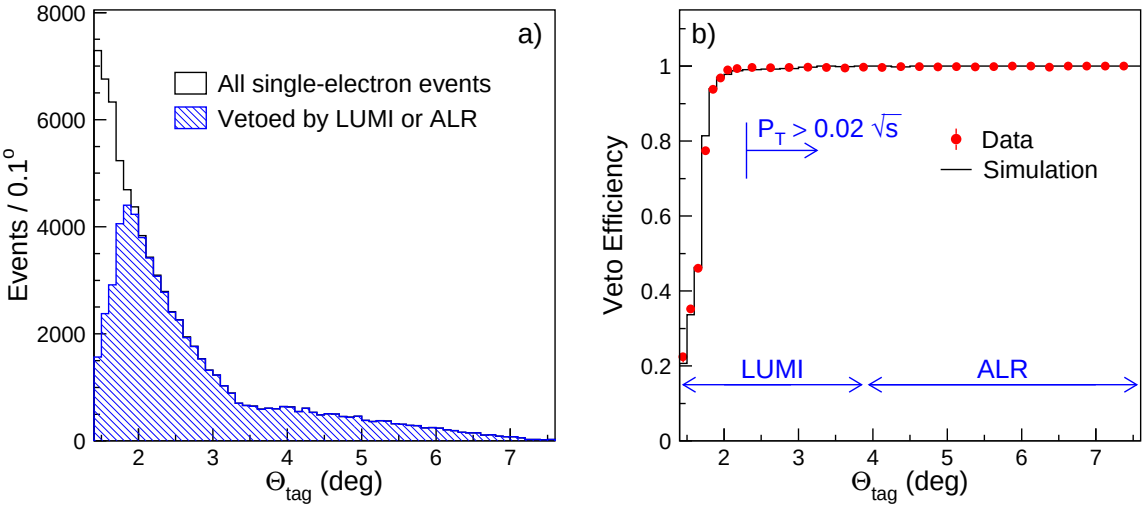

Figure 6.7: a) Distribution of the θ_{tag} angle for the selected single-electron events. b) Veto efficiency as a function of θ_{tag} obtained using this event sample. Events with $\theta_{tag} > 90°$ are included using $\theta_{tag} \to 180° - \theta_{tag}$.

single-electron candidates, detected in these ϕ-ranges, were discarded only if they had $7° < \theta_{tag}(180° - \theta_{tag}) < 12°$.

6.3.4 Photon Conversion

Electron candidates were removed by requiring that the number of hits in the TEC within an azimuthal angle of $\pm 8°$ around the path of the photon candidate must be less than the 40% of that expected for an electron, $N_{hits}/N_{exp} < 0.4$. The discrimination power of this cut on TEC occupancy was well tested by other physics analyses of L3. For example, it was used in the "official" L3 studies of the di-photon [158] and Bhabha [135] production processes.

This brings us to the problem of photon conversion. A significant fraction of photons converted into an e^+e^- pair before entering the L3 tracker. Figure 6.8 shows that such events would in general be rejected by the above cut on the TEC occupancy. In this section I describe my measurement of the photon conversion rates and my selection of the converted photons.

The probability for a photon to convert after traversing a length ℓ of material is

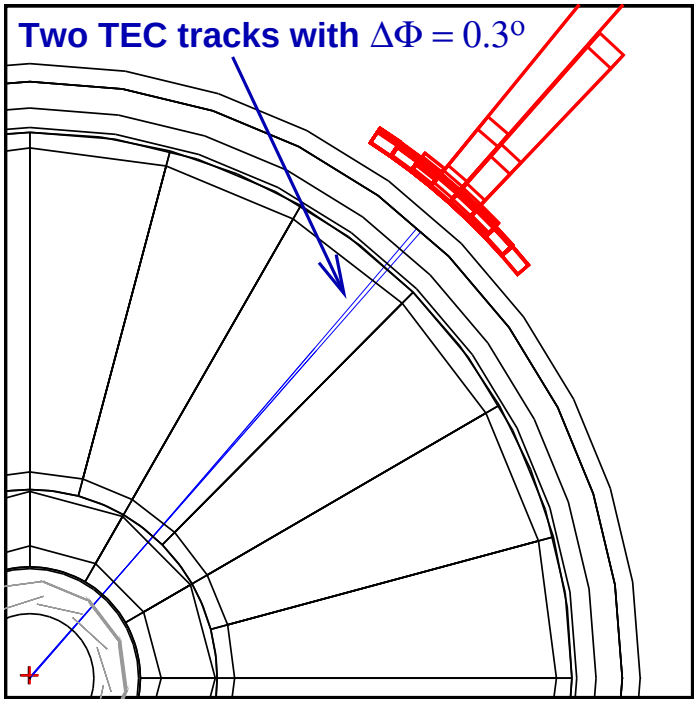

Figure 6.8: A photon conversion candidate. The two matching tracks are separated by about 0.3° in azimuth.

given by

$$P_{conv} = 1 - \exp(-\ell/[9/7X_0]) \,, \tag{6.4}$$

where X_0 is the radiation length of this material. This equation is expected to be accurate to within a few percent down to photon energies as low as 1 GeV [6]. As a cross check, I studied the energy dependence of the conversion probability using the detector simulation program of L3. The $P_{conv}(E)$ was found to slightly increase with energy, such that $P_{conv}(85\ \text{GeV})/P_{conv}(5\ \text{GeV}) = 1.04 \pm 0.02$. This result is in agreement with data from the NIST database [174]. In the following, the photon conversion is studied using samples of almost monochromatic photons so that the energy dependence of $P_{conv}(E)$ has no noticeable effect on my measurements.

Figure 6.9 shows the amount of dead material in front of the BGO calorimeter, as viewed from the beam interaction point. The plotted distributions correspond to

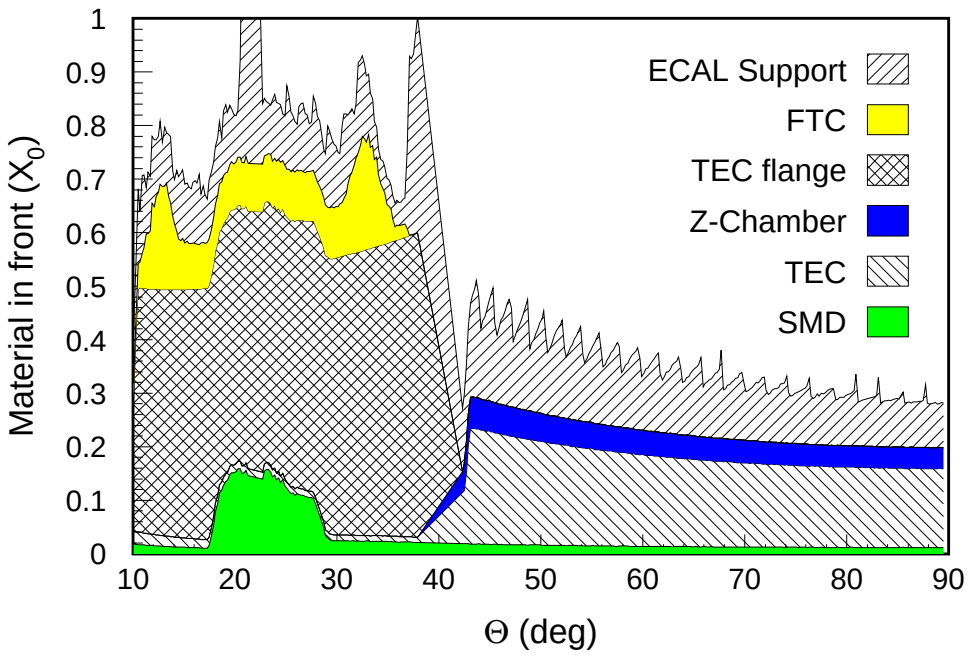

Figure 6.9: Plot of the amount of material in front of the BGO, measured in radiation lengths, as a function of the polar angle. Different layers show the contributions of various inner detector elements. Periodic variations in the amount of the BGO support material are due to steps used to support the individual crystals.

the structure of the L3 detector as used during the detector simulations.[11]

Most of the dead material was located in between the TEC and the BGO detectors. Thus, it did not lead to charged tracks in the TEC or to a significant deterioration of the energy resolution since the additional scattering and conversion were concentrated in a region just in front of the BGO crystals [172].

However, photons converted in the LEP beam pipe or in the silicon microvertex detector (SMD) would leave charged tracks in the TEC. According to Equation 6.4, the probability of such conversions was expected to be about 2% in the barrel region; it increased rapidly at low polar angles, reaching about 10% at $\theta \simeq 20°$. The sharp increase in the amount of dead material in front of the TEC at low polar angles, $\theta(180° - \theta) \simeq 15 - 25°$, was caused by the structure of the support system of the SMD (see Figure 6.9).

[11] This plot was provided by Dr. D. Kirkby [172] and is reproduced here with his permission.

The silicon microvertex detector was installed in 1993 and became fully operational in 1994, five years after the beginning of the LEP physics program. As a result, the Monte Carlo simulation of the detector did not provide a reliable description of the photon conversion in the SMD. Previous studies have found that, in most cases, the simulation tended to significantly underestimate the photon conversion rate [120, 175]. Below I investigate this problem separately for the endcap and the barrel regions of the BGO.

Photon Conversion in the Endcaps

Figure 6.10a shows the recoil mass distribution of the single-photon candidates in the endcaps passing all selection criteria except the cut on the TEC occupancy, $N_{hits}/N_{exp} < 0.4$. While the shape of this distribution is in agreement with the prediction, a clear discrepancy in the overall normalization can be seen. Most of the data events were observed in the region of the the Z-return peak ($M_{\rm rec} \simeq 91$ GeV), as was expected for single-photon events from the $e^+e^- \to \nu\bar{\nu}\gamma$ process. The dominant background was predicted to come from the single-electron production in the four-fermion processes and the Bhabha scattering process. The $M_{\rm rec}$ distribution of the background was expected to be relatively flat. Therefore, I relaxed the TEC occupancy cut for the single-photon candidates in the endcaps with $80 < M_{\rm rec} < 130$ GeV.

I also used the selected sample of events with $M_{\rm rec} = 80-130$ GeV to estimate the photon conversion rate. The polar angle distribution of such events is shown in Figure 6.10b. The conversion rate was calculated as a ratio of the number of conversion candidates to the total number of single-photon events selected in this recoil mass window. As shown in Figure 6.10c, the Monte Carlo simulation substantially underestimated the conversion rate in the region of the SMD flanges, $\theta(180^\circ - \theta) < 25^\circ$. For $\theta(180^\circ - \theta) = 15-25^\circ$, the conversion rate was measured to be $R_{conv}^{DATA} = 18.7 \pm 2.1\%$, two times higher than the Monte Carlo prediction of $R_{conv}^{MC} = 9.3 \pm 0.1\%$. This result was in good agreement with the value of $R_{conv}^{DATA} = 15.1 \pm 2.6\%$, obtained by an independent study of the $e^+e^- \to q\bar{q}\gamma$ and $e^+e^- \to \gamma\gamma$ processes[12] [175].

[12]In the study [175], a slightly tighter cut on the TEC occupancy was used.

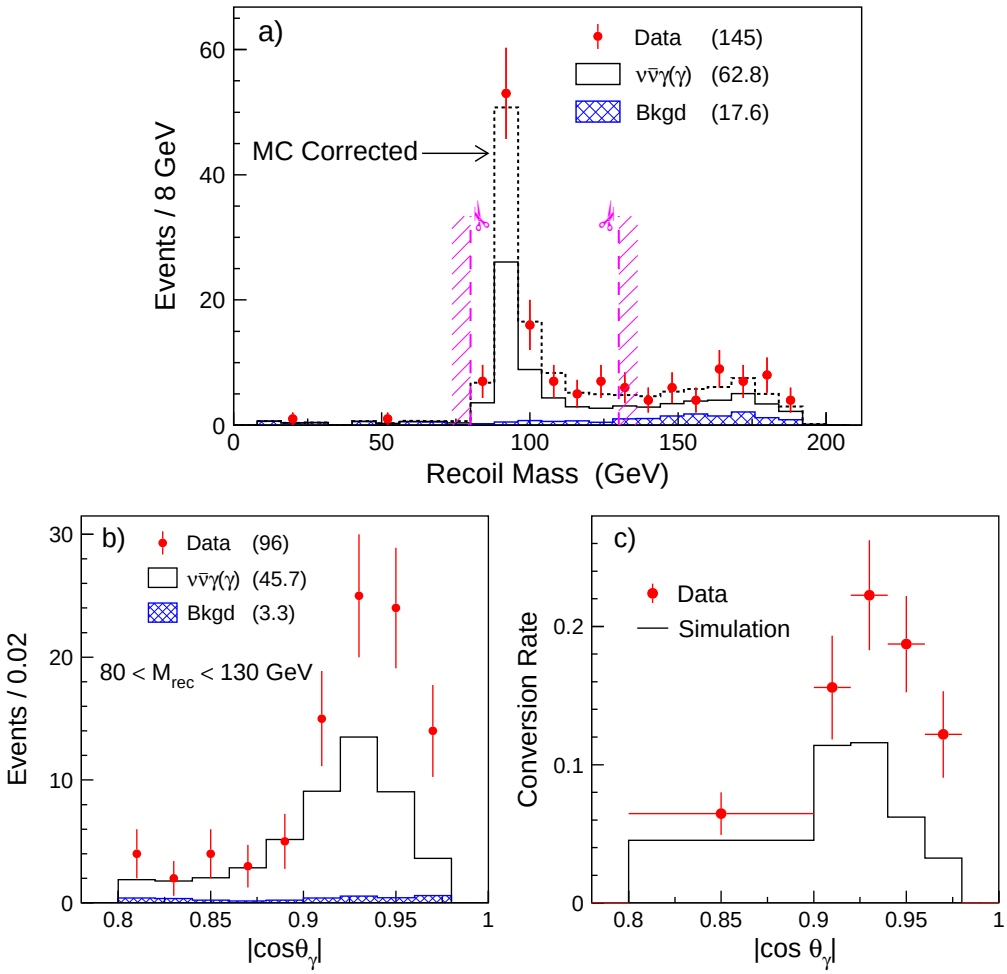

Figure 6.10: Distributions of a) the recoil mass for the single-photon events not passing the TEC occupancy cut and b) of the polar angle for events with $80 < M_{\rm rec} < 130$ GeV. c) Conversion probability as a function of the polar angle. The dashed histogram in plot a) shows the expected distribution after correction factors are applied. The event statistics are indicated on the plots.

The photon conversion rate, measured as a function of the polar angle (Figure 6.10c), was then used to correct the conversion rate in the simulation of the $e^+e^- \to \nu\bar{\nu}\gamma$ process. The recoil mass distribution of the conversion candidates in the endcaps was in good agreement with the corrected prediction, as shown in Figure 6.10a. The TEC occupancy cut was applied only in the region $M_{\rm rec} \neq 80 - 130$ GeV, where it rejected 49 events in data with 31 ± 3 and 14 events expected from the single-photon production and the background processes, respectively. As I discussed above, the events from the window $M_{\rm rec} = 80 - 130$ GeV were used for the

measurement of conversion rate and, at the same time, were included in the selected sample of single-photon events. Therefore, the statistical and systematic errors in my measurement of the $e^+e^- \to \nu\bar{\nu}\gamma(\gamma)$ cross section became correlated (see Section 7.1). This effect was taken into account in the systematic error calculation and was found to be small compared to the total systematic error on the measured cross section.

Photon Conversion in the Barrel

In the barrel region, I studied the effect of photon conversion using events from the di-photon production process, $e^+e^- \to \gamma\gamma(\gamma)$. Such events were selected in the sample of events with two back-to-back BGO bumps which I used in the absolute calibration of the BGO calorimeter (the corresponding selection criteria were given in Section 5.6.2). The di-photon candidates were identified by requiring that at least one of the two photon candidates pass the cut on TEC occupancy, $N_{hits}/N_{exp} < 0.4$. In total, I selected 1,527 events in data with 1,568 and 26 events expected from the di-photon and Bhabha scattering processes, respectively. The numbers of selected and expected events were in good agreement with the published L3 results [158].

To measure the conversion rate as a function of the polar angle, I used the distribution of the polar angle of the event, shown in Figure 6.11a. Here, the polar angle of the event (θ^*) is defined as

$$\cos\theta^* = |\sin(\frac{\theta_1 - \theta_2}{2}) / \sin(\frac{\theta_1 + \theta_2}{2})|\,, \tag{6.5}$$

where θ_1 and θ_2 are the polar angles of the two most energetic photons in the event.[13]

Events with one converted photon were further selected by requiring that the second photon candidate did not pass the cut on TEC occupancy. In total, I selected 161 such events in data with about 74 and 15 events expected from the di-photon and Bhabha scattering processes, respectively. The corresponding distribution of the polar angle of the event is shown in Figure 6.11b.

Denoting with R_c and N_0, respectively, the photon conversion rate and the number

[13] For events with perfectly back-to-back photons, $\cos\theta^* = |\cos\theta_1| = |\cos\theta_2|$.

of di-photon events in the preselected sample of events with back-to-back BGO bumps, the number of all di-photon events selected above and the number of events with one converted photon can be expressed as

$$N_{\gamma\gamma}^{tot} = N_0 \cdot (1 - R_c)^2 \,, \quad N_{\gamma\gamma}^{conv} = N_0 \cdot 2R_c(1 - R_c) \,. \tag{6.6}$$

Then, the photon conversion rate can be calculated as

$$R_c = \frac{r}{2 - r} \,, \text{ with } \; r = \frac{N_{\gamma\gamma}^{conv}}{N_{\gamma\gamma}^{tot}} \,, \tag{6.7}$$

where the values of $N_{\gamma\gamma}^{conv}$ and $N_{\gamma\gamma}^{tot}$ were obtained by subtracting the expected Bhabha background from the data. It should be noted that the above method was not very efficient for the region of the BGO endcaps due to much higher Bhabha background, which was caused by a rapid increase of the Bhabha cross section and a lower efficiency of the TEC.

Assuming that the thickness of the LEP beam pipe and the SMD detector was uniform in the barrel region, the angular dependence of the conversion rate would be given by a function $R_c(\theta) = R/\sin\theta$. Figure 6.11c shows that both for the data and Monte Carlo, the observed angular dependence was well described by this function. The fitted values of the parameter R were found to be equal to $R_{Data} = 4.3 \pm 0.4\%$ and $R_{MC} = 2.1 \pm 0.1\%$ for the data and Monte Carlo, respectively.

As was the case for the endcap region, the measured photon conversion rate was about two times higher than the prediction of the detector simulation program, $R_{Data}/R_{MC} = 2.1 \pm 0.2$. This value was in good agreement with previous studies of the photon conversion in the barrel, where it was measured to be $R_{Data}/R_{MC} = 2.5 \pm 0.4$ [120] and $R_{Data}/R_{MC} = 2.1 \pm 0.4$ [58]. Thus, in my samples of simulated single-photon events, I increased the fraction of events with converted photons in the barrel by a factor of 2.1.

The barrel region of the BGO calorimeter coincided with the most sensitive region of the L3 tracker ($\theta > 44°$), where the traversing charged tracks could be measured by

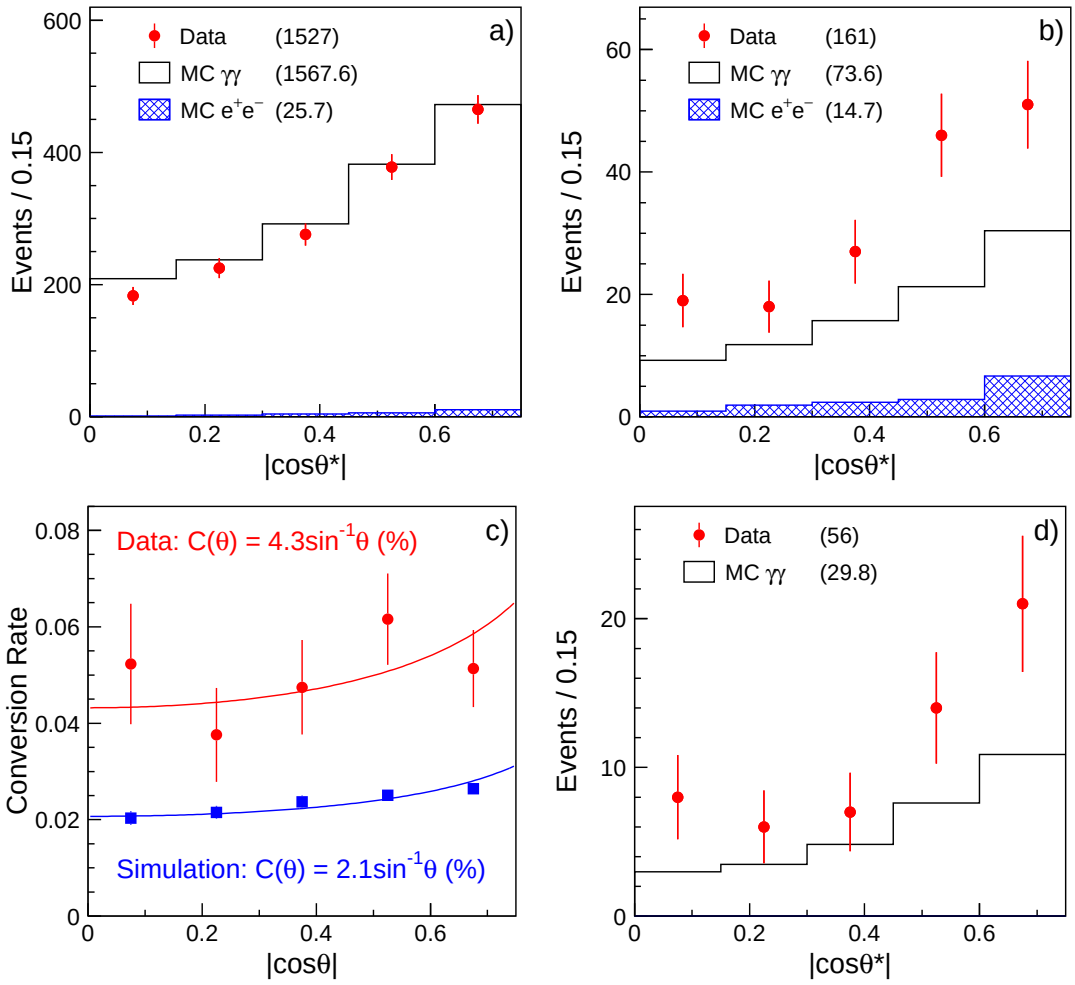

Figure 6.11: Distributions of $\cos\theta^*$ a) for all selected di-photon events, b) for events with one converted photon, and d) for events with two tracks matching to the converted photon; the event statistics are indicated on the plots. c) Photon conversion rate as a function of the polar angle.

all anode wires (see Section 4.2.2). Consequently, for a significant fraction of converted photons in the barrel, the two charged tracks of the produced e^+e^- pair could be resolved from one another. Such photon candidates, called "golden" conversions, were selected by requiring two matching tracks with an azimuthal opening angle $\Delta\Phi_{tracks} < 15°$ (the quality criteria for the matching tracks were given in footnote 10 on p. 150). An example of a golden photon conversion is shown in Figure 6.8.

The distribution of the polar angle of the event for di-photon events with one golden converted photon is shown in Figure 6.11d. For 100 GeV photons, the fraction

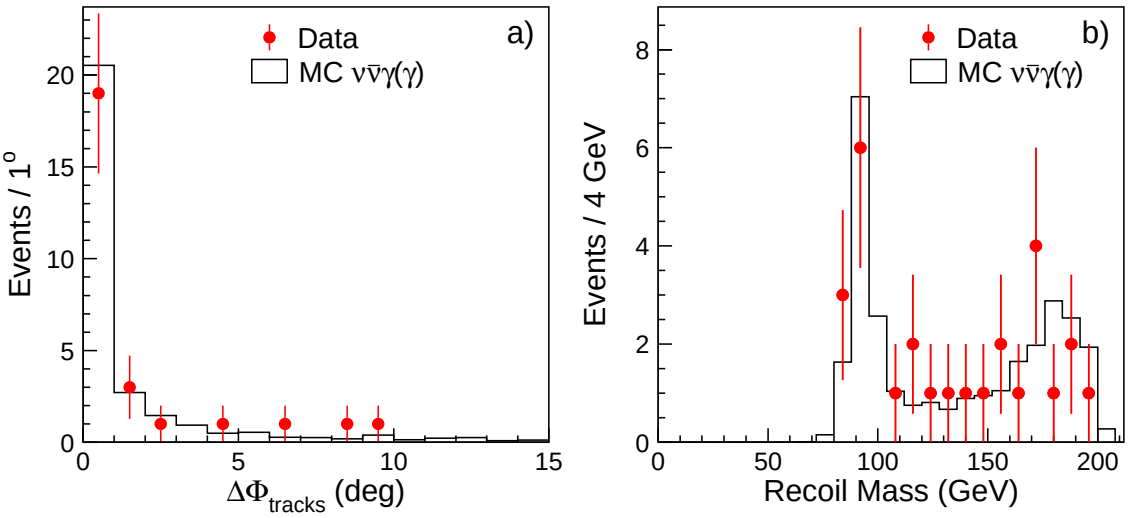

Figure 6.12: Distributions a) of the azimuthal angle between two matching tracks and b) of the recoil mass for the single-photon candidates accepted by the conversion selection in the barrel.

of golden conversions for 100 GeV photons was measured to be $38 \pm 4\%$, which was in agreement with the Monte Carlo prediction of 40%. This result was also in good agreement with an earlier study of golden conversions [58].

Figure 6.11d shows that the real electrons could not fake the golden photon conversions. Therefore, I included such events in my selected sample of single-photon candidates in the barrel, i.e., for such events I relaxed the cut on TEC occupancy. In total, I selected 27 single-photon events with a golden conversion in the data with about 28.2 events expected from Monte Carlo. The distributions of the $\Delta\Phi_{tracks}$ variable and of the recoil mass for these single-photon candidates are shown in Figure 6.12.

Summary

I studied the effect of photon conversion using samples of events from the $e^+e^- \to \nu\bar{\nu}\gamma$ and $e^+e^- \to \gamma\gamma$ processes. The average conversion rates were determined to be about 13% and 5% in the endcap and barrel regions, respectively. The detector simulation program was found to significantly underestimate the amount of dead material in

front of the L3 tracker, and the corresponding discrepancy in the conversion rate was taken into account.

By accepting single-photon events in the region of the radiative return to the Z (endcaps) and with golden photon conversions (barrel), I reduced the total efficiency loss caused by photon conversions to only about 2.8%. The above study represents the most accurate measurement of the photon conversion in L3 and is in good agreement with previous studies [58, 120, 175]. This allowed me to minimize the efficiency loss and the systematic uncertainties associated with this effect for my measurement of the single- and multi-photon production at LEP (see Section 7.1).

6.3.5 Cosmic Contamination

The earth's atmosphere is being continuously bombarded by a flux of high-energy particles, *primary cosmic rays*, which consists mainly of protons and heavier nuclei. Primary cosmic rays strike air molecules in the upper atmosphere, initiating an avalanche of secondary particles. Among the final products of such air showers, cosmic muons were of particular interest to LEP physics analyses.

The L3 detector was located 45 m underground and protected from the cosmic rays by about 30 m of solid rock. However, due to their relatively long lifetime of 2.2 μs and a relatively low rate of energy loss in matter, a significant fraction of cosmic muons with energies above 20 GeV reached the L3 detector.[14]

The cosmic muon events presented a source of unwanted background[15] for several L3 analyses, including my study of single- and multi-photon production at LEP. Cosmic muons traversing the BGO calorimeter could emit a bremsstrahlung photon and, thus, fake a single-photon event. The cosmic muons passed through the BGO

[14] For vertically incident cosmic muons, the mean energy loss to ionization in the rock overburden and in the L3 magnet corresponded to about 19 GeV [176].

[15] At the same time, a precise measurement of the cosmic muon flux is of great interest, as it allows one to predict the associated neutrino flux. At L3, such a measurement was performed with the upgraded setup of the L3 detector, known as L3+C [177]. It consisted of the L3 muon chambers, two arrays of scintillator counters installed outside the main L3 detector, and a dedicated trigger and data-acquisition system. In 1999-2000, the L3+C experiment recorded a total of 1.2×10^{10} cosmic muon triggers at an average trigger rate of 450 Hz. This resulted in one of the most precise measurements of the absolute muon flux for energies between 20 GeV and 3 TeV [176].

calorimeter at a rate of about 5 Hz [148]. Only a few percent of such events would be in coincidence with the beam-crossing window of LEP, and only a small fraction of muons would radiate a sufficiently hard photon in the BGO, since the bremsstrahlung cross section goes roughly as $1/\nu$, where ν is the fractional energy loss [6]. Nevertheless, each year thousands of cosmic ray events produced bremsstrahlung photons with an energy above 1 GeV in the BGO. In order to eliminate such events, I used a set of anti-cosmic cuts whose performance I describe below.

A picture of a cosmic ray event is shown in Figure 6.13. In this event, the cosmic muon entered the BGO calorimeter at a large angle with respect to the crystal axis and traversed about 30 crystals before radiating the bremsstrahlung photon. Since the photons were almost always emitted in the flight direction of the muon, the transverse profile of the resulting BGO shower would in general be oblong if the cosmic muon traversed the BGO at a significant angle to the crystal axis. Such cosmic ray events were then eliminated by the requirement that the shower roundness should be greater than 0.4 (see Section 6.3.1); for instance, the photon in Figure 6.13 had a roundness of 0.014. Thus, cosmic photons passing the cut on shower roundness were typically emitted by muons traversing the BGO calorimeter almost parallel to the crystal axis. The azimuthal distribution for such photons peaked at $\phi \simeq 90^\circ$ and $\phi \simeq 270^\circ$, as most of the cosmic ray muons were vertically incident.

Anti-Cosmic Cuts

The cosmic ray events did not originate from the beam collision, and their time of occurrence did not generally coincide with the beam crossing. Since the BGO calorimeter did not provide any timing information, the event time relative to the beam crossing was taken from the scintillation counters (time-of-flight system). As described in Section 4.2.4, the scintillation counters were located between the BGO and hadron calorimeters and had the timing resolution of 0.8 ns in the barrel and 1.9 ns in the endcaps. More than 99% of the cosmic ray events could be eliminated by a requirement that there should be at least one scintillator hit in time with the beam crossing within ± 5 ns, $N_{scnt}(\pm 5 \text{ ns}) > 0$.

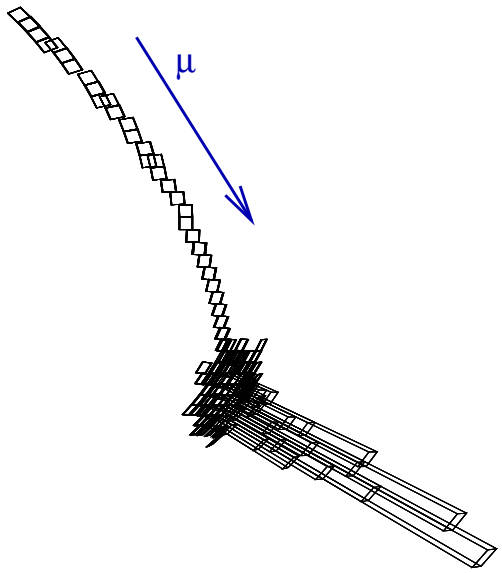

Figure 6.13: A typical cosmic ray event with a cosmic muon traversing the BGO calorimeter and emitting a bremsstrahlung photon.

For events with electrons or photons in the final state, the time-of-flight hits were produced by the shower particles emerging from the rear end of the BGO calorimeter. Because of this, I required that at least one in-time scintillator hit should be within a 15° cone around the direction of the photon. The longitudinal shower leakage decreased with shower energy, and so did the efficiency of this cut on the measured event time. To investigate the performance of this cut, I used control samples of tagged single-electron and back-to-back Bhabha events. These event samples were described in Sections 6.3.1 and 6.3.2, where they were used to study the performance of the shower-shape selection and the trigger efficiency. Because the single-electron events were tagged by a matching cluster in the forward calorimeters and the back-to-back Bhabha events had two bumps with an energy above $0.25\sqrt{s}$, these two event samples could be assumed to be virtually free of cosmic contamination.

Figure 6.14 shows the efficiency of the timing requirement, $N_{scnt}(\pm 5 \text{ ns}) > 0$, measured as a function of the shower energy. The fraction of showers satisfying this requirement increased from about 40% for $E_{shower} = 5$ GeV to about 99% for $E_{shower} = 45$ GeV. As a result, this cut would reject about 20% of the genuine single-

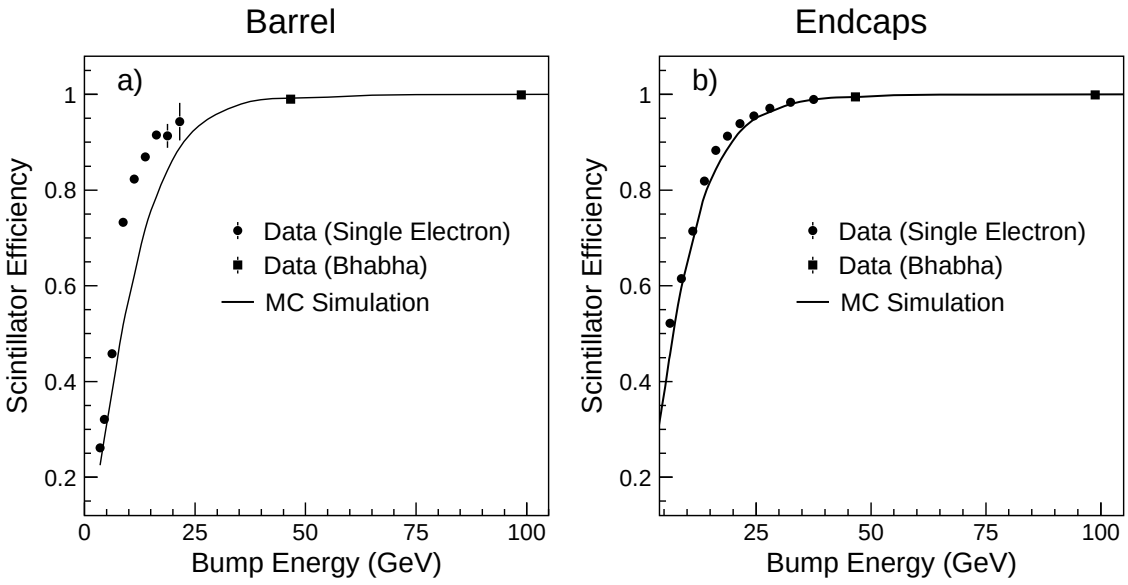

Figure 6.14: Scintillator efficiency as a function of the BGO shower energy a) for the BGO barrel and b) for the BGO endcaps.

photon events with $E_{shower} < 45$ GeV, which corresponded to the net efficiency loss of about 7%. Moreover, for showers with an energy below about 40 GeV, there is a noticeable discrepancy between the data and Monte Carlo. Since the longitudinal shower leakage was underestimated in the detector simulation (see the next section), the measured efficiency was significantly higher than the prediction of the detector simulation.

However, in the region $E_{shower} \geq 45$ GeV, a good agreement between data and Monte Carlo was observed. For 45 GeV Bhabha electrons, the scintillator efficiency was found to be about $99.15 \pm 0.07\%$ in the barrel and $99.49 \pm 0.04\%$ in the endcaps. These measured values were in good agreement with the Monte Carlo predictions of $99.24 \pm 0.04\%$ and $99.43 \pm 0.03\%$, respectively. For 100 GeV showers, the scintillator efficiency reached 99.9% both for the data and the detector simulation.

Therefore, in order to maximize the selection efficiency and minimize the associated systematic errors, I applied the timing cut of $N_{scnt}(\pm 5 \text{ ns}) > 0$ only to single-photon candidates with an energy above 45 GeV. For photons with lower energies, this cut was replaced by a requirement that there should be no scintillator hits more

than 50 ns out-of-time with respect to the beam crossing ($T_{scnt} > 50$ ns). For such events, I also imposed an additional cut on the number of muon track segments.

The entire L3 detector was surrounded by a high-precision muon spectrometer, which consisted of three layers of drift chambers arranged in eight octants (barrel) and two endcaps (see Section 4.2.6). The design on the muon spectrometer was optimized for a detection of muons originating from the beam interaction point. Due to the presence of dead cells and inactive zones between the neighboring octants, only 90% of such muons would leave hits in at least two of the three layers of the muon chambers [118]. For cosmic muons the detection efficiency was expected to be even lower since they typically did not fly through the beam interaction region.

Thus, in order to reject a maximum possible fraction of the cosmic ray events, I required that there should be no muon track segments detected in any layer of the muon chambers, $N_{\mathrm{MUTK}} = 0$. Due to a significant level of noise in the individual drift chambers of the muon spectrometer,[16] this cut also eliminated about 3% of the genuine single-photon events (with $E_\gamma < 45$ GeV). This is a sizable loss of selection efficiency. However, it was much lower than if I had required the in-time scintillator hits for all single-photon candidates.

As I discussed above, most of the cosmic ray events that passed the cut on shower roundness were produced by cosmic muons traversing the BGO calorimeter nearly parallel to the crystal axis. Such cosmic muons would thus traverse two sides of the BGO calorimeter and produce a second BGO cluster in the hemisphere opposite to the bremsstrahlung photon, as shown in Figure 6.15.

Muons with an energy between several hundred MeV and several hundred GeV lose energy in matter primarily by ionization and atomic excitation. In this energy range, the mean rate of energy loss depends only slightly on the muon energy [6]. Thus, the total energy deposited by such a muon in the BGO calorimeter depended mainly on the length of the muon track in the BGO material. Muons from the LEP collisions traversed the full length of the crystal and deposited on average between 200

[16] This level of noise was much higher than for a typical muon selection of L3 as I did not require that there should be several muon track segments matching to each other.

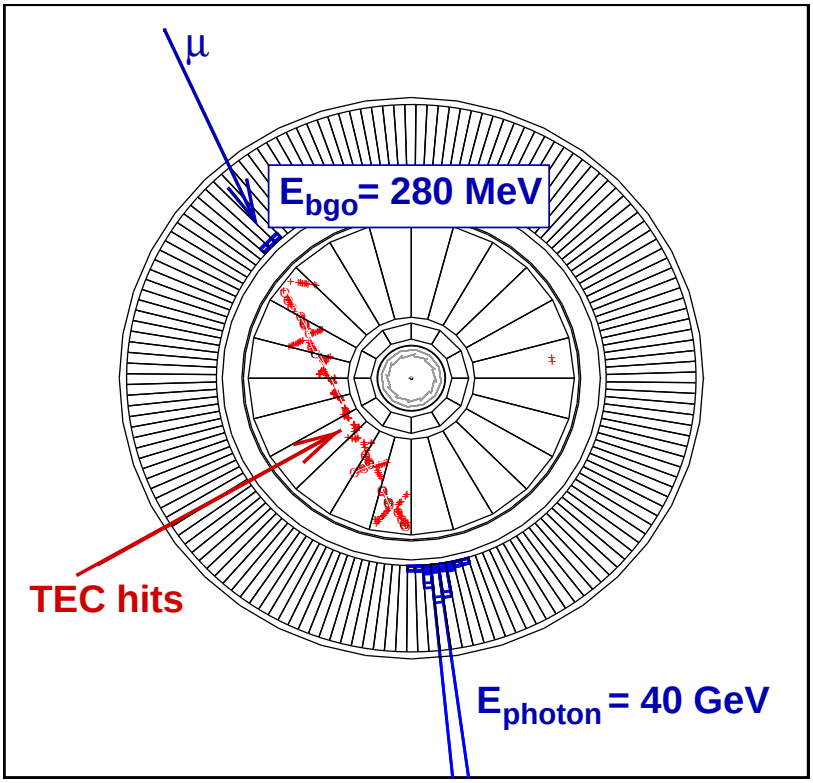

Figure 6.15: A typical cosmic ray event with a cosmic muon traversing the TEC before radiating a bremsstrahlung photon. The number of TEC hits in the 1 cm wide road between the photon candidate and the second BGO cluster was found to be equal to 136.

and 250 MeV [108]. For a cosmic ray muon, both the muon energy and the length of its track in the BGO could be substantially larger so that the energy deposited in the BGO could be as high as several hundred MeV.

Figure 6.15 shows that cosmic muons traversing two sides of the BGO would also leave a charged track in the TEC. Therefore, in order to further suppress the cosmic ray background, I applied the following cut: if there was a second BGO cluster with an energy $E_2 = 150 - 750$ MeV, no more than 20 hits should be found in the central tracking chamber in a 1 cm wide road between the photon candidate and the second BGO cluster, $N_{\rm TEC}(1\text{ cm road}) \leq 20$. Since the TEC reconstruction algorithm was optimized to detect in-time tracks originating from the beam interaction region, I used a dedicated pattern-recognition algorithm that was developed specifically for

the single-photon analysis at LEP1. More information on this algorithm can be found in Reference [173].

The above anti-cosmic cuts can be summarized as:

1. $N_{scnt}(\pm 5 \text{ ns}) > 0$ if $E_\gamma \geq 45$ GeV, or there should be no scintillator hits with $T_{scnt} > 50$ ns if $E_\gamma < 45$ GeV.

2. $N_{\text{MUTK}} = 0$ if $E_\gamma < 45$ GeV.

3. $N_{\text{TEC}}(1 \text{ cm road}) \leq 20$ if there was a second BGO cluster with an energy $E_2 = 150 - 750$ MeV.

Performance of the Anti-Cosmic Selection

To test the rejection power of the anti-cosmic cuts, I selected an independent sample of out-of-time cosmic ray events. First, I required that such events should contain at least one scintillator hit with 50 ns $< T_{scnt} <$ 700 ns with respect to the beam crossing. Second, I used the large difference between the 2 μs integration time of the BGO trigger system and the 11 μs integration time of the offline readout of the BGO (see Section 4.2.9). For in-time BGO showers, the ratio of the energy measured by the fast trigger ADCs (FERA) to the energy obtained from the offline reconstruction should be close to one, $E_{\text{FERA}}/E_{\text{BGO}} \simeq 1$. Therefore, to select only out-of-time cosmic events, I applied another cut: $0.15 < E_{\text{FERA}}/E_{\text{BGO}} < 0.5$. The out-of-time cosmic ray events were also required to satisfy all cuts of the single-photon selection except the anti-cosmic cuts. As a cross check, I applied the same selection to the control sample of 100,000 tagged single-electron events that was used to study the efficiency of the BGO triggers (see Section 6.3.2). No single-electron events were selected as out-of-time cosmic candidates.

Figure 6.16 shows the energy spectrum and the azimuthal angle distribution for photons in the selected out-of-time cosmic events. The energy spectrum is dominated by soft photons, as expected for a photon-bremsstrahlung process. The azimuthal distribution has clear peaks at $\phi_\gamma \simeq 90^\circ$ and $\phi_\gamma \simeq 270^\circ$ caused by the cut on shower roundness, as discussed above.

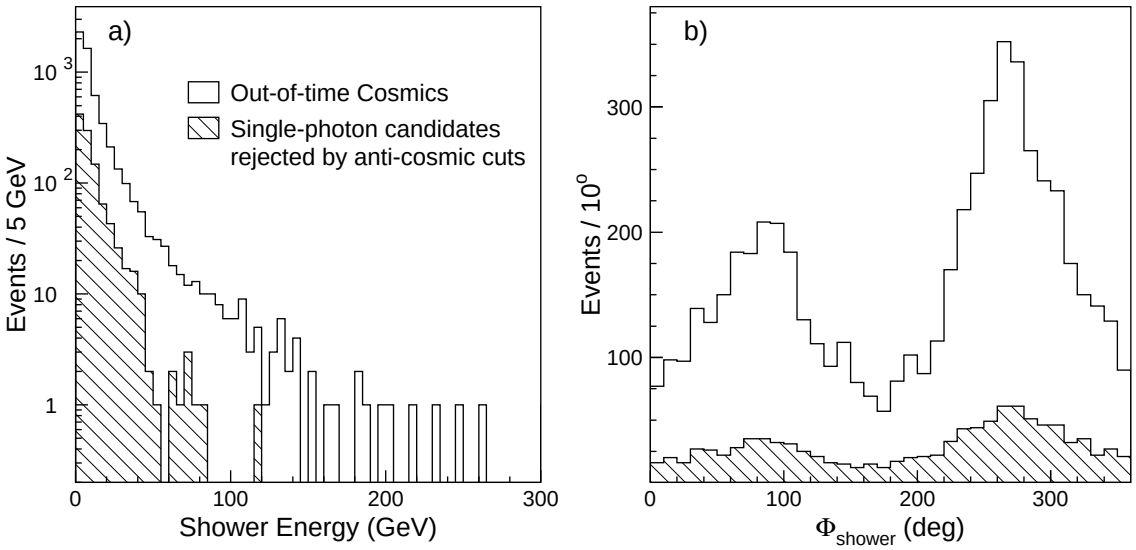

Figure 6.16: a) Energy and b) azimuthal distributions of the photons in the out-of-time cosmic ray events. Also shown are the corresponding distributions of the single-photon candidates rejected by the anti-cosmic cuts.

Next, I applied my anti-cosmic cuts on the number of muon track segments and on the number of hits in TEC to this sample of out-of-time cosmic events. Each of these two cuts was found to eliminate more than 90% of the out-of-time cosmic ray events. The rejection power of the anti-cosmic selection was then estimated as the ratio of the events not surviving these cuts to the total number of out-of-time events.

For the single-photon event topology ($P_t^\gamma > 0.02\sqrt{s}$ and $\theta_\gamma > 14°$), only 14 of the 3,745 out-of-time cosmic events survived the anti-cosmic cuts, corresponding to a rejection power of $P_{rej} = 99.6 \pm 0.1\%$. For the soft-photon event topology ($0.008\sqrt{s} < P_t^\gamma < 0.02\sqrt{s}$ and $\theta_\gamma > 43°$), 12 of the 2,010 out-of-time cosmic events survived the anti-cosmic cuts, corresponding to a rejection power of $P_{rej} = 99.4 \pm 0.2\%$.

The cosmic ray background in the final sample of single-photon events could then be estimated as

$$N_{\rm cosm} = (1 - P_{rej}) \cdot (N_{\rm data} - N_{\rm MC}) \,, \tag{6.8}$$

where $N_{\rm data}$ was the number of single-photon candidates selected in data before the application of the anti-cosmic cuts on the activity in the muon chambers and TEC,

and $N_{\rm MC}$ was the corresponding Monte Carlo prediction for the Standard Model processes. These event numbers were found to be $N_{\rm data} = 2,629$ and $N_{\rm MC} = 1,957.2$, and the corresponding cosmic contamination was calculated to be $N_{\rm cosm} = 2.6 \pm 0.7$ events, which amounted to only about 0.1% of the final sample of single-photon events. For the soft-photon event topology, these event numbers were found to be $N_{\rm data} = 927$ and $N_{\rm MC} = 595.9$, which corresponded to a cosmic contamination of $N_{\rm cosm} = 2.0 \pm 0.6$ events.

As a cross check, I compared the energy and azimuthal distributions of the out-of-time cosmic ray events to the corresponding distributions of the single-photon and soft-photon candidates passing all selection criteria except the anti-cosmic cuts. As expected, the shapes of these distributions were found to be similar (see Figure 6.16).

Finally, for the multi-photon event topology ($E_{\gamma_2} > 1$ GeV), Equation 6.8 cannot be applied directly since no multi-photon candidates were rejected only by the anti-cosmic cuts. This is explained by the fact that the cosmic ray events rarely contained two sufficiently hard photons. Indeed, only 16 of the 5,769 out-of-time cosmic ray events had a second photon candidate with an energy above 1 GeV. None of these events survived the anti-cosmic cuts. For the multi-photon cosmic events, the rejection power of the anti-cosmic selection was expected to be about the same as for the single-photon cosmic events. Therefore, the cosmic contamination in the multi-photon channel could be assumed to be negligible.

6.3.6 Longitudinal Shower Leakage

As described in Section 6.3.1, photon candidates with significant shower leakage into the hadron calorimeter were rejected by requiring $E_{\rm HCAL}/E_{\rm BGO} < 0.2$, where $E_{\rm BGO}$ and $E_{\rm HCAL}$ were the energies measured in the BGO and HCAL calorimeters, respectively. Here, $E_{\rm HCAL}$ is defined as a sum of energies of the HCAL clusters in a 10° cone around the photon direction.

The $E_{\rm HCAL}/E_{\rm BGO}$ distribution for the 45 GeV Bhabha electrons (see Figure 6.3c) shows that the detector simulation substantially underestimated the effect of longitu-

dinal shower leakage. This discrepancy was related to a poor description of the BGO support structure located in gaps between the BGO crystals. For Bhabha showers with significant leakage, the impact point was almost always found to be near the crystal edges, meaning that the leakage occurred mainly through the gaps between the crystals. The gap width varied from 200 μm to 900 μm *in situ*, but was fixed to a constant value of 200 μm in the Monte Carlo simulation [151].

This imperfection of the simulation program did not lead to a significant discrepancy in the efficiency of the shower-shape selection (see Section 6.3.1). However, the effect of longitudinal shower leakage had to be taken into account in order to avoid a systematic bias in the reconstructed photon energy.[17] To study this effect, I used the same samples of back-to-back Bhabha events as the ones that I used to study the performance of the shower-shape selection. While the average amount of shower leakage was measured to be quite small, $< E_{\rm HCAL}/E_{\rm BGO} > \simeq 0.8\%$, significant event-by-event fluctuations were observed and the ratio $E_{\rm HCAL}/E_{\rm BGO}$ was found to vary from zero to almost one (see Figure 6.3c).

To take into account energy losses caused by the longitudinal shower leakage, I developed a simple procedure that used the HCAL calorimeter as an improvised tail-catcher for electromagnetic showers. The corrected shower energy was calculated, on an event-by-event basis, as

$$E_{shower} = E_{\rm BGO} + \alpha \cdot (E_{\rm HCAL} - \beta \cdot E_{\rm BGO}) \,, \tag{6.9}$$

where the parameter α gave the response of the hadron calorimeter to electromagnetic clusters and the term $\beta \cdot E_{\rm BGO}$ represented the average shower leakage for Bhabha electrons used in the absolute calibration of the BGO calorimeter.[18] Because of significant differences in granularity and module design [87], the constants α and β were estimated separately for the barrel and the endcap regions of the HCAL. By

[17] The particle reconstruction algorithm of L3 calculated the energies of photons and electrons using information from the BGO calorimeter only, i.e., it assumed $E_{shower} = E_{\rm BGO}$.

[18] As described in Section 5.6.2 of Chapter 5, Bhabha electrons used in the absolute calibration of the BGO were required to satisfy $E_{\rm HCAL}/E_{\rm BGO} < 0.08$.

using the fact that the back-to-back Bhabha electrons were kinematically constrained to have an energy close to the beam energy, I obtained $\alpha = 1.25$ and $\beta = 0.6\%$ for the barrel region and $\alpha = 0.85$ and $\beta = 0.5\%$ for the endcap region. No significant differences were observed in the amount of relative shower leakage ($E_{\rm HCAL}/E_{\rm BGO}$) measured for the 45 GeV and 100 GeV Bhabha electrons.

For showers with low longitudinal leakage, the performance of this procedure suffered from contamination from random uranium and electronic noise in the HCAL. In addition, the HCAL response to low-energy electromagnetic clusters was not well understood. As a result, I found that my correction procedure was effective only for showers with $E_{\rm HCAL} > 3$ GeV.

The fraction of 100 GeV electrons with $E_{\rm HCAL} > 3$ GeV was measured to be about 6%. For such showers, the uncorrected energy measurement ($E_{shower} = E_{\rm BGO}$) was found to underestimate the true energy by 7% on average. Moreover, such significant shower leakage was found to degrade the relative energy resolution from 1% to about 5%. The correction procedure of Equation 6.9 not only corrected the absolute energy scale but also improved the relative resolution to about 2.5%.

I next applied this correction procedure to my single- and multi-photon candidates with $E_{\rm HCAL} > 3$ GeV and $E_{shower} > 40$ GeV. I found 89 such photon candidates in data corresponding to about 6.5% of the total sample of photons with $E_\gamma > 40$ GeV. Figure 6.17 shows that for such events the correction for leakage resulted in a clear improvement in the reconstruction of the Z-return peak. As I discuss in the next chapter, this was important for my measurement of the number of light neutrino species. I also applied the same correction procedure to my samples of simulated single-photon events, where the fraction of events with significant leakage was found to be only about 2.7%.

6.3.7 Detector Noise

The experimental signature of single-photon events was an electromagnetic shower and no other significant activity on the detector. This allowed me to reject background

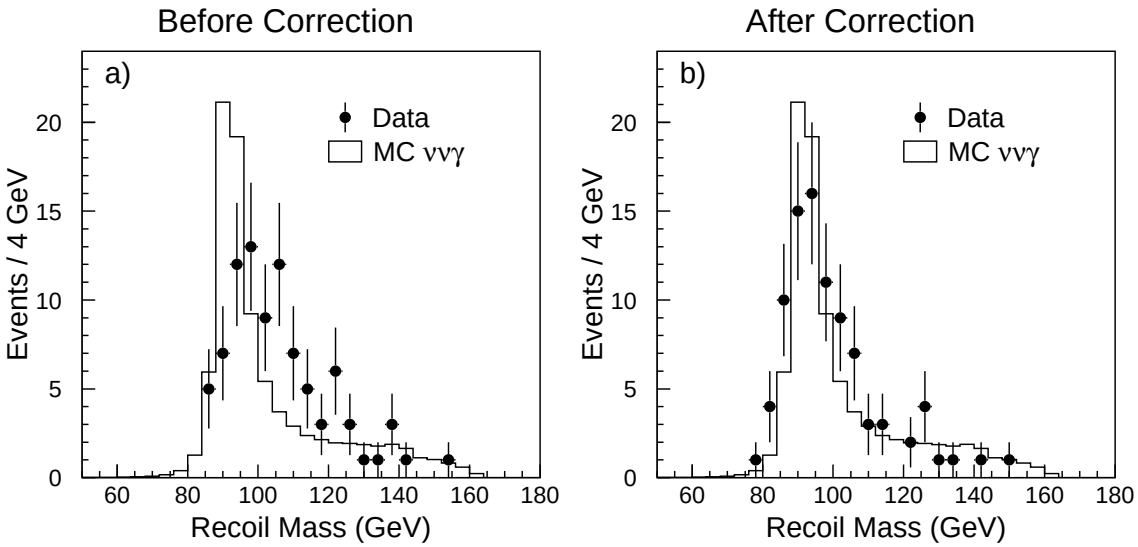

Figure 6.17: Recoil mass distribution for single-photon candidates with significant shower leakage into the HCAL, a) before and b) after the correction for leakage was applied. The data are compared to Monte Carlo prediction for single-photons with showers fully contained in the BGO calorimeter, where the Monte Carlo distribution was normalized to the number of data events.

events by using veto cuts on activity in various L3 subdetectors not associated with the identified photon candidate.

However, in the presence of detector noise, the veto cuts could also remove a sizable fraction of the genuine single-photon events. In order to study this effect, I used events randomly triggered at the beam crossing time. At L3, such events were obtained using a dedicated *beam-gate* trigger which accepted events at random time intervals based solely on the beam-crossing coincidence. The beam-gate events were collected at a rate of about 0.1 Hz, providing samples of about 500,000 beam-gate events per year of data-taking. I used these event samples to optimize the values of my veto cuts and to estimate the loss of selection efficiency (inefficiency) due to detector noise.

As mentioned in Section 6.3, all single-photon candidates had to satisfy the basic veto cuts which consisted of cuts on the following variables:

- Energy measured in the HCAL calorimeter $E_{\rm HCAL} < 7$ GeV

- Energy measured in the EGAP calorimeter $E_{\rm EGAP} < 7$ GeV
- Total visible energy (BGO+HCAL+EGAP) $E_{vis} < 10$ GeV
- Number of bumps in the BGO calorimeter $N_{bump} \leq 1$
- Number of good tracks[19] in the central tracker $N_{\rm GTRK} = 0$
- Number of good tracks[20] in the muon chambers $N_{\rm muon} = 0$.

Here, reconstructed objects matching to the identified photon candidates were excluded from the variables $E_{\rm HCAL}$, E_{vis}, N_{bump}, and $N_{\rm GTRK}$. Figures 6.18a-e show the corresponding distributions of the detector noise obtained using the beam-gate events from 1998-2000.

The inefficiency due to detector noise, associated with the basic veto cuts, was estimated to be only about 0.6%. As mentioned in Section 6.3.5, in order to suppress cosmic ray background I also required that there should be no muon track segments if the energy of the single-photon candidate was less than 45 GeV: $N_{\rm MUTK} = 0$ if $E_\gamma < 45$ GeV. For such events, the noise in muon chambers decreased the selection efficiency by about 3%. The distribution of the $N_{\rm MUTK}$ variable[21] for the beam-gate events is shown in Figure 6.18f.

Finally, to suppress background from radiative Bhabha events, I required that there should be no matching clusters in the forward calorimeters if the transverse momentum of the photon was less than 15 GeV, $P_t^\gamma < 15$ GeV (see Section 6.3.3). Specifically, I required that clusters in the ALR and LUMI calorimeters should satisfy $E_{\rm ALR} < 0.1$ GeV and $E_{\rm LUMI} < 1$ GeV if their acoplanarity with the photon candidate was less than 30°. Figure 6.19 shows that the level of noise in the forward calorimeters was relatively high[22] and, despite the acoplanarity requirement, this cut resulted in an additional loss of selection efficiency of about 0.9%.

[19] The quality criteria for good TEC tracks were given in footnote 10 on p. 150.

[20] The good tracks were required to have matching track segments in at least two of the three layers of the muon chambers.

[21] In the case of muon track segments, it was not always possible to resolve the left-right ambiguities, and the $N_{\rm MUTK}$ distribution had local maxima at even values of $N_{\rm MUTK}$ (see Figure 6.18f).

[22] In the forward calorimeters, the noise level was enhanced due to spurious beam-gas and beam-wall interactions and background from off-momentum beam-electrons [173].

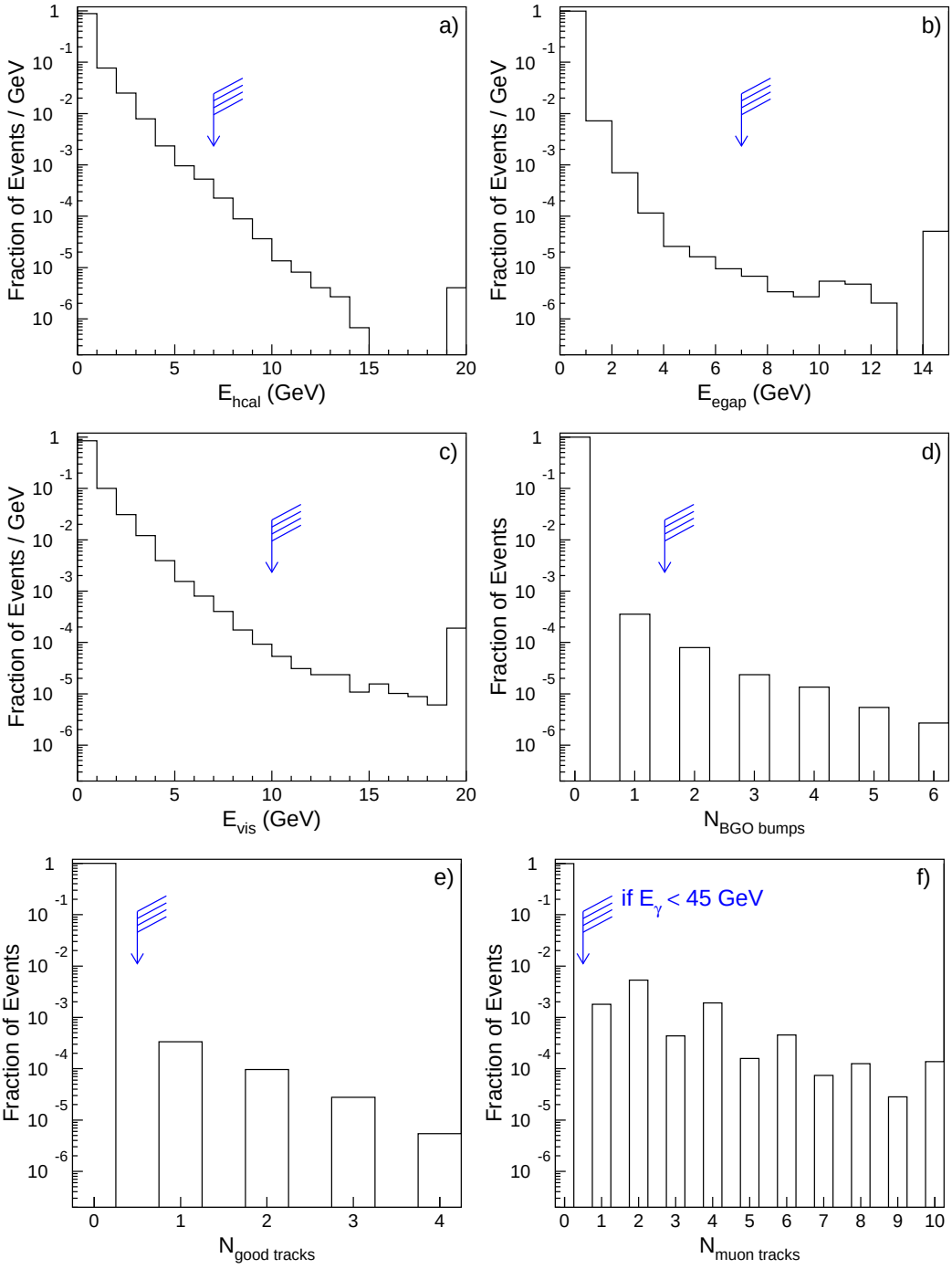

Figure 6.18: Distributions of the energies measured in a) the HCAL and b) the EGAP calorimeters, c) the total visible energy of the event, d) the number of BGO bumps, e) the number of good tracks in the TEC, and f) the number of tracks in the muon chambers for the 1998-2000 beam-gate event sample. The arrows indicate the values of the corresponding selection cuts. The last bin in each histogram contains the overflows.

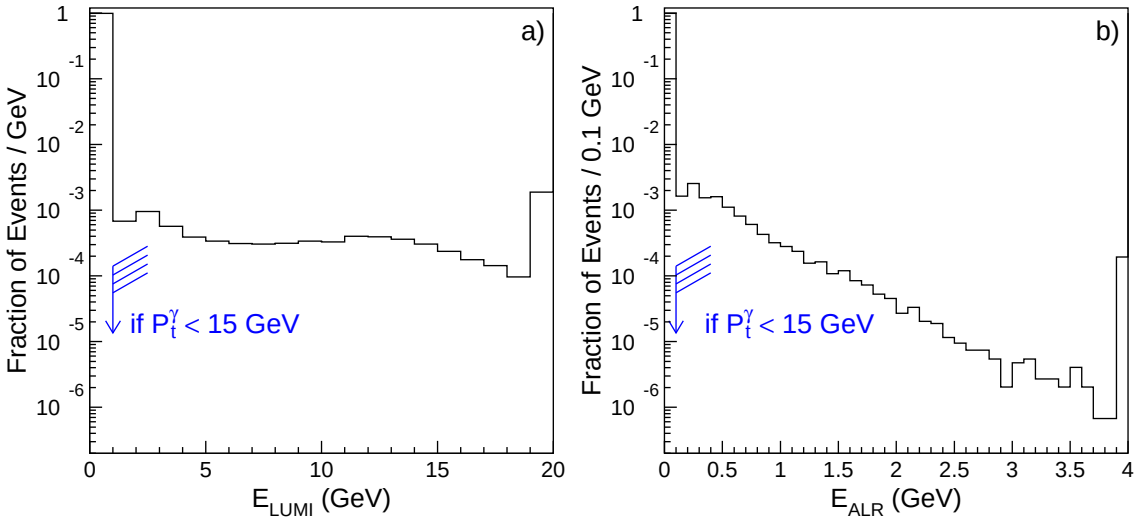

Figure 6.19: Distributions of the energies measured in a) LUMI and b) ALR forward calorimeters for the 1998-2000 beam-gate event sample. The arrows indicate the values of the corresponding selection cuts. The last bin in each histogram contains the overflows.

Since the beam-gate events were recorded at a constant trigger rate, the inefficiency due to noise in the detector was calculated as

$$\not{\epsilon}_{noise} = \sum_i \frac{\mathcal{L}_i \, n_i}{\mathcal{L} \, N_i} \,, \tag{6.10}$$

with $\mathcal{L}$ being the total luminosity, $\mathcal{L}_i$ the luminosity of the ith run,[23] N_i the total number of beam-gate events in the ith run, and n_i the number of beam-gate events in the ith run rejected by any of the above veto cuts. The obtained values of inefficiency are quoted in Table 6.4 for each of the four kinematic regions of my single-photon selection. The small year-to-year variations were taken into account.

As a cross check, I also measured the level of detector noise using the control samples of tagged single-electron and back-to-back Bhabha events. Such events had well-defined experimental signatures with few reconstructed objects in the detector and no activity expected in the outer subdetectors of L3 (HCAL and muon chambers). The obtained levels of noise in the individual subdetectors were found to be in

[23] Run is defined here as L3 data taken during an individual physics fill of LEP.

Kinematic Region	Fraction of Events	Inefficiency due to Detector Noise [%]		
		1998	1999	2000
$E_\gamma > 45$ GeV $P_t^\gamma > 15$ GeV	64.1%	0.51 ± 0.07	0.69 ± 0.06	0.70 ± 0.07
$E_\gamma > 45$ GeV $P_t^\gamma < 15$ GeV	0.6%	1.50 ± 0.07	1.53 ± 0.06	1.69 ± 0.07
$E_\gamma < 45$ GeV $P_t^\gamma > 15$ GeV	12%	3.61 ± 0.07	3.76 ± 0.06	3.47 ± 0.07
$E_\gamma < 45$ GeV $P_t^\gamma < 15$ GeV	23.2%	4.55 ± 0.07	4.54 ± 0.07	4.41 ± 0.07

Table 6.4: Inefficiency induced by the detector noise in 1998-2000 for the different kinematic regions of the single-photon selection. Also quoted is the fraction of events expected in each of the four kinematic regions.

agreement with those obtained using the beam-gate samples.

Averaging over the entire kinematic region of my single-photon selection gave an overall loss of selection efficiency of only about 1.9%.[24] The effects of the detector noise were completely ignored during the simulation of the detector response. To take into account such effects, I used a method described in Reference [173]. The detector simulation program of L3 assigned a run number to each simulated event according to the center-of-mass energy and the luminosity distribution of the LEP data. Then, for each Monte Carlo event, I randomly selected a beam-gate event from the same run in data and incorporated all reconstructed objects[25] from this beam-gate event into the original Monte Carlo event. The resulting loss of efficiency was found to be approximately the same as given by Equation 6.10 and Table 6.4.

6.3.8 Selection Results

A total of 1,921 events from the 1998-2000 data passed my single-photon selection. As described in Section 2.2.3 of Chapter 2, the Standard Model predictions for the single- and multi-photon production processes $e^+e^- \to \nu\bar{\nu}\gamma(\gamma)$ were obtained using the `KKMC` and `NUNUGPV` Monte Carlo generators. For the single-photon selection, the

[24] Due to optimization of the veto cuts, the resulting loss of selection efficiency was 2–4 times lower compared to other single-photon selections used in L3 at LEP1 and at the beginning of the LEP2 program [58, 120, 173].

[25] These included clusters in any of the calorimeters, as well as reconstructed tracks and individual hits in the TEC, SMD, and muon chambers.

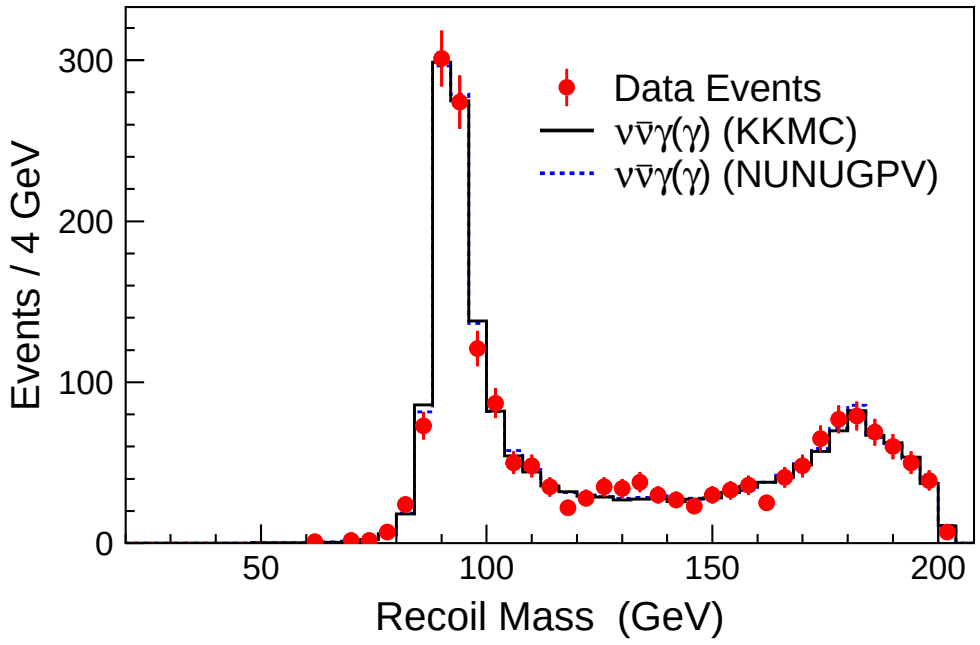

Figure 6.20: Recoil mass distribution of the single-photon candidates compared to the predictions of the KKMC and NUNUGPV Monte Carlo programs.

Monte Carlo expectations were found to be 1,917.5 events for KKMC and 1,930.7 events for NUNUGPV. The contributions from other sources were expected to give 15.2 events combined, including 8.3 events from the radiative Bhabha process $e^+e^- \to e^+e^-\gamma(\gamma)$, 3 events from the four-fermion processes $e^+e^- \to e^{\pm}\ell^{\mp}\nu_e\nu_\ell(\gamma)$ ($\ell = e, \mu, \tau$), 1.3 events from the di-photon process $e^+e^- \to \gamma\gamma(\gamma)$, and 2.6 events from cosmic contamination.

Thus, the purity of the selected single-photon sample was estimated to be higher than 99%. For simplicity, in the following figures and tables, the Monte Carlo expectation from the all sources is denoted as expectation from the $e^+e^- \to \nu\bar{\nu}\gamma(\gamma)$ process.

The recoil mass ($M_{\rm rec}$) distribution of the single-photon candidates is shown in Figure 6.20 together with predictions from the KKMC and NUNUGPV generators. Good agreement between data and Monte Carlo predictions was observed over the entire range of $0 < M_{\rm rec} < \sqrt{s}$. This distribution peaked near the Z pole ($M_{\rm rec} \simeq M_Z$) as explained in Section 2.2.2. In the region of the Z-return peak, $80 < M_{\rm rec} < 120$ GeV, 1,035 events were selected in data with 1,063.7 expected from the Monte Carlo (KKMC). The recoil mass of a photon candidate was calculated using its energy

$\sqrt{s}$ (GeV)	Data	KKMC		NUNUGPV	
		Expected	Efficiency[%]	Expected	Efficiency[%]
189	608	613.9	74.6 ± 0.2	613.5	74.8 ± 0.2
192	91	96.9	73.6 ± 0.2	98.8	74.2 ± 0.2
196	259	264.4	73.6 ± 0.2	265.1	73.9 ± 0.2
200	243	244.1	73.1 ± 0.2	249.0	73.7 ± 0.2
202	118	103.2	73.6 ± 0.2	104.9	73.5 ± 0.2
205	219	215.4	73.3 ± 0.2	216.9	73.7 ± 0.2
207	359	370.6	73.2 ± 0.2	373.4	73.6 ± 0.2
208	24	24.2	73.1 ± 0.2	24.3	73.4 ± 0.2
Total	1,921	1,932.7	73.7 ± 0.1	1,945.8	74.1 ± 0.1

Table 6.5: Summary of the single-photon selection giving (for each value of $\sqrt{s}$) the number of events selected in data together with the numbers of expected events and selection efficiencies calculated using the KKMC and NUNUGPV Monte Carlo programs, where the errors quoted are the statistical errors of the Monte Carlo samples.

(see Equation 6.1, p. 137), and the corresponding single-photon energy spectrum can be found in Figure D.1a (Appendix D). In addition, Figure D.2 shows the recoil mass distributions separately for each value of center-of-mass energy ($\sqrt{s}$).

The numbers of events selected at different $\sqrt{s}$ are listed in Table 6.5 together with the numbers of expected events obtained with the KKMC and NUNUGPV programs. Good agreement is observed both between data and Monte Carlo as well as between the predictions of KKMC and NUNUGPV within the 1% theoretical error quoted for these generators (see Section 2.2.3). In the following analysis, I will use Monte Carlo predictions obtained with the KKMC Monte Carlo generator.

Table 6.5 also lists the selection efficiencies calculated using the KKMC and NUNUGPV programs. Here, the selection efficiency is defined as the number of Monte Carlo events selected after the full simulation and all analysis cuts[26] divided by the number of events generated within the phase space of the single-photon topology, $14^\circ < \theta_\gamma < 166^\circ$ and $P_t^\gamma > 0.02\sqrt{s}$. The average selection efficiency was determined to

[26]Thus, here and in the following, quoted efficiencies include losses caused by noise in the detector and by inefficiency of the BGO trigger system.

be $73.7 \pm 0.1\%$ for `KKMC` and $74.1 \pm 0.1\%$ for `NUNUGPV`. In addition, the selection efficiency and the numbers of observed and expected events are provided in Table D.1 (Appendix D) in bins of $M_{\rm rec}$ and $|\cos\theta_\gamma|$.

The kinematic distributions of the single-photon candidates are shown in Figure 6.21. The distributions of the polar and azimuthal angles are shown in Figures 6.21a and 6.21b, respectively. The slight dips observed at $\phi_\gamma \simeq 90^\circ$ and $\phi_\gamma \simeq 270^\circ$ were mainly due to the RFQ holes in the BGO endcaps, and the slight dip at $\phi_\gamma \simeq 220^\circ$ was caused by a cluster of dead trigger cells in the BGO barrel. This structure of the azimuthal angle distribution was well reproduced by the Monte Carlo.

The transverse momentum distribution is shown in Figures 6.21c. The visible peak structures were caused by the phenomenon of the radiative return to the Z and by the gap between the BGO barrel and endcaps. This can be better understood by comparing Figures D.1b and D.1c (Appendix D) which show the transverse momentum distributions of the single-photon events in the BGO barrel and endcaps, respectively.

The trigger efficiencies and photon conversion rates were significantly different in the barrel and endcap regions (see Sections 6.3.2 and 6.3.4). It was therefore interesting to compare the observed and expected event rates separately for these two regions of my selection. In the BGO barrel, $\theta(180^\circ - \theta) > 43^\circ$, I selected 985 single-photon events in data with 971.6 expected from Monte Carlo. In the BGO endcaps, $14^\circ < \theta(180^\circ - \theta) < 37^\circ$, I selected 936 single-photon events in data with 961.1 expected from Monte Carlo. The recoil mass distributions of the single-photon candidates in the barrel and in the endcaps are shown in Figures 6.21d and 6.21e, respectively.

As shown in Figure 6.21a, the cross section of the reaction $e^+e^- \to \nu\bar{\nu}\gamma(\gamma)$ increased rapidly with decreasing $|\cos\theta_\gamma|$. Consequently, the numbers of single-photon events observed in the barrel and the endcaps were almost the same, even though the fiducial coverage of the BGO endcaps was about four times smaller than that of the BGO barrel. The selection efficiencies were found to be 81.9% for the barrel and 78.5% for the endcaps. These efficiencies are higher than the overall efficiency of my selection

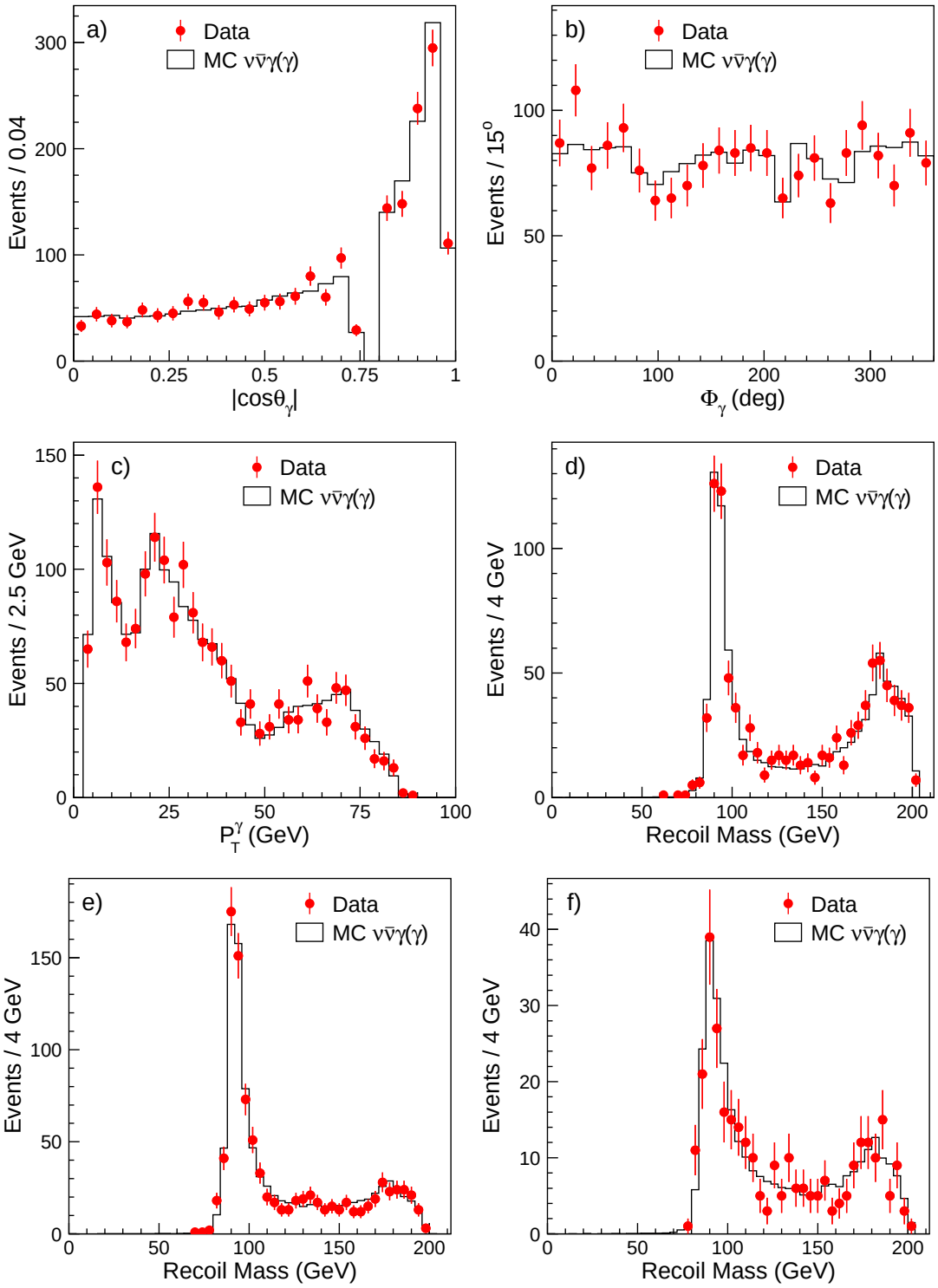

Figure 6.21: Distributions of a) the polar and b) the azimuthal angles and c) of the transverse momentum for the entire single-photon sample. Recoil mass distributions of the single-photon candidates d) in the barrel, e) in the endcaps, and f) near calorimeter edges or with dead channels in the shower.

(73.7%), which suffered from losses in the gaps between the barrel and endcaps of the BGO calorimeter.

As I have discussed in Section 6.3.1, photon candidates detected near the calorimeter edges or with a dead channel in the 3×3 crystal matrix were treated differently in my shower-shape analysis. In total, I selected 315 such single-photon events in data with 326.7 expected in Monte Carlo. The corresponding distribution of the recoil mass is shown in Figure 6.21f.

In summary, the observed event rates and kinematic distributions of my single-photon selection are found to be in good agreement with the Monte Carlo expectations. In the next chapter, I will use the selected sample of single-photon events to measure the cross section of the reaction $e\,e^+e^- \to \nu\bar{\nu}\gamma(\gamma)$ and to derive limits on deviations from the Standard Model in the framework of several new physics scenarios.

6.4 Multi-Photon Selection

As already mentioned in Section 6.2, multi-photon events with missing energy were defined as events with at least two photons, each with an energy above 1 GeV and a global transverse momentum $P_t^{\gamma\gamma} > 0.02\sqrt{s}$. In Section 2.2.2 of Chapter 2, I showed that the cross section of the multi-photon production process, $e^+e^- \to \nu\bar{\nu}\gamma\gamma(\gamma)$, should be about 15 times smaller than that of the single-photon production. The recoil mass[27] distribution is expected to have the familiar feature of the Z-return peak, and the energy spectrum of the second most energetic photon (E_{γ_2}) should be dominated by soft photons.

A multi-photon event recorded by the L3 detector is displayed in Figure 6.22. In my multi-photon sample, this event had the highest value of E_{γ_2} and therefore was one of the most interesting candidates for the process $e^+e^- \to YY \to XX\gamma\gamma$, where X and Y are new invisible particles. However, the recoil mass of this event was measured to be consistent with the Z mass, $M_{\rm rec} = 92.2$ GeV, indicating that this event was from the Standard Model process $e^+e^- \to \nu\bar{\nu}\gamma\gamma(\gamma)$.

[27] The recoil mass of a multi-photon event is calculated using Equation 6.1, p. 137.

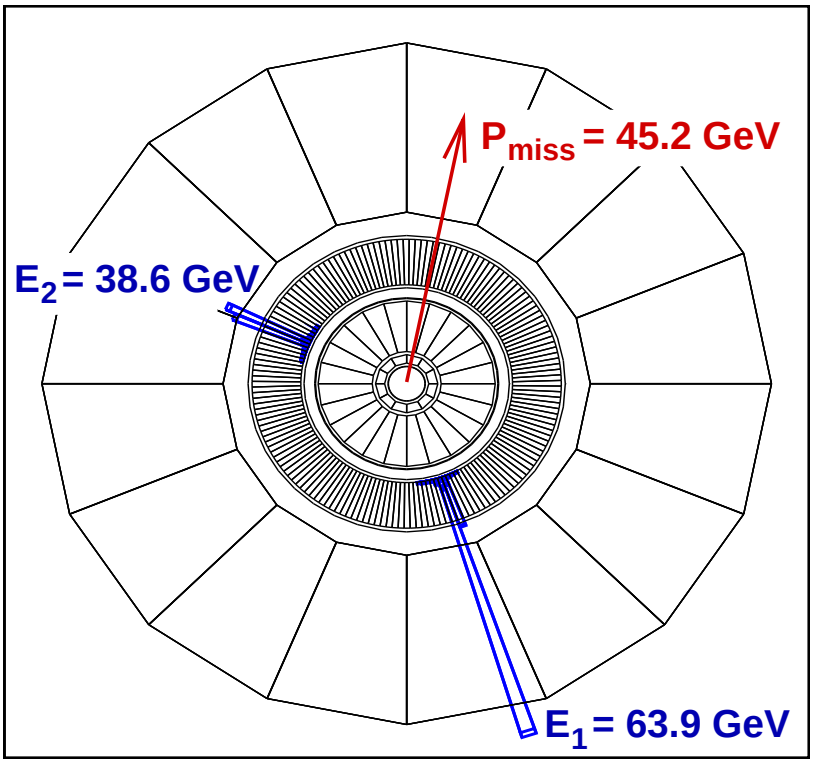

Figure 6.22: A multi-photon event recorded by the L3 detector, and displayed in the $x - y$ plane. This event was recorded in 2000 data at $\sqrt{s} = 205$ GeV.

Event Selection

The requirement of a second energetic photon in an event effectively eliminated backgrounds from cosmic ray events and from the radiative Bhabha and four-fermion processes which I had to consider in my single-photon analysis. On the other hand, it also significantly increased contamination from the di-photon process, $e^+e^- \to \gamma\gamma(\gamma)$.

Therefore, multi-photon events with missing energy were selected in a two-step procedure. In the first step, the veto cuts of the single-photon selection were applied[28] as defined in Sections 6.3 and 6.3.7. In addition, all photon candidates were required to pass the shower-shape cuts of Section 6.3.1 and the cut on TEC occupancy[29] of Section 6.3.4.

[28] For the clusters in the forward calorimeters, the acoplanarity angle was calculated with respect to the direction of the total momentum of the multi-photon system.

[29] Except for the golden converted photons in the barrel, which were also accepted.

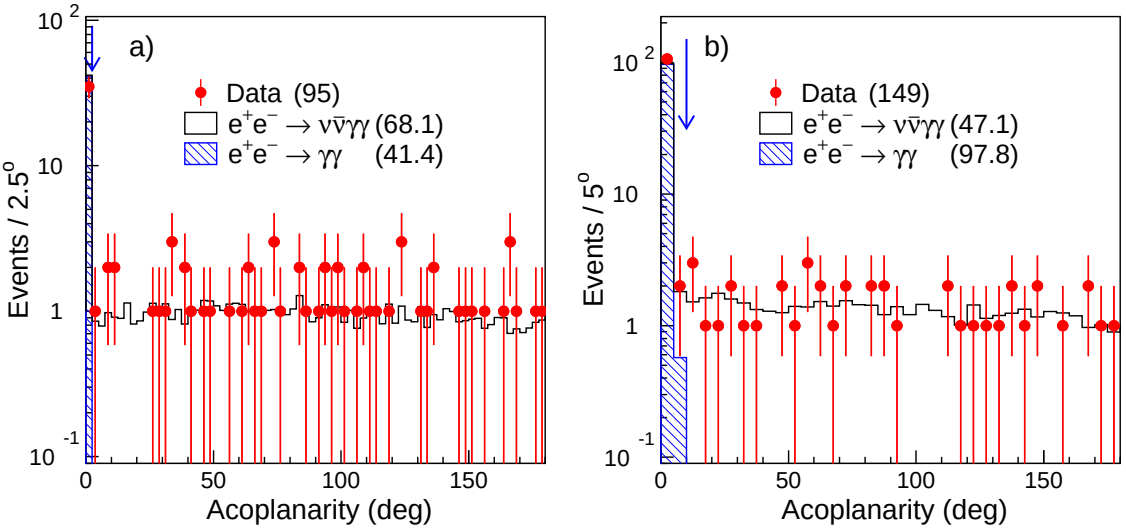

Figure 6.23: Distributions of the acoplanarity between the two most energetic photons after all other multi-photon selection cuts have been applied a) for events in which both photons were not near the calorimeter edges and did not contain dead channels and b) for events in which at least one of the photons did not satisfy these conditions. The arrows indicate the values of the cuts. The event statistics are also indicated on the plots.

After this preselection, 244 data events were retained with 254.6 expected from the Standard Model processes, including 115.3 events from the reaction $e^+e^- \to \nu\bar{\nu}\gamma\gamma(\gamma)$ and 139.2 events from the reaction $e^+e^- \to \gamma\gamma(\gamma)$. In order to further suppress the di-photon background, I required that the acoplanarity[30] between the two most energetic photons should be greater than 2.5°. About 20% of the photon candidates were detected near the calorimeter edges or had a dead channel in the 3×3 matrix centered on the most energetic crystal. For such showers, the uncertainty on the measurement of the photon direction was higher. Therefore I relaxed the acoplanarity cut to 10°, if an event contained at least one photon with dead or missing crystals in the shower. Figure 6.23 shows that this cut eliminated almost all di-photon contamination while retaining acceptance for $\nu\bar{\nu}\gamma\gamma(\gamma)$ events.

Finally, the remaining di-photon background was suppressed by requiring that the missing momentum vector should not point to the RFQ holes in the BGO endcaps. This cut eliminated 2 events in data with 1.4 expected from Monte Carlo.

[30] The definition of the acoplanarity angle was given in footnote 7 on p. 138.

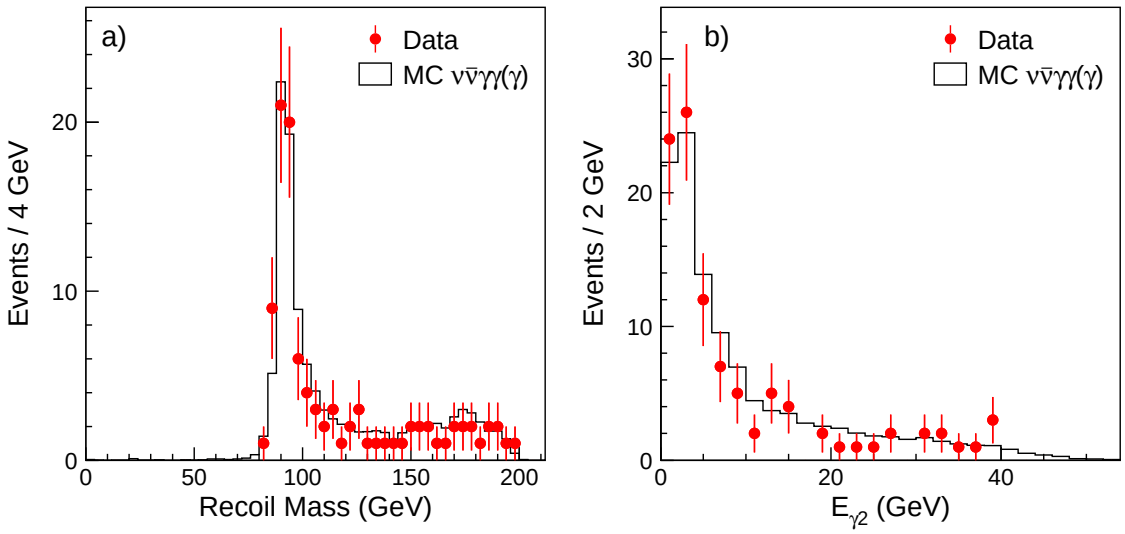

Figure 6.24: a) M_{rec} and b) E_{γ_2} distributions of the selected multi-photon events with missing energy.

Selection Results

The multi-photon selection applied to the 1998-2000 data yielded 101 events, in good agreement with the KKMC prediction of 111.6 events for the Standard Model $e^+e^- \to \nu\bar{\nu}\gamma\gamma(\gamma)$ contribution. The expected contribution for the di-photon background was found to be only 0.9 events and, for simplicity, in the following figures and tables it is added to the $\nu\bar{\nu}\gamma\gamma$ expectation. Figures 6.24a and 6.24b show, respectively, the M_{rec} and E_{γ_2} distributions of the selected multi-photon events with missing energy.

The numbers of events selected at different $\sqrt{s}$ are listed in Table 6.6 together with the numbers of expected events and the selection efficiencies obtained with the KKMC program. This table also lists the corresponding predictions for the NUNUGPV program, which was found to agree with KKMC within the the 5% theoretical error quoted for these Monte Carlo generators (see Section 2.2.3). Unless otherwise specified, in the following analysis I will use the predictions of KKMC.

The average selection efficiency, within the kinematic acceptance of this selection, was $57.1 \pm 0.4\%$. The efficiency of the multi-photon selection was significantly lower than that of the single-photon selection (73.7%) due to increased losses in the gaps

$\sqrt{s}$ (GeV)	Data	KKMC		NUNUGPV	
		Expected	Efficiency[%]	Expected	Efficiency[%]
189	26	35.3	58.5 ± 0.9	34.5	59.0 ± 0.7
192	11	5.6	58.6 ± 0.9	5.5	57.7 ± 0.7
196	17	15.2	56.2 ± 0.9	15.8	56.9 ± 0.7
200	15	14.5	56.9 ± 0.9	14.3	56.7 ± 0.7
202	3	5.9	55.9 ± 0.9	6.0	57.3 ± 0.7
205	10	12.6	55.2 ± 0.9	11.3	55.2 ± 0.8
207	17	22.1	56.7 ± 0.9	19.2	54.9 ± 0.8
208	2	1.4	55.7 ± 0.9	1.3	55.6 ± 0.8
Total	101	112.7	57.1 ± 0.4	107.8	56.9 ± 0.3

Table 6.6: Summary of the multi-photon selection giving (for each value of $\sqrt{s}$) the number of events selected in data together with the numbers of expected events and selection efficiencies calculated using the KKMC and NUNUGPV Monte Carlo programs, where the errors quoted are the statistical errors of the Monte Carlo samples.

between the barrel and endcaps of the BGO calorimeter. However, for the case when both photons were observed in the barrel of BGO calorimeter, the selection efficiency was determined to be 76.4%. This was important because most new physics signals were expected to be produced predominantly in the barrel region.

In Appendix D, Table D.2 gives the efficiencies of the multi-photon selection and the numbers of observed and expected events in bins of $M_{\rm rec}$ and E_{γ_2} for the full sample and for the case in which both photons were in the barrel. In addition, Figure D.3 shows the recoil mass distributions of the multi-photon events, separately, for each value of $\sqrt{s}$. The discussion of the results of the multi-photon selection will be continued in the next chapter, where I will use the multi-photon sample to search for signs of Supersymmetry and for anomalous quartic gauge-boson couplings.

6.5 Soft-Photon Selection

The soft-photon selection extended the transverse momentum range of the single-photon selection down to $P_t^\gamma = 0.008\sqrt{s}$ and covered only the BGO barrel region, where a single-photon trigger was implemented with a threshold around 1.5 GeV (see Figure 6.4b). Soft-photon events with missing energy were thus defined as events with only one photon with $43^\circ < \theta_\gamma < 137^\circ$ and $0.008\sqrt{s} < P_t^\gamma < 0.02\sqrt{s}$.

The selection of soft-photon events began by applying all cuts of the single-photon selection as described in Section 6.3. In this channel, most of the events were expected to come from the radiative Bhabha scattering process $e^+e^- \to e^+e^-\gamma$, in which both electrons were lost in the beam pipe and only a photon was scattered at a large polar angle. In order to reduce this background, I imposed the following additional cuts: no energy deposit was allowed in the forward calorimeters, there must be no other ECAL cluster with energy greater than 200 MeV, and the energy in the hadron calorimeter must be less than 5 GeV.

In total, 566 soft-photon candidates were selected in the 1998-2000 data with an expectation of 581.7, where 130 events were expected from the $e^+e^- \to \nu\bar{\nu}\gamma(\gamma)$ process, 448.4 from the $e^+e^- \to e^+e^-\gamma(\gamma)$ process, 1.4 events from the two-photon $e^+e^- \to e^+e^-e^+e^-(\gamma)$ process, and 2 events from cosmic contamination. Figure 6.25 compares the energy spectrum and polar angle distribution of the selected soft-photon events with the Monte Carlo predictions. Good agreement between data and Monte Carlo was observed.

Table 6.7 gives the numbers of events selected at different $\sqrt{s}$, together with the numbers of expected events and the selection efficiencies (`KKMC`). In Appendix D, Figure D.4 shows the energy spectrum of the soft-photon candidates, separately, for each value of $\sqrt{s}$.

In the next chapter, I will use the results of the soft-photon selection in my searches for extra dimensions and pair-produced gravitinos.

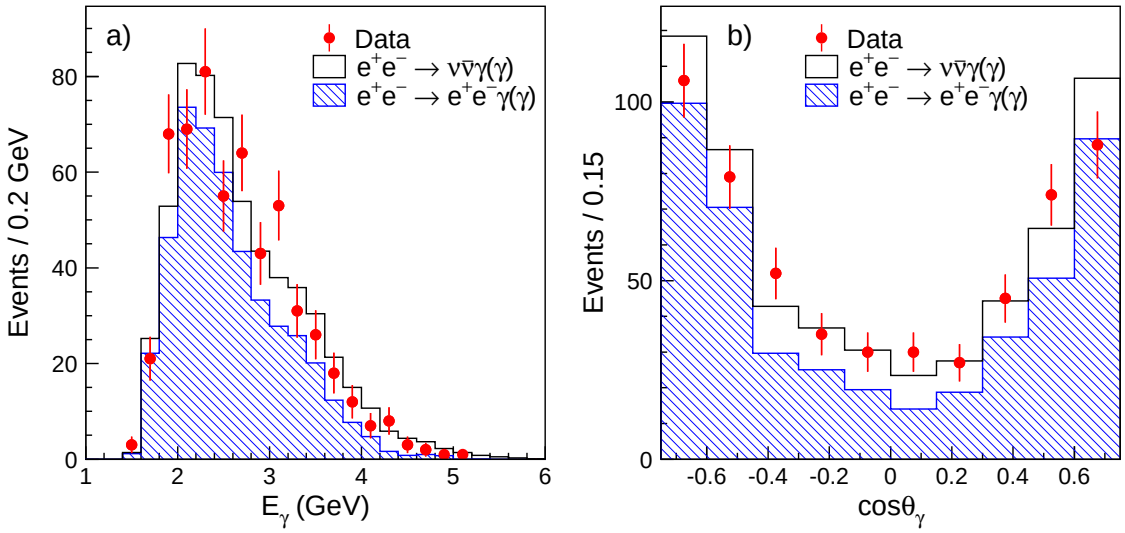

Figure 6.25: a) Energy spectrum and b) polar angle distribution of the soft-photon event sample.

$\sqrt{s}$ (GeV)	Data	Expectation			Efficiency[%]
		$\nu\bar{\nu}\gamma$	Background	Combined	
189	160	37.0	128.9	165.9	48.3 ± 0.8
192	34	6.3	23.6	29.9	49.8 ± 0.8
196	79	17.7	67.3	85.0	50.6 ± 0.8
200	77	16.8	63.5	80.3	50.1 ± 0.8
202	36	7.3	28.8	36.1	48.6 ± 0.8
205	74	15.8	49.0	64.7	51.9 ± 0.8
207	97	27.4	85.0	112.3	51.8 ± 0.8
208	9	1.8	5.6	7.4	52.2 ± 0.8
Total	566	130.0	451.7	581.7	50.1 ± 0.3

Table 6.7: Summary of the soft-photon selection giving (for each value of $\sqrt{s}$) the number of events selected in data together with the number of expected events and selection efficiency calculated using KKMC, where the errors quoted are the statistical errors of the Monte Carlo samples.

Chapter 7

Neutrino Production and Searches for New Physics

In the previous chapter I described how I selected my samples of photonic events with missing energy. In this chapter I describe how I used these event samples to study the neutrino production at LEP and to search for manifestations of physics beyond the Standard Model.

Section 7.1 covers my measurements of the $e^+e^- \to \nu\bar{\nu}\gamma(\gamma)$ cross section and of the number of light neutrino species. In this section, I also discuss the systematic uncertainties in these measurements. In Sections 7.2 and 7.3, I describe my searches for Supersymmetry and for manifestations of large extra dimensions, respectively. Section 7.4 is devoted to measurements of gauge-boson couplings.

In the next chapter these results will be compared with results from other high-energy physics experiments. Finally, combinations of my results with those of the other LEP experiments are described in Appendix E.

7.1 Measurement of the Neutrino Production

As I described in Sections 6.3.8 and 6.4, both the single-photon and multi-photon samples were expected to consist almost purely of events from the neutrino pair-production accompanied by the emission of one or more photons, $e^+e^- \to \nu\bar{\nu}\gamma(\gamma)$. Therefore, to study this Standard Model process I used the combined single- and multi-photon event sample.

This combined sample consisted of 2,022 events selected in 1998-2000 L3 data that was in good agreement with the Monte Carlo expectation of 2,045 events, where 2,029 events were expected to come from the $e^+e^- \to \nu\bar{\nu}\gamma(\gamma)$ process and the rest from the

background Standard Model processes and cosmic contamination. Thus, the purity of the combined $\nu\bar{\nu}\gamma(\gamma)$ sample was estimated to be 99.2%. Unless otherwise stated, in this chapter the Monte Carlo predictions for the $e^+e^- \to \nu\bar{\nu}\gamma(\gamma)$ process are obtained using the KKMC event generator, which was described in detail in Section 2.2.3.

7.1.1 Measurement of the $e^+e^- \to \nu\bar{\nu}\gamma(\gamma)$ cross section

The kinematic region of the combined single- and multi-photon selection corresponds to $14^\circ < \theta_\gamma < 166^\circ$ and $P_t^\gamma > 0.02\sqrt{s}$ or $P_t^{\gamma\gamma} > 0.02\sqrt{s}$ (see Section 6.2). The selection efficiency was then calculated as the ratio of the number of Monte Carlo events accepted after the full detector simulation and all analysis cuts to the total number of events generated within this phase space region. The obtained selection efficiency is given in Table 7.1 for each of the eight subsets of the L3 data used in my analysis.[1] The average selection efficiency was found to be 72.5%.

The cross section of the $e^+e^- \to \nu\bar{\nu}\gamma(\gamma)$ process ($\sigma_{\nu\bar{\nu}\gamma}^{meas}$) was then determined from the number of selected data events N_{data}, the number of expected background events N_{bg}, the selection efficiency ε, and the integrated luminosity $\mathcal{L}$, using the following formula:

$$\sigma_{\nu\bar{\nu}\gamma}^{meas} = \frac{N_{data} - N_{bg}}{\varepsilon\mathcal{L}} \,. \tag{7.1}$$

The measured and expected cross sections are listed in Table 7.1 and are shown as a function of $\sqrt{s}$ in Figure 7.1a. This figure also shows previous L3 measurements performed[2] with data collected at lower center-of-mass energies at the beginning of the LEP2 program [178].

To quantify possible deviations from the Standard Model expectations, I computed

[1] As discussed in Section 6.1, these eight subsets represent the data collected by the L3 detector during 1998-2000 at $\sqrt{s} = 189 - 208$ GeV. The corresponding integrated luminosities and center-of-mass energies were given in Table 6.1 (p. 132).

[2] These measurements were performed using a sample of 405 $e^+e^- \to \nu\bar{\nu}\gamma(\gamma)$ candidates selected in 88 pb^{-1} of data collected by L3 during 1995-1997 at $\sqrt{s} = 130 - 183$ GeV. The event selection is described in detail in Reference [58]. However, I re-evaluated the efficiency losses due to photon conversion using my measurements of the conversion probability (see Section 6.3.4). In addition, I used the more precise KKMC Monte Carlo generator which was not available at the time of the original publication [178]. It should be noted that the resulting corrections on the measured cross sections were not significant compared to the statistical precision of these measurements.

$\sqrt{s}$ (GeV)	$\varepsilon(\%)$	$\sigma^{meas}_{\nu\bar{\nu}\gamma}$(pb)	$\sigma^{exp}_{\nu\bar{\nu}\gamma}$(pb)	$\sigma^{meas}_{\nu\bar{\nu}}$(pb)	$\sigma^{exp}_{\nu\bar{\nu}}$(pb)
189	73.5	$4.86 \pm 0.19 \pm 0.05$	4.97	60.1 ± 2.5	61.6
192	72.6	$4.74 \pm 0.47 \pm 0.05$	4.77	60.4 ± 6.1	60.8
196	72.4	$4.52 \pm 0.27 \pm 0.05$	4.58	59.0 ± 3.6	59.8
200	71.9	$4.38 \pm 0.27 \pm 0.05$	4.39	58.7 ± 3.7	58.8
202	72.3	$4.78 \pm 0.44 \pm 0.05$	4.31	64.8 ± 6.0	58.4
205	72.0	$4.22 \pm 0.28 \pm 0.04$	4.20	58.1 ± 3.9	57.8
207	72.0	$3.98 \pm 0.21 \pm 0.04$	4.16	55.0 ± 2.9	57.5
208	71.8	$4.19 \pm 0.83 \pm 0.04$	4.13	58.1 ± 11.5	57.2

Table 7.1: Selection efficiency, measured and expected cross sections as a function of $\sqrt{s}$ for the $e^+e^- \to \nu\bar{\nu}\gamma(\gamma)$ process in the phase space region defined in the text. The first uncertainty on $\sigma^{meas}_{\nu\bar{\nu}\gamma}$ is statistical, the second systematic. The statistical uncertainty on the selection efficiency is 0.2% for each value of $\sqrt{s}$. The theoretical uncertainty on $\sigma^{exp}_{\nu\bar{\nu}\gamma}$ is 1% [24]. The last two columns give the measured and expected values of the extrapolated cross section for the $e^+e^- \to \nu\bar{\nu}(\gamma)$ process, where the error on $\sigma^{meas}_{\nu\bar{\nu}}$ is the quadratic sum of the statistical and systematic uncertainties.

the ratios of the measured and predicted cross sections at each center-of-mass energy as shown in Figure 7.1b. Averaging over the eight measurements yielded

$$R = \left\langle \frac{\sigma^{meas}_{\nu\bar{\nu}\gamma}}{\sigma^{exp}_{\nu\bar{\nu}\gamma}} \right\rangle = 0.987 \pm 0.022\,(stat) \pm 0.010\,(syst) \pm 0.010\,(theory)\,,$$

showing a good agreement between the data and the Standard Model predictions. This result also showed that while the total error was dominated by the statistical errors, the systematic and theoretical uncertainties could not be neglected. The total systematic uncertainty on the measured cross sections was estimated to be 1.1% for each value of $\sqrt{s}$ and was assumed to be almost fully correlated between all measurements. The sources of systematic errors will be described at the end of this section. The theoretical uncertainty on the predicted cross section was estimated to be 1% [24] as discussed in Section 2.2.3.

The measured $e^+e^- \to \nu\bar{\nu}\gamma(\gamma)$ cross section can then be extrapolated to the total

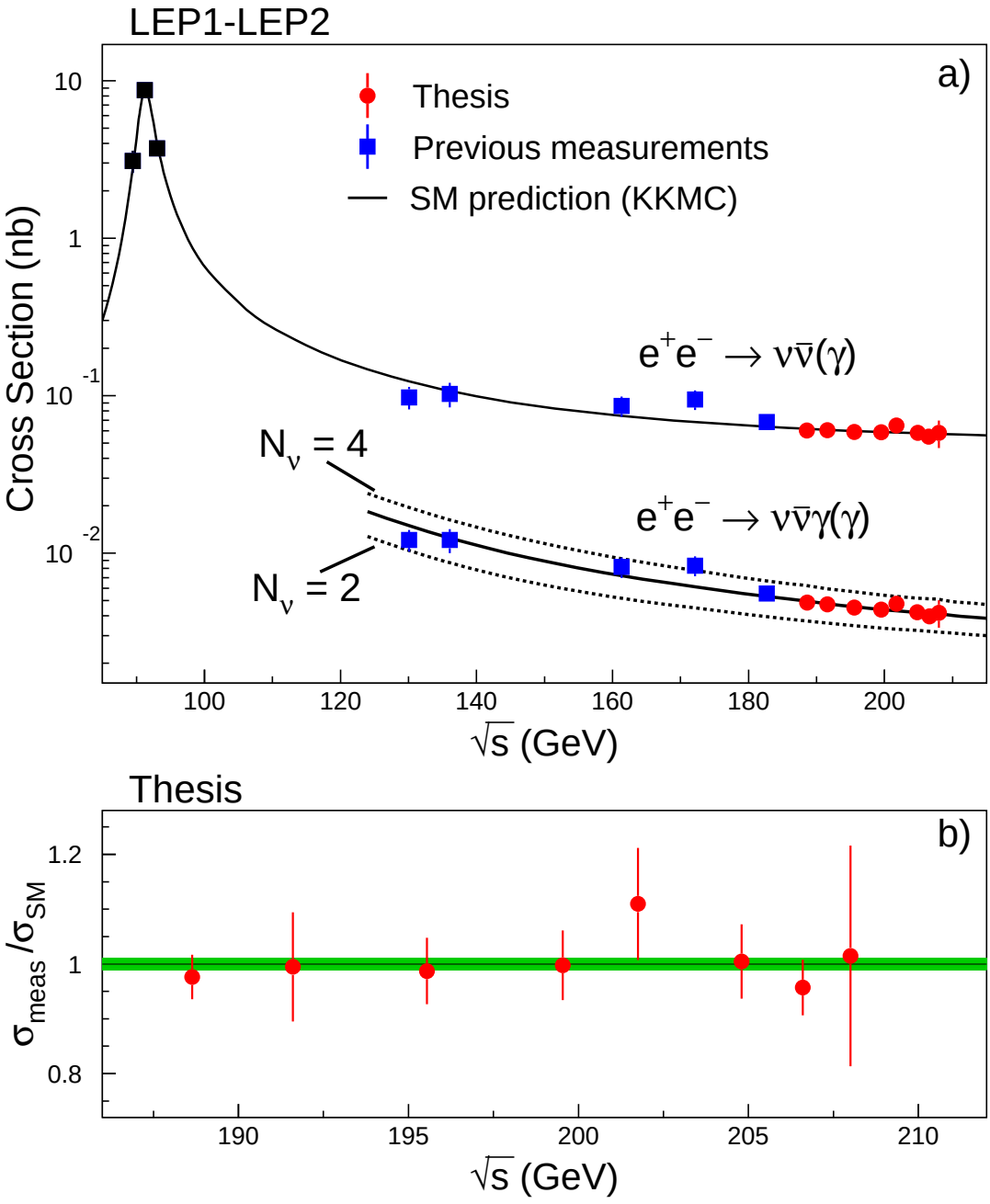

Figure 7.1: a) Cross sections of the $e^+e^- \to \nu\bar{\nu}(\gamma)$ and $e^+e^- \to \nu\bar{\nu}\gamma(\gamma)$ processes as a function of $\sqrt{s}$. The cross section of the latter process refers to the kinematic region defined in the text. The full line represents the theoretical prediction (KKMC) for $N_\nu = 3$ and the dashed lines are predictions for $N_\nu = 2$ and 4, as indicated. b) The ratio of the measured and the Standard Model predicted cross sections as a function of $\sqrt{s}$, where the error bars are the combined statistical and systematic uncertainties. The shaded region represents the theoretical uncertainty of 1% [24].

cross section of the neutrino pair-production process:

$$\sigma_{\nu\bar{\nu}}^{meas} = \sigma_{\nu\bar{\nu}\gamma}^{meas} \cdot \frac{\sigma_{\nu\bar{\nu}}^{exp}}{\sigma_{\nu\bar{\nu}\gamma}^{exp}}, \tag{7.2}$$

where $\sigma_{\nu\bar{\nu}}^{exp}$ is the predicted cross section of the $e^+e^- \to \nu\bar{\nu}(\gamma)$ process, obtained using the KKMC program. The results of this extrapolation are also listed in Table 7.1 and shown as a function of $\sqrt{s}$ in Figure 7.1a, which also shows results from previous measurements at LEP1 [179][3] and at the beginning of LEP2 [178].

Systematic Errors

The term *systematic error* is generally taken as signifying any error not due to statistical fluctuations in the data sample under study [180]. Therefore, the relative statistical and systematic errors on the measured $e^+e^- \to \nu\bar{\nu}\gamma(\gamma)$ cross section (see Equation 7.1) can be parametrized as

$$\frac{\delta_{stat}}{\sigma_{\nu\bar{\nu}\gamma}^{meas}} = \frac{\sqrt{N_{data}}}{N_{data} - N_{bg}} \tag{7.3}$$

$$\frac{\delta_{syst}}{\sigma_{\nu\bar{\nu}\gamma}^{meas}} = \sqrt{\left(\frac{\delta\varepsilon}{\varepsilon}\right)^2 + \left(\frac{\delta\mathcal{L}}{\mathcal{L}}\right)^2 + \left(\frac{\delta N_{bg}}{N_{data} - N_{bg}}\right)^2}, \tag{7.4}$$

where the three terms arise from systematic errors on the selection efficiency $\delta\varepsilon$, the integrated luminosity $\delta\mathcal{L}$, and the background contamination δN_{bg}. Below I provide a detailed description of the main sources of these systematic errors.

Trigger efficiency: In Section 6.3.2 I determined the BGO trigger efficiency using a sample of single-electron events from the radiative Bhabha scattering process, $e^+e^- \to e^+e^-\gamma(\gamma)$. The corresponding error on the selection efficiency was then estimated to be $(\delta\varepsilon/\varepsilon)_{trig} = 0.6\%$, mainly due to the limited statistics of the single-electron sample. This estimate was further confirmed by an independent measurement of the trigger efficiency that I performed using back-to-back Bhabha events.

[3] The LEP1 measurements were performed using 100 pb^{-1} of data collected during 1991-1994 at $\sqrt{s} = 89.5 - 93.8$ GeV.

Photon conversion: In Section 6.3.4 I measured the rate of photon conversion in the dead material in front of the central tracker using samples of events from the $e^+e^- \to \gamma\gamma$ (barrel) and $e^+e^- \to \nu\bar{\nu}\gamma$ (endcaps) processes. The precision of this measurement was limited by statistics of these control samples, and the resulting error on the selection efficiency was then estimated to be $(\delta\varepsilon/\varepsilon)_{conv} = 0.5\%$. This estimate was found to be consistent with previous studies of this effect [120, 175].

Monte Carlo modelling: To estimate the systematic uncertainty due to modelling of the $e^+e^- \to \nu\bar{\nu}\gamma(\gamma)$ process, I determined the efficiency of my event selection using two independent Monte Carlo programs, `KKMC` and `NUNUGPV`. As discussed in Appendix A, these programs employ different algorithms to simulate higher-order QED corrections. In particular, the `KKMC` generator predicts a higher probability for the emission of additional ISR photons with finite, detectable transverse momentum. Since I rejected events with significant energy depositions in the forward calorimeters (see Section 6.3.3), the average selection efficiency was found to be slightly lower for `KKMC` than for `NUNUGPV`: $<\varepsilon>_{\texttt{kkmc}} = 72.54 \pm 0.09\%$ and $<\varepsilon>_{\texttt{nunugpv}} = 72.91 \pm 0.07\%$. I take the obtained relative difference in efficiency as the systematic uncertainty due to Monte Carlo modelling: $(\delta\varepsilon/\varepsilon)_{MC} = 0.5\%$. This estimate was found to be consistent with results of a similar study performed by the OPAL collaboration [181].

Monte Carlo statistics: The statistical error on the selection efficiency can be calculated as $\Delta\varepsilon = \sqrt{\varepsilon(1-\varepsilon)/N_{gen}}$, where N_{gen} is the number of Monte Carlo events generated within the kinematic region of my single- and multi-photon selection. The corresponding systematic uncertainty was then determined to be $(\delta\varepsilon/\varepsilon)^{MC}_{stat} = 0.3\%$. It should be noted that this uncertainty was uncorrelated between the eight data sets.

Shower-shape selection: The photon candidates were required to pass a set of cuts based on the shower profile measured in the BGO calorimeter. The performance of this shower-shape selection was studied in Section 6.3.1 using large samples of single-electron and back-to-back Bhabha events and cross checked using a control sample of di-photon events, $e^+e^- \to \gamma\gamma(\gamma)$. By comparing the efficiencies obtained with these independent samples and by varying the shower-shape cuts around the nominal values, I estimated the associated systematic uncertainty to be $(\delta\varepsilon/\varepsilon)_{shape} =$

0.3%. This estimate was also confirmed by a previous study of a similar shower-shape selection [58].

Background level: The background contamination from other Standard Model processes was dominated by the radiative Bhabha events. Such events were eliminated using a set of veto cuts on activity in the forward calorimeters. As described in Section 6.3.3, the veto efficiency was studied using a control sample of single-electron events and was found to be in good agreement with predictions of the detector simulation. The statistical precision of this measurement was then translated into an error on the number of expected background events, $\delta N_{bg} = 3$ events. Additional contributions came from the theoretical uncertainty on the $e^+e^- \to e^+e^-\gamma(\gamma)$ cross section (5% for the `TEEGG` generator [168]) and from uncertainties due to limited Monte Carlo statistics. Combining the above error sources, I estimated that the uncertainty on the level of background contributed about 0.2% to the total systematic error on the measured cross sections.

Luminosity: The systematic error on the integrated luminosity was estimated to be about $\delta\mathcal{L}/\mathcal{L} = 0.2\%$ [182]. It was dominated by the theoretical uncertainty on the accepted Bhabha cross section, by the uncertainty due to the selection procedure, and by the geometrical uncertainties in the position and alignment of the luminosity detectors (see Section 4.2.8). Therefore, the systematic error on the integrated luminosity was treated as common to all eight data sets that I used in my measurements [182].

Calorimeter geometry: An incorrect description of the geometry of the BGO calorimeter might lead to a systematic mismeasurement of the polar angle of the photon, which in turn might affect the cross section measurement. The difference of the definition of the polar angle between data and Monte Carlo was found to be less than 0.1° [183], translating to a systematic error of 0.2% on my cross section measurements.

Calorimeter calibration: As I described in Chapter 5, the BGO calorimeter was accurately calibrated using the RFQ calibration system. The BGO energy resolution was determined with a relative precision of about 15% (see Section 5.6.3). The error on

the BGO energy scale was estimated by comparing the reconstructed masses of the π^0 and η mesons with their nominal values (see Figure 5.21) and by studying the effects of the BGO aging and non-linearity (see Appendix C). The resulting uncertainty on the photon energy scale was found to be less than 0.5%. I then varied the BGO energy scale and resolution within their errors during the detector simulation and assigned the observed shift in the selection efficiency to the systematic error due to the calorimeter calibration: $(\delta\varepsilon/\varepsilon)_{calib} = 0.1\%$.

Cosmic contamination: As described in Section 6.3.5, the cosmic ray background was studied using a control sample of out-of-time cosmic events and was expected to contribute only about 3 ± 1 events to the selected single- and multi-photon sample. I also took into account the uncertainty on the efficiency of the L3 scintillator system which was measured to a precision of about 0.05% using control samples of Bhabha and di-photon events. Combining these two error sources gave an additional systematic error of about 0.1% on the cross section measurement.

Detector noise: The noise in various subdetectors was studied using events randomly triggered at the beam crossing time (see Section 6.3.7). The resulting efficiency loss was estimated to be about 1.9%, and the Monte Carlo predictions were scaled accordingly. The statistical error on this correction factor (see Table 6.4) directly translated into a systematic error on the selection efficiency, $(\delta\varepsilon/\varepsilon)_{noise} = 0.1\%$.

The systematic errors on the measured cross sections are summarized in Table 7.2. Adding all contributions in quadrature, I obtained a total systematic error of 1.1%. As I discussed in Section 6.1, the same Monte Carlo models and calibration procedures were used throughout my analysis. Therefore, I assumed all systematic uncertainties, except that from Monte Carlo statistics, to be fully correlated when combining results obtained at different center-of-mass energies.

Source	Uncertainty (%)
Trigger efficiency	0.6
Photon conversion	0.5
Monte Carlo modelling	0.5
Monte Carlo statistics	0.3
Shower-shape selection	0.3
Background level	0.2
Luminosity	0.2
Calorimeter geometry	0.2
Calorimeter calibration	0.1
Cosmic contamination	0.1
Detector noise	0.1
Total	1.1

Table 7.2: Summary of the systematic uncertainties on the measurement of the $e^+e^- \to \nu\bar{\nu}\gamma(\gamma)$ cross section, itemized by the source of uncertainty.

7.1.2 Determination of the Number of Light Neutrino Species

In the Standard Model of the electroweak interactions, the reaction $e^+e^- \to \nu\bar{\nu}\gamma(\gamma)$ proceeds through s-channel Z exchange for all neutrino flavors ($\nu_l = \nu_e, \nu_\mu, \nu_\tau$) and through t-channel W exchange for electron neutrinos only.[4] As a consequence, the cross section of this process depends linearly on the number of light neutrino species N_ν and can be written as

$$\sigma_{\nu\bar{\nu}\gamma} = N_\nu \cdot \sigma_Z + \sigma_{WZ} + \sigma_W \,, \tag{7.5}$$

where σ_Z, σ_{WZ}, and σ_W denote the contributions from the s-channel Z production, the W$-$Z interference, and the t-channel W exchange, respectively.

Figure 7.2 compares the recoil mass spectrum ($M_{\rm rec}$) of the combined single- and multi-photon event sample to the expectations for $N_\nu = 2, 3$, and 4. The data clearly preferred the Standard Model value of $N_\nu = 3$. In order to quantify this agreement,

[4] The production mechanisms of this process as well as the expected cross sections and kinematic distributions have been examined in detail in Section 2.2 of Chapter 2 and in Appendix A.

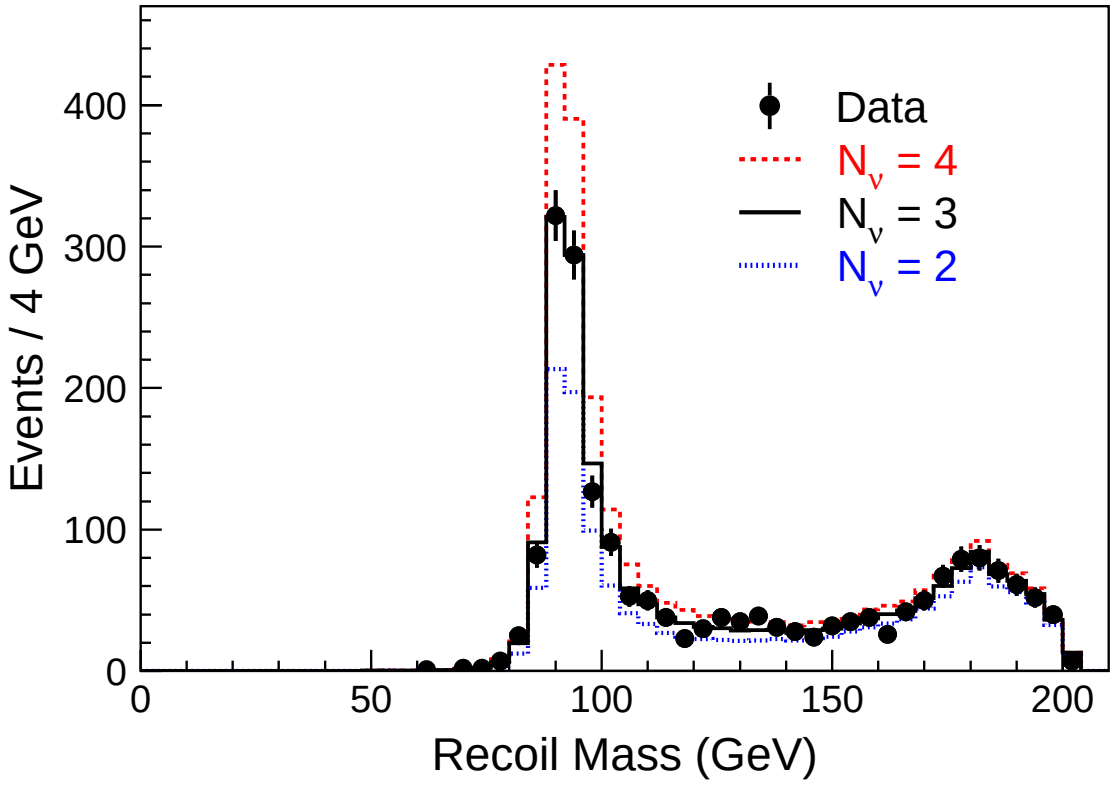

Figure 7.2: Recoil mass spectrum of the combined single- and multi-photon event sample, compared to the expected spectra for $N_\nu = 2, 3$ and 4.

I performed a binned fit to the two dimensional distribution of $M_{\rm rec}$ *vs.* $|\cos\theta_\gamma|$ of the selected $\nu\bar{\nu}\gamma(\gamma)$ events. Due to the different contributions from the t-channel $\nu_{\rm e}\bar{\nu}_{\rm e}\gamma$ production and the s-channel $\nu\bar{\nu}\gamma$ production, this method was more powerful than using the total cross section measurement. As shown in Figures 2.7c,d (p. 21), the s-channel Z exchange was expected to produce predominantly events in the region of the Z-return peak ($M_{\rm rec} \simeq M_Z$), whereas the W-related contributions dominated in the region of high recoil masses ($M_{\rm rec} \gtrsim 140$ GeV).

To determine the number of light neutrino species, I used the *method of maximum likelihood*. In the general case of binned data, the log-likelihood function is defined as [184]

$$\ln L = \sum_{m=1}^{N} k_m \ln \mu_m(\boldsymbol{\theta}) - \mu_{\rm m}(\boldsymbol{\theta}) \,, \tag{7.6}$$

where N is the total number of bins, k_m is the number of events observed in bin m,

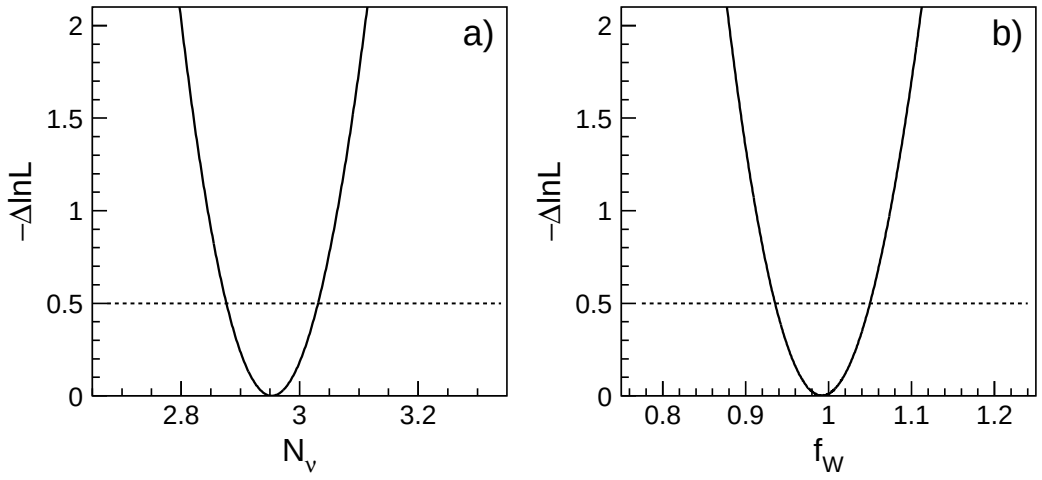

Figure 7.3: The negative log-likelihood functions of the fits for a) N_ν and b) $f_{\rm W}$. The $f_{\rm W}$ measurement is described at the end of this section (p. 202).

$\mu_m(\boldsymbol{\theta})$ is the corresponding number of expected events, and $\boldsymbol{\theta}$ is the set of parameters which are allowed to vary in the fit. In this particular case, $\boldsymbol{\theta} = \{N_\nu\}$ and the expected number of events μ_m depended on N_ν according to Equation 7.5.

The number of light neutrino species was then determined by maximizing the log-likelihood function. As shown in Figure 7.3a, the obtained log-likelihood function was parabolic and the standard-deviation statistical error (δN_ν) was estimated by solving numerically the following equation:

$$\ln L(\hat{N}_\nu \pm \delta N_\nu) = \ln L(\hat{N}_\nu) - \frac{1}{2}\,, \tag{7.7}$$

where $\hat{N}_\nu$ denotes the fitted value of N_ν. The result of this maximum likelihood fit was

$$N_\nu = 2.95 \pm 0.08\,(stat) \pm 0.03\,(syst) \pm 0.03\,(theory)\,.$$

The systematic error was estimated by evaluating the shifts in the fitted value of N_ν associated with different sources of systematic uncertainties,[5] where the considered systematic effects were the same as for the cross section measurement (see Table 7.2).

[5]This method will be described in more detail in Section 7.4, where it will be used to estimate systematic errors in my measurements of gauge-boson couplings. It should be noted that this method was adopted by the W-physics group of L3 [185].

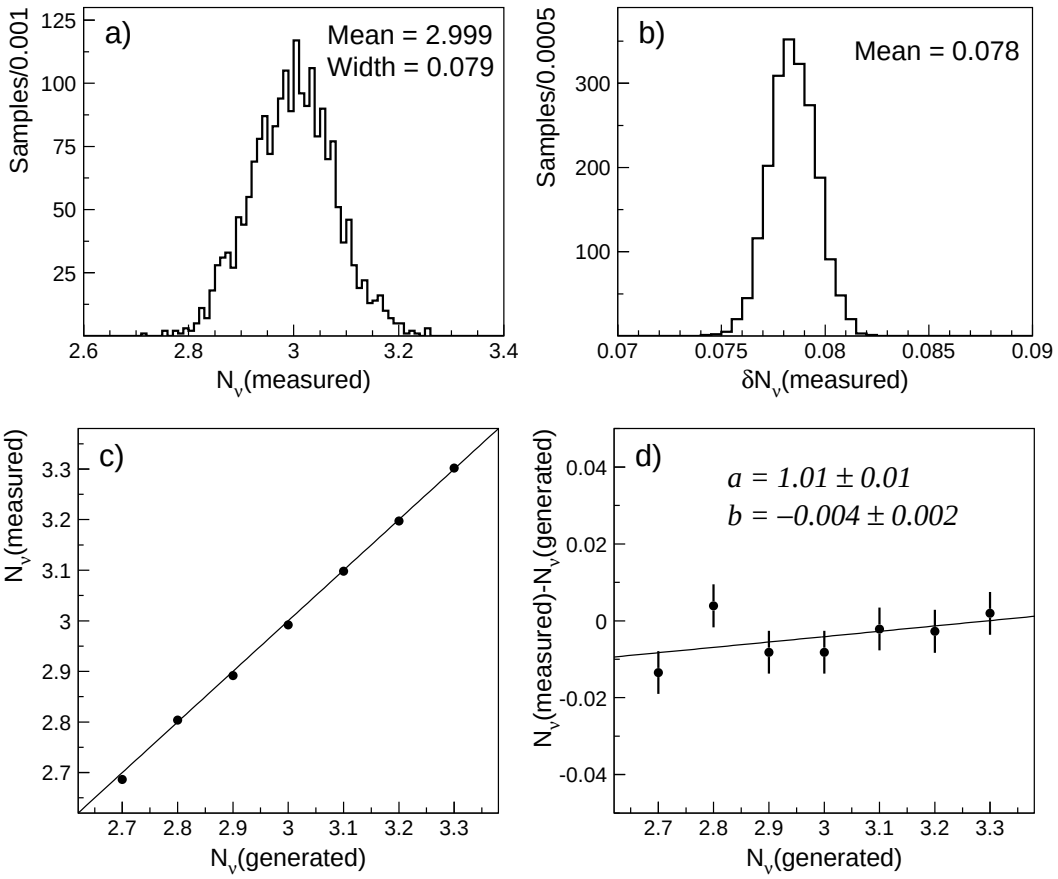

Figure 7.4: Distributions of a) the fitted values of N_ν and b) fit errors for small Monte Carlo samples corresponding to $N_\nu = 3$. The statistical parameters of interest are indicated on the plots. Results of the fit bias tests: c) the average fitted value of N_ν for small Monte Carlo samples with different N_ν, and d) the corresponding $N_\nu^{fit} - N_\nu^{gen}$ distribution. The statistical uncertainties on the averages and the results of the linear regression are also given.

The last uncertainty includes the theoretical uncertainty on the expected cross section [24] as well as an additional uncertainty on the shape of the recoil mass spectrum, estimated by comparing `KKMC` with `NUNUGPV`.

The performance of the fitting procedure was investigated with the standard Monte Carlo methods [184, 185]. First, I constructed small Monte Carlo samples by randomly combining Monte Carlo events in numbers given by the Poisson distribution around the expected number of events for a given value of N_ν. The reliability of the statistical error was then tested by fitting two thousand small Monte Carlo

samples with the Standard Model value $N_\nu = 3$. The RMS width of the distribution of the fitted central values agreed well with the mean of the distribution of the fit uncertainties (see Figures 7.4a,b).

In order to check for any bias, I used Monte Carlo samples constructed for several different values of N_ν. The average fitted values (N_ν^{fit}) were compared to the "true" generated values (N_ν^{gen}), as shown in Figures 7.4c,d. This comparison was parameterized by a fit

$$(N_\nu^{fit} - 3) = a \cdot (N_\nu^{gen} - 3) + b\,, \tag{7.8}$$

which gave a linearity coefficient $a = 1.01 \pm 0.01$ compatible with 1 and a negligible bias $b = -0.004 \pm 0.002$. In addition, the fitting procedure was found to be stable with respect to changes in the bin size. Since the observed systematic effects were negligible compared to the total systematic error, no additional systematic errors were assigned as a result of these cross checks.

Combination with Previous Measurements

This result can be combined with measurements of the $e^+e^- \to \nu\bar{\nu}\gamma(\gamma)$ process performed at the beginning of LEP2 and at LEP1. Using single- and multi-photon events selected in the data collected by L3 during 1995-97 at $\sqrt{s} = 130 - 183$ GeV, I obtained[6] $N_\nu = 3.23 \pm 0.18\,(stat) \pm 0.06\,(syst)$.

The LEP1 measurement [173, 179] was performed with a sample of 2,091 single-photon candidates selected in 100 pb^{-1} of data collected from 1991 to 1994 at energies near the Z resonance, $\sqrt{s} = 89.5 - 93.8$ GeV. Since the reaction $e^+e^- \to \nu\bar{\nu}\gamma(\gamma)$ proceeded almost exclusively through s-channel Z exchange, the resulting photon energy spectrum was quite soft, $E_\gamma \simeq$ 1-4 GeV. The number of light neutrino species was then determined by fitting the total production cross section, measured as a function of $\sqrt{s}$. The fit result was $N_\nu = 2.98 \pm 0.07\,(stat) \pm 0.07\,(syst)$ [179]. As described in Chapter 4, the L3 detector was significantly upgraded at the end of the LEP1 program. In particular, the installation of the RFQ accelerator allowed me to

[6] The analysis of the $\sqrt{s} = 130 - 183$ GeV data was described in footnote 2 on page 190.

significantly improve the quality of the calorimeter calibration (see Chapter 5), which was one of the dominant sources of systematic uncertainty at LEP1.

To combine the above results with my measurement of N_ν, I used the BLUE[7] method [186] which allowed me to take into account correlations between the systematic uncertainties of these measurements.[8] The combination gave

$$N_\nu = 2.98 \pm 0.05\,(stat) \pm 0.04\,(syst)\,,$$

where the theoretical uncertainties were included in the total systematic error. This result is in agreement with the Standard Model prediction of $N_\nu = 3$ and is more precise than the present world average of measurements obtained by studying the reaction $e^+e^- \to \nu\bar{\nu}\gamma(\gamma)$ [6]. It also agrees with the indirect measurement of invisible Z width at LEP1 ($N_\nu = 2.978 \pm 0.014$ [183]), while being sensitive to different systematic and theoretical uncertainties [179].

Study of the $e^+e^- \to \nu_e\bar{\nu}_e\gamma(\gamma)$ Process

The selected sample of single- and multi-photon events could also be used to measure the size of the t-channel W exchange contributions in the reaction $e^+e^- \to \nu_e\bar{\nu}_e\gamma(\gamma)$. These contributions were parameterized by a multiplicative scale factor f_W, defined to be 1 for the Standard Model expectation. The number of neutrino species was assumed to be equal to 3, as indicated by the above measurement. The cross section of the single- and multi-photon production process could then be written as

$$\sigma_{\nu\bar{\nu}\gamma} = 3 \cdot \sigma_Z + f_W \cdot (\sigma_{WZ} + \sigma_W)\,, \tag{7.9}$$

[7] The BLUE (Best Linear Unbiased Estimate) method is widely used in high-energy physics for combining correlated measurements such as W mass measurements at LEP [10] and Tevatron [187].

[8] Since the LEP1 and LEP2 measurements used different theoretical calculations and Monte Carlo generators, their theoretical uncertainties were assumed to be uncorrelated. The experimental systematic errors in both measurements were mainly due to limited statistics of various control samples. In addition, the LEP1 analysis considered only photons in the BGO barrel, whereas about half of the photon candidates used in the LEP2 analyses were in the BGO endcaps. As a consequence, the experimental systematic errors of the LEP1 and LEP2 measurements were also largely uncorrelated. The main sources of correlated systematic errors were: the integrated luminosity measurement, the description of the calorimeter geometry, and the simulation of the single-photon trigger near the threshold. On the contrary, the LEP2 measurements obtained with the $130 - 183$ GeV and $189 - 208$ GeV data were strongly correlated because they were performed using the same Monte Carlo programs and the same corrections for photon conversion effects.

with σ_Z, σ_{WZ}, and σ_W denoting the Standard Model predictions for the contributions from the s-channel Z production, the W$-$Z interference, and the t-channel W exchange,[9] respectively.

To measure the scale factor f_W, I used the same kinematic distribution and fitting procedure as for the N_ν measurement. However, in this case the contributions from the s-channel Z exchange constituted an important source of irreducible background. As a consequence, the f_W measurement mainly probed the recoil mass region above the Z-return peak, $M_{\rm rec} \gtrsim 140$ GeV (see Figures 2.7c,d p. 21). The result of the binned maximum likelihood fit was

$$f_W = 0.99 \pm 0.06\,(stat) \pm 0.02\,(syst) \pm 0.02\,(theory)\,,$$

in good agreement with the Standard Model value $f_W = 1$. The obtained log-likelihood curve is shown in Figure 7.3b (p. 199). Contrary to the LEP1 measurement of $f_W = 0.2 \pm 0.6 \pm 0.4$ [173], this result clearly established that the W-contributions were observed and were consistent with the expectations from the Standard Model.

7.2 Searches for SUSY Signatures

Supersymmetry (SUSY) constitutes one of the most interesting and promising extensions of the Standard Model. The main aspects of this theory have been discussed in Chapter 3. Especially interesting are SUSY scenarios leading to production of neutralinos and gravitinos in e^+e^- collisions at LEP, as such processes can be detected by analyzing the selected samples of single- and multi-photon events. In this section I present the results of my searches for such SUSY signatures. The corresponding signal topologies and search strategies have been described in Section 3.2 of Chapter 3, to which I will frequently refer in the following discussion.

The kinematic cuts of both the single- and multi-photon selections were sufficiently loose so that no further optimization was found to be necessary. However, I developed

[9] These predictions were obtained using the KKMC generator, assuming Standard Model couplings of electrons and neutrinos. At LEP2 energies, the W-related contributions were expected to be dominated by the W amplitude squared: $\sigma_{WZ}/\sigma_W \simeq 0.3$.

a special selection to search for events with photons not originating from the beam vertex, the "non-pointing" photons. In all cases the dominant background came from the Standard Model process $e^+e^- \to \nu\bar{\nu}\gamma(\gamma)$, which has been studied in the beginning of this chapter.

The selection efficiency for the signal was estimated using large samples of Monte Carlo events simulated using the SUSYGEN Monte Carlo generator [66]. The signal efficiency was defined as the number of selected signal events divided by the the total number of generated events. For each signal mass point about 5,000 MC events were produced. Unless otherwise stated, no phase space cuts were applied during the generation of signal Monte Carlo samples. All generated events were passed through the L3 detector simulation program as described in Section 4.2.10 of Chapter 4.

The rest of this section is organized as follows. In the next section, I describe the statistical procedure that I used to quantify the results of my searches. Single-photon and multi-photon signatures are investigated in Sections 7.2.2 and 7.2.3, respectively. Section 7.2.4 is devoted to searches for events with non-pointing photons.

7.2.1 Calculating Limits on New Physics

The observed event rates and kinematic distributions were found to be in good agreement with the Standard Model expectations (see Sections 6.3.8 and 6.4). In the absence of a clear evidence for the signal, the goal of a search is to place the most stringent possible limits on the signal cross section which can then be used to constrain the parameters of the underlying theory. Below I describe the statistical procedure that I used for calculating such limits on new physics.

The first step of this procedure consists of constructing the likelihood as a function of the number of expected signal events. To determine the likelihood function, one needs to choose a distribution discriminating the new physics signal from the Standard Model background. For searches in the single-photon channel, I used the two dimensional distribution $M_{\rm rec}$ *vs.* $|\cos\theta_\gamma|$ which fully described the kinematics of the selected single-photon events. In the multi-photon channel, I used the distribution of

the final discriminant variable computed from the reconstructed recoil mass and the measured photon energies and polar angles as described in Section 7.2.3.

The likelihood function is defined as a product of Poisson probabilities of observing n_i data events in bin i of the discriminating distribution:

$$\mathcal{L}(s) \;=\; \prod_{i=1}^{n_{bin}} \frac{\mathrm{e}^{-(s_i+b_i)}(s_i+b_i)^{n_i}}{n_i!}\,, \tag{7.10}$$

where n_{bin} is the total number of bins, s_i and b_i are the numbers of expected signal and background events, respectively, and $s = \sum_i s_i$ is the total number of expected signal events. Since the signal cross section usually increases with the center-of-mass energy, the likelihood functions are computed separately for each $\sqrt{s}$. The combined likelihood function is then obtained by multiplying together the individual likelihoods:

$$\mathcal{L}(s) \;=\; \prod_{k=1}^{n_{sample}} \mathcal{L}(s_k)\,, \tag{7.11}$$

where $n_{sample} = 8$ is the number of energy points considered in my analysis (see Table 6.1 p. 132) and $s = \sum_k s_k$ is the total expected signal. The likelihood method uses information from both the total event rate and the shape of the discriminating distribution. Thus, no further optimization of the event selection is necessary, in contrast to the event-counting method where further cuts on the discriminating variables are typically required to improve the sensitivity of the search.

The next step of the statistical procedure consists of constructing the estimator *(test-statistic)* which can be used to evaluate the compatibility of the data with the predicted signal. There exist several choices of test-statistic. I used the test-static given by the normalized integral of the likelihood function [188]:[10]

$$X(s) \;=\; \frac{\int_s^\infty \mathcal{L}(x)dx}{\int_0^\infty \mathcal{L}(x)dx}\,, \tag{7.12}$$

[10]In L3, this test-statistic has been used to set limits on the mass of the Standard Model Higgs boson [189]. Another popular choice is the likelihood ratio $X(s) = \mathcal{L}(s)/\mathcal{L}(0)$, which has been adopted for the combination of LEP results on searches for Higgs bosons [11]. Extensive studies have shown that these two estimators provide similar sensitivity to signal [190]. As a cross check, I repeated my analysis using the likelihood-ratio method and found no noticeable changes in the observed or expected limits on new physics.

which can be interpreted as the Bayesian confidence level assuming a uniform prior distribution. A high value of $X(s)$ indicates that the observed data agrees better with the signal+background hypothesis, while a low value favors the background-only hypothesis. This property of the test-statistic is then used to derive limits on the signal cross section.

First, the value of test-statistic $X_{\rm obs}$, measured in data, is compared to the test-statistic distribution obtained from a large number of reference Monte Carlo samples ($N_{\rm MC}$). Each Monte Carlo sample corresponds to a possible outcome of a real experiment in the presence of both the signal and the background. The fraction of outcomes with the test statistic value less than that of the data ($X_{s+b} < X_{\rm obs}$) gives the confidence level for the signal+background hypothesis:

$$\mathrm{CL}_{s+b}(s) \;=\; \frac{N_{X_{s+b}<X_{\rm obs}}}{N_{\rm MC}}\,. \tag{7.13}$$

Similarly, the confidence level for the background-only hypothesis $\mathrm{CL}_b(s)$ is computed using Monte Carlo experiments generated assuming the absence of a signal.

The frequentist exclusion limit is usually computed from the confidence $\mathrm{CL}_{s+b}(s)$. The signal hypothesis is considered to be excluded at the 95% confidence level if an observation is made such that $\mathrm{CL}_{s+b}(s)$ is less than 0.05. However, this procedure may lead to the following undesired possibility: a large downward fluctuation in data would allow to exclude hypotheses for which the experiment should have no sensitivity. This problem can be avoided by introducing the ratio $\mathrm{CL}_s = \mathrm{CL}_{s+b}/\mathrm{CL}_b$ [191]. The signal hypothesis is considered to be excluded at the 95% confidence level (C.L.) if the corresponding confidence CL_s satisfies

$$1 - \mathrm{CL}_s(s) \geq 0.95\,. \tag{7.14}$$

The 95% C.L. upper limit on the total number of signal events is then derived by finding the minimum value of s which still satisfies the above condition.

As mentioned above, the L3 data used in my searches for new physics were

recorded at eight different center-of-mass energies ranging from 189 GeV to 208 GeV. Therefore, the upper limit on the signal cross section at a reference center-of-mass energy ($\sqrt{s_0}$) can be calculated as

$$\sigma_s^{95}(\sqrt{s_0}) = \frac{s_{95}}{\sum_{k=1}^{8} \mathcal{L}_k \, \varepsilon_k \, \frac{\sigma_s(\sqrt{s_k})}{\sigma_s(\sqrt{s_0})}} , \tag{7.15}$$

where s_{95} is the 95% C.L. upper limit on the total number of signal events and $\sigma_s(\sqrt{s})$ is the signal cross section as a function of $\sqrt{s}$. The summation is performed over the eight energy points $\sqrt{s_k}$ with $\mathcal{L}_k$ and ε_k being the integrated luminosity and the selection efficiency for signal events, respectively. The reference energy point is chosen to be $\sqrt{s_0} = 207$ GeV, which approximately corresponds to the highest center-of-mass energy reached at LEP.

Systematic errors on the signal and background expectations can be conveniently taken into account during the generation of Monte Carlo experiments [191]. In each trial experiment, candidates are generated according to the signal and background distributions which are smeared to account for systematic errors on the selection efficiency, integrated luminosity, and predicted cross sections of the background processes. The smearing is performed using a set of Gaussian distributions with standard deviations equal to the individual systematic uncertainties [191]. In my analysis, the relative systematic uncertainties were at a level of 1% (see Table 7.2), and their effects on the obtained limits were found to be negligible.[11]

The Monte Carlo method can also be used to estimate the exclusion power of a search. This is usually done by computing the expected upper limit on the signal cross section, defined as the median limit from an ensemble of the Monte Carlo experiments generated assuming the absence of a signal.

[11] As a cross check, I also evaluated the systematic effects using the method of Cousins and Highland [192]. The two estimates were found to agree with each other.

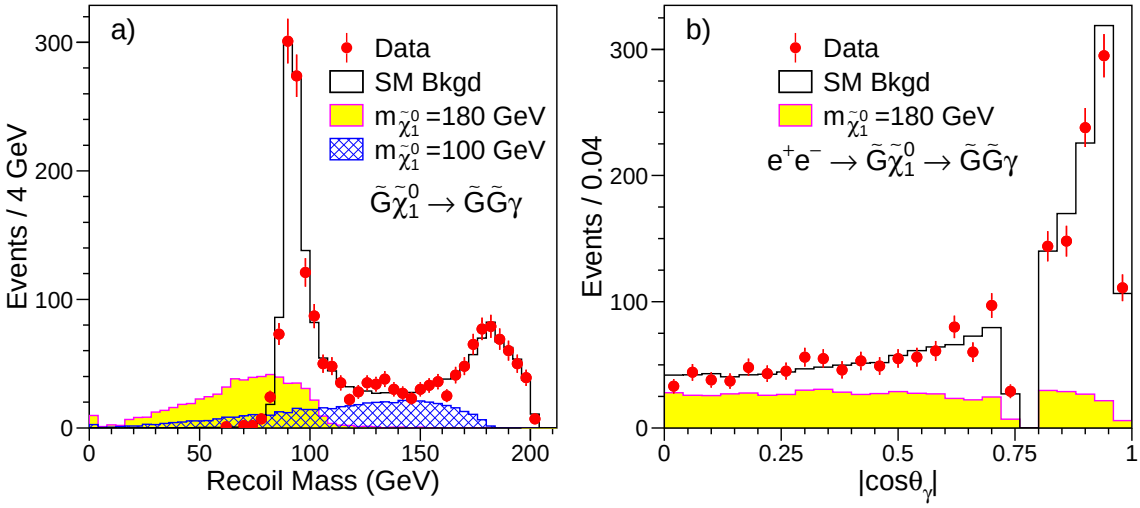

Figure 7.5: a) Recoil mass spectra and b) polar angle distributions of the fully simulated $e^+e^- \to \tilde{\chi}_1^0\tilde{G} \to \tilde{G}\tilde{G}\gamma$ Monte Carlo events that were accepted by the single-photon selection for the mass hypotheses $m_{\tilde{\chi}_1^0} = 100$ and 180 GeV. Also shown are the corresponding distributions for the data and background. The normalization for the signal Monte Carlo is arbitrary.

7.2.2 Single-Photon Signatures

$e^+e^- \to \tilde{\chi}_1^0\widetilde{G} \to \widetilde{G}\widetilde{G}\gamma$

As discussed in Section 3.2.4, in no-scale supergravity models the gravitino can become "superlight" (10^{-6} eV $\lesssim m_{\widetilde{G}} \lesssim 10^{-4}$ eV), leading to a sizable cross section for the reaction $e^+e^- \to \tilde{G}\tilde{\chi}_1^0$. Since the dominant decay mode is expected to be $\tilde{\chi}_1^0 \to \tilde{G}\gamma$, this process would lead to events with a single photon and missing energy in the final state.

Signal efficiencies for this process were found to range between 75% at the kinematic limit and 69% for $m_{\tilde{\chi}_1^0} = 5$ GeV. The kinematically allowed range of the photon recoil mass depends on the neutralino mass and is given by

$$0 < M_{\rm rec} < \sqrt{s - m_{\tilde{\chi}_1^0}}\,. \tag{7.16}$$

Figure 7.5a compares the recoil mass spectrum of the signal events accepted by the single-photon selection with those of the data and the Standard Model background.

Because the $\nu\bar{\nu}\gamma$ background peaked at $M_{\rm rec} \simeq M_Z$, the region of the highest sensitivity corresponded to $M_{\rm rec} \lesssim 80$ GeV. No excess over the Standard Model expectation was observed. In particular, in the region of interest, $M_{\rm rec} < 70$ GeV, 2 events were found in data with 3.8 ± 0.8 events expected from background. It should be noted that the RFQ calibration (see Chapter 5) played an important role in improving the sensitivity of this search. For comparison, with calibrations used during 1989-1996 the number of background events in the region $M_{\rm rec} < 70$ GeV would have been 3-4 times higher.

Figure 7.5b shows that the $|\cos\theta_\gamma|$ distribution of the signal events was almost flat. Therefore, this distribution could also be used to discriminate the signal from the $\nu\bar{\nu}\gamma$ background. To derive upper limits on the signal cross section, I performed a fit to the two-dimensional distribution $M_{\rm rec}$ *vs.* $|\cos\theta_\gamma|$. Figure 7.6a shows the observed and expected 95% C.L. limits derived at $\sqrt{s} = 207$ GeV. Data collected at lower $\sqrt{s}$ were included assuming the signal cross section to scale as β^8/s with $\beta = \sqrt{1 - m^2_{\tilde{\chi}^0_1}/s}$ [193].

In the LNZ model, there are only two free parameters – the gravitino and the neutralino masses (see Section 3.2.4). Thus, the obtained cross section limits could be translated into an excluded region in the $(m_{\tilde{\chi}^0_1}, m_{\tilde{\rm G}})$ mass plane as shown in Figure 7.6b. Gravitino masses below 10^{-5} eV were excluded for neutralino masses below 175 GeV.

$e^+e^- \to$ XY with X $\to$ Yγ

The selected single-photon events were also used to search for evidence of new physics processes of type $e^+e^- \to XY \to YY\gamma$, where X and Y were new neutral undetectable particles[12] and the $X \to Y\gamma$ decay was assumed to occur with a 100% branching ratio. For many SUSY processes, including the reaction $e^+e^- \to \tilde{\chi}^0_1\tilde{G} \to \tilde{G}\tilde{G}\gamma$ considered above and the reaction $e^+e^- \to \tilde{\chi}^0_2\tilde{\chi}^0_1 \to \tilde{\chi}^0_1\tilde{\chi}^0_1\gamma$ described in Section 3.2.3, the distributions for the production and decay angles were expected to be approximately

[12]Such searches are often called model-independent because no further assumptions on the nature of these new particles are made.

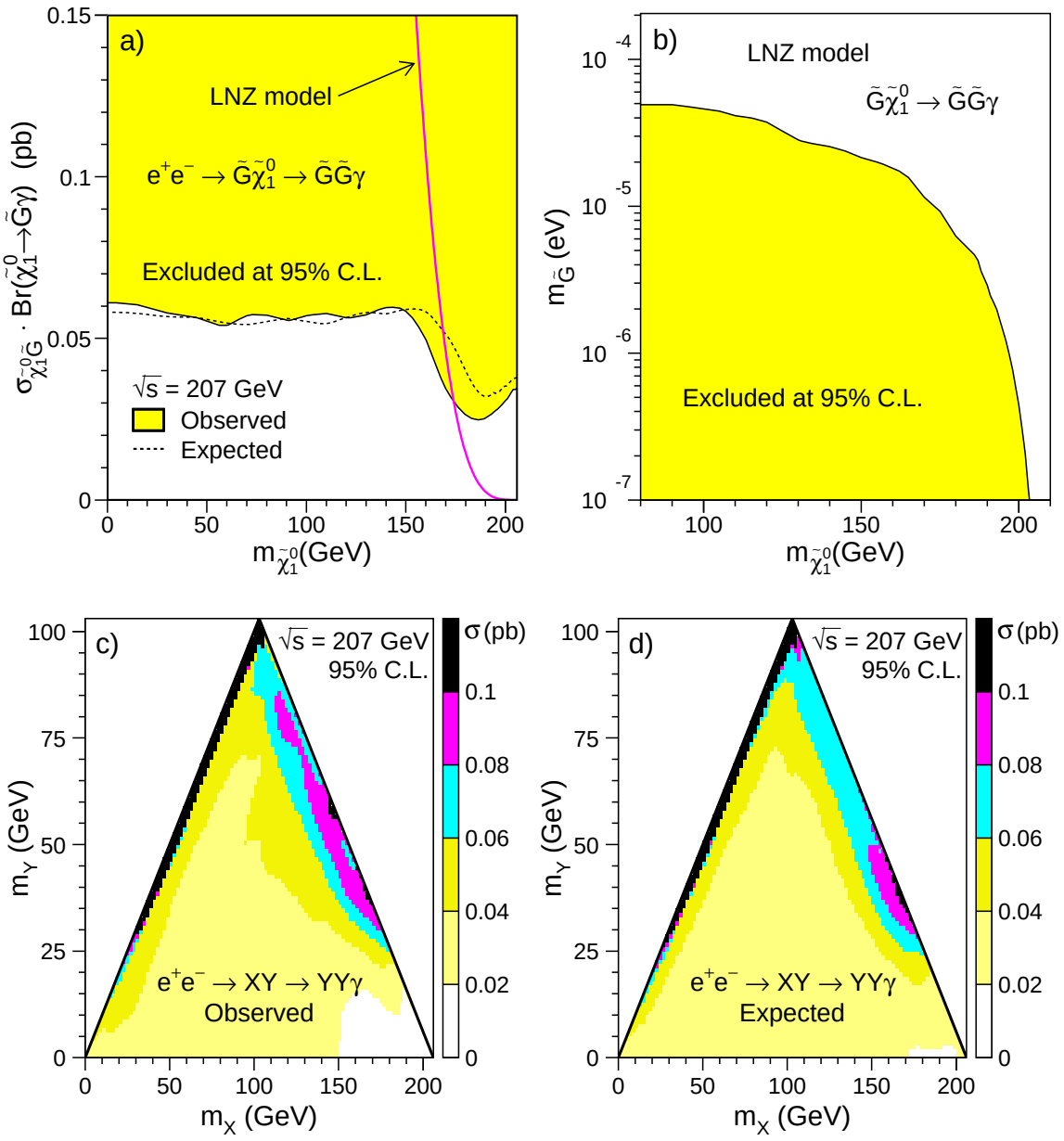

Figure 7.6: **a)** Observed and expected 95% confidence level upper limits on the production cross section of the reaction $e^+e^- \to \tilde{G}\tilde{\chi}_1^0 \to \tilde{G}\tilde{G}\gamma$. The cross section predicted by the LNZ model [193] for $m_{\tilde{G}} = 10^{-5}$ eV is also shown. Data collected at lower $\sqrt{s}$ were included assuming the signal cross section to scale as β^8/s. **b)** Region excluded for the LNZ model in the $(m_{\tilde{\chi}_1^0}, m_{\tilde{G}})$ mass plane. **c)** Observed and **d)** expected cross section upper limits from the search for a generic process $e^+e^- \to XY$ with $X \to Y\gamma$. The limits were obtained at the 95% C.L. for $\sqrt{s} = 207$ GeV. Data collected at lower $\sqrt{s}$ were included assuming the signal cross section to scale as β_0/s, where β_0 is defined in the text.

isotropic. I therefore also performed this search under the assumption of isotropically distributed production and decay angles. This resulted in a substantial increase in experimental sensitivity because not only the total number of observed events but also the angular and recoil mass distributions could be used to differentiate the signal from the $e^+e^- \to \nu\bar{\nu}\gamma$ background.

No significant deviation from the Standard Model expectations was observed, and cross section limits were derived for all allowed values of the masses m_X and m_Y in steps of 3 GeV. The limits were obtained at $\sqrt{s} = 207$ GeV, and data collected at lower $\sqrt{s}$ were included assuming the signal cross section to scale[13] as β_0/s, where $\beta_0 = \sqrt{1 - 2(x_1 + x_2) + (x_1 - x_2)^2}$ with $x_1 = m_X^2/s$ and $x_2 = m_Y^2/s$.

Figures 7.6c,d show that the obtained limits were in good agreement with the expectation. For most of the kinematically allowed values of m_X and m_Y, the obtained cross section limits were in the range of 0.02-0.05 pb.

Comparable cross section limits were also obtained for the special case of the reaction $e^+e^- \to \tilde{\chi}_2^0\tilde{\chi}_1^0 \to \tilde{\chi}_1^0\tilde{\chi}_1^0\gamma$. The LEP combined search for this process will be discussed in Appendix E.

$e^+e^- \to \widetilde{G}\widetilde{G}\gamma$

Models with superlight gravitinos may also lead to pair-production of gravitinos accompanied by a photon from initial-state radiation, $e^+e^- \to \tilde{G}\tilde{G}\gamma$, giving rise to a single-photon and missing energy signature. Even if the masses of all other SUSY particles were above $\sqrt{s}$, this process could still provide a means to detect Supersymmetry at LEP.

As discussed in Section 3.2.4 (p. 51), the photon energy spectrum was expected to be soft. Therefore, for this search I considered only events from the combined single- and soft-photon sample with $x_\gamma < 0.5$, where $x_\gamma = E_\gamma/E_{beam}$. In total, I selected 1,286 such events in data with 1,303.6 events expected from Standard Model processes. The corresponding distributions of the photon energy and polar angle are

[13] Since the energy spread at LEP2 was relatively small, I assumed that a possible dependence of the matrix element on $\sqrt{s}$ was negligible.

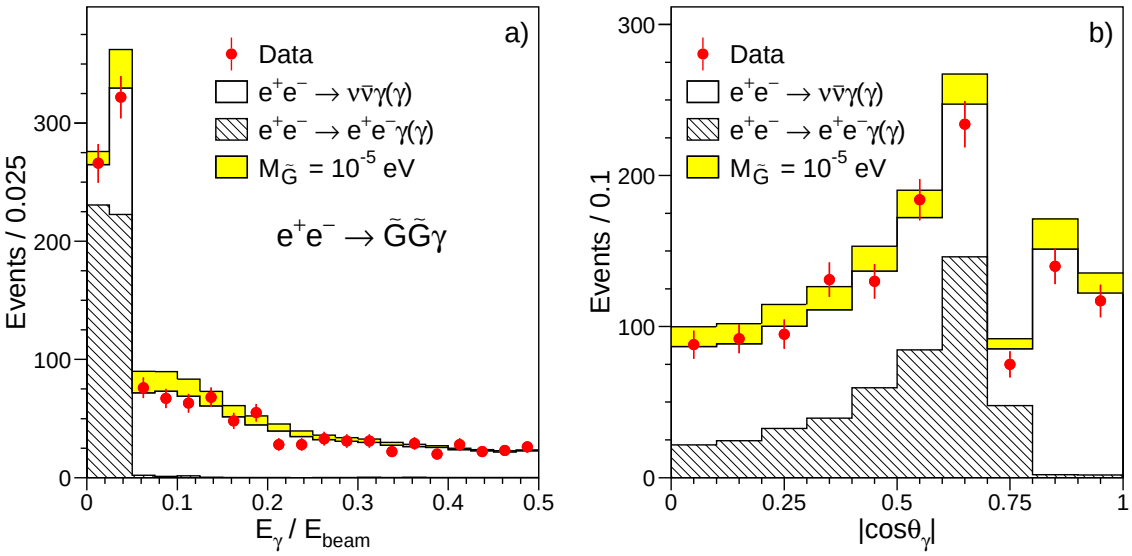

Figure 7.7: Distributions of a) the ratio of the photon energy to the beam energy (x_γ) and b) the photon polar angle for events with $x_\gamma < 0.5$ from the combined single- and soft-photon sample. Signal expected from the reaction $e^+e^- \to \tilde{G}\tilde{G}\gamma$ is also shown for $m_{\tilde{G}} = 10^{-5}$ eV.

shown in Figure 7.7. The predictions for the signal were obtained using a sample of 40,000 fully simulated Monte Carlo events. The signal efficiency within the above kinematic acceptance region was estimated to be 62%.

The inclusion of the soft-photon sample resulted in a significant increase in the accepted signal cross section. The achieved improvement in the search sensitivity was equivalent to increasing the integrated luminosity by approximately 50%.

In order to place an upper limit on the signal cross section, I performed a two-dimensional fit to the x_γ *vs.* $|\cos\theta_\gamma|$ distribution. As the signal cross section was proportional to $1/m_{\tilde{G}}^4$, this limit could be translated into a lower limit on the gravitino mass:

$$m_{\tilde{G}} > 1.35 \times 10^{-5} \text{ eV},$$

at the 95% confidence level, which in turn corresponded to a lower limit on the SUSY breaking scale $\sqrt{F} > 238$ GeV. The expected lower limit on the gravitino mass was estimated to be 1.32×10^{-5} eV.

7.2.3 Multi-Photon Signatures

Neutralino Production in GMSB

In models with gauge-mediated SUSY breaking (GMSB), the lightest supersymmetric particle (LSP) is always a light gravitino, 10^{-2} eV $\lesssim m_{\widetilde{\mathrm{G}}} \lesssim 10^{2}$ eV. If the next-to-lightest supersymmetric particle (NLSP) is the lightest neutralino, it is expected to decay predominantly through $\tilde{\chi}_1^0 \to \widetilde{\mathrm{G}}\gamma$. In this scenario pair-production of the lightest neutralinos, $\mathrm{e^+e^-} \to \tilde{\chi}_1^0\tilde{\chi}_1^0$, would lead to a multi-photon plus missing energy signature. A detailed description of this SUSY process was provided in Section 3.2.1.

In order to differentiate the signal from the $\mathrm{e^+e^-} \to \nu\bar{\nu}\gamma\gamma$ background, I used the following five kinematic variables: the energies of the two most energetic photons, their polar angles, and the recoil mass to the multi-photon system. Figure 7.8 compares the corresponding distributions of the signal for $m_{\tilde{\chi}_1^0} = 90$ GeV[14] with those of the data and the Standard Model background for events accepted by the multi-photon selection (see Section 6.4). All measured distributions were found to agree with the Standard Model predictions. In particular, no candidates with $E_{\gamma_2}/E_{beam} > 0.45$ or $M_{\mathrm{rec}} < 75$ GeV were found in the data. As shown in Figure 7.8, the observation of such events would have been a clear indication of the signal.

To combine information from these kinematic variables, I used the following procedure. First, I computed probability distributions for each of the five input variables, separately for each signal mass hypothesis and the Standard Model background. These probability distributions were then combined in a final discriminant variable.

Let us take s_i and b_i to be the probability distributions for variable i for a given signal hypothesis and the background, respectively. For a single variable, the probability for an event to belong to signal is then given by

$$p_i(x_i) = \frac{s_i(x_i)}{s_i(x_i) + b_i(x_i)}\,, \tag{7.17}$$

[14] The signal distributions were obtained from a large sample of Monte Carlo events processed through the full detector simulation. Similar distributions for other values of the neutralino mass can be found in Figure 3.8 (p. 45).

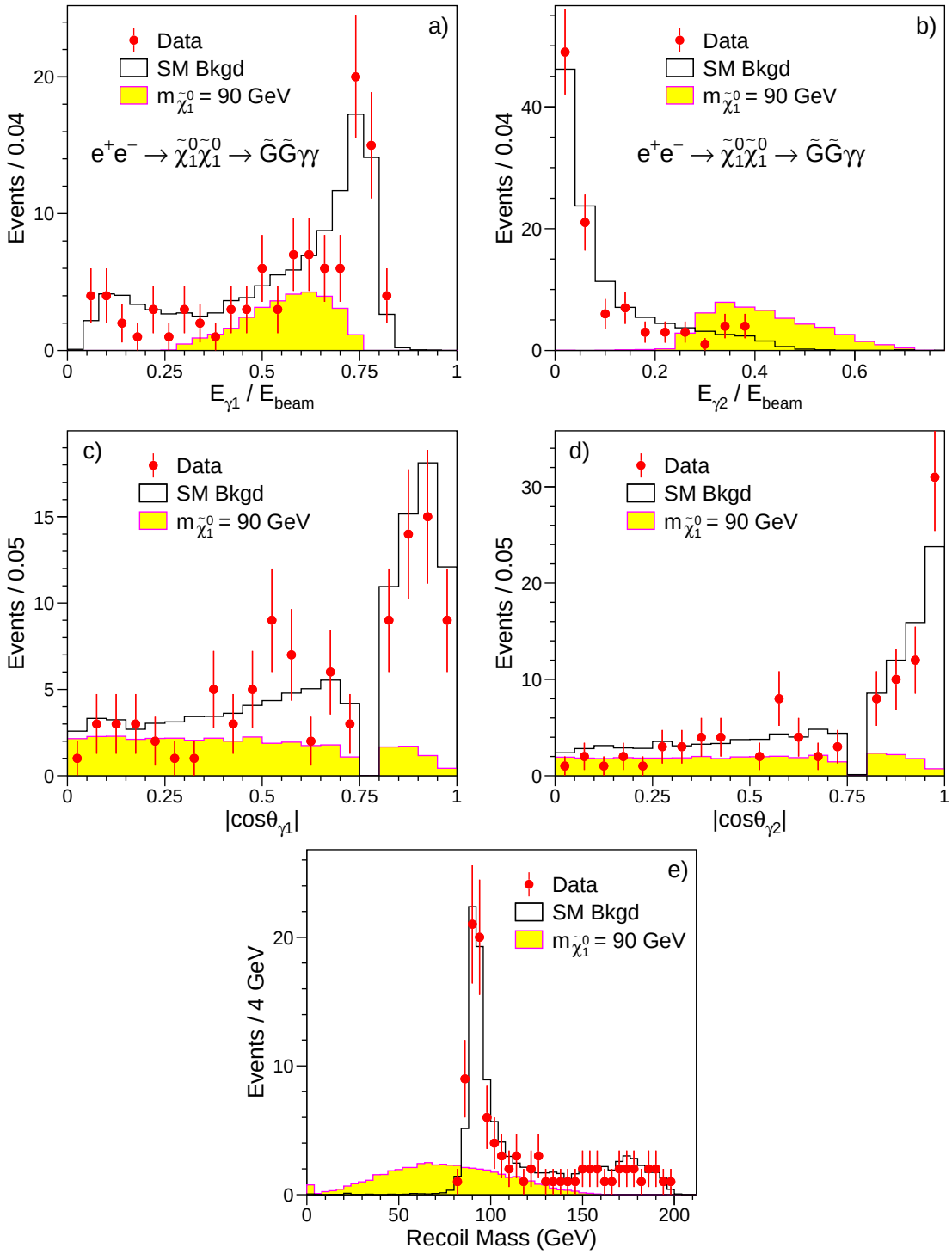

Figure 7.8: Distributions of (a,b) the photon energies and (c,d) the photon polar angles and e) the recoil mass spectrum of the fully simulated $e^+e^- \to \tilde{\chi}_1^0\tilde{\chi}_1^0 \to \tilde{G}\tilde{G}\gamma\gamma$ Monte Carlo events that were accepted by the multi-photon selection for $m_{\tilde{\chi}_1^0} = 90$ GeV. Also shown are the corresponding distributions for the data and the Standard Model background. The normalization for the signal Monte Carlo is arbitrary.

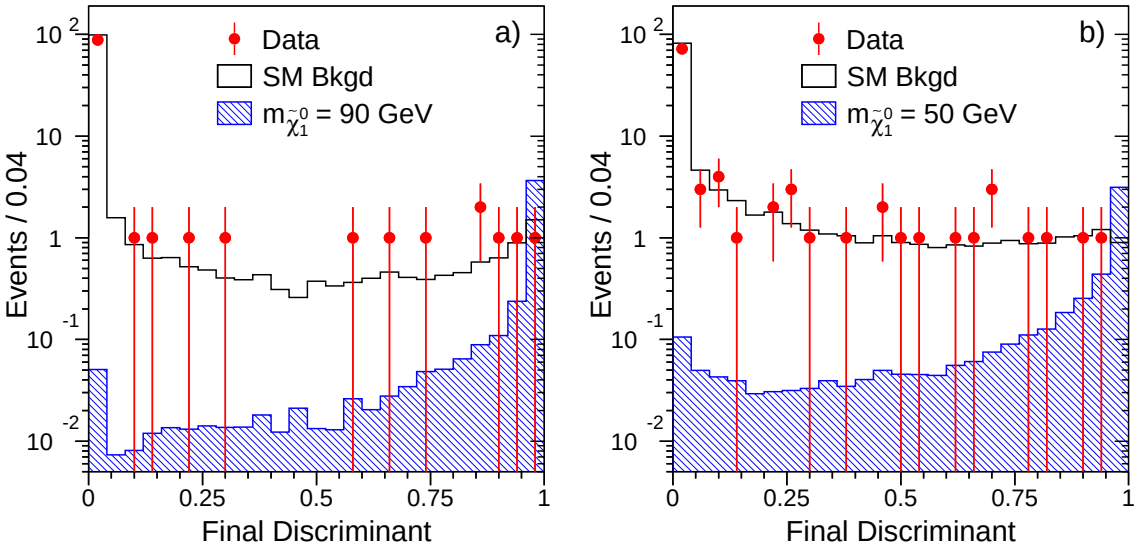

Figure 7.9: Distributions of the final discriminant variable used in the search for pair-produced neutralinos $\tilde{\chi}_1^0\tilde{\chi}_1^0 \to \tilde{G}\tilde{G}\gamma\gamma$ a) for $m_{\tilde{\chi}_1^0} = 90$ GeV and b) for $m_{\tilde{\chi}_1^0} = 50$ GeV. The signals correspond to the upper limits of a) 4.7 and b) 5.2 events derived for these mass points.

where x_i is the value of this variable measured for this event. Similarly, the probability that this event belongs to the background is given by

$$q_i(x_i) = \frac{b_i(x_i)}{s_i(x_i) + b_i(x_i)}\,. \tag{7.18}$$

The final discriminant variable is then computed by multiplying the individual probabilities from each of the five input variables:

$$F(\vec{x}) = \frac{\prod_{i=1}^{5} p_i(x_i)}{\prod_{i=1}^{5} p_i(x_i) + \prod_{i=1}^{5} q_i(x_i)}\,. \tag{7.19}$$

For a more signal-like event, F would be close to one, while for a very background-like event, $F \to 0$.

Figure 7.9 shows the distributions of the final discriminant variable for two neutralino mass hypotheses: $m_{\tilde{\chi}_1^0} = 90$ GeV and $m_{\tilde{\chi}_1^0} = 50$ GeV. In both cases, the signal was almost completely separated from the background and no excess in the signal region $F \gtrsim 0.9$ was observed in the data. The same held for other mass points.

Upper limits on the signal cross section were derived from fits to the obtained final discriminant distributions. The signal efficiency for this process was found to decrease from 70% for $m_{\tilde{\chi}_1^0} \simeq 100$ GeV to 40% for $m_{\tilde{\chi}_1^0} = 5$ GeV. The observed and expected limits derived at $\sqrt{s} = 207$ GeV are shown in Figure 7.10a as a function of the neutralino mass. Data collected at lower $\sqrt{s}$ were included assuming the signal cross section to scale according to the MGM model [194]. In this model, the neutralino is pure bino and the masses of scalar electrons are related to the neutralino mass through $m_{\tilde{e}_L} = 1.1 \times m_{\tilde{\chi}_1^0}$ and $m_{\tilde{e}_R} = 2.5 \times m_{\tilde{\chi}_1^0}$. The signal cross section predicted by the MGM model is also shown in Figure 7.10a. The neutralino mass limit obtained for this model was

$$m_{\tilde{\chi}_1^0} > 99.5 \text{ GeV}$$

at the 95% confidence level. Figure 7.10b shows the excluded region in the $(m_{\tilde{e}_R}, m_{\tilde{\chi}_1^0})$ mass plane obtained after relaxing the mass relations of the MGM. Also shown is the region suggested by the interpretation [68] of the rare CDF event in the scalar electron scenario (see Section 3.2.2). This interpretation was ruled out by my analysis.

The multi-photon selection used in this search was devised for photons originating from the interaction point, and the above limits were derived under the assumption of a neutralino mean decay length shorter than about 5 cm. In the next section I will describe a dedicated analysis that I developed for the special case of a non-negligible neutralino lifetime.

Neutralino Production in SUGRA Models

In gravity-mediated SUSY breaking models (SUGRA) the lightest neutralino is expected to be the LSP. This scenario may lead to a new source of multi-photon events from the reaction $e^+e^- \to \tilde{\chi}_2^0\tilde{\chi}_2^0$ followed by the decay $\tilde{\chi}_2^0 \to \tilde{\chi}_1^0\gamma$ as described in Section 3.2.3. The signal kinematic distributions were expected to very similar to those from the GMSB reaction $e^+e^- \to \tilde{\chi}_1^0\tilde{\chi}_1^0$ considered above. Therefore the same analysis procedure was used.

No significant deviation from the Standard Model expectations was observed and

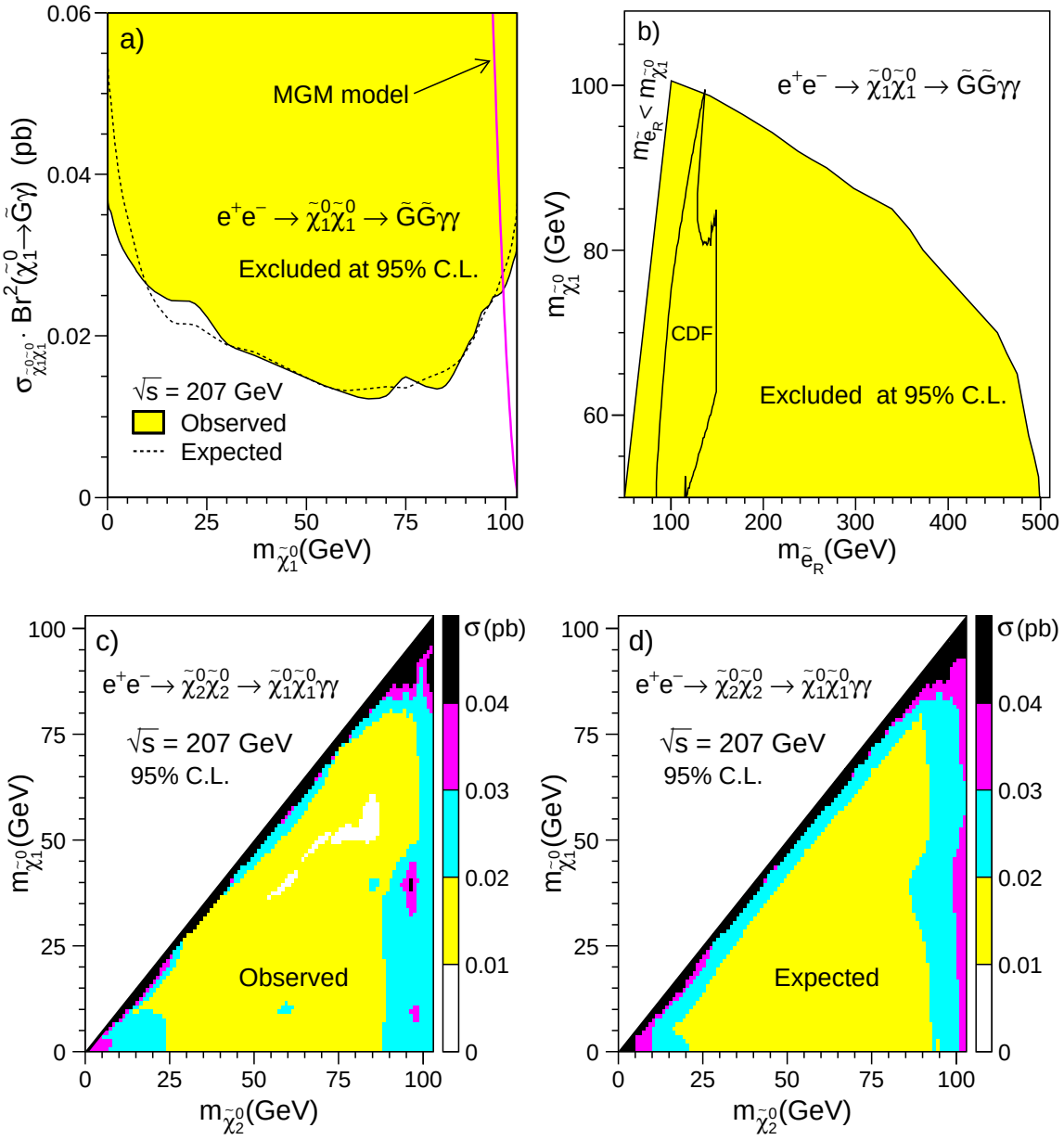

Figure 7.10: **a)** Observed and expected 95% confidence level upper limits on the production cross section of the reaction $e^+e^- \to \tilde{\chi}_1^0\tilde{\chi}_1^0 \to \tilde{G}\tilde{G}\gamma\gamma$. The cross section predicted by the MGM model [194] is also shown. **b)** Region excluded for a pure bino neutralino model in the $(m_{\tilde{e}_R}, m_{\tilde{\chi}_1^0})$ mass plane. The region compatible with the GMSB interpretation of the CDF event [68] is also shown. **c)** Observed and **d)** expected cross section upper limits from the search for the process $e^+e^- \to \tilde{\chi}_2^0\tilde{\chi}_2^0 \to \tilde{\chi}_1^0\tilde{\chi}_1^0\gamma\gamma$. The limits were obtained at the 95% C.L. for $\sqrt{s} = 207$ GeV. Data collected at lower $\sqrt{s}$ were included assuming the signal cross section to scale according to Equation 3.22 (p. 49). For simplicity, the branching fraction for the $\tilde{\chi}_2^0 \to \tilde{\chi}_1^0\gamma$ decay was assumed to be 100%.

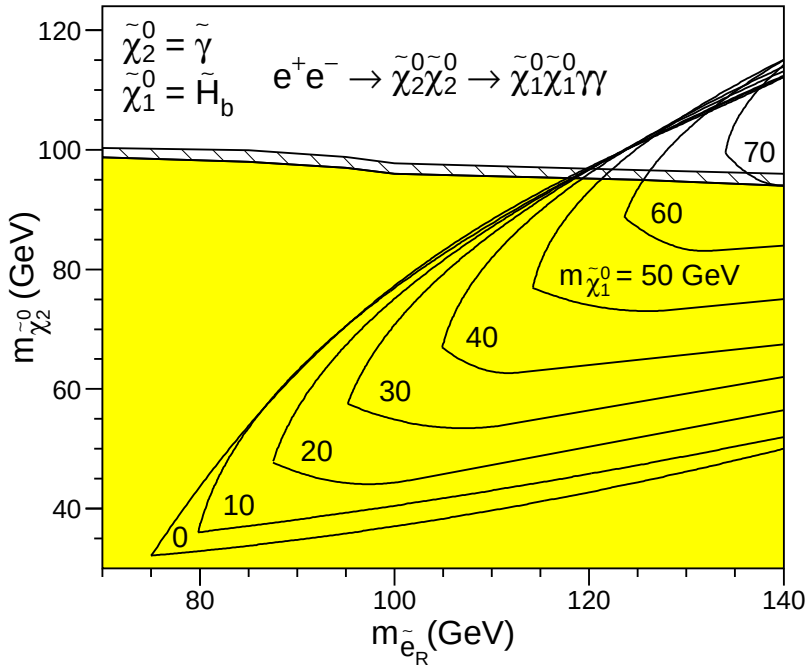

Figure 7.11: Region excluded at the 95% confidence level in the $(m_{\tilde{e}_R}, m_{\tilde{\chi}_2^0})$ mass plane. The shaded region corresponds to $m_{\tilde{e}_L} \gg m_{\tilde{e}_R}$ and the hatched region is additionally excluded when $m_{\tilde{e}_L} = m_{\tilde{e}_R}$. The mass difference between $\tilde{\chi}_2^0$ and $\tilde{\chi}_1^0$ was assumed to be greater than 10 GeV. The regions kinematically allowed for the CDF event [69] as a function of $m_{\tilde{\chi}_1^0}$ are also indicated.

cross section limits were derived for all kinematically allowed values of neutralino masses in steps of 3 GeV. The limits were obtained at $\sqrt{s} = 207$ GeV, and data collected at lower $\sqrt{s}$ were included assuming the signal cross section to scale according to Equation 3.22 (p. 49). The observed and expected limits are shown in Figures 7.10c,d. For most of the kinematically allowed values of $m_{\tilde{\chi}_1^0}$ and $m_{\tilde{\chi}_2^0}$, the obtained cross section limits were in the range of 0.01-0.03 pb.

The $\tilde{\chi}_2^0 \to \tilde{\chi}_1^0\gamma$ decay has a branching fraction close to 100% if one of the two neutralinos is pure photino and the other pure higgsino. This scenario is suggested by the SUGRA interpretation of the ee$\gamma\gamma$ event observed by CDF (see Section 3.2.2). With this assumption, a lower limit on the $\tilde{\chi}_2^0$ mass was calculated as a function of $m_{\tilde{e}_R}$ using the most conservative cross section upper limit for any mass difference between $\tilde{\chi}_2^0$ and $\tilde{\chi}_1^0$ greater than 10 GeV. Figure 7.11 shows the regions of the $(m_{\tilde{\chi}_2^0}, m_{\tilde{e}_R})$ plane excluded at the 95% C.L. Two distinct scenarios were investigated: $m_{\tilde{e}_L} = m_{\tilde{e}_R}$ and

$m_{\tilde{e}_L} \gg m_{\tilde{e}_R}$, where $m_{\tilde{e}_L}$ and $m_{\tilde{e}_R}$ denote the masses of the left- and right-handed scalar electrons. The regions kinematically allowed for the SUGRA interpretation of the CDF event [69] are also indicated.

7.2.4 Searches for Events with Non-Pointing Photons

As discussed in Section 3.2 of Chapter 3, the neutralino in GMSB models can have a non-negligible lifetime. The neutralino decay length is proportional to the gravitino mass squared (see Equation 3.21 p. 45) and, for $m_{\widetilde{G}} \sim 100$ eV, it can be comparable to or even larger than the size of the L3 detector. In this scenario, one or both of the neutralinos produced in the reaction $e^+e^- \to \tilde{\chi}_1^0\tilde{\chi}_1^0 \to \tilde{G}\tilde{G}\gamma\gamma$ may decay within the sensitive volume of the detector, but at a distance from the primary vertex. This results in a topology with sizable missing energy carried away by the gravitinos and with one or two visible energetic photons which, in general, do not point back to the interaction region. The single-photon topology can be produced if one of the neutralinos decays outside the active detector region.

In this section I describe a dedicated analysis that I developed to search for such events with non-pointing photons and missing energy. To improve the sensitivity, I searched for non-pointing photons not only in the BGO but also in the hadron calorimeter of L3. This was important because for this search the compactness of the BGO crystal calorimeter presented a disadvantage.

Figure 7.12 shows a simulated $e^+e^- \to \tilde{\chi}_1^0\tilde{\chi}_1^0 \to \tilde{G}\tilde{G}\gamma\gamma$ event with two non-pointing photons. In this event one of the neutralinos decayed in front of the BGO calorimeter, giving rise to an electromagnetic shower in the BGO crystals, while the other decayed and produced a shower inside the hadron calorimeter. This example suggests a study of the following event signatures:

- Events with one or two non-pointing photons in the BGO.
- Events with one or two non-pointing photons in the HCAL.
- Events with photon candidates in both the BGO and the HCAL.

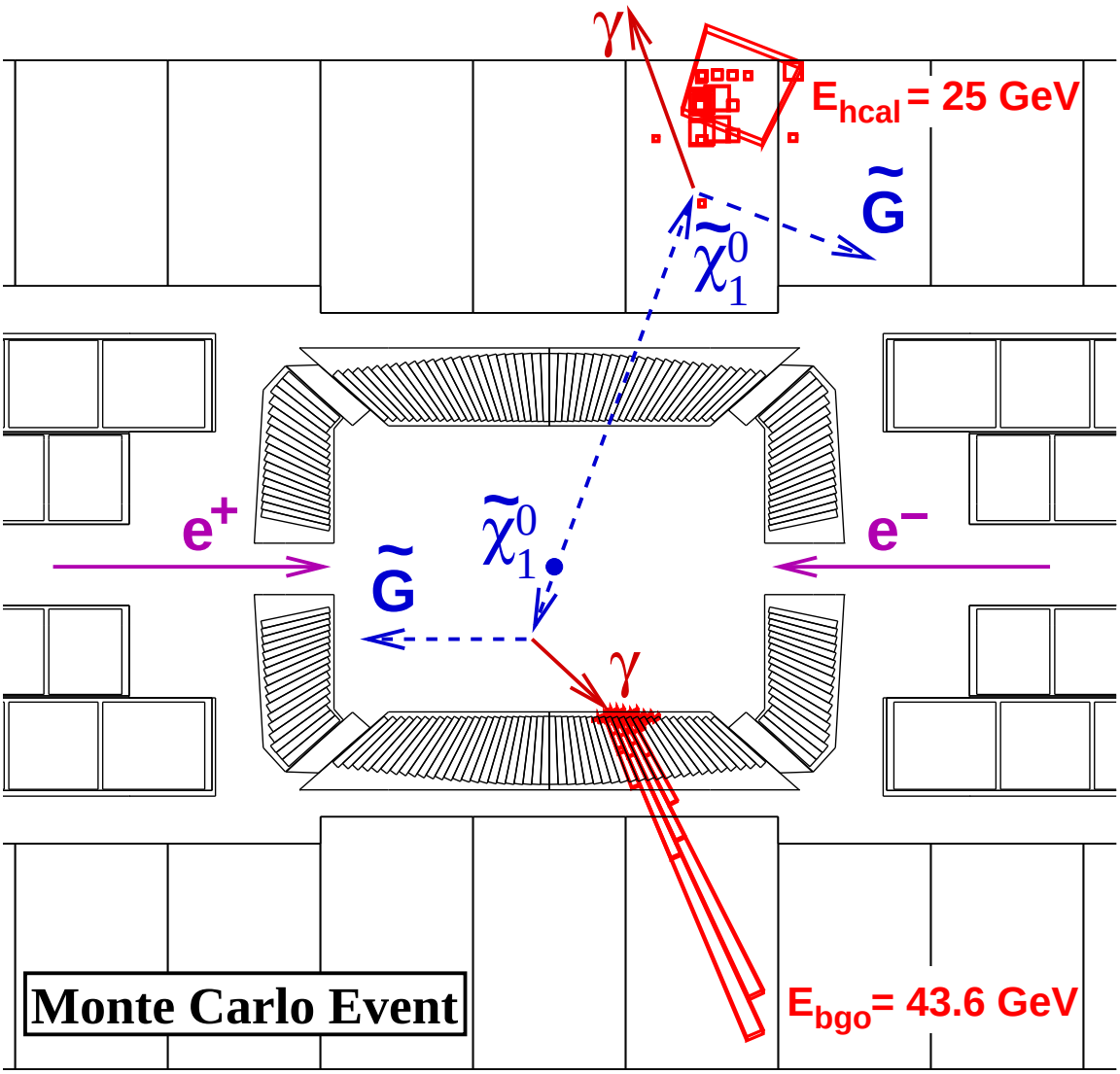

Figure 7.12: Schematic diagram of a simulated $e^+e^- \to \tilde{\chi}_1^0\tilde{\chi}_1^0 \to \tilde{G}\tilde{G}\gamma\gamma$ event with non-pointing photons. The event is displayed in a plane parallel to the beam axis. The arrows indicate the directions of flight of the produced particles. One of the two neutralinos decayed in front of the BGO calorimeter after traveling a distance of 0.3 m, and the other decayed in the HCAL after traveling 1.6 m. This event was taken from a Monte Carlo sample generated with $m_{\tilde{\chi}_1^0} = 95$ GeV and $\sqrt{s} = 207$ GeV and processed through the full detector simulation. Energy deposits in the BGO are shown as towers whose height is proportional to the crystal energy. Hits in the HCAL are shown as squares whose size is proportional to the deposited energy. The reconstructed shower energies are also indicated.

Non-pointing Photons in the BGO

Contrary to photons produced near the interaction region, non-pointing photons were expected to enter the BGO calorimeter at a significant angle with respect to the crystal axis (see Figure 7.12). As a consequence, electromagnetic showers produced by non-pointing photons could be identified by studying the transverse shower profile. In particular, a measure of shower's transverse circularity was provided by the variable *shower roundness* (see Equation 6.2 p. 140). For photons produced near the primary vertex, the transverse shower profile was almost circular so that their roundness was typically close to one. In contrast, showers produced by non-pointing photons were expected to be oblong, which would result in lower values of shower roundness.

For this event signature I applied the same basic event selection criteria as those used in the selection of single- and multi-photon events from the process $e^+e^- \to \nu\bar{\nu}\gamma(\gamma)$ (see Sections 6.3 and 6.4), except that I did not apply the cuts based on the measured lateral shower profile.[15] Instead I required that at least one photon candidate have a shower roundness less than 0.4. In addition, I required that the central crystal of this shower not be in one of the edge rings of the BGO.[16]

As shown in Figure 7.8, photons produced in the neutralino decays were expected to be energetic. Therefore, an event was not selected if any of the photon candidates had an energy below 20 GeV. This cut significantly reduced the background from cosmic rays. To further reduce cosmic contamination, I required that there should be at least one scintillator hit in time with the beam crossing within ± 5 ns.

No candidate events were observed in the data after applying these cuts. Figure 7.13a shows that the cut on the shower roundness eliminated almost all background from the Standard Model processes. The residual background from the reaction $e^+e^- \to \nu\bar{\nu}\gamma(\gamma)$ was found to be 0.3 ± 0.1 events. The cosmic contamination was estimated using the methods described in Section 6.3.5 and found to be 0.2 ± 0.1 events.

[15] That is, I relaxed the cuts on the shower roundness and S_9^c/S_{25}^c variable (see Section 6.3.1).

[16] Shower leakage into the gaps between the BGO barrel and endcaps affected the measurement of the shower roundness. This effect can be seen by comparing Figures 6.3e and 6.3f (p. 142). The shower leakage effects were also discussed in Section C.2 of Appendix C.

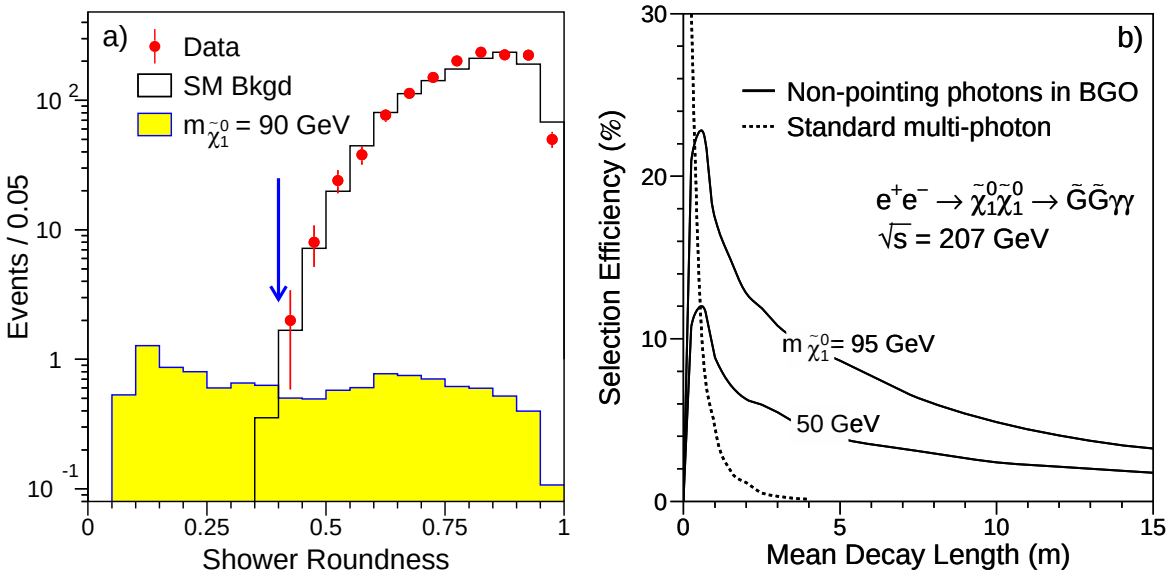

Figure 7.13: a) Distribution of the shower roundness for a sample of fully simulated $e^+e^- \to \tilde{\chi}_1^0\tilde{\chi}_1^0 \to \tilde{G}\tilde{G}\gamma\gamma$ events after all other selection cuts have been applied. The signal events were generated for a mean decay length of $L_{\tilde{\chi}_1^0}$ = 3 m and $m_{\tilde{\chi}_1^0}$ = 90 GeV. The arrow indicates the value of the cut. Also shown are the corresponding distributions for the data and the Standard Model background. The normalization for the signal is arbitrary. b) Selection efficiency as a function of the neutralino mean decay length for the standard multi-photon and the BGO-based non-pointing photon selections.

The efficiency of this selection was estimated using large samples of Monte Carlo events generated for $\tilde{\chi}_1^0$ decay lengths up to 100 m and processed through the full detector simulation. The signal efficiency was found to depend both on the neutralino mass and the neutralino lifetime. For lighter neutralinos, the majority of photons produced in the $\tilde{\chi}_1^0 \to \tilde{G}\gamma$ decays would be boosted in the direction of the neutralino's flight and, thus, eliminated by the cut on the shower roundness. Figure 7.13b shows the obtained signal efficiency as a function of the neutralino mean decay length in the laboratory frame ($L_{\tilde{\chi}_1^0}$). For $m_{\tilde{\chi}_1^0}$ = 95 GeV and $\sqrt{s}$ = 207 GeV, the efficiency reached a maximum value of about 25% at $L_{\tilde{\chi}_1^0} \simeq 1$ m and exponentially decreased after the peak. Figure 7.13b also shows that the "standard" multi-photon selection used in the previous section became ineffective for $L_{\tilde{\chi}_1^0} \geq 1$ m.

Non-pointing photons in the HCAL

In this analysis I made use of the barrel hadron calorimeter (HCAL) and the muon filter (see Figure 4.13 p. 82). An overview of these subdetectors was given in Section 4.2.5. The HCAL surrounded the BGO calorimeter and was made of depleted uranium and brass absorber plates interleaved with proportional wire chambers. The HCAL barrel was 4.7 m long and had an inner radius of about 0.9 m and an outer radius of about 1.8 m, covering the polar angle range $25^\circ < \theta < 155^\circ$. The signal wires of the proportional chambers were grouped to form readout towers which provided a segmentation of 10 layers in the radial direction. The amount of absorber material between two neighboring layers corresponded to about 10 radiation lengths (equivalent to approximately half a BGO crystal). Thus, the electromagnetic showers produced by photons and electrons in the HCAL were expected to be very compact.

The muon filter was designed to absorb the tail of hadronic showers and to track muons between the HCAL and the muon chambers. It was located just outside of the HCAL barrel and divided into eight octants, each made of six layers of brass absorber plates interleaved with five layers of proportional chambers. As described below, I used the muon filter to suppress the cosmic ray background. Since the HCAL endcaps were not covered by the muon filter, they were not used in this search.

Prior to their installation in L3, the assembled HCAL modules had been tested in beams of hadrons and electrons. These studies showed that the hadron calorimeter was capable of reconstructing not only hadronic but also electromagnetic showers [195].

In order to study the HCAL performance *in situ*, I used events from the Bhabha scattering process $e^+e^- \to e^+e^-$ in which both scattered electrons passed through the gaps between the BGO barrel and endcaps and produced two showers in the HCAL barrel. An example of such an event is displayed in Figure 7.14. In 1996 the gaps between the BGO barrel and endcaps were equipped with the EGAP calorimeter. Therefore, for this study I used 30 pb^{-1} of data collected by L3 in 1995 at or near the Z resonance, $\sqrt{s} \simeq 91$ GeV.

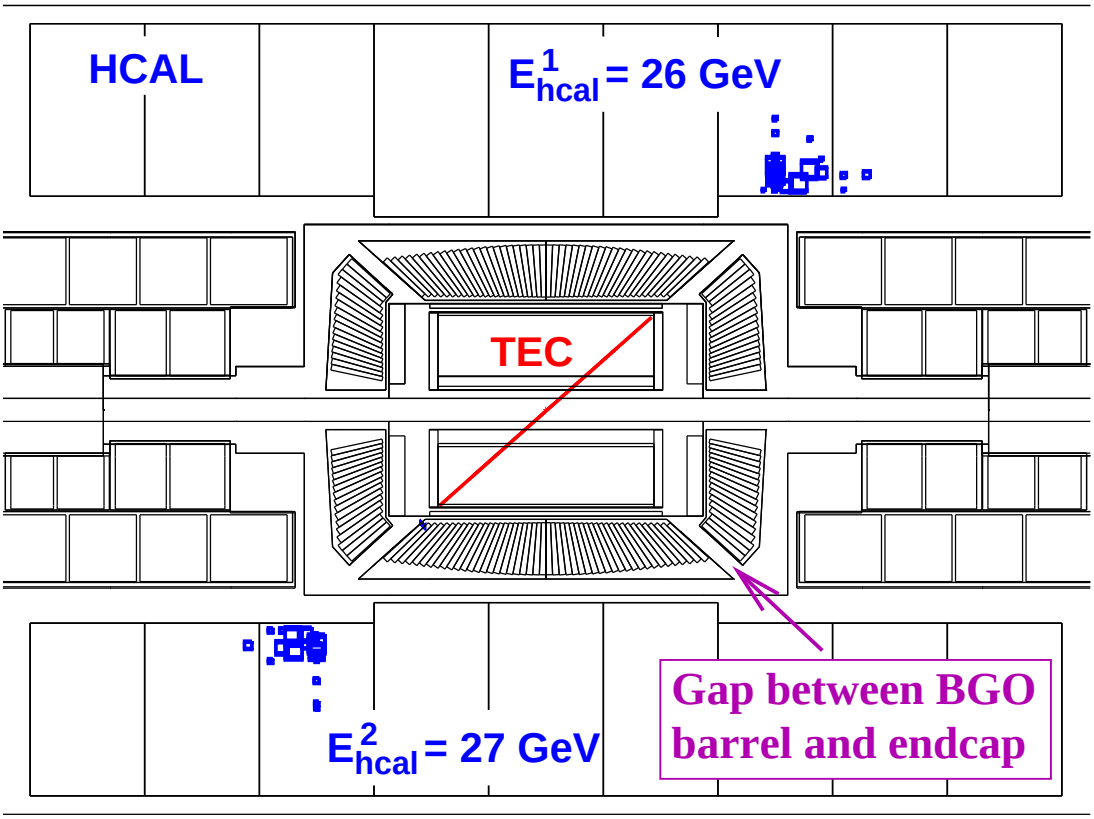

Figure 7.14: Display of a typical $e^+e^- \to e^+e^-$ event in which both electrons produced showers in the hadron calorimeter. This candidate event was recorded in 1995 at $\sqrt{s} = 91$ GeV. The L3 detector is displayed in a plane parallel to the beam axis. Tracks reconstructed in the TEC are shown as back-to-back lines, and hits in the HCAL are shown as squares whose size is proportional to the deposited energy.

To select Bhabha events with electrons in the HCAL, I required two back-to-back clusters in the hadron calorimeter and no significant energy deposits in the BGO and forward calorimeters. In particular, I rejected events with a total energy deposited in the BGO above 1 GeV. In total, I selected 1,110 such events in data with about 1,048 expected from Monte Carlo.

Figure 7.15a shows the measured energy spectrum of the selected Bhabha electrons. The relative energy resolution of the HCAL for 45 GeV electrons was found to be $\sigma_{DATA} = 23\%$, in good agreement with the resolution predicted by the detector simulation $\sigma_{MC} = 21\%$. Since the HCAL calorimeter was calibrated using hadronic

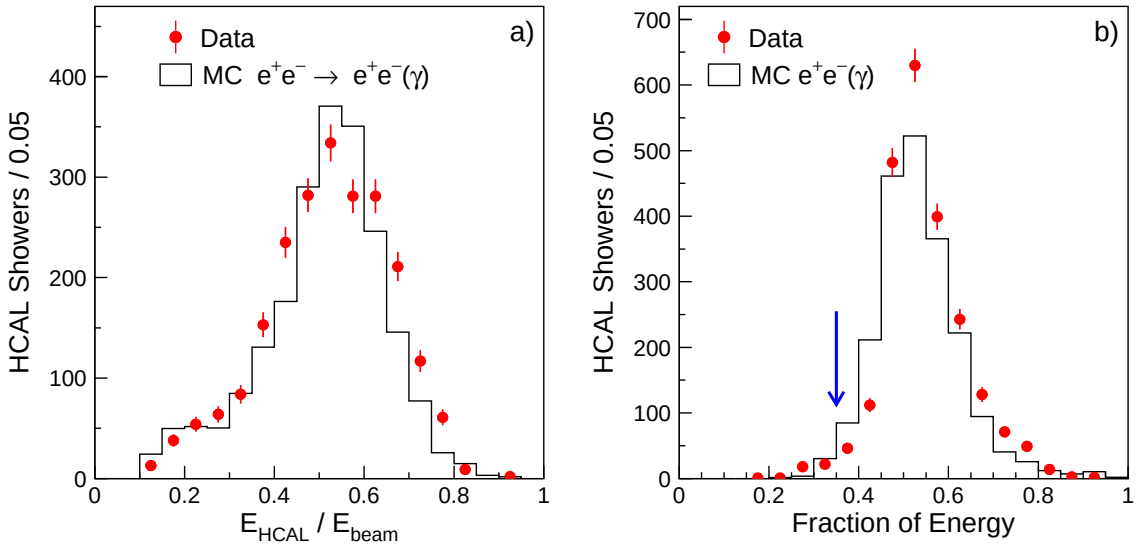

Figure 7.15: Distributions a) of the reconstructed shower energy and b) of the fraction of the shower energy deposited in the central layer for Bhabha events with showers in the HCAL. The event sample was selected using the L3 data collected in 1995 at $\sqrt{s} = 91$ GeV.

jets, for such highly energetic electromagnetic showers its energy scale was below one. The relative energy scale was measured to be $P_{DATA} = 0.54$, in good agreement with the prediction of the detector simulation $P_{MC} = 0.53$. These measurements are consistent with the results of a similar study described in Reference [196].

The test beam studies showed that electromagnetic showers could be distinguished from hadronic ones using a quantity T_1, defined as a ratio of energy deposited in the layer with the maximum energy deposition to the total shower energy. Since showers produced by electrons and photons were expected to be very compact, a cut $T_1 > 0.35$ eliminated only about 2% of such showers (see Figure 7.15b). In contrast, most of the hadronic showers did not survive this cut [195].

The above study demonstrated that the hadron calorimeter could be used to search for $e^+e^- \rightarrow \tilde{\chi}_1^0\tilde{\chi}_1^0$ events in which one or both of the neutralinos decayed in the HCAL. To select candidate events, I required one or two isolated clusters in the HCAL, each with a reconstructed shower energy above 15 GeV and $T_1 > 0.35$. There should be no other activity in the detector apart from what was consistent with noise. In particular, an event was rejected if more than 1 GeV was deposited in the BGO or EGAP

calorimeters within a 15° cone around the cluster in the HCAL. I found that this requirement eliminated all background from Standard Model processes. By studying a sample of events randomly triggered at the beam crossing time (see Section 6.3.7), I also found that such highly energetic clusters could not be produced by the electronic and uranium noise in the HCAL.

However, an important source of background came from cosmic ray events. Cosmic muons traversing the hadron calorimeter could emit a a bremsstrahlung photon[17] and, thus, fake a non-pointing photon produced in the neutralino decay. Figure 7.16 shows a typical cosmic ray event with a bremsstrahlung photon in the HCAL.

To suppress this source of background, I required that there should be no track segments detected in any layer of the muon chambers $N_{\rm MUTK} = 0$ and no hits in the muon filter $N_{\rm MF} = 0$. No candidate events were found in the data after applying these anti-cosmic cuts. To estimate the expected cosmic ray background, I used a sample of $N_0 = 179$ events which satisfied all other selection criteria. Of these, 172 events were eliminated by the cut $N_{\rm MUTK} = 0$ and 166 events by the cut $N_{MF} = 0$, which corresponded to rejection powers of $R_{\rm MUTK} = 96 \pm 2\%$ and $R_{\rm MF} = 92 \pm 2\%$, respectively.[18] Then, the expected cosmic contamination could be calculated as $N_{\rm cosm} = N_0 \cdot (1 - R_{\rm MUTK}) \cdot (1 - R_{MF}) = 0.6 \pm 0.4$ events.

Events with non-pointing photons in the HCAL could be triggered only by the HCAL energy trigger. To estimate the efficiency of this trigger, I used cosmic ray events since such events could also be accepted by the muon trigger. In total, I selected 257 such cosmic ray events with a single HCAL cluster above 15 GeV, of which 242 events were also accepted by the HCAL energy trigger. Thus, the HCAL trigger efficiency was estimated to be $\varepsilon_{Data} = 94 \pm 1\%$, in good agreement with the Monte Carlo prediction of $\varepsilon_{MC} = 96\%$.

The efficiency of this selection was estimated using large samples of fully simulated $e^+e^- \to \tilde{\chi}_1^0\tilde{\chi}_1^0$ events generated for $\tilde{\chi}_1^0$ decay lengths up to 100 m. As shown in

[17] This production mechanism was described in detail in Section 6.3.5.

[18] The rejection power of the cut $N_{\rm MUTK} = 0$ was cross checked using a sample of out-of-time cosmic events as described in Section 6.3.5. The rejection power of the cut $N_{\rm MF} = 0$ was in agreement with an estimate of 91% provided by earlier tests of the performance of the muon filter [128].

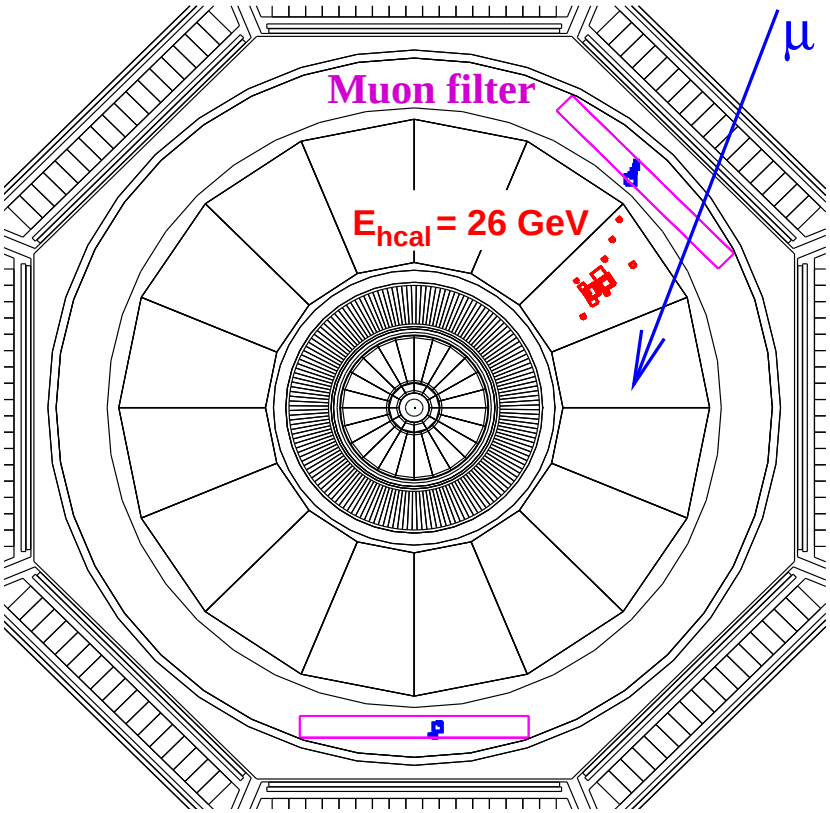

Figure 7.16: A cosmic ray event in which the cosmic muon emitted a bremsstrahlung photon in the HCAL. The event is displayed in the plane perpendicular to the beam axis. The arrow indicates the flight direction of the cosmic muon, as determined from the two clusters in the muon filter.

Figure 7.17a, the signal efficiency reached a maximum of 15% at $L_{\tilde{\chi}_1^0} \simeq 3$ m and, for larger lifetimes, was significantly higher than the efficiency of the BGO-based selection. In addition, the HCAL-based selection was not sensitive to the flight direction of the photon candidates and, therefore, its efficiency was almost the same for all allowed values of the neutralino mass. In contrast, the BGO-based search became ineffective for $m_{\tilde{\chi}_1^0} \lesssim 50$ GeV.

Non-pointing photons in the BGO and HCAL

This unique event topology could be produced if one of the neutralinos decayed in front of the BGO calorimeter and the other in the HCAL as shown in Figure 7.12. For this search I required a shower in the BGO with an energy above 20 GeV and a

cluster in the HCAL with an energy above 15 GeV. There should be no other activity in the detector apart from what was consistent with noise. To reject single-photon events with shower leakage from the BGO into the HCAL, I required that the two photon candidates be separated by more than 20°.

No data events satisfied these selection criteria and no events were expected from Standard Model processes. The efficiency of this selection for the process $e^+e^- \to \tilde{\chi}_1^0\tilde{\chi}_1^0$ is shown in Figure 7.17a as a function of the neutralino decay length. It reached a maximum value of about 20% at $L_{\tilde{\chi}_1^0} \simeq 1$ m and rapidly decreased after the peak. This search strategy became ineffective for $L_{\tilde{\chi}_1^0} \gtrsim 10$ m since such lifetimes would have implied that at least one of the produced neutralinos decayed outside the detector.

Results

Since signal events could not be accepted by more than one selection, the total signal efficiency was obtained by adding together the efficiencies of the three individual selections. The total signal efficiency is shown in Figure 7.17b as a function of the $\tilde{\chi}_1^0$ decay length for three mass hypotheses: $m_{\tilde{\chi}_1^0} = 95, 50,$ and 10 GeV. The signal efficiency increases with the neutralino mass, reaching a maximum value of about 40% at $L_{\tilde{\chi}_1^0} \simeq 1.5$ m near the kinematic limit $m_{\tilde{\chi}_1^0} = \sqrt{s}/2$.

No candidate events had been found for any of the final state topologies, and upper limits on the signal cross section were derived using the statistical procedure described in Section 7.2.1. For $L_{\tilde{\chi}_1^0} \leq 2\,\mathrm{m}$, the limits were derived by combining the results of the searches for the non-pointing photon and standard multi-photon[19] signatures. The obtained limits on the $e^+e^- \to \tilde{\chi}_1^0\tilde{\chi}_1^0$ cross section at $\sqrt{s} = 207$ GeV are shown in Figure 7.10c as a function of the $\tilde{\chi}_1^0$ decay length. Data collected at lower $\sqrt{s}$ were included assuming the signal cross section to scale according to the MGM model [194], which was discussed in the previous section.

The systematic error on efficiency of the non-pointing selection was dominated by the systematic errors associated with the modelling of the shower development and the uncertainty on the HCAL trigger efficiency. It was estimated to be at most 5%

[19] The search for multi-photon $e^+e^- \to \tilde{\chi}_1^0\tilde{\chi}_1^0 \to \tilde{G}\tilde{G}\gamma\gamma$ events was described in the previous section.

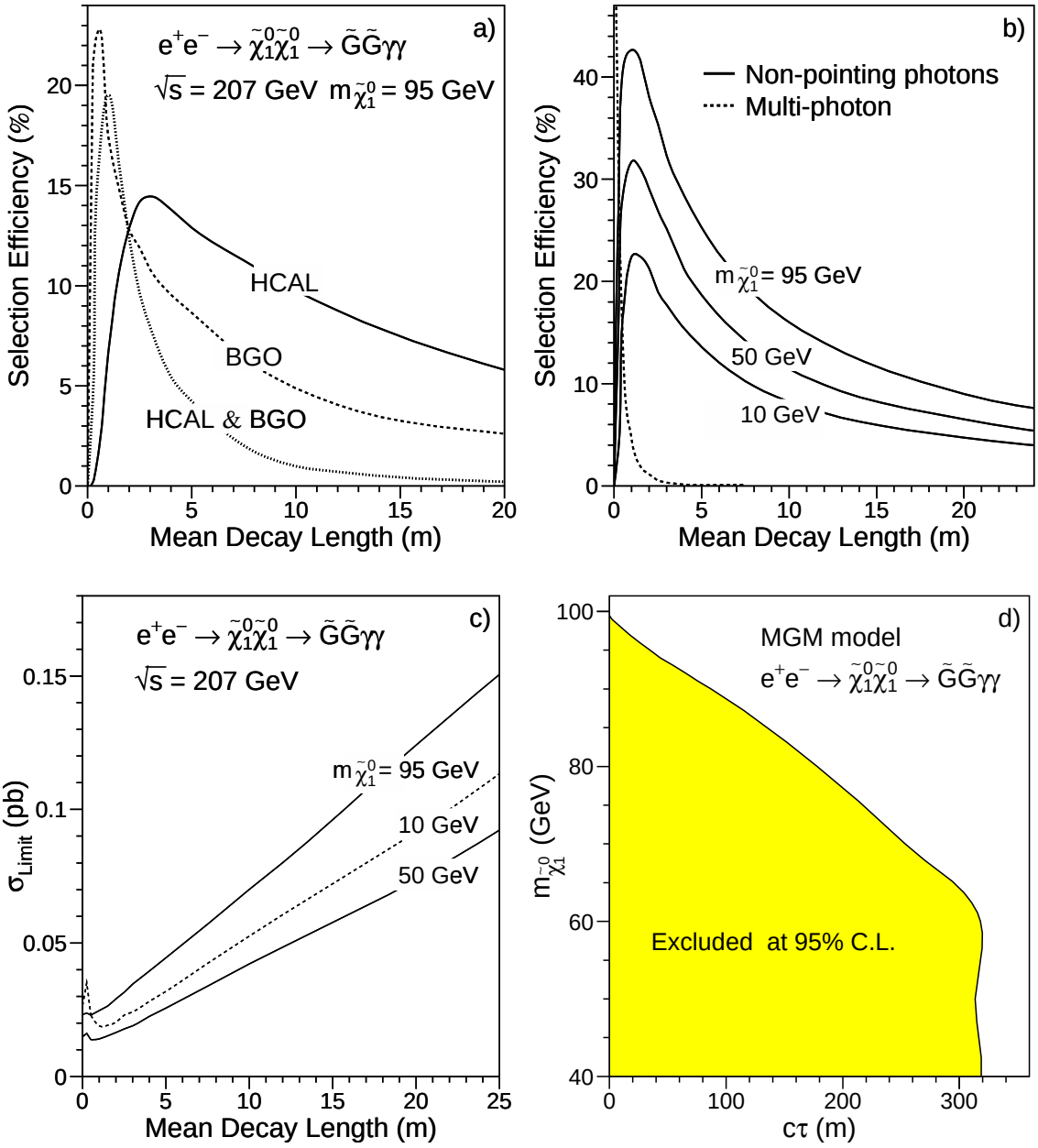

Figure 7.17: **a)** Efficiencies for the HCAL-based, BGO-based, and HCAL+BGO selections of $e^+e^- \to \tilde{\chi}_1^0\tilde{\chi}_1^0 \to \tilde{G}\tilde{G}\gamma\gamma$ events with non-pointing photons for $m_{\tilde{\chi}_1^0} = 95$ GeV and $\sqrt{s} = 207$ GeV. **b)** Signal efficiencies and **c)** upper limits at the 95% C.L. on the production cross section for three different neutralino mass hypotheses $m_{\tilde{\chi}_1^0} = 95, 50,$ and 10 GeV. Data collected at lower $\sqrt{s}$ were included assuming the signal cross section to scale according to the MGM model [194]. All curves are shown as a function of the neutralino mean decay length in the laboratory frame. **d)** Region excluded in the $(c\tau_{\tilde{\chi}_1^0}, m_{\tilde{\chi}_1^0})$ plane at the 95% C.L. under the assumptions of the MGM.

N_{mess}	1	2	3	4
Λ (TeV)	61.5	36.3	25.5	20.3
M_{mess} (TeV)	75	130	10^5	$5.6 \cdot 10^6$
$m_{\tilde{\mathrm{G}}}$ (eV)	1.1	1.2	620	$2.7 \cdot 10^4$
$m_{\tilde{\chi}_1^0}$ (GeV)	78.6	83.8	88.0	104.2
$m_{\tilde{\tau}_1}$ (GeV)	82.1	87.1	90.8	106.3
$m_{\tilde{\mathrm{e}}_\mathrm{R}}, m_{\tilde{\mu}_\mathrm{R}}$ (GeV)	107.6	102.2	92.1	107.1

Table 7.3: Lower limits at the 95% C.L. on the universal mass scale of the SUSY particles Λ, the messenger mass scale M_{mess}, and the gravitino, neutralino, and slepton masses as functions of the number of messenger pairs N_{mess}. The limits were derived from a scan over the parameter space of the minimal GMSB model, assuming the $\tilde{\chi}_1^0$ NLSP scenario with $L_{\tilde{\chi}_1^0} \leq 100\,\mathrm{m}$.

and had a negligible effect on the derived limits.

In the framework of the MGM model, the cross section limits can be translated into an excluded region in the $(c\tau_{\tilde{\chi}_1^0}, m_{\tilde{\chi}_1^0})$ plane. Here, $\tau_{\tilde{\chi}_1^0}$ denotes the proper lifetime of the neutralino, which is related to mean decay length in the laboratory frame through $L_{\tilde{\chi}_1^0} = \gamma\beta c\tau_{\tilde{\chi}_1^0}$. As shown in Figure 7.17d, neutralino masses below 88.6 GeV were excluded for $c\tau_{\tilde{\chi}_1^0}$ values smaller than 100 m.

The results of this search can also be interpreted in the framework of the minimal gauge-mediated SUSY breaking (GMSB) model. The assumptions and parameters of this model were described in Section 3.1.3 (p. 38).

To set limits on the model parameters and masses of SUSY particles, a scan over the GMSB parameter space was performed [197]. In total, $5.6 \cdot 10^6$ points in the parameter space were tested. At each point the complete mass spectrum, production cross sections, and branching ratios were calculated using the `ISAJET` program [198]. A point in the parameter space was excluded if it was kinematically accessible and the expected $\mathrm{e^+e^-} \to \tilde{\chi}_1^0\tilde{\chi}_1^0$ cross section was higher than my cross section limit for the corresponding $\tilde{\chi}_1^0$ mass. In addition, the Higgs boson masses and couplings were also computed and the lower limit on the Higgs mass, $m_\mathrm{h} > 84.5$ GeV [199], was used to extend the exclusion domain. The results of this scan are summarized in Table 7.3.

7.3 Searches for Extra Dimensions

Models with large extra dimensions predict a gravity scale (M_D) as low as the electroweak scale. In such models, gravitons may be produced via the $e^+e^- \to \gamma G$ process as described in Section 3.3.1 of Chapter 3. Since the graviton would escape undetected, this reaction could provide a new source of single-photon events at LEP.

To calculate the predicted signal rates and distributions, I used the results of the single- and soft-photon selections (Sections 6.3.8 and 6.5). The efficiency for the $e^+e^- \to \nu\bar{\nu}\gamma$ process was derived in an x_γ *vs.* $|\cos\theta_\gamma|$ grid similar to that of Table D.3 (p. 296). This grid, together with the analytical differential cross section (see Equation 3.29 p. 57), allowed me to calculate the signal efficiencies and expectations as a function of M_D and the number of extra dimensions (n). Effects of initial-state radiation were taken into account using the radiator function given in Reference [20].

To check the validity of this method, I applied the same procedure to the gravitino pair-production process, $e^+e^- \to \tilde{G}\tilde{G}\gamma$. The kinematic distributions of photons from this process were similar to those of the extra dimensions signals. However, in this case the signal expectations could also be obtained from a large sample of fully simulated Monte Carlo events (see Section 7.2.2). The signal efficiencies calculated using the grid method and the Monte Carlo sample were found to be consistent within their statistical errors.

Since the energy spectrum of the photons produced in the $e^+e^- \to \gamma G$ process was expected to be soft, only events from the single- and soft-photon samples with $x_\gamma < 0.5$ were considered. In total, I selected 1,286 such events in data with 1,303.6 events expected from Standard Model processes. Expected effects of extra dimensions on the energy and polar angle distributions are shown in Figure 7.18. The signal efficiency was found to slightly decrease with n: from 63% for $n = 2$ to 59% for $n = 8$.

No excess was observed beyond the Standard Model expectation, and limits on the graviton-photon emission were derived from a likelihood fit to the x_γ *vs.* $|\cos\theta_\gamma|$ two-dimensional distribution. Since the signal cross section scaled with $(1/M_D)^{n+2}$, this variable was taken as the fit parameter. The results of the fit are given in Table 7.4,

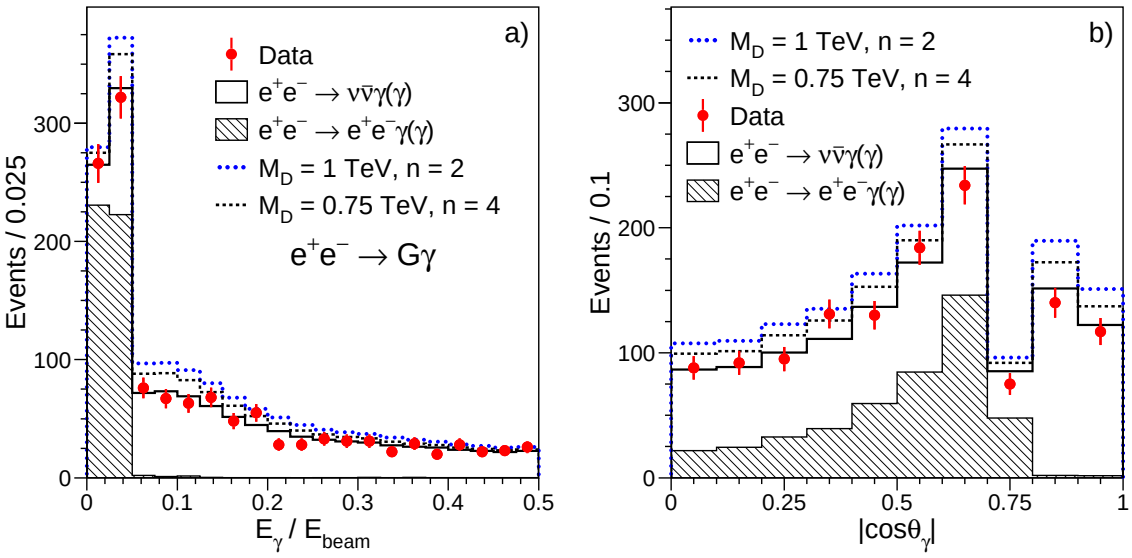

Figure 7.18: Distributions of a) the ratio of the photon energy to the beam energy (x_γ) and b) the photon polar angle for events with $x_\gamma < 0.5$ from the combined single- and soft-photon sample. Signals for extra dimensions for $M_D = 1$ TeV and 0.75 TeV and $n = 2$ and 4 are also shown.

where the error on the parameter $(1/M_D)^{n+2}$ corresponds to a change in the negative log-likelihood with respect to its minimum of 0.5. Table 7.4 also lists the observed and expected limits on the new scale of gravity and on the size of extra dimensions. These limits were derived following the statistical procedure described in Section 7.2.1.

The combination of my results with those of other LEP experiments will be described in Appendix E. The LEP combined search excluded, at the 95% C.L., the gravity scales below 1.6 TeV and 0.66 TeV for $n = 2$ and $n = 6$, respectively.

Searches for Branons

In models with extra dimensions the presence of a three-dimensional brane as an additional physical body leads to the appearance of additional degrees of freedom. These may manifest themselves as new scalar particles, $\tilde{\pi}$, called branons. As described in Section 3.3.2, branons could be pair-produced at LEP in the reaction $e^+e^- \to \tilde{\pi}\tilde{\pi}\gamma$. Because branons do not interact in the detector, this process would to lead to a single photon and missing energy in the final state. The signal cross section depends only

n	$(1/M_D)^{n+2}$	M_{D95} (TeV)	M_{exp} (TeV)	R_{95} (cm)	CL_b
2	-0.03 ± 0.10 TeV $^{-4}$	1.50	1.49	2.1×10^{-2}	43%
3	-0.10 ± 0.28 TeV $^{-5}$	1.14	1.12	2.9×10^{-7}	40%
4	-0.5 ± 1.0 TeV $^{-6}$	0.91	0.89	1.1×10^{-9}	37%
5	-2.2 ± 3.9 TeV $^{-7}$	0.76	0.75	4.2×10^{-11}	38%
6	-11.2 ± 17.7 TeV $^{-8}$	0.65	0.64	4.7×10^{-12}	37%
7	-67 ± 87 TeV $^{-9}$	0.57	0.56	1.0×10^{-12}	34%
8	-400 ± 460 TeV $^{-10}$	0.51	0.51	3.2×10^{-13}	35%

Table 7.4: Fitted values of $(1/M_D)^{n+2}$ together with the observed (M_{D95}) and expected (M_{exp}) lower limits on the gravity scale as a function of the number of extra dimensions (n). Upper limits on the size of the extra dimensions (R_{95}) are also given. All limits are at the 95% confidence level. Assuming there is no signal, CL_b gives the probability to obtain a limit on M_D better than the one observed.

on two parameters: the brane tension f and the branon mass M_π.

The signal properties were expected to be very similar to those of the graviton-photon emission considered above so that the same analysis procedure could be used. Figure 7.19a shows how the branon production was expected to affect the photon energy spectrum. Since no deviations from the Standard Model predictions were observed, limits on the branon production were derived from a fit to the x_γ *vs.* $|\cos\theta_\gamma|$ two-dimensional distribution. The region excluded in the (f, M_π) plane is shown in Figure 7.19b. In the massless branon scenario, the brane tension must be greater than 180 GeV, whereas for very elastic branes ($f \to 0$) branon masses below 103 GeV were excluded at the 95% confidence level [200].

7.4 Measurements of Gauge-Boson Couplings

In the previous sections I described how I searched for manifestations of new physics by searching for evidence of new processes leading to photonic events with missing energy. The existence of anomalous couplings between the photon and heavy gauge bosons is expected to affect the $e^+e^- \to \nu\bar{\nu}\gamma(\gamma)$ process. Therefore, such deviations

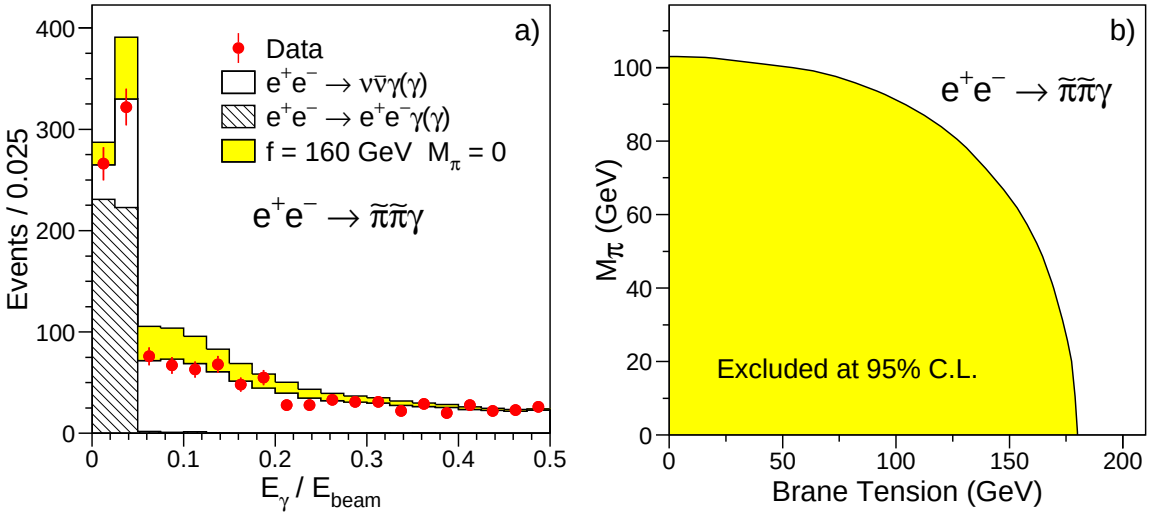

Figure 7.19: a) Distribution of the ratio of the photon energy to the beam energy (x_γ) for the combined single- and soft-photon event sample. Expected signal from the branon-photon production is also shown for $M_\pi = 0$ and $f = 160$ GeV. b) Region in the (f, M_π) plane excluded by this search.

from the Standard Model can be probed directly by measuring the total and differential cross sections of this process. Below I describe how I used my single- and multi-photon samples to extract the triple and quartic gauge-boson couplings, respectively. The corresponding event selections were described in Sections 6.3.8 and 6.4, where I also showed that the purities of the selected $\nu\bar{\nu}\gamma$ and $\nu\bar{\nu}\gamma\gamma$ event samples were estimated to be higher than 99%.

7.4.1 Searches for Anomalous Quartic Gauge Couplings

In the Standard Model self-interactions of the vector boson fields arise due to the $-\frac{1}{4}\mathbf{W}_{\mu\nu} \cdot \mathbf{W}^{\mu\nu}$ term in the electroweak Lagrangian (see Equation 2.10 p. 11). In addition to the triple gauge couplings, this term leads to quartic gauge couplings (QGCs) of the form: WWWW, WWZZ, WW$\gamma\gamma$, and WWZγ. The strength of the coupling at these vertices is specified by the $SU(2) \times U(1)$ gauge invariant form of the electroweak sector. Studying processes to which these QGCs can contribute may therefore yield further confirmation of the non-Abelian structure of the Standard Model or signal the presence of new physics at as yet unprobed energy scales. Unfortunately, the

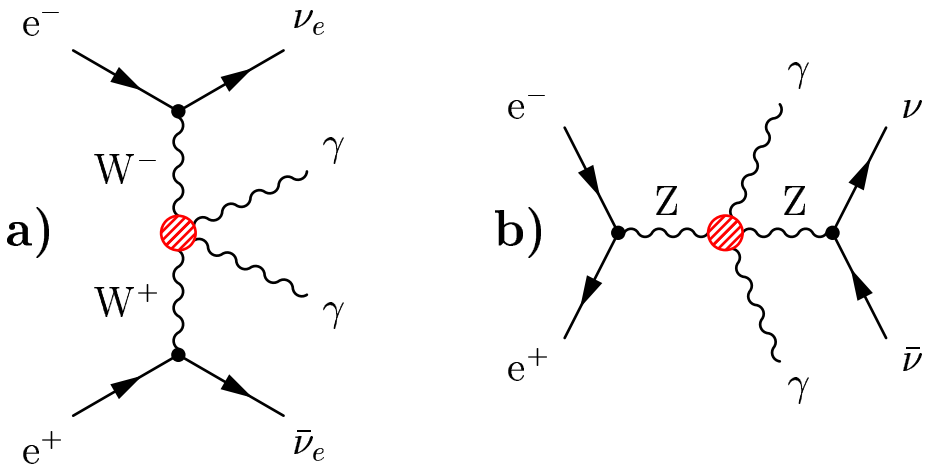

Figure 7.20: Feynman diagrams contributing to the $e^+e^- \to \nu\bar{\nu}\gamma\gamma$ process and containing the a) $W^+W^-\gamma\gamma$ and b) $ZZ\gamma\gamma$ vertices.

contributions of the Standard Model QGCs are too small to be directly observed at LEP2 energies. For instance, the contribution of the $W^+W^-\gamma\gamma$ vertex (Figure 7.20a) to the cross section of the $e^+e^- \to \nu\bar{\nu}\gamma\gamma$ process is only about 1-2 fb [201].

The triple and quartic gauge-boson couplings probe different aspects of the weak interactions. The triple gauge couplings directly test the non-Abelian gauge structure. Their possible deviations from the Standard Model predictions have been extensively studied and tightly constrained by measurements of the $e^+e^- \to W^+W^-$ production at LEP2 [202].

In contrast, the quartic couplings can be regarded as a more direct window on electroweak symmetry breaking or, more generally, on new physics which couples to electroweak bosons. In this respect it is quite possible that the quartic couplings deviate from their Standard Model values while the triple gauge couplings do not [203]. For example, if the mechanism of electroweak symmetry breaking does not reveal itself through the discovery of new particles such as the Higgs boson, supersymmetric particles, or technipions, it is possible that anomalous quartic couplings can provide the first evidence of new physics in this sector of the electroweak theory [204].

Parametrization of Quartic Gauge Couplings

The formalism for the extra genuine quartic terms has been developed in Reference [205]. Here, genuine quartic terms refer to those that give no contribution to the triple-gauge-boson vertices. In this parametrization, the two lowest dimension terms that give rise to genuine quartic couplings involving at least one photon are

$$\begin{aligned} \mathcal{L}_6^0 &= -\frac{e^2}{16}\frac{a_0}{\Lambda^2} F_{\mu\nu}F^{\mu\nu}\vec{W}^\alpha \cdot \vec{W}_\alpha, \\ \mathcal{L}_6^{\rm c} &= -\frac{e^2}{16}\frac{a_{\rm c}}{\Lambda^2} F_{\mu\alpha}F^{\mu\beta}\vec{W}^\alpha \cdot \vec{W}_\beta, \end{aligned} \tag{7.20}$$

where $F^{\mu\nu} = \partial_\mu A_\nu - \partial_\nu A_\mu$ is the photon field strength tensor. These are obtained by assuming C and P conservation and imposing the $U(1)$ gauge invariance and the global custodial $SU(2)$ symmetry that keeps the $\rho = M_W/M_Z\cos^2\theta_W$ parameter close to the measured value of 1.

The custodial $SU(2)$ field vector is given by

$$\vec{W}_\alpha = \begin{pmatrix} \frac{1}{\sqrt{2}}(W_\alpha^+ + W_\alpha^-) \\ \frac{i}{\sqrt{2}}(W_\alpha^+ - W_\alpha^-) \\ Z_\alpha/\cos\theta_W \end{pmatrix},$$

which yields in terms of the physical fields W_α^+, W_α^- and Z_α:

$$\begin{aligned} \mathcal{L}_6^0 &= -\frac{e^2}{8}\frac{a_0^{\rm W}}{\Lambda^2} F_{\mu\nu}F^{\mu\nu}W^{+\alpha}W_\alpha^- - \frac{e^2}{16\cos^2\theta_W}\frac{a_0^{\rm Z}}{\Lambda^2} F_{\mu\nu}F^{\mu\nu}Z^\alpha Z_\alpha, \\ \mathcal{L}_6^{\rm c} &= -\frac{e^2}{16}\frac{a_{\rm c}^{\rm W}}{\Lambda^2} F_{\mu\alpha}F^{\mu\beta}(W^{+\alpha}W_\beta^- + W^{-\alpha}W_\beta^+) - \frac{e^2}{16\cos^2\theta_W}\frac{a_{\rm c}^{\rm Z}}{\Lambda^2} F_{\mu\alpha}F^{\mu\beta}Z^\alpha Z_\beta\,. \end{aligned}$$

Therefore, both the $\mathcal{L}_6^0$ and $\mathcal{L}_6^{\rm c}$ Lagrangian terms give rise to the $\rm W^+W^-\gamma\gamma$ and $\rm ZZ\gamma\gamma$ interactions, which can be described by two sets of anomalous QGCs: $\{a_0^{\rm W}, a_{\rm c}^{\rm W}\}$ and $\{a_0^{\rm Z}, a_{\rm c}^{\rm Z}\}$. The $\rm W^+W^-\gamma\gamma$ and $\rm ZZ\gamma\gamma$ couplings can be assumed to be independent, as suggested by a more general treatment of quartic terms performed in Reference [206]. In all cases the strengths of the quartic couplings are proportional to $1/\Lambda^2$, where Λ is interpreted as the energy scale of the new physics.

Sensitivity of the $e^+e^- \to \nu\bar{\nu}\gamma\gamma$ Process to Anomalous QGCs

The $W^+W^-\gamma\gamma$ and $ZZ\gamma\gamma$ interactions are expected to affect the $e^+e^- \to \nu\bar{\nu}\gamma\gamma$ process in a different manner [201, 207]. The existence of $W^+W^-\gamma\gamma$ anomalous QGCs leads to the WW−fusion $e^+e^- \to \nu_e\bar{\nu}_e\gamma\gamma$ process as shown in Figure 7.20a. The majority of signal events are expected to be produced in the recoil mass region below the Z-return peak, $M_{\rm rec} \lesssim 80$ GeV, where the Standard Model background is very low.[20]

On the other hand, the existence of the $ZZ\gamma\gamma$ vertex affects the $e^+e^- \to \nu\bar{\nu}\gamma\gamma$ process via the s-channel Z exchange diagram (see Figure 7.20b). This contribution is expected to increase the production cross section in the region of the Z-return peak, $80 < M_{\rm rec} < 120$ GeV, since the Z bosons are produced mostly on-shell. Thus, the $W^+W^-\gamma\gamma$ and $ZZ\gamma\gamma$ interactions are expected to manifest themselves in different regions of the recoil mass spectrum. However, in both cases the anomalous contributions would lead to an excess of multi-photon events with two energetic photons.[21]

Figure 7.21a shows that the production cross section depends quadratically on the anomalous QGCs. Figures 7.21a,b also show that the size of anomalous contributions increases rapidly with the center-of-mass energy.

In order to search for manifestations of anomalous QGCs, I used the sample of multi-photon events selected at $\sqrt{s} = 189 - 208$ GeV as described in Section 6.4. The Standard Model contributions were further suppressed by requiring that the recoil mass to the multi-photon system should be below 140 GeV, $M_{\rm rec} < 140$ GeV, and the energy of the second most energetic photon should be above 5 GeV, $E_{\gamma_2} > 5$ GeV.

After these cuts, 38 events were selected in the data while 45.4 events were expected from the Standard Model $e^+e^- \to \nu\bar{\nu}\gamma\gamma$ process. In this analysis the Standard Model predictions and anomalous contributions were simulated using the latest version of the `NUNUGPV` Monte Carlo program [207]. The independent `KKMC` program was used as a cross check on the Standard Model expectations.

[20] In the Standard Model the reaction $e^+e^- \to \nu\bar{\nu}\gamma\gamma$ proceeds mainly via initial state radiation from the incoming electrons and positrons. As discussed in Section 2.2.2, the recoil mass distribution has a peak near $M_{\rm rec} \simeq M_Z$, while the energy spectrum for the second most energetic photon is expected to be soft.

[21] The form of the quartic terms $\mathcal{L}_6^0$ and $\mathcal{L}_6^c$ dictates that anomalous contributions to the $\nu\bar{\nu}\gamma\gamma$ matrix element scale linearly with the energy of the photons [201].

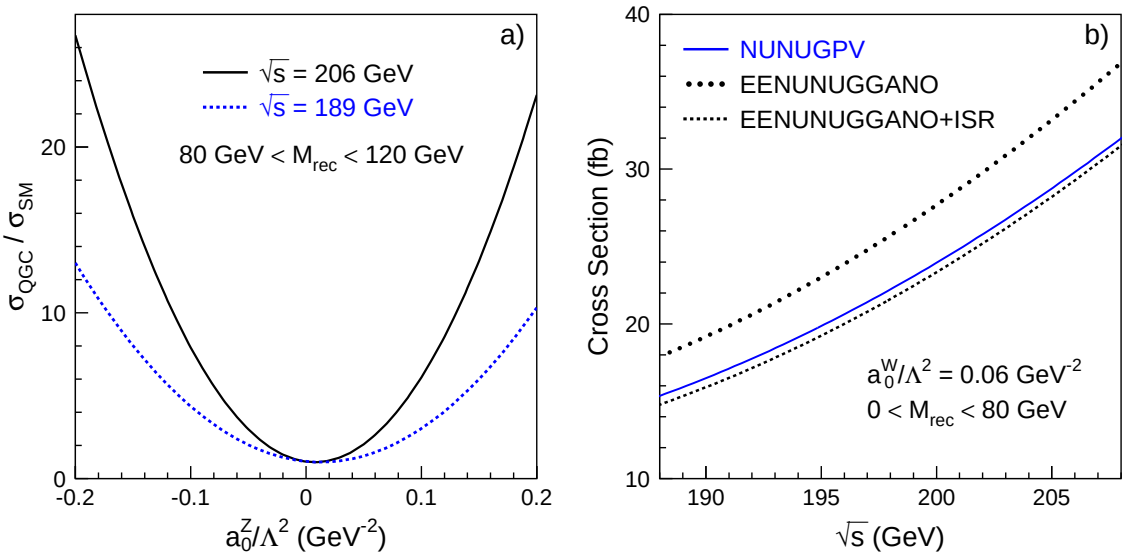

Figure 7.21: a) The ratio of the accepted $e^+e^- \to \nu\bar{\nu}\gamma\gamma$ cross section to the Standard Model prediction as a function of the coupling a_0^Z/Λ^2. The cross sections were calculated with the `NUNUGPV` program after applying the kinematic cuts $E_{\gamma_2} > 5$ GeV and $80 < M_{\rm rec} < 120$ GeV. b) The accepted cross section as a function of the $\sqrt{s}$ for $a_0^W/\Lambda^2 = 0.06$ GeV^{-2}, as predicted by the `NUNUGPV` and `Eenunuggano` programs. In this case the kinematic cuts were $E_{\gamma_2} > 5$ GeV and $M_{\rm rec} < 80$ GeV.

Figure 7.22 shows the obtained recoil mass and E_{γ_2} spectra for the selected multi-photon sample. The expected effects of anomalous QGCs on these distributions are also shown. In both cases the data were well described by the Standard Model expectations.

Fit Method and Systematic Errors

Constraints on anomalous QGCs were derived using the binned maximum likelihood method described by Equation 7.6 (p. 198). The fits were performed using two-dimensional $M_{\rm rec}$ *vs.* E_{γ_2} distribution. For a given set of quartic couplings $\Psi_{\rm fit}$ varied in the fit, the expectation was calculated by reweighting each Monte Carlo event with the ratio

$$R(p_n, \Psi_{\rm fit}, \Psi_{\rm gen}) = \frac{|\mathcal{M}(p_n, \Psi_{\rm fit})|^2}{|\mathcal{M}(p_n, \Psi_{\rm gen})|^2}, \qquad (7.21)$$

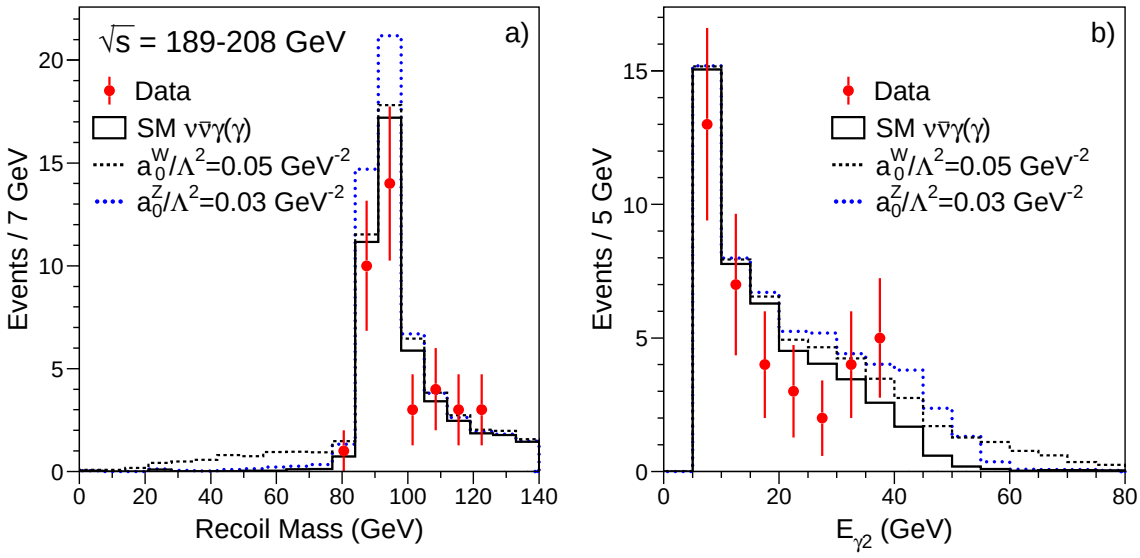

Figure 7.22: a) $M_{\rm rec}$ and b) E_{γ_2} spectra of the accepted multi-photon events. Also shown are the effects of possible anomalous QGCs for $a_0^{\rm W}/\Lambda^2 = 0.03$ GeV^{-2} and $a_0^{\rm W}/\Lambda^2 = 0.05$ GeV^{-2}. In each case the other three anomalous QGCs were set to zero.

where $\mathcal{M}$ is the matrix element computed with the NUNUGPV program [207] using the generated four-momenta p_n and $\Psi_{\rm gen}$ denotes the QGC values with which this event was originally generated. The fitted values of couplings were then determined by maximizing the log-likelihood function.

One-parameter fits were performed by allowing one coupling to vary while fixing the others to the Standard Model values of zero. For such fits the 68% and 95% confidence intervals were obtained by finding the values of the fitted coupling that corresponded to a change in the negative log-likelihood with respect to its minimum of 0.5 and 1.92, respectively[22] (see also Equation 7.7 p. 199).

To estimate the systematic uncertainties on the measured couplings, I used the following method [185]. Let us assume that z is a parameter (e.g., selection efficiency) known with some limited accuracy: $z = z_0 \pm \sigma_z$. To estimate the impact of this systematic uncertainty σ_z on the measurement of a coupling α, the fit is repeated by

[22] For a non-Gaussian likelihood function these intervals do not correspond exactly to the claimed coverage probability [184]. However, this method was adopted by the L3 and LEP electroweak groups since it was relatively simple to use for the combination of several channels or experiments.

setting z in the Monte Carlo simulation to z_0, $z_0 + \sigma_z$ and $z_0 - \sigma_z$, giving

$$\begin{aligned} \alpha(z_0) &= \alpha_0 \pm \sigma_0 \,, \\ \alpha(z_0 + \sigma_z) &= \alpha_0 + \Delta\alpha_+ \pm \sigma_+ \,, \\ \alpha(z_0 - \sigma_z) &= \alpha_0 + \Delta\alpha_- \pm \sigma_- \,, \end{aligned}$$

where, for simplicity, the fit error is assumed to be symmetric and taken to be half the 68% C.L. interval. Then, the systematic error assigned to this source of uncertainty can be estimated as

$$(\delta\alpha)_z^2 = \left(\frac{|\Delta\alpha_+| + |\Delta\alpha_-|}{2}\right)^2 + \max\left(\frac{\sigma_+^2 + \sigma_-^2 - 2\sigma_0^2}{2}, 0\right) . \qquad (7.22)$$

Thus, this method takes into account both the change in the sensitivity of the fit and the shift in the position of the maximum of the likelihood.

The main sources of systematic uncertainty are described below.

Contributions from anomalous QGCs: This error was estimated by calculating differences between the predictions of the `NUNUGPV` program and other theoretical calculations. For the $W^+W^-\gamma\gamma$ couplings, the `NUNUGPV` was compared with the `Eenunuggano` program [201] as shown in Figure 7.21b. For the $ZZ\gamma\gamma$ couplings, the predictions of Bélanger et al. [206] were used as a cross check. In both cases, the theoretical uncertainty on the signal cross section was estimated to be $\pm 4\%$.

Standard Model $\nu\bar{\nu}\gamma\gamma$ cross section: The theoretical uncertainty on the accepted cross section of the Standard Model reaction $e^+e^- \to \nu\bar{\nu}\gamma\gamma$ was assigned to be $\pm 5\%$ [24]. This estimate agreed well with the observed difference between the expectations of the `NUNUGPV` and `KKMC` Monte Carlo generators: 45.4 and 47.8 events, respectively.

Experimental uncertainties: The dominant experimental uncertainties came from the modelling of photon conversion effects and the systematic error on the trigger efficiency. The other considered systematic effects were the same as those studied in the context of the $e^+e^- \to \nu\bar{\nu}\gamma(\gamma)$ cross section measurement (see Table 7.2). The

total systematic error on the selection efficiency was estimated to be about 1.5%

For each center-of-mass energy, a sample of 10,000 $\nu\bar{\nu}\gamma\gamma$ events was generated and processed through the full L3 simulation. As a result, the related MC statistical error was negligible. In addition, the fitting and reweighting procedures were tested by fitting large Monte Carlo samples generated for different values of anomalous QGCs. No significant biases were observed.

Limits on Anomalous QGCs

Figures 7.23a-d show the log-likelihood curves derived from one-parameter fits to the four anomalous QGCs. The following 68% confidence level results were obtained from these fits:

$$a_0^{\mathrm{Z}}/\Lambda^2 = 0.001^{+0.009}_{-0.007} \pm 0.002 \qquad a_{\mathrm{c}}^{\mathrm{Z}}/\Lambda^2 = 0.010^{+0.017}_{-0.027} \pm 0.006\,,$$
$$a_0^{\mathrm{W}}/\Lambda^2 = 0.001 \pm 0.014 \pm 0.004 \qquad a_{\mathrm{c}}^{\mathrm{W}}/\Lambda^2 = 0.000 \pm 0.038 \pm 0.009\,,$$

where the first error was statistical and the second systematic. In each measurement the systematic error was much smaller than the statistical uncertainty. The fitted couplings were found to be in good agreement with the Standard Model expectations of zero, and the corresponding 95% C.L. limits are listed in Table 7.5.

I also performed two-parameter fits to the two pairs of couplings describing the $\mathrm{ZZ}\gamma\gamma$ and $\mathrm{W^+W^-}\gamma\gamma$ vertices. In these fits, the two chosen couplings were allowed to vary simultaneously while the other pair was fixed to the Standard Model value of zero. Figure 7.24 shows the derived 95% C.L. contours which correspond to a change of 3.0 in the negative log-likelihood with respect to its minimum. The fitted parameters were found to be strongly correlated, with correlation coefficients of -56% and -70% for the $\{a_0^{\mathrm{Z}}, a_{\mathrm{c}}^{\mathrm{Z}}\}$ and $\{a_0^{\mathrm{W}}, a_{\mathrm{c}}^{\mathrm{W}}\}$ pairs of couplings, respectively. The limits obtained from the two-parameter fits are

$$-0.018\ \mathrm{GeV}^{-2} < a_0^{\mathrm{Z}}/\Lambda^2 < 0.030\ \mathrm{GeV}^{-2} \qquad -0.062\ \mathrm{GeV}^{-2} < a_{\mathrm{c}}^{\mathrm{Z}}/\Lambda^2 < 0.051\ \mathrm{GeV}^{-2},$$
$$-0.049\ \mathrm{GeV}^{-2} < a_0^{\mathrm{W}}/\Lambda^2 < 0.048\ \mathrm{GeV}^{-2} \qquad -0.135\ \mathrm{GeV}^{-2} < a_{\mathrm{c}}^{\mathrm{W}}/\Lambda^2 < 0.137\ \mathrm{GeV}^{-2}.$$

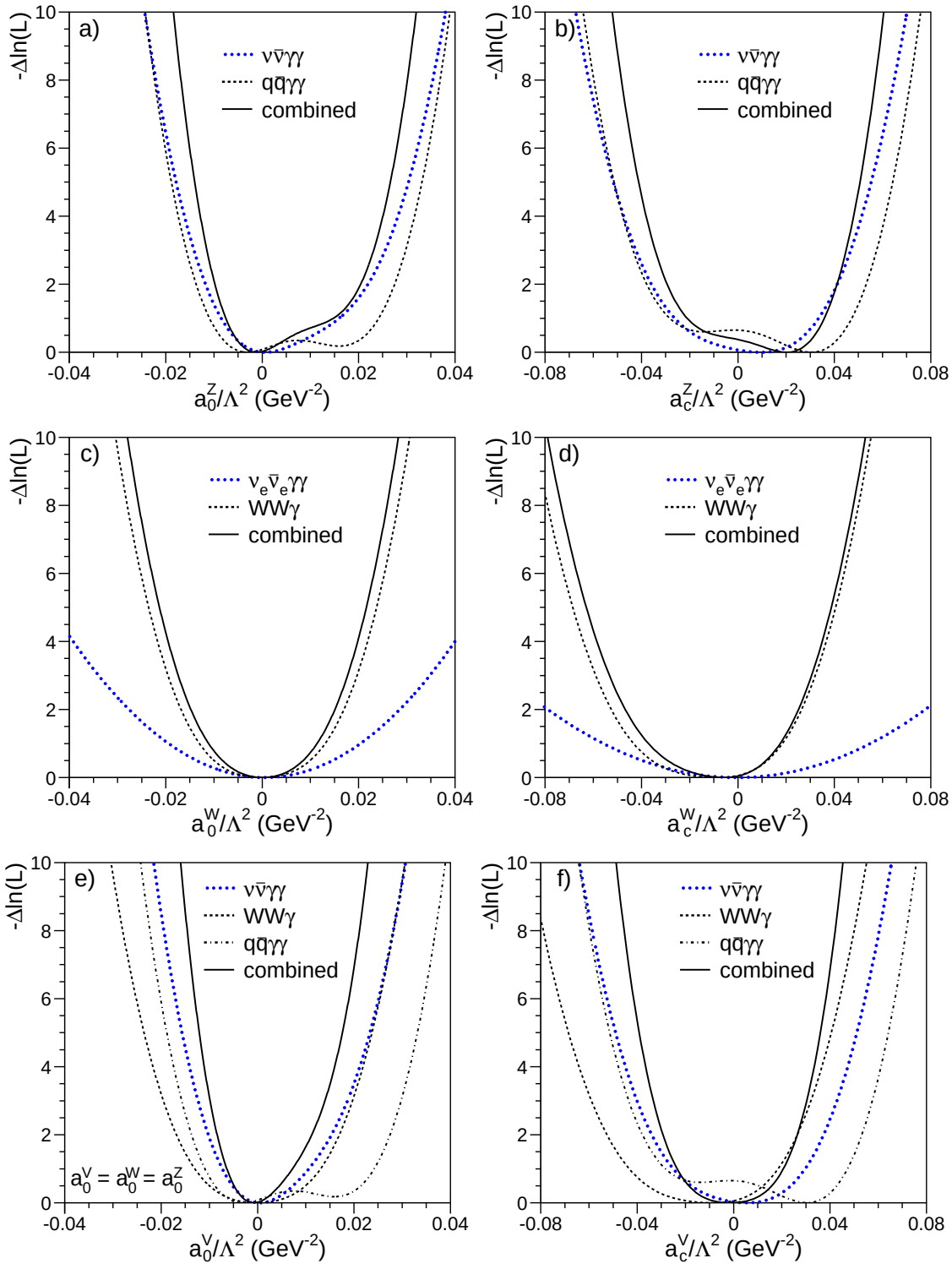

Figure 7.23: The negative log-likelihood functions of the fits for anomalous QGC. All likelihood curves include the effects of systematic uncertainties and correspond to the case where only the coupling in question is allowed to vary from zero. Contributions from different channels are indicated.

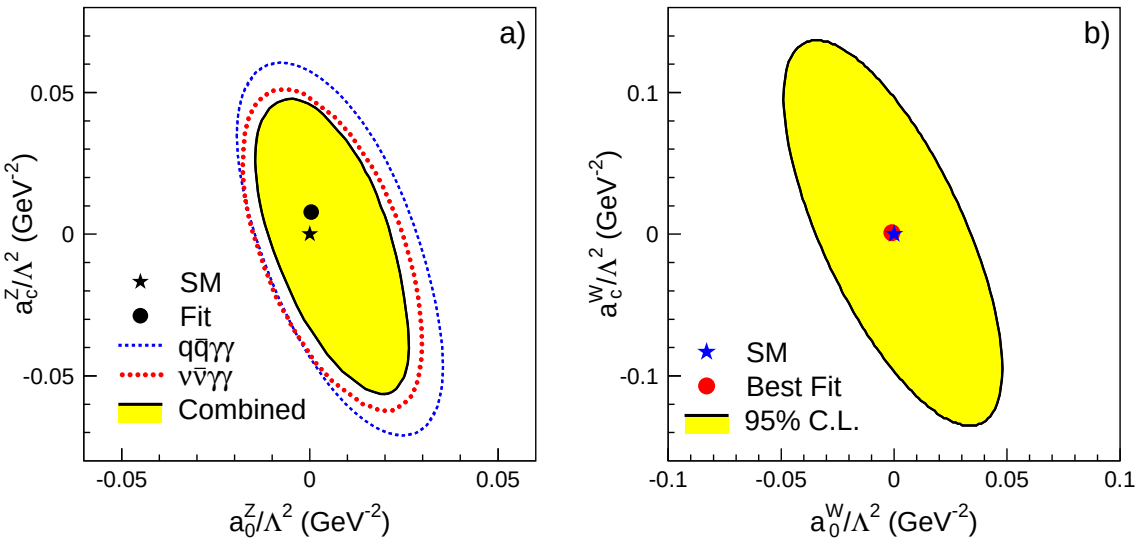

Figure 7.24: The 95% C.L. contours from the two-parameter fits for anomalous QGCs in a) $\{a_0^Z, a_c^Z\}$ and b) $\{a_0^W, a_c^W\}$ planes. In plot a) the results from the $\nu\bar{\nu}\gamma\gamma$ and $q\bar{q}\gamma\gamma$ channels and the combined contour are shown separately.

Combination with Other L3 results

Limits on anomalous quartic couplings have also been obtained by L3 from studies of two other production processes. The $e^+e^- \to W^+W^-\gamma$ process is sensitive to anomalous contributions from the s-channel photon exchange diagram containing the $W^+W^-\gamma\gamma$ vertex [208], whereas the $e^+e^- \to q\bar{q}\gamma\gamma$ process can be used to search for anomalous $ZZ\gamma\gamma$ couplings [209]. In this case the anomalous QGC diagram is the same as the one shown in Figure 7.20b, except that the Z boson decays into quarks. These two analyses also found no deviations from the Standard Model. The obtained limits on anomalous QGCs are listed in Table 7.5.

The $\nu\bar{\nu}\gamma\gamma$, $q\bar{q}\gamma\gamma$, and $W^+W^-\gamma$ channels were combined by adding together the corresponding log-likelihoods as shown in Figure 7.23. No significant sources of correlated systematic uncertainties between the three channels were found.

The individual and combined one-parameter likelihood curves for the couplings $\{a_0^Z, a_c^Z\}$ are shown in Figures 7.23a,b. The $\nu\bar{\nu}\gamma\gamma$ and $q\bar{q}\gamma\gamma$ analyses were found to have almost the same sensitivity to these anomalous QGCs. This combination gave

Process	Coupling	95% C.L. Limit
$e^+e^- \to \nu\overline{\nu}\gamma\gamma$	a_0^Z	$-0.012\,\mathrm{GeV}^{-2} < a_0^Z/\Lambda^2 < 0.022\,\mathrm{GeV}^{-2}$
	a_c^Z	$-0.035\,\mathrm{GeV}^{-2} < a_c^Z/\Lambda^2 < 0.041\,\mathrm{GeV}^{-2}$
	a_0^W	$-0.027\,\mathrm{GeV}^{-2} < a_0^W/\Lambda^2 < 0.028\,\mathrm{GeV}^{-2}$
	a_c^W	$-0.077\,\mathrm{GeV}^{-2} < a_c^W/\Lambda^2 < 0.076\,\mathrm{GeV}^{-2}$
$e^+e^- \to q\bar{q}\gamma\gamma$	a_0^Z	$-0.014\,\mathrm{GeV}^{-2} < a_0^Z/\Lambda^2 < 0.027\,\mathrm{GeV}^{-2}$
	a_c^Z	$-0.037\,\mathrm{GeV}^{-2} < a_c^Z/\Lambda^2 < 0.053\,\mathrm{GeV}^{-2}$
$e^+e^- \to W^+W^-\gamma$	a_0^W	$-0.017\,\mathrm{GeV}^{-2} < a_0^W/\Lambda^2 < 0.017\,\mathrm{GeV}^{-2}$
	a_c^W	$-0.052\,\mathrm{GeV}^{-2} < a_c^W/\Lambda^2 < 0.026\,\mathrm{GeV}^{-2}$

Table 7.5: Summary of the 95% C.L. limits on the anomalous quartic couplings obtained by L3 from studies of three different production processes at LEP2. All limits were derived using one-parameter fits, and the systematic uncertainties were taken into account.

the following 95% C.L. limits on the $ZZ\gamma\gamma$ couplings:

$$-0.010\ \mathrm{GeV}^{-2} < a_0^Z/\Lambda^2 < 0.020\ \mathrm{GeV}^{-2},$$
$$-0.029\ \mathrm{GeV}^{-2} < a_c^Z/\Lambda^2 < 0.041\ \mathrm{GeV}^{-2}.$$

The two-parameter fits to the $ZZ\gamma\gamma$ couplings were also combined. The obtained 95% C.L. contour is shown in Figure 7.24a.

In the case of the $W^+W^-\gamma\gamma$ couplings, the inclusion of the $e^+e^- \to W^+W^-\gamma$ channel considerably improved the sensitivity of the search [208]. The combined one-parameter likelihood curves are shown in Figures 7.23c,d. The corresponding 95% C.L. limits on anomalous contributions to the $W^+W^-\gamma\gamma$ vertex are

$$-0.015\ \mathrm{GeV}^{-2} < a_0^W/\Lambda^2 < 0.015\ \mathrm{GeV}^{-2},$$
$$-0.046\ \mathrm{GeV}^{-2} < a_c^W/\Lambda^2 < 0.025\ \mathrm{GeV}^{-2}.$$

As suggested in Reference [210], the couplings describing the $ZZ\gamma\gamma$ and $W^+W^-\gamma\gamma$

vertices may be identical, $a_i^{\mathrm{Z}} = a_i^{\mathrm{W}} \equiv a_i^{\mathrm{V}}$. For completeness, this scenario was also investigated. Figures 7.23e,f show the one-parameter likelihood curves obtained by combining the results from the $\nu\bar{\nu}\gamma\gamma$, $\mathrm{q\bar{q}}\gamma\gamma$, and $\mathrm{W^+W^-}\gamma$ channels. The combined likelihoods yielded the following 95% C.L. limits:

$$-0.008\ \mathrm{GeV}^{-2} < a_0^{\mathrm{V}}/\Lambda^2 < 0.011\ \mathrm{GeV}^{-2},$$
$$-0.029\ \mathrm{GeV}^{-2} < a_c^{\mathrm{V}}/\Lambda^2 < 0.026\ \mathrm{GeV}^{-2}.$$

7.4.2 Measurement of Triple Gauge Boson Couplings

The selected sample of single- and multi-photon events may also be used to measure the triple gauge couplings (TGCs) of the W boson. As shown in Figure 7.25, the $\mathrm{W^+W^-}\gamma$ vertex contributes to the $\mathrm{e^+e^-} \to \nu_{\mathrm{e}}\bar{\nu}_{\mathrm{e}}\gamma(\gamma)$ process through photon production in W-boson fusion. Assuming electromagnetic gauge invariance, this vertex can be described by two CP-conserving couplings, κ_γ and λ_γ [211].

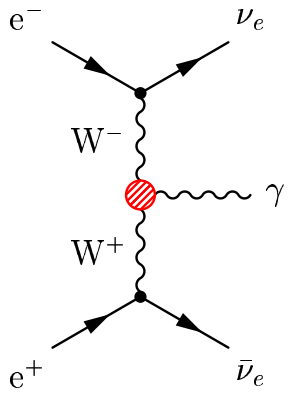

Figure 7.25: Feynman diagram of the WW−fusion $\mathrm{e^+e^-} \to \nu_{\mathrm{e}}\bar{\nu}_{\mathrm{e}}\gamma$ process.

Deviations from the Standard Model values of $\kappa_\gamma = 1$ and $\lambda_\gamma = 0$ could be detected by studying the photon energy spectrum. In particular, such anomalous couplings were expected to lead to an excess of events with photon energies above those corresponding to the radiative return to the Z. Figure 7.26a shows that the measured energy spectrum was in good agreement with the Standard Model expectation. In particular, in the region of highest sensitivity, $E_\gamma/E_{beam} > 0.86$, 4 events were found in data with 5.8 ± 1.0 events expected from background.

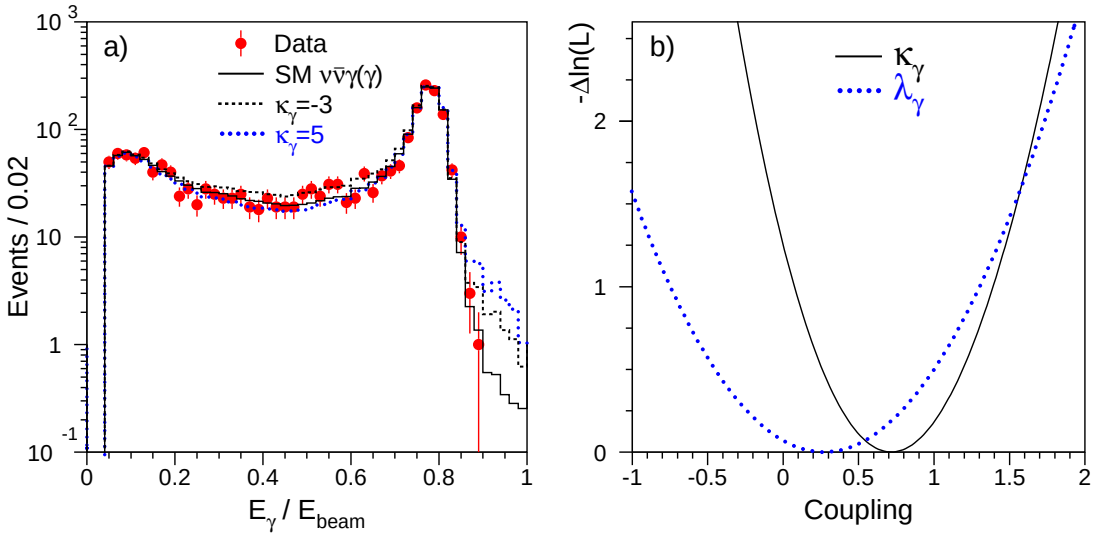

Figure 7.26: a) The energy spectrum of the combined single- and multi-photon sample. The expected effects of anomalous TGCs are also shown for $\kappa_\gamma = -3$ and $\kappa_\gamma = 5$. In each case the λ_γ coupling was set to zero. b) The negative log-likelihood functions for one-parameter fits to κ_γ and λ_γ.

To extract the triple gauge couplings, I used the same methods as in the QGC analysis described in the previous section. The KKMC program was used to simulate the Standard Model process $e^+e^- \to \nu\bar{\nu}\gamma(\gamma)$, while the effects of TGC's were estimated using a reweighting procedure from Reference [212]. Figure 7.26b shows the log-likelihood curves obtained from the binned maximum likelihood fits to the photon energy and polar angle. The triple gauge couplings were measured to be

$$\begin{aligned} \kappa_\gamma &= 0.7 \pm 0.5\,(stat) \pm 0.3\,(syst)\,, \\ \lambda_\gamma &= 0.3 \pm 0.7\,(stat) \pm 0.4\,(syst)\,, \end{aligned}$$

in good agreement with the Standard Model prediction of $\kappa_\gamma = 1$ and $\lambda_\gamma = 0$.[23] The systematic uncertainties were dominated by uncertainties on the selection efficiency (see Section 7.1.1), on the $\nu\bar{\nu}\gamma$ cross section [24], and on the TGC modelling [213].

[23] A much more precise result was obtained by L3 from a study of W-pair production at LEP2: $\kappa_\gamma = 1.01 \pm 0.07$ and $\lambda_\gamma = -0.02 \pm 0.03$ [202]. However, the W-pair production was also sensitive to the WWZ couplings which could not be disentangled from the WWγ couplings. Moreover, in this study the triple-gauge-boson vertices were tested at a momentum-transfer scale of $Q^2 = s$, while the $\nu\bar{\nu}\gamma$ production occurred at $Q^2 = 0$.

Chapter 8

Summary and Conclusions

In this thesis I examined the production of events consisting of one or more photons and characterized by missing transverse energy using the L3 detector at the LEP electron-positron collider. I analyzed 619 pb^{-1} of data collected from 1998 through 2000 at center-of-mass energies $\sqrt{s} = 189 - 208$ GeV, the highest energies ever attained in an e^+e^- collider. Using these data, I selected a high-purity sample of well-reconstructed single- and multi-photon events with missing energy. This allowed me to study the production of neutrinos in e^+e^- collisions and to search for manifestations of new physics processes in a previously inaccessible range.

In this chapter I briefly summarize the main results of this thesis and compare them with results from other experiments. I conclude with a discussion on the potential of the upcoming Large Hadron Collider to probe the same types of physics beyond the Standard Model that I searched for in this thesis.

8.1 Summary of Results

Calibration of the BGO Calorimeter Using an RFQ Accelerator

In order to measure the energy and direction of photons, I used the BGO electromagnetic calorimeter of the L3 detector. A thorough understanding of its performance was essential for my analyses.

The Caltech L3 group pioneered a precise and rapid calibration technique using a pulsed H^- beam from a Radiofrequency Quadrupole accelerator to bombard a lithium target permanently installed inside the BGO calorimeter. The radiative capture re-

action ${}^{7}_{3}\mathrm{Li}(\mathrm{p},\gamma){}^{8}_{4}\mathrm{Be}$ produced an intense flux of 17.6 MeV photons which we used to intercalibrate the 11,000 BGO crystals on a crystal-by-crystal basis. I analyzed the calibration data collected during 1997-2000 and determined the statistical precision of the RFQ intercalibration to be approximately 1%.

The absolute calibration of the BGO calorimeter was performed using events from the Bhabha scattering process $\mathrm{e^+e^-} \to \mathrm{e^+e^-}$, which I selected in the data collected by L3 during 1995-2000. I was able to improve the calibration algorithm and achieve a calibration precision of 0.5%, both for the barrel and endcaps of the BGO calorimeter. The BGO energy resolution was measured to be

$$\frac{\sigma_E}{E} = \frac{3.2\,\%}{\sqrt{E}} \oplus 0.85\,\% \;\; (E \text{ in GeV}),$$

giving a 1% resolution for photons with energies above 30 GeV. Equally important was the elimination of the resolution tails which substantially increased the sensitivity of my searches for new physics. For comparison, calibrations used during 1989-1996 provided a resolution of approximately 2% with significant resolution tails.

By measuring the effects of the BGO aging and non-linearity, I was able to determine the photon energy scale to a precision better than 0.5%. This significantly reduced the associated systematic uncertainty in my measurements of the cross section of the reaction $\mathrm{e^+e^-} \to \nu\bar{\nu}\gamma(\gamma)$. I also found that the detector simulation program substantially underestimated the effects of shower leakage from the BGO into the hadron calorimeter. To address this problem, I developed a dedicated correction procedure.

Beginning in 1997, the RFQ calibration was used in the L3 data reconstruction and was shown to improve the quality of several physics analyses.[1] The experience gained in calibrating the BGO calorimeter is now successfully used for the calibration of the CMS lead tungstate calorimeter [166, 167].

[1]Including searches for singlet heavy neutrinos in the decay channel $N \to \mathrm{eW}$, where the implementation of the RFQ calibration facilitated the suppression of the $\mathrm{W^+W^-}$ background. This work was performed in collaboration with Dr. Sergey Shevchenko (Caltech) and resulted in stringent limits on the masses and couplings of heavy singlet neutrinos [214].

Measurement of Neutrino Production

In order to study neutrino production at LEP, I selected a sample of 2,022 single- and multi-photon events with missing energy. This sample consisted almost purely of events from neutrino pair-production accompanied by the emission of one or more photons, $e^+e^- \to \nu\bar{\nu}\gamma(\gamma)$. The residual background from other Standard Model processes and cosmic contamination was estimated to be below 1%.

As part of this work, I performed studies of the detector hermeticity, trigger efficiency, photon conversion, and cosmic contamination. In particular, my study of the photon conversion in the dead material in front of the central tracker eliminated the problem of large systematic effects seen by other photonic analyses of L3. I also developed a new anti-cosmic selection scheme by combining information from both the muon chambers and the scintillation counters. This anti-cosmic selection significantly reduced contamination from cosmic ray background while retaining acceptance for the $e^+e^- \to \nu\bar{\nu}\gamma(\gamma)$ events.

The cross section of the $e^+e^- \to \nu\bar{\nu}\gamma(\gamma)$ process was determined from the number of selected events. To quantify possible deviations from the Standard Model expectations, I computed the ratio of the measured to expected cross section at each center-of-mass energy. Averaging over the eight measurements yielded

$$\left\langle \frac{\sigma^{meas}_{\nu\bar{\nu}\gamma}}{\sigma^{exp}_{\nu\bar{\nu}\gamma}} \right\rangle = 0.987 \pm 0.022\,(stat) \pm 0.010\,(syst) \pm 0.010\,(theory)\,.$$

In the Standard Model of the electroweak interactions, the reaction $e^+e^- \to \nu\bar{\nu}\gamma(\gamma)$ proceeds through s-channel Z exchange for all neutrino flavors ($\nu_l = \nu_e, \nu_\mu, \nu_\tau$) and through t-channel W exchange for electron neutrinos only. Separating out the s-channel contributions gives a direct measurement of the invisible Z width, which in turn gives the effective number of light neutrino species N_ν. By performing a likelihood fit to the kinematic distributions of the selected $\nu\bar{\nu}\gamma(\gamma)$ events, I obtained

$$N_\nu = 2.95 \pm 0.08\,(stat) \pm 0.03\,(syst) \pm 0.03\,(theory)\,,$$

in good agreement with the Standard Model prediction of $N_\nu = 3$.

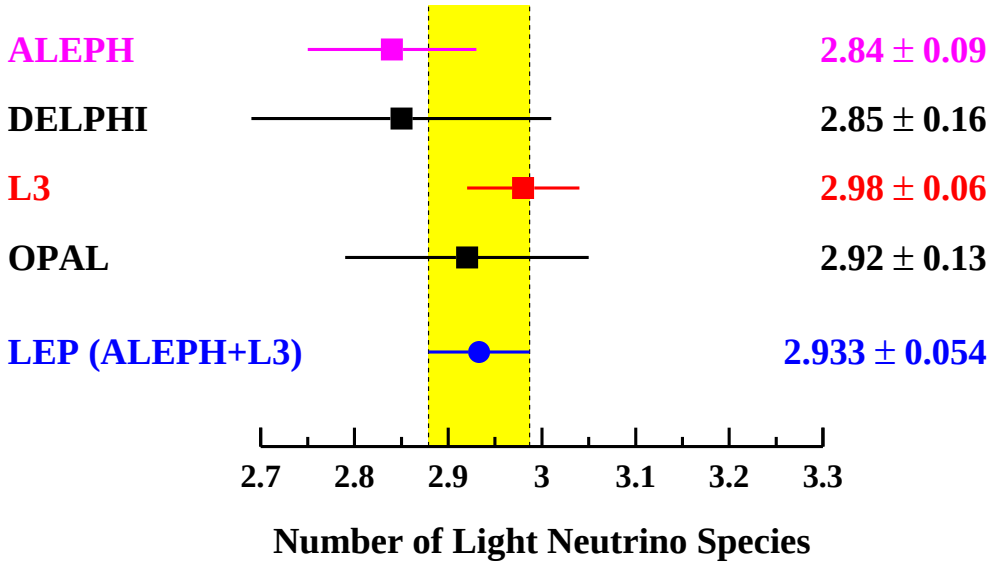

Figure 8.1: Measurements of the number of light neutrino species performed by the four LEP experiments. The error bars show combined statistical and systematic uncertainties. For comparison, the LEP−combined value of N_ν is also shown. In this combination, I considered the theoretical uncertainties to be completely correlated.

I combined my result with the L3 measurements performed at the beginning of LEP2 ($\sqrt{s} = 130 - 183$ GeV) and at LEP1 ($\sqrt{s} \simeq 91$ GeV), obtaining

$$N_\nu = 2.98 \pm 0.05\,(stat) \pm 0.04\,(syst)\,.$$

This result is in agreement with the indirect measurement of invisible Z width performed by L3 at LEP1 ($N_\nu = 2.978 \pm 0.014$ [183]), while being sensitive to different systematic and theoretical uncertainties.

The other three LEP experiments — ALEPH, DELPHI, and OPAL — have also studied the $e^+e^- \to \nu\bar{\nu}\gamma(\gamma)$ process. In Figure 8.1, I show a comparison of their measurements of N_ν with the result that I obtained in this thesis. OPAL has not the analyzed data collected during 1999-2000 at $\sqrt{s} = 192 - 202$ GeV [215], while the analysis performed by DELPHI suffered from significant systematic errors due to trigger inefficiencies and calorimeter calibration [216]. As a consequence, their measurements were substantially less accurate than my measurement. Compared to

OPAL and DELPHI, the ALEPH collaboration has reported a more precise measurement of N_ν [111]. However, combining my and ALEPH measurements provides little improvement over my result alone (see Figure 8.1).

I also used the selected sample of single- and multi-photon events to measure the size of the t-channel W exchange contributions in the reaction $e^+e^- \to \nu_e\bar{\nu}_e\gamma(\gamma)$. These contributions were parameterized by a multiplicative scale factor f_W, defined to be 1 for the Standard Model prediction. Assuming three light neutrino generations, I obtained

$$f_W = 0.99 \pm 0.06\,(stat) \pm 0.02\,(syst) \pm 0.02\,(theory)\,.$$

Contrary to the LEP1 measurement of $f_W = 0.1 \pm 0.5 \pm 0.3$ [173, 217], my measurement clearly established that the W-contributions were observed and were consistent with the expectations from the Standard Model. Therefore, this result can be interpreted as the first direct evidence for the reaction $e^+e^- \to \nu_e\bar{\nu}_e\gamma(\gamma)$.

Searches for New Physics

Photonic final states provide a rich hunting ground for new physics at e^+e^- colliders. I was able to use my samples of single- and multi-photon events to search for manifestations of Supersymmetry, extra spatial dimensions, and anomalous gauge-boson couplings. I found no evidence for physics beyond the Standard Model and derived limits on the corresponding signal cross sections and model parameters. The main results of my searches are summarized below. All limits are quoted at the 95% confidence level.

Searches for SUSY Signatures

Different mechanisms have been suggested for symmetry breaking in SUSY models [31], which imply three different scenarios: "superlight," "light," and "heavy" gravitinos. At LEP, these scenarios could give rise to several distinct single- or multi-photon and missing energy signatures.

In no-scale supergravity models such as the LNZ model [193], the gravitino can

become "superlight" (10^{-6} eV $\lesssim m_{\widetilde{\mathrm{G}}} \lesssim 10^{-4}$ eV), leading to a sizable cross section for the reaction $\mathrm{e^+e^-} \to \widetilde{\mathrm{G}}\tilde{\chi}_1^0$ with $\tilde{\chi}_1^0 \to \widetilde{\mathrm{G}}\gamma$. I searched for this process and excluded gravitino masses below 10^{-5} eV for neutralino masses below 175 GeV.

Models with superlight gravitinos may also lead to pair-production of gravitinos accompanied by a photon from initial-state radiation, $\mathrm{e^+e^-} \to \widetilde{\mathrm{G}}\widetilde{\mathrm{G}}\gamma$ [72]. Even if the masses of all other SUSY particles were above $\sqrt{s}$, this process could still provide a means to detect Supersymmetry at LEP. My search resulted in the following lower limit on the gravitino mass:

$$m_{\widetilde{\mathrm{G}}} > 1.35 \times 10^{-5}\ \mathrm{eV}\,,$$

which in turn corresponds to a lower limit on the SUSY breaking scale $\sqrt{F} > 238$ GeV. OPAL [215] and DELPHI [216] have also searched for this process, excluding gravitino masses below 0.87×10^{-5} eV and 1.09×10^{-5} eV, respectively. In addition, the CDF experiment at the Tevatron $p\bar{p}$ collider performed a search for the $q\bar{q} \to \widetilde{\mathrm{G}}\widetilde{\mathrm{G}}\gamma$ process and set the following limit: $m_{\widetilde{\mathrm{G}}} > 1.17 \times 10^{-5}$ eV [218].

In gravity-mediated SUSY breaking models (SUGRA) the lightest neutralino is expected to be the lightest supersymmetric particle (LSP). This scenario may lead to a new source of multi-photon events from the reaction $\mathrm{e^+e^-} \to \tilde{\chi}_2^0\tilde{\chi}_2^0$, followed by the decay $\tilde{\chi}_2^0 \to \tilde{\chi}_1^0\gamma$ [62]. I found no evidence for this process and ruled out most of the SUSY parameter space allowed for the SUGRA interpretation of the rare ee$\gamma\gamma$ event observed by CDF in 1995 (see Figure 7.11 p. 218).

In models with gauge-mediated SUSY breaking (GMSB) [55], the LSP is always a light gravitino, 10^{-2} eV $\lesssim m_{\widetilde{\mathrm{G}}} \lesssim 10^2$ eV. If the next-to-lightest supersymmetric particle is the lightest neutralino, it decays predominantly through $\tilde{\chi}_1^0 \to \widetilde{\mathrm{G}}\gamma$, and the reaction $\mathrm{e^+e^-} \to \tilde{\chi}_1^0\tilde{\chi}_1^0 \to \widetilde{\mathrm{G}}\widetilde{\mathrm{G}}\gamma\gamma$ gives rise to a multi-photon plus missing energy signature. My search resulted in the following lower limit on the neutralino mass:

$$m_{\tilde{\chi}_1^0} > 99.5\ \mathrm{GeV},$$

where I assumed the mass relations of the Minimal Gauge Model [194]. This search ruled out the GMSB interpretation of the CDF event, (see Figure 7.10b p. 218).

The other LEP experiments have also searched for this process and reported similar limits [111, 215, 216]. In addition, the Tevatron experiments have investigated the GMSB SUSY scenario by searching for anomalous production of di-photon events with missing energy. They have recently reported the following limits: $m_{\tilde{\chi}_1^0} > 93$ GeV by CDF [219] and $m_{\tilde{\chi}_1^0} > 108$ GeV by D$\emptyset$ [220].

All of the above results were obtained assuming a negligible neutralino decay length. However, for much of the GMSB parameter space the neutralino has a macroscopic lifetime. In this case, one or both of the neutralinos produced in the reaction $e^+e^- \to \tilde{\chi}_1^0\tilde{\chi}_1^0$ may decay within the sensitive volume of the detector, but at a distance from the primary vertex. I investigated this scenario by searching for events with non-pointing photons not only in the BGO but also in the hadron calorimeter of L3. I found no candidate events in data, excluding neutralino masses below 89 GeV for $\tilde{\chi}_1^0$ proper decay lengths smaller than 100 m. For this scenario, only ALEPH have reported comparable limits [111].

Searches for Extra Dimensions

Models with extra spatial dimensions [77] predict a gravity scale to be as low as the electroweak scale, naturally solving the hierarchy problem. In such models, Kaluza-Klein gravitons could be produced at LEP via the reaction $e^+e^- \to \gamma G$. Since the energy spectrum of the produced photons was expected to be soft, I extended my single-photon selection to include photons with transverse momenta as low as 1.5 GeV. For comparison, the other analyses performed at LEP had to apply a threshold cut of $P_t^\gamma \geq 5 - 7$ GeV. I found no evidence of extra dimensions, excluding gravity scales as high as 1.5 TeV. These limits are substantially tighter than those derived by other LEP experiments (see Table E.2 p. 304).

I also searched for branons $\tilde{\pi}$, new stable particles expected to be produced by brane fluctuations in extra spatial dimensions [82]. In this model, extra dimensions would manifest themselves at LEP through the reaction $e^+e^- \to \tilde{\pi}\tilde{\pi}\gamma$, leading to a single-photon signature. In the massless branon scenario, my search excluded brane tensions below 180 GeV. This is currently the best limit on branon production.

Measurements of Gauge-Boson Couplings

The existence of anomalous couplings between the photon and heavy gauge bosons would affect both the total cross sections and the differential distributions of the reactions $e^+e^- \to \nu\bar{\nu}\gamma$ and $e^+e^- \to \nu\bar{\nu}\gamma\gamma$.

In order to constrain possible anomalous quartic gauge couplings, I used the results of my multi-photon analysis. Combining with previous L3 results from studies of the $q\bar{q}\gamma\gamma$ and $W^+W^-\gamma$ final states, I obtained the following limits on the anomalous coupling parameters:

$$-0.010\ \text{GeV}^{-2} < a_0^Z/\Lambda^2 < 0.020\ \text{GeV}^{-2}, \quad -0.029\ \text{GeV}^{-2} < a_c^Z/\Lambda^2 < 0.041\ \text{GeV}^{-2},$$
$$-0.015\ \text{GeV}^{-2} < a_0^W/\Lambda^2 < 0.015\ \text{GeV}^{-2}, \quad -0.046\ \text{GeV}^{-2} < a_c^W/\Lambda^2 < 0.025\ \text{GeV}^{-2},$$

where Λ is the energy scale of new physics. The analysis by OPAL has established similar bounds on the anomalous $ZZ\gamma\gamma$ couplings $\{a_0^Z, a_c^Z\}$ [221]. However, our limits on the $W^+W^-\gamma\gamma$ couplings $\{a_0^W, a_c^W\}$ are more stringent than those obtained by other LEP experiments.

I also used the results of my single- and multi-photon analyses to probe the electromagnetic couplings of the W boson describing the triple-gauge-boson vertex $W^+W^-\gamma$. I measured these triple gauge couplings to be

$$\kappa_\gamma = 0.7 \pm 0.5\,(stat) \pm 0.3\,(syst)\,, \qquad \lambda_\gamma = 0.3 \pm 0.7\,(stat) \pm 0.4\,(syst)\,,$$

in good agreement with the Standard Model prediction of $\kappa_\gamma = 1$ and $\lambda_\gamma = 0$.

Combinations with Other LEP Experiments

The LEP collaborations have performed combinations of their results on searches for photonic signatures expected in Supersymmetry. As I discuss in Appendix E, these combinations did not result in a significant improvement over the results of my analyses alone, mainly due to the superior accuracy of the L3 BGO calorimeter which we precisely calibrated with the RFQ accelerator.

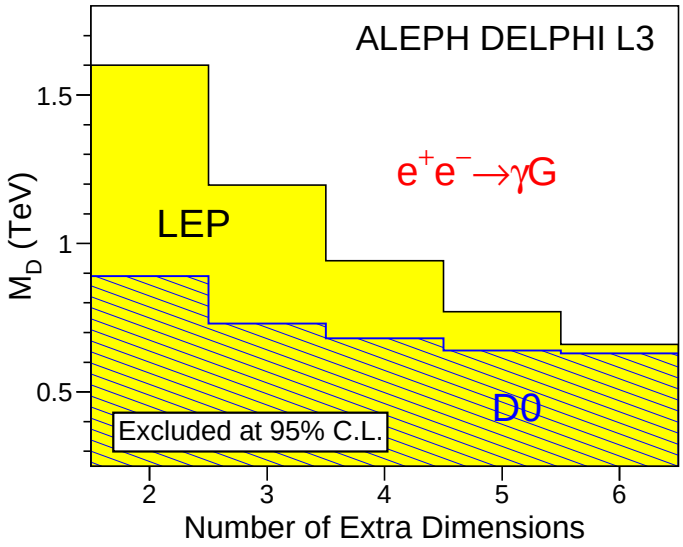

Figure 8.2: Constraints on the fundamental gravitational scale obtained by combining the LEP results on searches for extra spatial dimensions (ALEPH, DELPHI, and L3). Current limits [222] from the DØ experiment at Tevatron are also shown (CDF has quoted similar limits [223]).

As described in Section E.3, I also combined the LEP results on searches for the reaction $e^+e^- \to \gamma G$, predicted to occur in models with extra spatial dimensions. This LEP–combined search excluded gravity scales below between 1.6 TeV and 0.66 TeV for the number of extra dimensions (n) between 2 and 6. Figure 8.2 shows that for $n < 6$ the LEP limits are the best bounds to date on direct graviton emission in collider experiments.

8.2 Prospects at LHC

The Large Hadron Collider is scheduled to begin operation in 2007, with the first physics runs in early 2008. The LHC will collide proton beams at a center-of-mass energy of 14 TeV. After the first year of data taking, its two main detectors — CMS [224] and ATLAS [225] — are expected to collect about 10 fb^{-1} of integrated luminosity, which will increase to 100 fb^{-1} per year during the second and third years. In this section, I briefly describe the projected physics reach of these experiments with an emphasis on the new physics models I considered in this thesis.

The main motivation for building the LHC is to shed light on the mechanism responsible for electroweak symmetry breaking. The mass of the Standard Model Higgs should be above the current experimental limit from LEP, $M_H > 114.4$ GeV, and below the unitarity limit, $M_H \lesssim 1$ TeV. The CMS and ATLAS experiments have been designed to discover a Higgs boson in this mass range after just one year of physics running [226].

The LHC is also expected to provide a definitive answer on the existence of TeV-scale Supersymmetry. The squark and gluino production cross sections are expected to be as high as several hundred fb. If these SUSY particles are lighter than about 1.5 TeV, they should be discovered within the first few months or even weeks of data taking [226, 227]. The existence of extra spatial dimensions would lead to the emission of a graviton and a hadronic jet: $q\bar{q} \to g\mathrm{G}$, $qg \to q\mathrm{G}$, and $gg \to q\mathrm{G}$. With about 100 fb^{-1} of data, the LHC experiments should be able to detect this process for gravitational scales below $5-10$ TeV [228]. Finally, the quartic gauge-boson couplings will be probed by studying the vector-boson fusion processes. This analysis is expected to be sensitive to anomalous quartic couplings as low as 10^{-5} GeV^{-2} [229], improving the current limits from LEP by three orders of magnitude.

8.3 Conclusion

In this thesis I have studied the production of photonic events with missing energy in $\mathrm{e^+e^-}$ collisions at LEP. The results of my studies were reported in eight publications [149, 200, 202, 208, 230] and three notes from the LEP working groups [231, 232].

Within the accuracy of my measurements, no deviations from the Standard Model predictions were observed. As of this writing, the same holds true for other physics analyses performed at LEP or any other collider experiments. The upcoming Large Hadron Collider will provide the first exciting opportunity to investigate the production of elementary particles at multi−TeV scales. The LHC is bound to either confirm the Standard Model by discovering the Higgs boson or challenge and extend our present understanding of Nature's laws and principles.

Appendix A

Monte Carlo Simulation of Single- and Multi-Photon Events

A theoretical description of the reaction $e^+e^- \to \nu\bar{\nu}\gamma(\gamma)$ was given in Chapter 2. In this appendix I describe in detail the algorithms used to simulate the higher-order QED corrections and give a formula for the differential cross section for the $\mathcal{O}(\alpha)$ process $e^+e^- \to \nu\bar{\nu}\gamma$.

A.1 The Reaction $e^+e^- \to \nu\bar{\nu}\gamma$ at Tree Level

In order to achieve an accurate simulation of the single- and multi-photon production at LEP, one needs to know the exact cross sections of the reactions $e^+e^- \to \nu\bar{\nu}\gamma$ and $e^+e^- \to \nu\bar{\nu}\gamma\gamma$ which correspond to the tree-level (*bare*) single- and double-photon emissions. Neglecting the electron mass and photon radiation from the W boson propagator in the t–channel,[1] the differential cross section of the bare single-photon emission,

$$e^+(p_+) + e^-(p_-) \longrightarrow \bar{\nu}(q_+) + \nu(q_-) + \gamma(k), \tag{A.1}$$

was calculated analytically in Reference [233] and is given by

$$\frac{d\sigma}{d\cos\theta_\gamma\, dE_\gamma} = \frac{G_F^2\,\alpha}{6\pi^2}\frac{s'}{s^2 E_\gamma \sin^2\theta_\gamma}\left[(s-\kappa_+)^2 F(\eta_+) + (s-\kappa_-)^2 F(\eta_-)\right], \tag{A.2}$$

[1] At LEP2 energies, $\sqrt{s} \simeq 200$ GeV, photon emission from the W boson in the t–channel adds only about 0.5% to the total cross section of this process [18]. As shown in Figure 2.6e, this diagram contains two W propagators and, thus, is suppressed by an additional factor of $1/M_W^2$. However, it should be noted that photon radiation from the W propagator is included in the calculation of the exact matrix elements used in the KKMC [17] and NUNUGPV [27] MC event generators.

with

$$\eta_{\pm} = \frac{s - \kappa_{\pm}}{M_W^2}\,, \tag{A.3}$$

$$F(\eta_{\pm}) = N_\nu \left(g_L^2 + g_R^2\right)\frac{\mathrm{M_Z}^4}{|Z|^2} + 3g_L\frac{M_Z^2\,\mathrm{Re}Z}{|Z|^2}\frac{1}{\eta_{\pm}}\left[3 + \frac{2}{\eta_{\pm}} - 2\left(1 + \frac{1}{\eta_{\pm}}\right)^2 \ln\left(1 + \eta_{\pm}\right)\right]$$

$$+ \frac{3}{\eta_{\pm}^2}\left[\left(1 + \eta_{\pm}\right)\left(1 - \frac{2}{\eta_{\pm}}\ln\left(1 + \eta_{\pm}\right)\right) + 1\right]\,, \tag{A.4}$$

where E_γ and θ_γ are the energy and the polar angle of the emitted photon, N_ν denotes the number of neutrinos species, $g_R = \sin^2\theta_W$, and $g_L = -\frac{1}{2} + \sin^2\theta_W$. The following notation is used in the above equations:

$$\begin{aligned} s &= (p_+ + p_-)^2\,, \\ s' &= (q_+ + q_-)^2\,, \\ \kappa_{\pm} &= 2p_{\pm}k \;=\; 2E_{\mathrm{e}}E_\gamma\left(1 \pm \cos\theta_\gamma\right)\,, \\ Z &= s' - \mathrm{M_Z}^2 + i\mathrm{M_Z}\Gamma_{\mathrm{Z}}\,. \end{aligned} \tag{A.5}$$

The three terms of Equation A.4 are identified easily within the Feynman calculus: the first one describes the two s–channel Z exchange diagrams (Figure 2.6a,b), the last term corresponds to the two t–channel W exchange diagrams (Figure 2.6c,d), and the middle term accounts for the interference between the s– and t–channel diagrams.

At low photon energies and polar angles, the differential cross section given by Equation A.2 behaves[2] as $\sim 1/(E_\gamma \sin^2\theta_\gamma)$. Therefore, the cross section of this process is divergent at tree level when the photon becomes soft, $E_\gamma \to 0$ (*infrared divergence*), or when the electron (positron) and the emitted photon become collinear, $\sin\theta_\gamma \to 0$. The collinear divergence can be eliminated if we take account the nonzero electron mass, whereas the infrared divergence can be canceled by including the $\mathcal{O}(\alpha)$ diagrams containing virtual photon loops [234].

[2]It should be noted that, as expected, this expression has the same singularities as the radiator function defined in Section 2.2.2.

A.2 Structure Function Techniques

In e^+e^- collisions, the large QED corrections introduced by the undetected initial state radiation (soft and/or collinear photon emission) can be successfully described within the framework of the QED *structure functions* [235]. In this formalism, the incoming electron (positron) is assumed to consist of a "cloud" of virtual electrons and photons, and the emitted photons are assumed to be almost collinear with the incoming electron. To include effects of the ISR, the total cross section of a given process $e^+e^- \to X$ can then be calculated as

$$\sigma_{ISR}(s) = \int dx_1\, dx_2\; D(x_1,s) D(x_2,s)\, \sigma_0(x_1 x_2 s)\,, \tag{A.6}$$

where $\sigma_0(s)$ is the non-radiative cross section as a function of center-of-mass energy squared (s) and $D(x,s)$ is the structure of the incoming electron (positron), defined as the probability that, after the initial state radiation, the electron energy is equal to $x\sqrt{s}/2$.

The $\mathcal{O}(\alpha^2)$ structure function $D(x,s)$ can be obtained by solving the Lipatov–Altarelli–Parisi evolution equation and is given by [236]

$$\begin{aligned} D(x,s) &= \frac{\exp\left\{\frac{1}{2}\beta\left(\frac{3}{4}-\gamma_E\right)\right\}}{\Gamma\left(1+\frac{1}{2}\beta\right)} \frac{\beta}{2}(1-x)^{\frac{\beta}{2}-1} - \frac{\beta}{4}(1+x) \\ &+ \frac{1}{32}\beta^2\left[-4(1+x)\ln(1-x) + 3(1+x)\ln x - 4\frac{\ln x}{1-x} - 5 - x\right], \end{aligned} \tag{A.7}$$

where $\beta = 2\,\frac{\alpha}{\pi}\,(L-1)$, $L = \ln\left(s/m_e^2\right)$ is the collinear logarithm, γ_E is the Euler constant, and $\Gamma(z)$ is the gamma function. The first exponentiated Gribov–Lipatov term describes multi-photon soft emission, and the second and third terms come from the single and double hard collinear bremsstrahlung processes, respectively [21, 237].

This formalism is simple and intuitive, and it was shown that for e^+e^- processes at LEP2 energies this procedure can provide a precision of up to 0.1% [238]. However, since the structure functions are derived by integrating over all photon energies and polar angles, this approach is limited to situations in which only the ISR-corrected

cross section is of interest. Additional phase space cuts are difficult to implement. Specific photonic observables (for instance the fraction of photons above a given energy or angular threshold) are impossible to extract.

In order to address this problem, the authors of the `NUNUGPV` Monte Carlo program [27] have introduced a corrected structure function $\tilde{D}(x, \cos\theta_\gamma; s)$ which is suitable for simulating the emission of ISR photons with finite, detectable transverse momentum:

$$\tilde{D}(x, \cos\theta_\gamma; s) = D(x; s)\, f(\cos\theta_\gamma; s)\,, \tag{A.8}$$

where the angular function $f(\cos\theta_\gamma; s)$ was chosen to reproduce the leading order behavior of $1/(p_e \cdot k_\gamma)$ and $D(x; s)$ is the collinear structure function, as given by Equation A.8. The higher-order QED corrections are then included in the total cross section of the reaction $e^+e^- \to \nu\bar{\nu}\gamma(\gamma)$ as

$$\begin{aligned} \sigma_{\nu\bar{\nu}\gamma(\gamma)} &= \int dx_1 dx_2 dc_\gamma^{(1)} dc_\gamma^{(2)}\, \tilde{D}(x_1, c_\gamma^{(1)}; s)\tilde{D}(x_2, c_\gamma^{(2)}; s)\, \Theta(cuts) \\ &\quad \times (\sigma_{1\gamma} + \sigma_{2\gamma} + \sigma_{3\gamma})\ , \end{aligned} \tag{A.9}$$

where $c_\gamma \equiv \cos\theta_\gamma$; $\sigma_{1\gamma}, \sigma_{2\gamma}, \sigma_{3\gamma}$ denote the exact cross sections of the tree-level processes $e^+e^- \to \nu\bar{\nu}n\gamma$, $n = 1, 2$, and 3. The quantities $\sigma_{n\gamma}$ are evaluated for the photon energies and polar angles above a chosen set of cuts, $E_\gamma > E_{min}$ and $\sin\theta_\gamma > \sin\theta_{min}$. In Equation A.9, the function $\Theta(cuts)$ restricts the photons in $\tilde{D}(x, c_\gamma; s)$ to be below the thresholds E_{min} and θ_{min}, thus avoiding the overlap.

In a similar fashion, the QED corrected cross section of the reaction $e^+e^- \to \nu\bar{\nu}\,\gamma\gamma(\gamma)$ can be calculated as

$$\begin{aligned} \sigma_{\nu\bar{\nu}\gamma\gamma(\gamma)} &= \int dx_1 dx_2 dc_\gamma^{(1)} dc_\gamma^{(2)}\, \tilde{D}(x_1, c_\gamma^{(1)}; s)\tilde{D}(x_2, c_\gamma^{(2)}; s)\, \Theta(cuts) \\ &\quad \times (\sigma_{2\gamma} + \sigma_{3\gamma})\ . \end{aligned} \tag{A.10}$$

A.3 The YFS Scheme

A general treatment of the infrared divergences occurring in QED was given by D.R. Yennie, S.C. Frautschi, and H. Suura in their classic paper [239], which also described a very powerful and accurate way of estimating radiative corrections to high-energy processes known as the YFS scheme.

The idea behind the YFS scheme is to separate the phase space available for the emission of real photons into two regions via a cut on the photon energy such that photons are considered "infrared" if their energies are below $\varepsilon \cdot E_{beam}$. The parameter ε can be set arbitrarily low, e.g., in the KKMC generator it is typically chosen to be $\varepsilon = 10^{-5}$, so that this cut has no effect on the simulation of the real photon emission. The contribution of the infrared photons can then be used to cancel the virtual infrared divergences to all orders of α. After the cancellation, the real and virtual infrared contributions can be summed into a universal YFS form factor [240]:

$$F^{\mathrm{YFS}}(\varepsilon) \;=\; \exp\left[\frac{\alpha}{\pi}\left(\frac{1}{2}\ln\frac{s}{{m_e}^2} - 1 + \frac{\pi^2}{3}\right) + \frac{2\alpha}{\pi}\left(\ln\frac{s}{{m_e}^2} - 1\right)\ln\varepsilon\right] . \quad \text{(A.11)}$$

The emission of the visible real photons can then be corrected to reproduce exact results as given by the corresponding matrix elements. For example, for the reaction $\mathrm{e}^+(p_1)\,\mathrm{e}^-(p_2) \to \nu(q_1)\,\bar{\nu}(q_2)$, the total cross section including an arbitrary number of real and virtual photons can be calculated as

$$\begin{aligned}\sigma \;=\; & F^{\mathrm{YFS}}(\varepsilon) \int \frac{d^3\vec{q}_1}{q_1^0}\frac{d^3\vec{q}_2}{q_2^0} \sum_{n=0}^{\infty}\left\{\frac{1}{n!}\left[\prod_{i=1}^{n}\frac{d^3\vec{k}_i}{k_i^0}\,\tilde{S}(p_1,p_2,k_i)\,\Theta\!\left(\frac{2k_i^0}{\sqrt{s}} - \varepsilon\right)\right]\times\right. \\ & \times\,\delta^4\left(p_1 + p_2 - q_1 - q_2 - \sum_{i=1}^{n} k_i\right)\times \\ & \left.\times\left(\beta_0 + \sum_{j=1}^{n}\frac{\beta_1(k_j)}{\tilde{S}(k_j)} + \sum_{j,l=1,j\neq l}^{n}\frac{\beta_2(k_j,k_l)}{\tilde{S}(k_j)\tilde{S}(k_l)} + \ldots\right)\right\} . \end{aligned} \quad \text{(A.12)}$$

The YFS form factor $F^{\mathrm{YFS}}(\varepsilon)$ covers the contribution of factorizing infrared real and virtual photons to all orders. The integral over the phase space of the final-state particles consists of an integration over the two outgoing momenta, q_1 and q_2,

multiplied by a sum over all possible numbers of photons k_i with an energy above the "infrared" threshold εE_{beam}. The conservation of the four-momentum is enforced by the δ-function in the second line. The cross section of the reaction $e^+e^- \to \nu\bar{\nu}(\gamma)$ and higher-order corrections to the hard-photon radiation are included in the hard photon residuals β_i, e.g., β_0 is equal to the Born-level differential cross section $\sigma(e^+e^- \to \nu\bar{\nu})$ and β_1 includes the exact differential cross section of the reaction $e^+e^- \to \nu\bar{\nu}\gamma$ (see Section A.1). The function $\tilde{S}(k)$ denotes the universal factorizing "eikonal factor" of the real-photon radiation. For a pair of two external charged lines with four–momenta p_1 and p_2, it is given by

$$\tilde{S}(k) \;=\; \frac{\alpha}{4\pi}\left[\frac{p_2}{kp_2} - \frac{p_1}{kp_1}\right]^2 . \qquad \text{(A.13)}$$

The YFS technique is applicable to arbitrary initial and final state particles. The number of photons that are explicitly produced is not constrained. The calculated cross section is independent of the parameter ε. In addition, contrary to the structure function formalism, any photon emission process can be corrected by the appropriate matrix elements to the chosen order of α, including interference effects for the multi-photon final states. Details of the actual implementation of the YFS scheme can be found in Reference [240].

The YFS technique has been used in many theoretical calculations and Monte Carlo generators. In this thesis, the reaction $e^+e^- \to \nu\bar{\nu}\gamma(\gamma)$ is simulated mainly with the `KKMC` generator [17], which employs a more advanced Coherent Exclusive Exponentiation (CEEX) method to simulate higher-order QED corrections [25]. The CEEX technique is based on the YFS scheme; however, the CEEX is formulated in terms of spin amplitudes, i.e., the higher-order effects are included before the spin summation.

Appendix B

RFQ System in Detail

The RFQ calibration system, method, and results were presented in Chapter 5. In this appendix I describe in detail the individual components of the RFQ system.

It should be noted that the design of the L3 RFQ calibration system was unique, as it was the only physics experiment requiring the use of such a highly energetic neutral particle beam (NPB). Interestingly enough, a very similar system was used as part of the development of NPB technology for strategic defense applications. *The Beam Experiments Aboard a Rocket* (BEAR) was launched aboard a sounding rocket in New Mexico in July 1989 [241]. The core of this experiment was an RFQ accelerator which produced an H^0 beam with an energy of about 1 MeV and a flux equivalent to a current of 10 mA. As in the L3 RFQ system, an H^- ion source and a gas cell neutralizer were used. The BEAR experiment was successful; however, the NPB weapon system does not appear to be practical in the near future [242]. Another interesting example of NPB applications can be found in fusion plasma experiments, where an injection of a neutral beam, typically with an energy of about 100 keV, is used as one the fundamental plasma heating methods [243].

During its six years of operation at L3, the RFQ calibration system proved to be robust and reliable, and the last calibration run performed in September 2000 showed no evidence of aging of the RFQ system hardware. Therefore, at the end of LEP program it was decided to move the RFQ system from the L3 cavern to a storage room at CERN. In January 2001 we successfully transferred the RFQ system together with all readout electronics to the designated storage area. Only minimal changes were made to the RFQ setup so that the system is ready to resume working. Figure B.1 shows the RFQ system after it was lifted from the L3 cavern.

Figure B.1: Photograph of the RFQ system taken prior to its transfer to the storage area. The beam pipe and the most downstream cryopump have already been removed. Standing in front of the system are members of the Caltech group involved in the RFQ dismantling, from left: M. Gataullin, S. Shevchenko, and X. Lei.

B.1 RFQ Accelerator System

The RFQ Accelerator System (RAS), shown in Figure 5.11, consists of the ion source, RFQ accelerator, high-energy beam transport, and neutralizer. The RAS was built by AccSys Technology Inc. [244] under the U.S. Department of Energy's Small Business Innovation Research program. It has been extensively modified and upgraded by the Caltech L3 group. Here I describe the RFQ system in its present configuration. The general system specifications are summarized in Table B.1.

To ensure proper internal alignment of the system, the RAS was mounted on a rigid frame (see Figures 5.11 and B.1). As shown in Figure 5.10, the RFQ target was located inside the BGO calorimeter and the RFQ frame was therefore tilted to an angle of about 22° with respect to the floor. The orientation of the most downstream cryopump was set by the requirement not to interfere with the sweep of the L3 magnet

1. Ion Source:	
Type	RF excited volume H^- source
Plasma Trigger	Hairpin filament
RF frequency and power	2 MHz, 30–50 kW
Extraction energy	30 keV
Pulse length and frequency	50μs, up to 150 Hz
Output H^- current	7.5 mA
2. RFQ Accelerator:	
Nominal output energy	1.85 MeV
Operating frequency	425 MHz
Beam pulse width	1–25 μsec
Beam repetition rate	1–150 Hz
Intervane voltage	65 kV
Maximum surface gradient	35 MV/m
Required RF power (peak)	200 kW minimum
Output beam current (peak)	up to 30 mA
Residual vacuum	$< 3 \times 10^{-6}$ Torr
Output energy spread (90%)	$\pm$20 KeV
Transmission efficiency	$\simeq$ 75%
3. Neutralizer:	
Type	Gas (N_2) filled
Optimum pressure	5–9$\times 10^{-4}$ Torr
Length and inside diameter	1 m, 40 mm
Efficiency	Up to 55%
Output H^0 flux (pulsed)	Up to 4 mA (equivalent)

Table B.1: Specifications of the RFQ accelerator system components: 1) ion source, 2) RFQ accelerator, and 3) neutralizer.

doors.

The RAS can produce beam pulses up to 50 μs of length with a repetition rate as high as 150 Hz. However, as explained in Section 5.6, it was typically run with a pulse length of about 5 μs and a repetition rate of 80 Hz.

B.1.1 Ion Source

The H^- ion source follows the RF-driven *volume* source design invented at LBL [245]. It was further developed and built by the AccSys Technology Inc. [244]. The ion

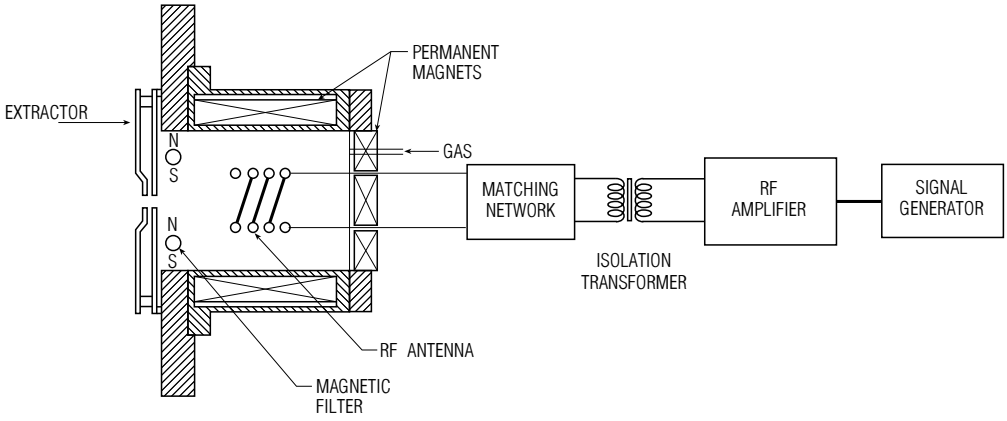

Figure B.2: A schematic showing the RF-driven H^- ion source.

source is compact and can be operated remotely for periods of several weeks with little or no maintenance. Meeting these requirements was essential for all elements of the L3 RFQ system, as the space allocated for the system was limited and the L3 cavern was not accessible during LEP operation. In addition, the RF-driven ion sources have a longer lifetime compared to the conventional ion sources driven by filament cathodes.

A schematic diagram of the ion source is shown in Figure B.2. The plasma chamber of the ion source is a copper bucket surrounded by columns of permanent magnets arranged in a longitudinal line cusp configuration. Its back flange also consists of permanent magnets that provide longitudinal confinement. Hydrogen is pumped into the chamber using a pulsed electromechanical valve and ionized using a helicoidal antenna. Typically, 30 to 50 kW pulsed 2 MHz RF power is fed to the antenna. The antenna is made out of 2.5 turns of glass-coated, 4 mm diameter, copper tubing and is cooled by water circulating in the tubing. A hot wire (hairpin filament) is used as a starter for the plasma. A 4 mm wide extraction aperture, opposite to the back flange, is separated from the the rest of the plasma chamber by a pair of water cooled permanent magnet rods. The magnet filter rods provide a transverse magnetic field of about 120 G, necessary to enhance the H^- yield [245].

The extraction of the negatively charged beam (populated mostly by electrons) is achieved by applying a -30 kV potential to the plasma bucket and grounding

the extraction electrodes. The extracted beam is decelerated to -14 kV and the e^- component (up to a few amperes) is removed using a magnetic spectrometer. The H^- beam is then re-accelerated to 30 keV and focused into the RFQ by an electrostatic lens. Since most of the ion source operates at -30 kV, it is isolated from the RF generator using a ferrite RF transformer and is connected to the RAS control system via an optical cable.

The obtained H^- current is typically about 7 mA, which requires a hydrogen gas flow of about 8 sccm to maintain the pressure in the plasma chamber at the optimum level of 35-40 mTorr. The hydrogen is evacuated by a 3 klps cryopump and the residual vacuum near the extraction electrodes is better than 5×10^{-6} Torr. The pressure in the plasma chamber is measured and controlled using a Pirani gauge.

As discussed in Section 5.6, the intensity of the RFQ calibration photon flux was well below the optimum level. Essentially this was because the H^- ion source of the RFQ system, the first commercial prototype in the world, was not capable of providing a large enough output current. The H^- current can be enhanced by introducing a trace amount of cesium in the extraction region of the source. An improved version of our ion source, built by the LBL group for the SSC laboratory, provided an output current of $70 - 100$ mA ($30 - 35$ mA without cesiation) [246].

B.1.2 RFQ Accelerator

The RFQ is a quasi-electrostatic accelerator, which offers advantages of a very compact size (typically 1-3 m long) and a high beam current (up to 100 mA). It derives its name from its use of radio-frequency voltages and quadrupole focusing [247]. Manufactured by AccSys Technology, the 1.85 MeV L3 RFQ accelerator is a 1.626 m long copper plated mild iron structure of a four vane type. It is tuned to a resonant frequency of 425 MHz and has a transmission efficiency of 75% for the injected 30 keV H^- beam. The L3 RFQ can be operated with a repetition frequency of $1 - 150$ Hz and its pulse length can be varied between 1 and 25 μs. The input RF power of 240 kW is provided by a three stage parallel planar triode array based on Varian Eimac tri-

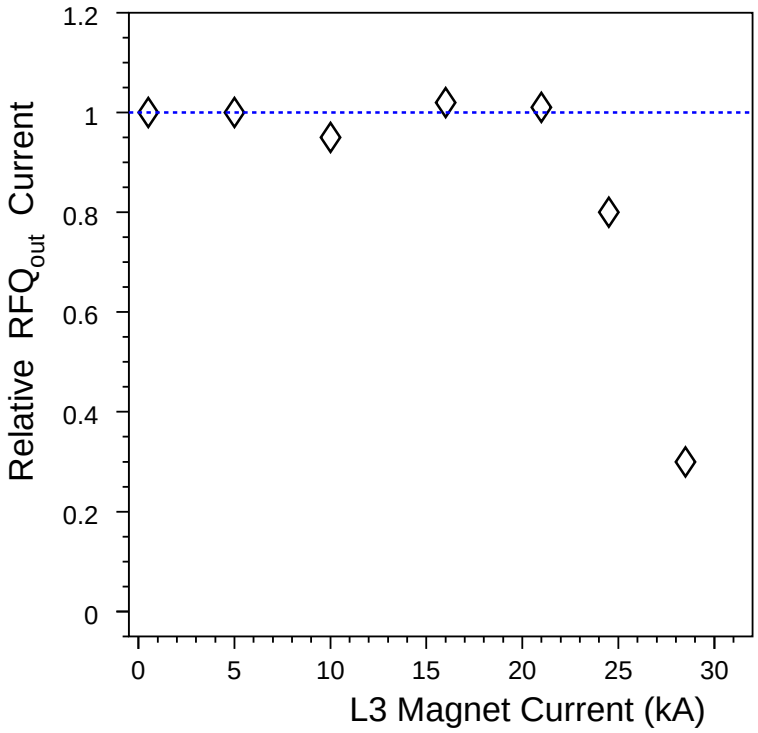

Figure B.3: Relative H^- current from the RFQ accelerator as a function of the L3 magnet current. The nominal L3 magnet current was 30 kA.

ode tubes [248]. The RFQ is evacuated by a 1.5 klps cryopump which maintains the residual vacuum in the RFQ (with beam) below 1×10^{-6} Torr.

The output beam current from the RFQ is measured using a toroidal coil. Before entering the gas-cell neutralizer, the beam is focused and steered by a set of quadrupole and dipole magnets.

Magnetic Shielding

Early *in situ* tests of the RFQ system demonstrated that the output current from the RFQ accelerator decreased with the L3 magnet current. Figure B.3 shows that about 80% of the beam was lost at the nominal magnet current of 30 kA. The L3 spectrometer magnet (see Section 4.2.1) provided a field of 5 kG which was, however, well contained inside the detector. The fringe magnetic field near the RFQ site was measured to be $50 - 100$ G. After extensive calculations had shown that such a low

magnetic field could not affect the propagation of the H^- beam, it was realized that the soft iron RFQ vanes could concentrate the field in the intervane gaps, producing local fields substantially higher than expected. This effect was particularly severe at the input stage, where the resulting fields deflected most of the beam out of the acceptance range of the RFQ. The problem was solved by enclosing the ion source and the RFQ inside a shielding box made out of 15 mm thick soft-iron plates. With the magnetic shielding, the RFQ system proved to be completely insensitive to the fringe field and several RFQ calibration runs were successfully performed with the L3 magnet on.

Control System

The ion source and the RFQ amplifier were controlled with a PC installed with a MIL-STD-1553B standard controller board. The control program, written in Turbo Pascal, provided access to several I/O channels which could be configured without modifying the source code. All machine settings were transferred to the PC every few seconds. A system of software interlocks (in addition to the already existing hardware ones) was implemented to allow the user to ramp the high voltage while watching other critical machine parameters. The control system was also used to monitor and adjust the nitrogen pressure in the neutralizer cell. This was done by using a Perkin Elmer pressure controller, which allowed to adjust the gas flow through a piezoelectric valve.

B.1.3 Beam Neutralizer

The focused and steered H^- beam was neutralized in a N_2 gas cell ($H^- \rightarrow H^0 + e^-$) so that the neutral beam could pass undisturbed through the 0.5 T L3 magnetic field. The neutralizer consisted of two coaxial steel cylinders, each with a length of about 1 m. The inner cylinder had several hundred holes (diameter $\phi < 1$ mm) through which the nitrogen diffused into the central region. Two 3 klps cryopumps were used to evacuate the gas cell, one on each side. Thus, a dense gas column was maintained

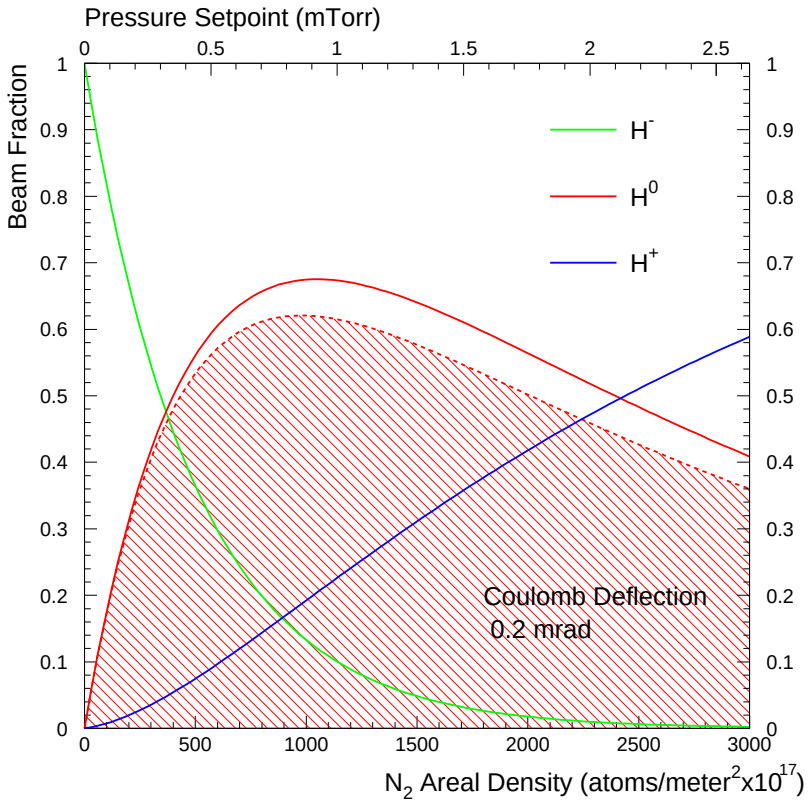

Figure B.4: Relative intensities of the H^-, H^0, and H^+ beams (after the neutralizer), calculated as functions of pressure in the gas cell. The hatched area represents the neutralization efficiency with the Coulomb scattering taken into account.

in the cell, while the pressure at the ends of the cell was below 1×10^{-6} Torr. The gas pressure in the inner cylinder was measured and the nitrogen flow into the outer cylinder was controlled using a piezoelectric valve.

At an optimum pressure of $0.6-0.9$ mTorr, the maximum neutralization efficiency of about 55% can be reached with this gas cell. This result is in good agreement with measurements performed with similar gas neutralizers [249]. Figure B.4 shows relative intensities of the H^-, H^0, and H^+ beams (after the neutralizer), calculated as functions of pressure in the gas cell.

B.2 Neutral Beam Transport

At this stage the beam was focused, steered, and neutralized, ready to be transported through a 10 m long beam pipe penetrating the L3 magnet, support tube, and calorimeters (see Figure 5.10) to reach a lithium target near one of the BGO endcaps. Figure 4.11 shows the location of the RFQ target and the end portion of the RFQ beam pipe with respect to the BGO calorimeter.

The RFQ neutral beam transport was made of two narrow tubes (inside diameter 40 mm). A manifold consisting of three KF-25 and one CF-40 flanges was mounted on the inner surface of the L3 support tube. One end of this manifold was attached to one of the tubes connected to the neutralizer, while the other end was connected to the other tube holding the target. Due to size limitations, the end portion of this tube was twice as narrow (inside diameter 20 mm). The beam pipe was electrically isolated from the rest of the RFQ system and its alignment was ensured using a dedicated laser system.

A 20 lps Varian StarCell ion pump mounted on the CF-40 flange of the manifold was used to evacuate the beam pipe. The ion pump was designed to be driven by the L3 magnetic field; however, a coil dipole magnet was also installed to allow the operation of the pump with the L3 magnet off. The dipole magnet produced a magnetic field of 850 G, which was sufficient to drive the ion pump at 60% of the maximum pumping speed. The vacuum in the beam pipe (with beam) was better than 5×10^{-6} Torr. Maintaining such high vacuum was necessary because the cross section of single electron loss by a hydrogen atom in nitrogen ($H^0 \rightarrow H^+ + e^-$) was quite large, about 6×10^{-17} cm^{-2} [250]. The energetic protons produced in this reaction would bend in the L3 magnetic field and hit the walls of the beam pipe. Such collisions produced unwanted radiative capture backgrounds and liberated thousands of gas molecules from the pipe's walls (outgassing), which in turn increased the pump load. This problem was mitigated by lining the last 80 cm of the beam pipe with a thin tantalum foil.

In general, the hydrogen atoms were lost in the neutral beam transport mainly

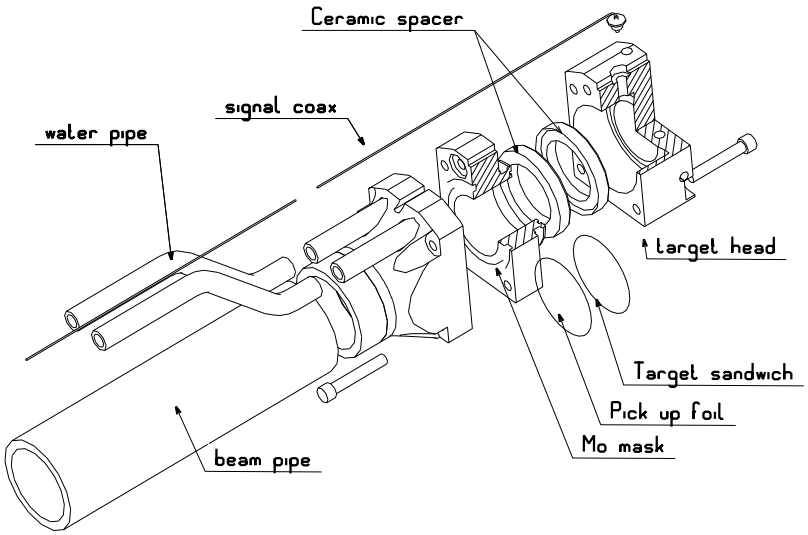

Figure B.5: The mechanical structure of the target.

because it was impossible to focus and steer the H^0 beam. The total beam loss was calculated to be about 50% and occurred mostly in the last portion of the beam pipe, which was forced to taper down due to the geometry of the BGO calorimeter.This result agreed well with a direct measurement of the H^0 beam intensity, which was carried out during one of the LEP shutdowns. The RFQ target was replaced with a specially designed Faraday cup, consisting of a 25 μm thick aluminum foil, a dipole magnet, and a charge collection plate. The foil was used to strip electrons from the incoming hydrogen atoms, while the secondary electrons were suppressed using the dipole magnet. The H^+ and H^- fractions of the beam were eliminated using another bending magnet installed after the neutralizer. The resulting H^+ current was measured to be about 1.5 mA or $\simeq$ 30% of the H^- current from the RFQ accelerator, consistent with the calculated losses due to neutralization (45%) and neutral beam transport (50%).

B.3 Target

The original design of the RFQ target is shown in Figure B.5. The target was made out of a 50 μm thick lithium foil sandwiched between two circular molybdenum or

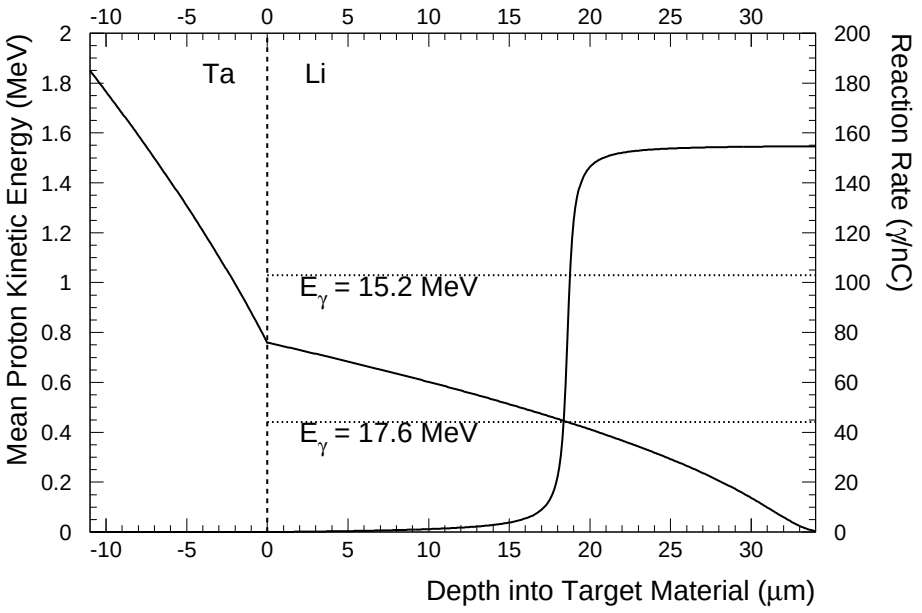

Figure B.6: Mean proton kinetic energy and proton radiative capture yield as functions of the depth into the target material. This plot shows calculations performed for a 11 μm thick tantalum foil. However, it is also approximately valid for a 12 μm molybdenum foil, as these metals have almost the same stopping power for 1 MeV protons: $dE/dx(\mathrm{Ta}) = -105$ keV/μm and $dE/dx(\mathrm{Mo}) = -97$ keV/μm [252].

tantalum foils (6 μm and 50 μm thick). To avoid oxidation of the lithium, the foils were hot-pressed (melted) together in a pure argon atmosphere. The foil sandwich was encapsulated in a water-cooled molybdenum holder with the 6 μm molybdenum foil facing the beam. Another 6 μm thick molybdenum foil was mounted on ceramic rings, about 2 mm upstream of the target. The molybdenum foils served two purposes:

(1) **As an energy degrader:** The reaction $^{7}_{3}\mathrm{Li}(\mathrm{p},\gamma)\,^{8}_{4}\mathrm{Be}$ has a narrow resonance[1] at a proton energy of 441 keV and a broader resonance at about 1.03 MeV. These two resonances produce photons with different energies, 17.6 MeV and 15.2 MeV, respectively. Therefore, to produce a monochromatic calibration photon flux, the incoming protons had to be slowed down. As shown in Figure B.6, the molybdenum (or tantalum) foils reduced the beam energy from 1.85 MeV to

[1] This resonance has a width of $\Delta E_p = 12$ keV (FWHM) and the maximum cross section of about 6 mb [153, 251].

below 0.8 MeV. Protons then slowed down in the lithium, hitting the 441 keV resonance while avoiding the undesired resonance at 1.03 MeV.

(2) **As a Faraday cup:** The upstream foil was used to strip electrons from the incident hydrogen atoms. The resulting negative charge was measured, providing an estimate of the neutral beam intensity.

The molybdenum (or tantalum) foils were used because these metals are stable at high temperatures and have low radiative capture cross sections, thereby minimizing the unwanted γ ray background [150]. A 17.6 MeV photon yield of about 160 γ/nC was obtained with this target design.

In 1995 it was discovered that the molybdenum foils did not provide complete protection from the atmosphere and that, after a few months, the lithium would degrade into lithium hydroxide (LiOH). This effect reduced the photon yield from the target by almost 85%. Therefore the pure lithium foil was subsequently replaced with a pressed powder of lithium hydride (LiH), which was easy to handle and stable in dry air. Although the LiH target provided a photon yield of about half that of the original target design, it was preferred due to its long-term stability. In order to make the target sandwich sturdier, the two 6 μm thick molybdenum foils were replaced with a single 12 μm thick foil. Thus, the upstream foil was removed and the neutral beam was detected using other instruments as described in the next section.

B.4 Neutral Beam Detectors

The position and intensity of the steered H^0 beam was measured using two different instruments. The first one, a *single wire scatterer* (SWS), was based on the detection of protons produced by the Rutherford scattering of hydrogen atoms from a thin gold-plated tungsten wire (0.25 mm in diameter). The wire was mounted at the neutral beam transport manifold, about 5 m from the target, and oriented perpendicular to the beam direction. The scattered protons were detected using a small silicon surface barrier detector, which was installed on the inner surface of the manifold.

The resulting signal was used as a trigger for the RFQ data acquisition system. The SWS could also be used to focus the RFQ beam as the amplitude of its signal was proportional to the number of scattered hydrogen atoms.

In order to improve the neutral beam diagnostics and facilitate the tuning of the beam optics, a dedicated beam profile chamber was built in 1995. The chamber consisted of two orthogonal wire planes, each with 10 negatively biased sense wires interleaved with 11 ground wires. The 10 μm gold-plated tungsten wires were fixed on ceramic frames which were built using thick-film hybrid circuit technology. When the H^0 beam hit the sense wires, it knocked out secondary electrons that were repelled by the electric field created by the bias voltage. Therefore, a positive charge was left on the sense wires. Experimentally it was determined that this signal was proportional to the beam intensity and the cross-talk between the wires was negligible.

The charge deposited on the sense wires within 10 μs of the beam passage (typically 0.1 pC) was integrated and amplified by a preamplifier, the same as the ones used in the readout of the BGO calorimeter. After further amplification, the signal was transmitted to the counting room, where a sample-and-hold circuit produced a DC signal proportional to the collected charge and drove an LED display. The beam profile chamber was installed about 2 m upstream of the RFQ target, i.e., substantially closer than the SWS detector, and proved to be extremely useful for beam alignment.

B.5 Data Acquisition System

The RFQ runs were taken with the BGO calorimeter readout in the *local* standalone mode so that the BGO timing configuration was essentially the same as the one used during LEP data taking. The 5 μs RFQ beam pulse was tuned to arrive during the 11 μs integration window of the BGO. This was achieved by driving the RFQ accelerator system using the LEP beam-crossing time mark, which arrived with a period of 22 μs, and setting the BGO integration gate to start about 3 μs before the LEP time mark. The RFQ *trigger accept* signal was generated by the SWS neutral

beam detector. The trigger accept started the digitization of the BGO data and suspended the RFQ run. Once the BGO digitization process was complete, the RFQ system could be triggered by the next LEP time mark. With this timing scheme, an average readout speed of about 80 Hz was achieved, which was substantially faster than the L3 readout speed during the LEP runs (10 Hz).

The RFQ signals registered in the crystals were read out through the BGO token-passing network and further recorded by a specially designed online histogramming VHC module (Veto-Histogram-Counter). The VHC had a 256 channel histogram memory for 8192 crystals, so that only half of the BGO calorimeter was read out during each run. In order to reject BGO showers that were not contained in a single crystal, channels with hits in neighboring crystals were not histogrammed. The veto threshold for the neighboring hits was set to be equal to 1.5 σ above the pedestal. The threshold values were measured and updated before each RFQ run. The obtained histograms were then written to an RZ file which could be analyzed in PAW (*Physics Analysis Workstation*).

Appendix C

Studies of the BGO Performance

In this appendix I describe the technical aspects of my work on the calibration and monitoring of the BGO calorimeter. These include studies of the BGO non-linearity and aging, a special procedure that I developed to treat BGO showers with dead or missing crystals, and a description of the Crystal Ball lineshape fit. In addition, I also present the angular resolution functions for electromagnetic showers measured in both the barrel and endcap regions of the calorimeter.

C.1 Crystal Ball Lineshape Fit

As discussed in Section 5.6.2, the energy spectra of Bhabha electrons had a significant low-energy tail due to initial state radiation and, thus, could not be adequately described by a simple Gaussian distribution. In order to take this effect into account, I fitted the Bhabha spectra to the Crystal Ball lineshape (CBL) function.[1] This composite function consists of two parts, a Gaussian peak and a power-law tail, and is given by the following formula:

$$\Psi(E|E_p,\sigma,A,a,r) = \begin{cases} A\cdot\exp\left[\dfrac{-(E-E_p)^2}{2\sigma^2}\right] & \text{if } E > E_p - a\,\sigma \\ A\cdot\left(\dfrac{b}{a}\right)^b \dfrac{\exp(-a^2/2)}{\left[(E_p-E)/\sigma + \dfrac{b}{a} - a\right]^b} & \text{if } E \le E_p - a\,\sigma\,, \end{cases} \tag{C.1}$$

where E is the observed energy, E_p is the position of the peak, σ is the width of the peak, A gives the overall normalization, and a and b are the parameters describing

[1] This function was originally used by the Crystal Ball experiment to fit the energy response of its NaI(Tl) crystal calorimeter [152]. In L3, the CBL function was also used to fit the distributions of the forward-backward charge asymmetry in Bhabha scattering [135].

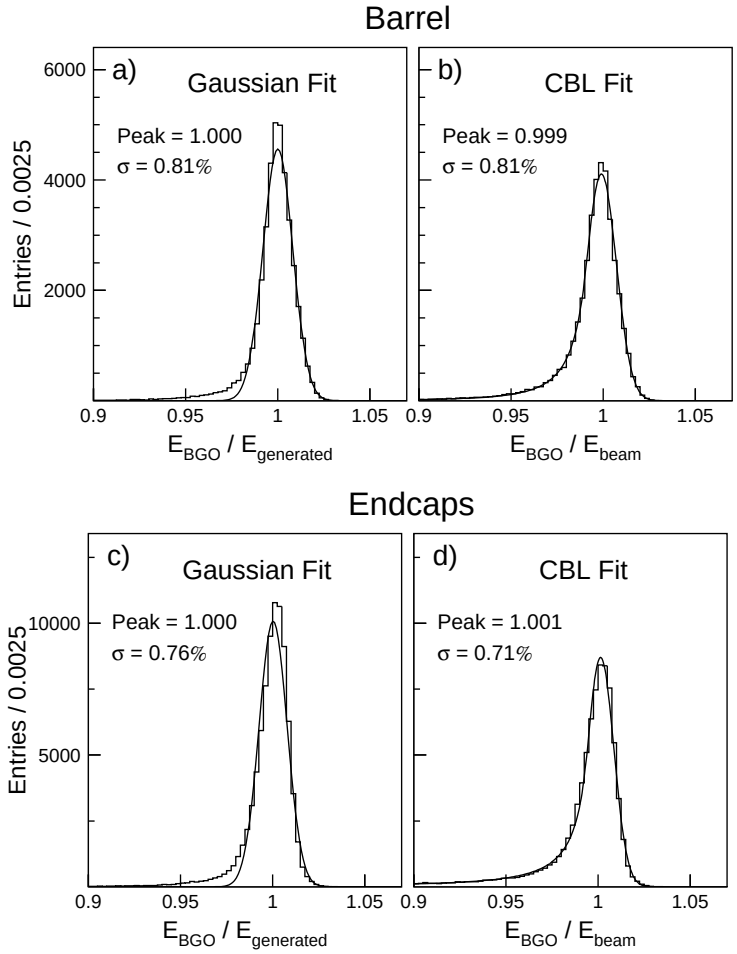

Figure C.1: Comparison between (a,c) the Gaussian and (b,d) the Crystal Ball lineshape fits to the distributions of the E_{BGO}/E_{gen} and E_{BGO}/E_{beam} variables, respectively. The obtained peak positions and resolutions are indicated on the plots. There are two entries per each MC event.

the power-law tail, where a defines the joining point and b gives the power. The above formula automatically ensures that both parts of the CBL function join continuously and are smooth in the first derivative. For the Bhabha energy spectra at LEP, the fitted values of the parameters a and b were in the ranges $1 < a < 2$ and $1.5 < b < 3$.

I studied the performance of the CBL fit using a sample of 70,000 back-to-back Bhabha events which I selected from a Monte Carlo sample generated at the Z peak, $\sqrt{s} = 91.3$ GeV, where the shower development in the BGO had been simulated assuming a perfect calibration and no temperature fit errors. Figures C.1a,c show the distributions of E_{BGO}/E_{gen}, where E_{BGO} is the reconstructed energy of the BGO

bump and E_{gen} gives the energy of the corresponding electron at the generator level. As can be seen, these distributions could be reasonably well fitted with a single Gaussian function, despite a noticeable low-energy tail caused by fluctuations in the shower development process (e.g., shower leakage effects or energy losses in the dead material between the crystals). The fitted width of the peak was then taken as the intrinsic energy resolution of the BGO calorimeter.

For the data, the true value of the electron energy (E_{gen}) was of course unknown and, to determine the energy resolution of the BGO, I had to use another variable, E_{BGO}/E_{beam}, where E_{beam} is the beam energy. The corresponding distributions fitted to the CBL function are shown in Figures C.1b,d.

Comparing the fitted values of the peak position and width obtained with these two methods, good agreement was observed in all cases. In addition, for both the data and Monte Carlo spectra, the fitted CBL curves provided a good description not only for the peak region but also for the the low-energy tail as can be seen from Figures C.1b,d and 5.20. Thus, it could be concluded that the Crystal Ball lineshape function worked well in fits to Bhabha energy spectra and provided a consistent estimate of the BGO energy resolution.

C.2 Showers with Dead or Missing Crystals

As discussed in Section 5.3.2, about 1.5% of the BGO channels were malfunctioning (*dead*) and therefore were not used in the shower reconstruction. In addition, the BGO calorimeter had six rings of crystals at the edges of the calorimeter, one in each half-barrel and two in each endcap. As a result, about 12% of the selected single-photon showers contained a dead channel in the 3×3 matrix around the crystal with the maximum energy deposition (bump crystal), and for additional 5% of the showers, the bump crystal was in one of the edge rings so that the 3×3 matrix contained three *missing* crystals. Such showers were also used in the absolute calibration of the BGO in order to calibrate crystals adjacent to the dead crystals and crystals near the detector edges.

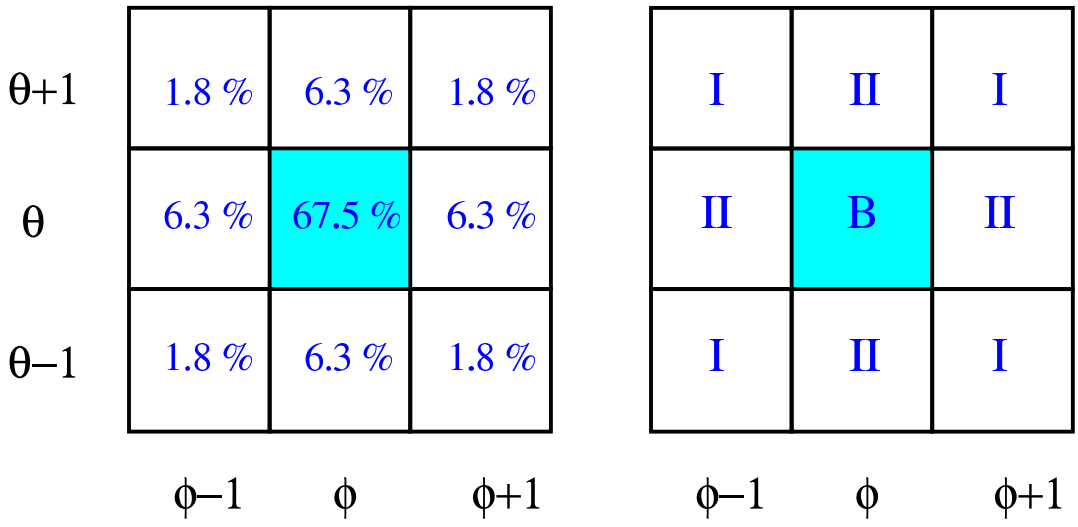

Figure C.2: **Left:** Average energy fractions in the 3×3 crystal matrix for the bumps with no dead or missing crystals (for 45 GeV electrons). **Right:** Definition of the Type I and Type II BGO bumps, where "B" denotes the bump crystal and "I" and "II" denote the possible positions of the dead crystals.

The standard BGO reconstruction algorithm treated the dead and missing crystals as crystals with zero energy depositions, resulting in a systematic underestimation of the measured bump energy. This effect was then accounted for by disabling the corresponding crystals during the Monte Carlo simulations of the BGO calorimeter. However, for some applications this approach proved to be insufficient. For example, the absolute calibration of the BGO was based on the assumption that the reconstructed electron energies in the back-to-back Bhabha events should be close to beam energy.

In order to correct for the presence of the dead and missing crystals, I used the following procedure.[2] First, the BGO bumps with missing or dead crystals were divided into three categories. The *Type* I bumps contained a dead crystal in one of the four corners of the 3×3 matrix, while for the *Type* II bumps, the dead crystal was

[2]This problem has also been investigated in 1997-98, and an alternative shower fitting procedure was developed [253] It was shown that this algorithm provided a substantial improvement in the reconstruction quality for the BGO bumps with dead or missing crystals. However, it also produced significant resolution tails and, thus, was not used in my analysis (or in any other L3 analyses).

Parameter	Type I		Type II		Type III	
	Barrel	Endcaps	Barrel	Endcaps	Barrel	Endcaps
P_{Data} [%]	98.4 ± 0.3	98.4 ± 0.3	97.3 ± 0.3	97.8 ± 0.2	96.4 ± 0.2	96.8 ± 0.2
P_{MC} [%]	98.6 ± 0.1	98.7 ± 0.2	97.6 ± 0.1	98.0 ± 0.1	96.8 ± 0.2	97.1 ± 0.1
σ_{Data} [%]	1.4	1.5	1.6	1.5	2.3	2.0
σ_{MC} [%]	1.6	1.6	1.7	1.5	2.3	2.1

Table C.1: Results of the CBL fits to the E_{bump}/E_{beam} distributions for the bumps with missing or dead crystals. Peak positions and resolutions are listed both for the data, P_{Data} and σ_{Data}, and Monte Carlo, P_{MC} and σ_{MC}.

adjacent to the bump crystal (see Figure C.2). The *Type* III bumps were the showers near the edges of the BGO which contained three missing crystals in the 3×3 crystal matrix. This particular classification was motivated by fact that the average energy loss in dead or missing crystals was different for each type of such bumps. Figure C.2 shows that for Type I showers, the systematic underestimation of the measured bump energy was expected to be substantially smaller than for bumps of Type II and III.

To estimate the systematic negative shift in the measured bump energy, I used back-to-back Bhabha events selected from a Monte Carlo sample generated at the Z peak, $\sqrt{s} = 91.3$ GeV, where the calibration and temperature fit errors had been taken into account during the detector simulation. The selection criteria that I used are listed in Section 5.6.2. It should be noted that the selected bumps had to satisfy the quality cuts on the shower shape, which rejected a significant fraction of Type II and Type III bumps. As a consequence, about 40% of the selected bumps with dead or missing crystals were of Type I and the rest was divided equally between the Types II and III.

The Bhabha energy spectra were fitted to the CBL function, and the fit results are given in Table C.1. The obtained correction factors were then applied during the absolute calibration of the BGO. To test this correction procedure, I used a sample of bumps with dead or missing crystals that were selected in the Z-peak calibration data collected from 1998 to 2000. Figure C.3 shows the Bhabha energy spectra for the

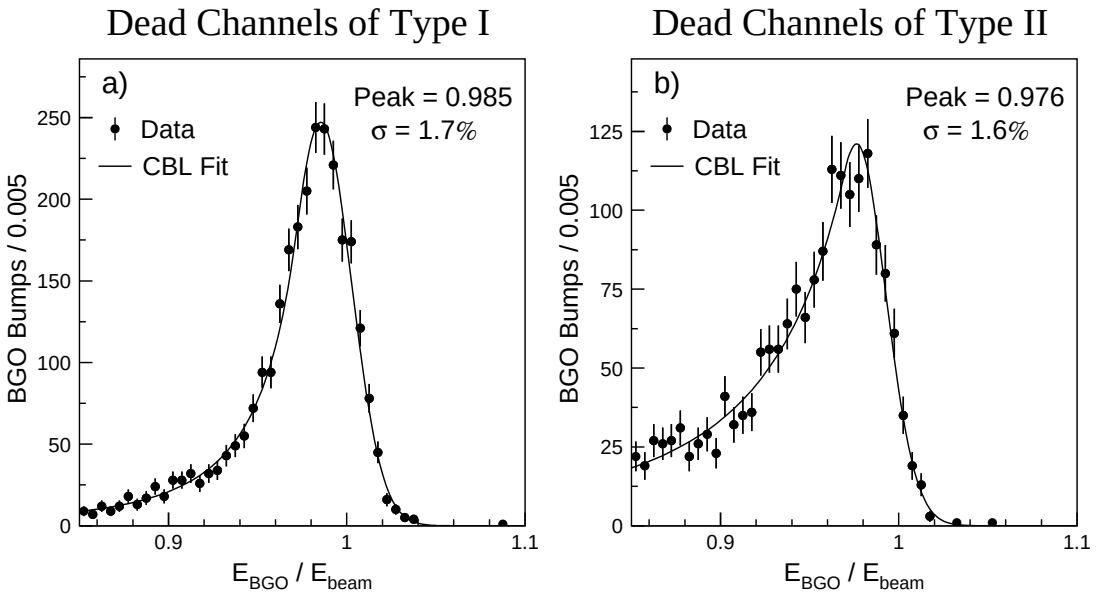

Figure C.3: Energy spectra of the Bhabha electrons selected in the 1998-2000 Z-peak calibration data a) for the BGO bumps of Type I and b) for the BGO bumps of Type II (barrel and endcaps combined). The peak positions and resolutions are indicated on the plots.

BGO bumps of Type I and II, and the fitted parameter values are listed in Table C.1. Comparing the fitted values of the peak position and width, good agreement between the data and Monte Carlo was observed in all cases. For 45 GeV electrons, the BGO energy resolution was measured to be about 1.5% for bumps of Type I and II and about 2% for bumps of Type III.

The shower-shape cuts that I used in the selection of the single- and multi-photon events were identical to the cuts used in the Bhabha selection. Therefore, the same correction procedure could also be applied to the selected single- and multi-photon samples. As shown in Figure 6.21f, this procedure corrected the position of the recoil-mass peak for the single-photon showers containing dead or missing crystals.

C.3 Aging of the BGO Calorimeter

At the beginning of the LEP program in 1989, it was noticed that the BGO response decreased with time at a rate of 2-3% per year. The BGO aging was then extensively

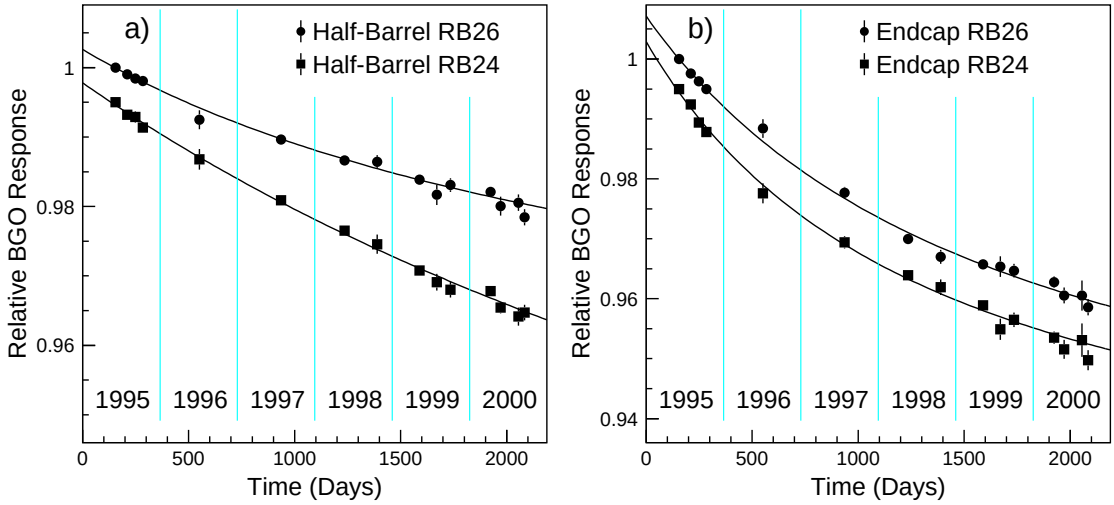

Figure C.4: Aging of the BGO during 1995-2000 a) for the two half-barrels and b) for the two endcaps. Each point represents a LEP run at or near the Z peak, $\sqrt{s} \simeq 91.3$ GeV. For better visibility, the aging curves for the RB24 side are shifted by -0.5%.

studied using the Xenon monitoring system and it was found that, fortunately, the decay rate also decreased with time [139, 134]. The measured decay trend could be parameterized by

$$R(t) = \frac{a}{t - t_0} + C, \tag{C.2}$$

where R is the relative BGO response, t is the elapsed time, and a, t_0, and C are constant parameters. Since the four subdetectors of the BGO were manufactured and installed separately, the decay functions $R(t)$ were different for each subdetector.

In order to estimate the BGO aging during the LEP2 phase, I used the back-to-back Bhabha events selected in the Z-peak calibration data.[3] Typically, during each year of the LEP2 program, two or three weeks were dedicated to LEP runs at the Z peak, $\sqrt{s} = 91.3$ GeV. For example, in 1999 such runs were performed in May, July, and September, and the L3 detector collected a total of about 4.0 pb^{-1} of the Z-peak calibration data. The Bhabha energy spectra from each calibration run[4] were then

[3] Using only electrons of fixed energy, 45.6 GeV, avoided the problem of the BGO non-linearity (see the next section).

[4] To avoid potential biases, energies of all Bhabha showers were reconstructed using the same set of the RFQ intercalibration constants.

fitted to the CBL function, and the BGO aging curves were obtained by plotting the fitted peak position versus the elapsed time (see Figure C.4).

The decay rate was higher in the endcaps because they were installed two years after the barrel calorimeter. As shown in Figure C.4, the aging of all four BGO subdetectors was well described by the parameterization of Equation C.2. The obtained aging curves were then used for both the BGO calibration and the BGO reconstruction. At the end of the LEP2 program, the relative energy response of the BGO changed by about -0.4% per year for the barrel and by about -0.6% per year for the endcaps. These results were in good agreement with a similar study carried out using the Xenon monitoring system [140].

Although the exact cause of aging of the BGO is unknown, it is suspected to be due to the degradation of the reflective paint which was used to coat the BGO crystals. The L3 LUMI detector made of non-coated BGO crystals did not exhibit any significant aging effects. Radiation damage could be excluded as a cause because the radiation flux of LEP peaked at low polar angles, while the rate of aging was uniform within a given BGO subdetector. Moreover, the measured radiation flux was very low [254].

C.4 Non-linearity of the BGO Calorimeter

In general, any electromagnetic calorimeter is expected to have a linear energy response, i.e., the measured shower energy should be proportional to the energy of the incident photon (electron). However, in practice, deviations from the signal linearity (*non-linearity*) can be caused by a variety of instrumental effects such as the light attenuation or shower leakage effects [108].

During the LEP1 program, the BGO non-linearity was studied using multi-GeV electrons where the bump energy measured in the BGO was compared to the momentum of the corresponding charged track reconstructed in the TEC (E/p) [139]. It was found that the relative energy response of the BGO changed by about 0.5% when going from 5 GeV to 45 GeV [149]. Because this effect was not reproduced by

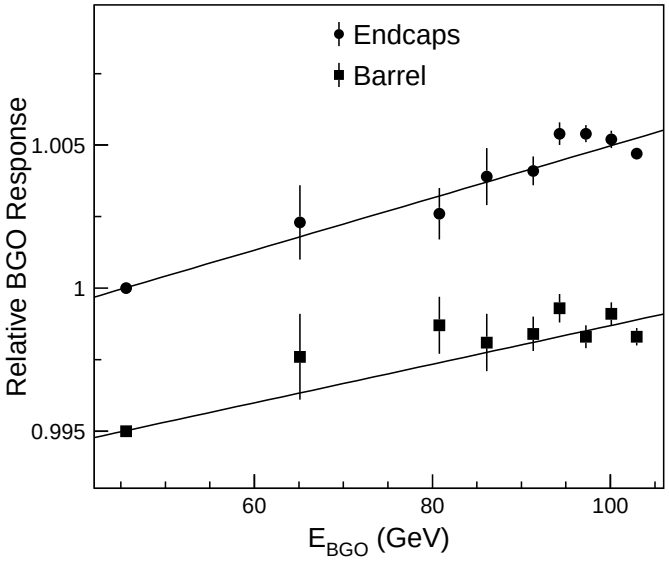

Figure C.5: Energy dependence of the BGO energy response. For better visibility, the non-linearity curve for the barrel is shifted by -0.5%.

the Monte Carlo simulations, the corresponding correction factors were included in the energy reconstruction algorithm of the BGO. For lower shower energies, the BGO non-linearity could be precisely studied using the mass peaks of the π^0 and η mesons reconstructed in their two-photon decay mode (see Section 5.6.3).

During the years 1995-2000, the LEP beam energy was gradually increased from 46 GeV up to 104 GeV. Thus, Bhabha samples selected at different center-of-mass energies could be used to investigate the linearity of the BGO response. For a given beam energy, I measured the BGO non-linearity by comparing the position of the corresponding Bhabha peak to the position of the Bhabha peak from the closest (in time) Z-peak calibration run.[5] The obtained non-linearity curves are shown in Figure C.5. The corresponding shift in the relative BGO response was measured to be about 0.5% for both the barrel and the endcaps, confirming the general trend observed at LEP1. Again, this behavior was not reproduced by the Monte Carlo simulations, and the corresponding correction factors were included in the energy reconstruction algorithm of the BGO.

[5]To avoid potential biases, the shower energies were reconstructed using the previous year's calibration, i.e., the data under investigation were not used to derive the corresponding calibration constants.

C.5 BGO Angular Resolution

As described in Section 5.1, the impact point of the incident particles was reconstructed using the energy depositions in the 3×3 crystal matrix and the actual positions of the crystal front faces (θ_i and ϕ_i). The corresponding angular resolution functions were derived in Reference [110] and are given by:

ϕ-Resolution:

Barrel

$$\sigma_\phi^B(E) = \frac{3.28 \text{ mrad}}{\sqrt{E}} + 0.82 \text{ mrad} \quad (E \text{ in GeV}) . \tag{C.3}$$

Endcaps

$$\sigma_\phi^E(E,\theta) = (1.21\,\sigma_\phi^B(E) + 2.56 \text{ mrad}) \left(\frac{4.76/|\tan\theta| + 3.81}{4.76/|\tan\theta_{ref}| + 3.81} \right) , \tag{C.4}$$

where $\tan\theta_{ref} = 523\ mm/758\ mm$ corresponds to the intersection of the barrel and endcap volumes.

θ-Resolution:

Barrel

$$\sigma_\theta^B(E,\theta) = \sigma_\phi^B(E) \left(\frac{5.55\sin\theta + 1.21}{5.55\sin\theta_0 + 1.21} \right) , \quad \theta_0 = \frac{\pi}{2} . \tag{C.5}$$

Endcaps

$$\sigma_\theta^E(E,\theta) = (0.77\,\sigma_\phi^B(E) + 0.99 \text{ mrad}) \left(\frac{6.06|\cos\theta| + 0.66}{6.06|\cos\theta_{ref}| + 0.66} \right) , \tag{C.6}$$

where the reference polar angle θ_{ref} is the same as in the expression for $\sigma_\phi^B(E)$ (Equation C.3). The longitudinal section of the BGO calorimeter (see Figure 4.11) was a rectangle, and therefore only the barrel ϕ-resolution function did not depend on the polar angle of the shower. In addition, since the BGO granularity was almost the same in the barrel and in the endcaps, the remaining resolution functions could be parameterized in terms of $\sigma_\phi^B(E)$ and θ.

As a cross check, I derived the ϕ-resolution function for the barrel using a Monte Carlo sample of single-photon events. Figure C.6a shows that it was in good agree-

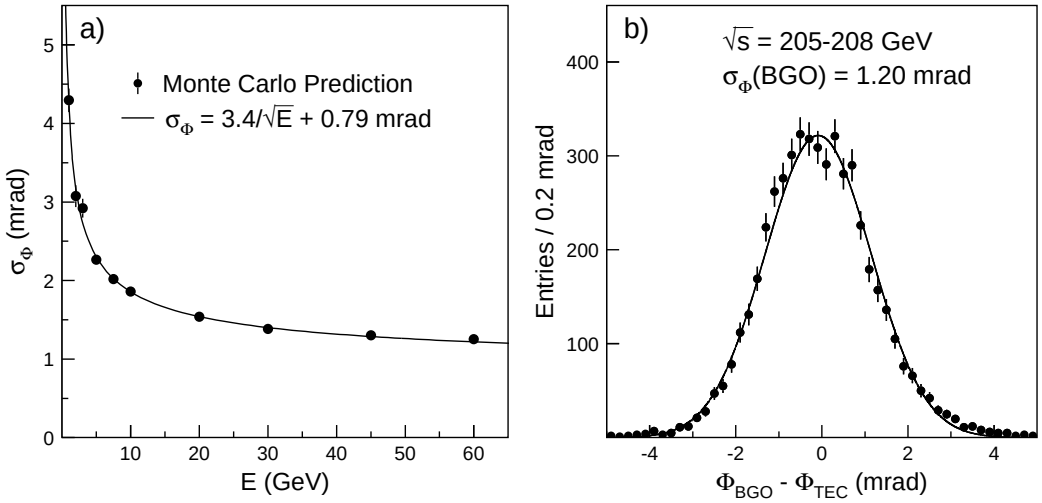

Figure C.6: a) BGO angular resolution as a function of the shower energy, as predicted by the Monte Carlo simulations. b) ϕ-resolution for the barrel measured using 103 GeV Bhabha electrons (two entries per event).

ment with the function $\sigma_\phi^B(E)$ given by Equation C.3.

For electrons in the barrel region, a much more precise measurement of the azimuthal angle was obtained by reconstructing the associated charged track using the TEC and SMD subdetectors of L3 (σ_ϕ(TEC) $\simeq$ 0.4 mrad). The ϕ-resolution of the BGO could then be estimated by comparing the azimuthal angle measured by the BGO and by the TEC (see Figure C.6b). The measured value of σ_ϕ^B(Data) = 1.17$\pm$0.02 mrad was in good agreement with the Monte Carlo prediction of σ_ϕ^B(MC) = 1.15 mrad. This result was also confirmed by a similar study described in Reference [140].

Appendix D

Additional Results of the Event Selection

In this appendix I provide additional figures and tables that further illustrate the results of the event selections described in Chapter 6.

Figure D.1a shows the energy spectrum of the single-photon candidates. Figures D.1b and D.1c show the transverse momentum distributions of the single-photon candidates in the barrel and endcaps, respectively. These plots complement the main results of the single-photon selection, described in detail Section 6.3.8 of Chapter 6.

Figures D.2 and D.3 show the recoil mass distributions of the single-photon and multi-photon events with missing energy, respectively, collected at different center-of-mass energies. Figure D.4 provides the energy spectra of the soft-photon candidates collected at different center-of-mass energies. These plots are of interest because production cross sections of most new physics signals increase with the center-of-mass energy of e^+e^- collisions.

The results of the single- and multi-photon selections are detailed in Tables D.1 and D.2, respectively. In addition, Table D.3 gives detailed results of the combined single- and soft-photon selections in the region of $x_\gamma < 0.5$, where x_γ is defined as the ratio of the photon energy to the beam energy.

The accessible format of these tables ensures that they can be used by any interested physicist[1] to test future models involving single- and multi-photon signatures at LEP. Table D.3 has already been used to search for branon production [200] and is currently used to search for several exotic SUSY signatures at LEP [256].

[1] These three tables were included in the final L3 paper on single- and multi-photon production at LEP [230] as part of the general data-archiving effort of L3. To a large extent, this effort was motivated by a recent example from the JADE experiment at PETRA e^+e^- collider. In 1998, twelve years after PETRA's shutdown, the JADE collaboration had to overcome significant difficulties in order to reanalyze its data with new theoretical models and improved analysis techniques [255].

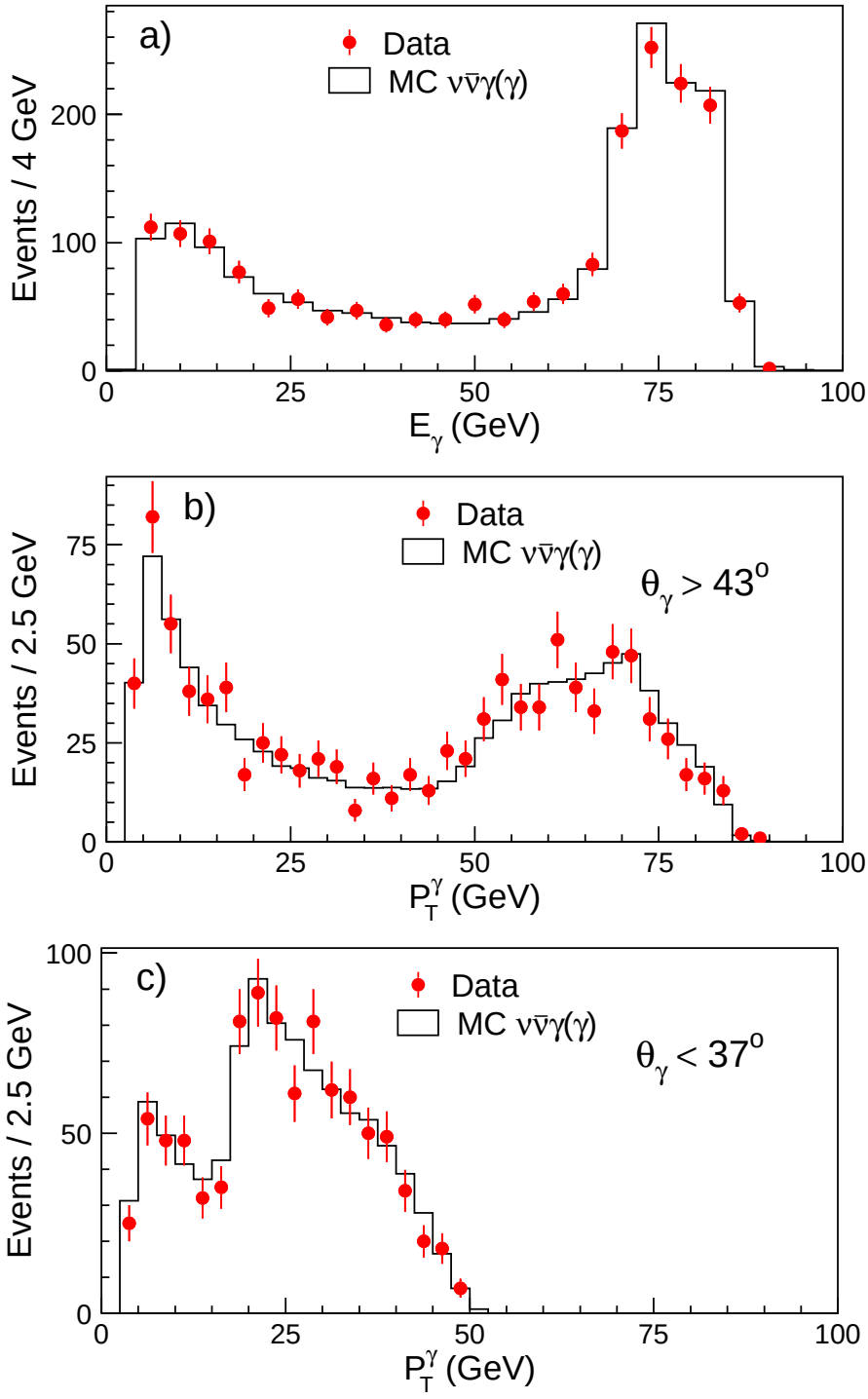

Figure D.1: a) Energy spectrum for the entire single-photon sample and transverse momentum distributions of the single-photon candidates b) in the barrel and c) in the endcaps.

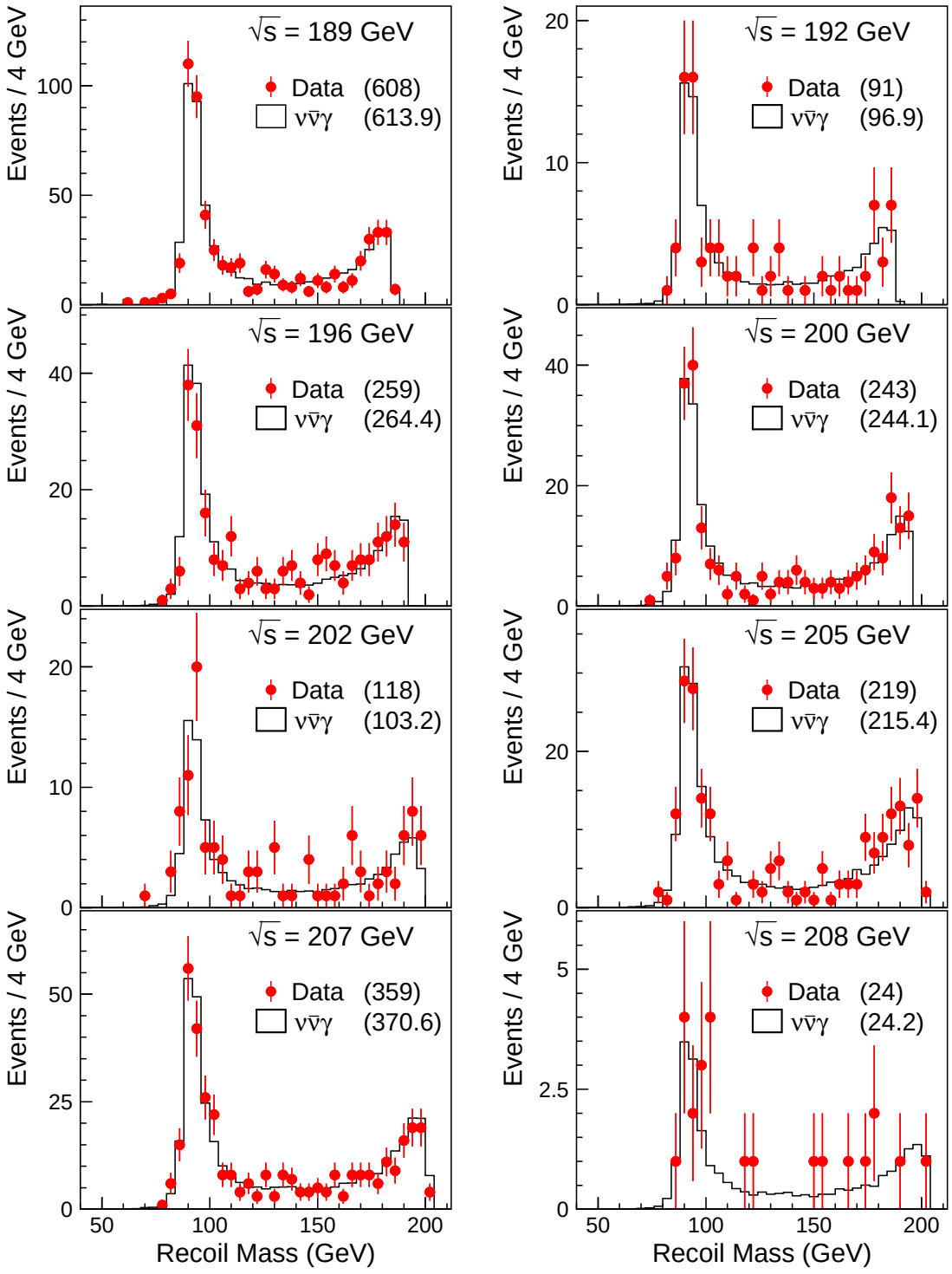

Figure D.2: Recoil mass distributions for the single-photon samples collected at different center-of-mass energies. The event statistics and values of $\sqrt{s}$ are indicated on the plots.

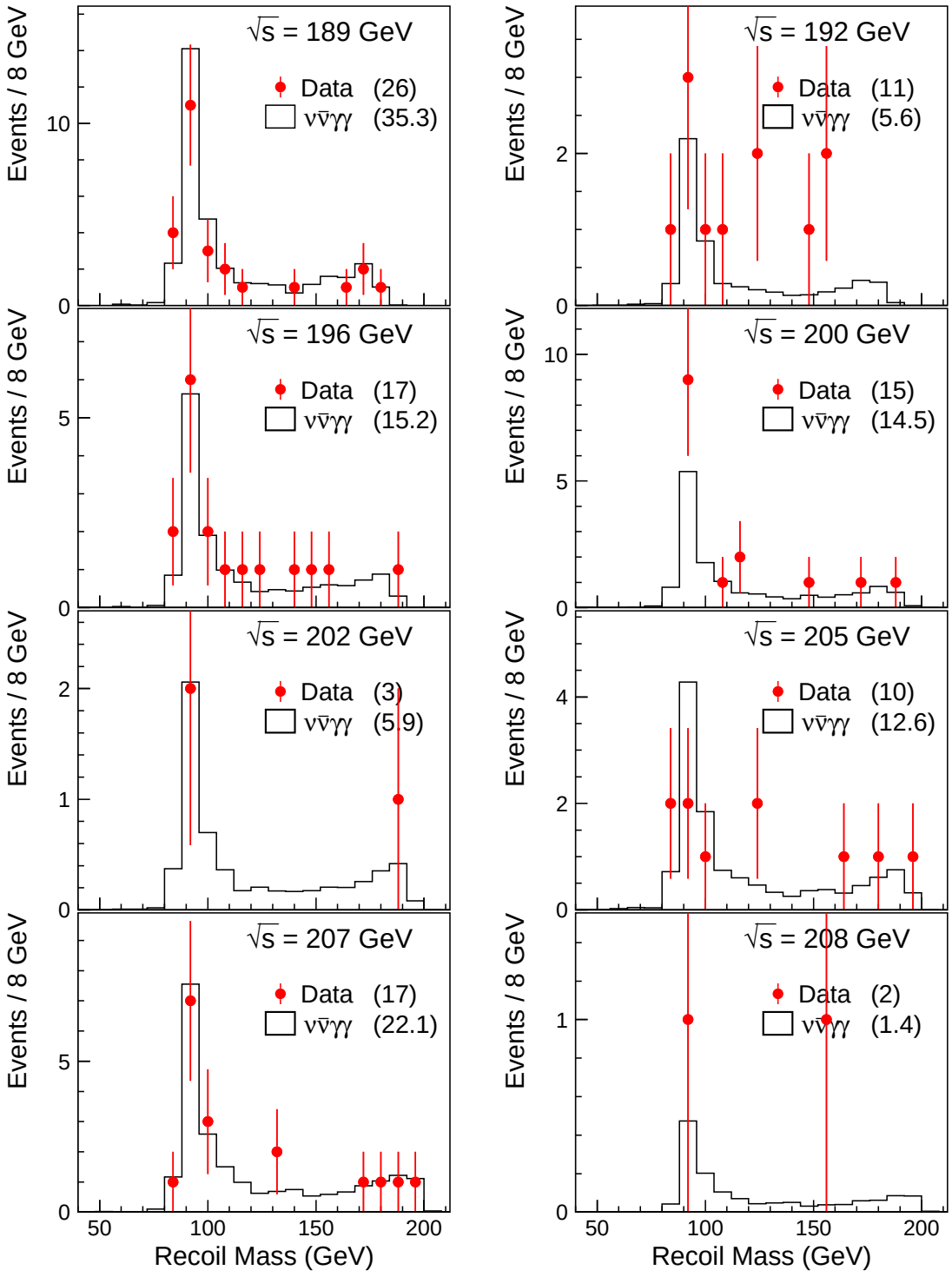

Figure D.3: Recoil mass distributions for the multi-photon samples collected at different center-of-mass energies. The event statistics and values of $\sqrt{s}$ are indicated on the plots.

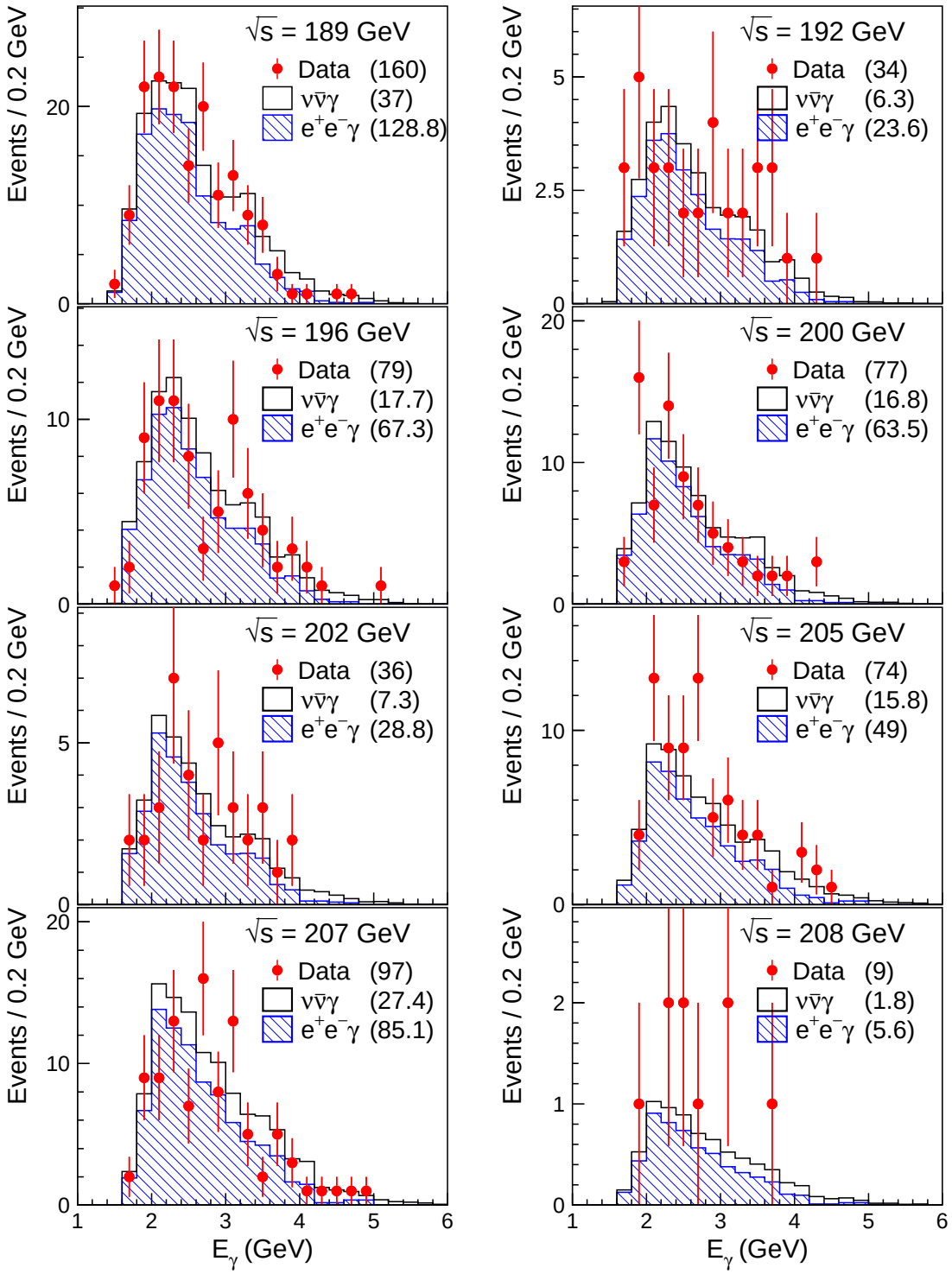

Figure D.4: Photon energy spectra for the soft-photon samples collected at different center-of-mass energies. The event statistics and values of $\sqrt{s}$ are indicated on the plots.

$\lvert\cos\theta_\gamma\rvert$	$M_{\rm rec}$ [GeV]					
	$0-70$	$70-95$	$95-120$	$120-145$	$145-170$	$170-210$
$0.000-0.200$	1/0.5/83	58/55.9/89	34/37.7/89	15/16.4/89	26/23.7/83	66/75.4/74
$0.200-0.400$	1/0.4/81	52/67.4/91	46/40.3/90	30/16.8/87	23/25.7/84	93/80.9/75
$0.400-0.600$	0/0.5/82	74/84.3/89	53/54.7/89	23/22.0/89	33/32.8/85	91/91.3/74
$0.600-0.730$	0/0.4/80	87/69.4/85	45/54.5/85	28/20.0/84	26/29.4/81	80/71.3/71
$0.800-0.870$	0/0.6/81	83/85.3/95	59/60.5/94	28/26.3/92	23/31.7/86	67/60.2/75
$0.870-0.920$	0/0.5/77	108/95.1/92	55/65.8/91	25/25.5/88	30/33.2/79	52/51.1/70
$0.920-0.953$	0/0.5/61	95/98.2/88	64/71.2/85	28/24.9/80	20/25.7/59	30/33.1/55
$0.953-0.972$	0/0.4/60	85/80.4/71	47/52.2/68	24/20.2/63	12/16.1/36	1/ 2.4/ 6

Table D.1: Number of events accepted by the single-photon selection in the 1998-2000 data, Standard Model expectations, and selection efficiencies (KKMC) in % as functions of the recoil mass and photon polar angle.

$M_{\rm rec}$ [GeV]	$E_{\gamma 2}$ [GeV]		
	$0-15$	$15-40$	$40-80$
Full sample			
$0-70$	0/ 0.2/62	0/ 0.1/66	0/0.2/64
$70-95$	38/30.7/64	12/12.4/53	0/1.5/57
$95-120$	15/21.7/65	5/ 7.9/56	0/0.4/53
$120-150$	9/10.2/60	2/ 2.5/51	—
$150-180$	13/16.8/54	0/ 0.7/46	—
$180-210$	7/ 7.4/41	—	—
Both Photons in Barrel ($43^\circ < \theta_\gamma < 137^\circ$)			
$0-70$	0/0.0/81	0/0.0/80	0/0.2/75
$70-95$	5/6.1/82	6/3.3/78	0/0.7/80
$95-120$	4/4.7/87	1/2.0/84	0/0.1/83
$120-150$	2/2.1/77	0/0.6/53	—
$150-180$	2/4.1/66	0/0.2/38	—
$180-210$	1/2.2/52	—	—

Table D.2: Numbers of observed and expected multi-photon events and selection efficiencies (KKMC) in % as functions of $E_{\gamma 2}$ and $M_{\rm rec}$ for the full sample and for the case in which both photons were in the barrel. These results are given for the combined 1998-2000 data sample.

x_γ	$\lvert\cos\theta_\gamma\rvert$																			
	$0-0.2$			$0.2-0.4$			$0.4-0.6$			$0.6-0.73$			$0.73-0.92$			$0.92-0.972$		
$0.00-0.02$	29	20.0		31	30.6		19	17.4		—			—			—		
	30	18		36	12		39	12		—			—			—		
$0.02-0.03$	39	39.6		58	53.2		111	112.7		111	129.9		—			—		
	54	31		54	25		51	13		53	9		—			—		
$0.03-0.05$	25	20.8		27	23.9		55	57.2		82	91.6		—			—		
	65	88		62	83		62	42		60	23		—			—		
$0.05-0.10$	28	28.7		36	30.3		36	37.1		31	31.0		12	18.1		—		
	69	100		70	100		68	98		63	95		17	96		—		
$0.10-0.20$	22	29.6		36	32.6		44	38.4		34	32.9		82	68.6		17	23.3	
	79	100		81	100		80	100		75	99		74	99		21	93	
$0.20-0.35$	24	22.7		21	25.6		28	30.5		34	27.2		43	57.7		24	30.4	
	82	100		83	99		84	100		81	100		79	99		38	100	
$0.35-0.50$	13	14.3		17	15.3		21	19.9		17	17.8		49	42.5		30	32.6	
	84	100		86	100		86	99		80	100		86	99		59	100	

Table D.3: Numbers of observed and expected single-photon events together with selection efficiencies and purities in % as functions of $|\cos\theta_\gamma|$ and of the ratio of the photon energy to the beam energy, x_γ. Results of the single- and soft-photon selections are combined for $x_\gamma < 0.5$. In the first row of each cell the left number represents the number of observed events and the right number the expectations from Standard Model processes. In the second row of each cell the left number is the selection efficiency (KKMC) and the right number is the purity. These results are given for the combined 1998-2000 data sample.

Appendix E

Combinations with Other LEP Experiments

The other three LEP experiments — ALEPH, DELPHI, and OPAL — have also studied the production of photonic events with missing energy and published descriptions of their work [111, 215, 216]. In this appendix I present the combinations of LEP results on the searches for photonic signatures expected in Supersymmetry and in models with extra dimensions. The LEP−combined samples of single- and multi-photon events with missing energy are also described. These combinations have been performed in the framework of the LEP SUSY [231] and Exotica [232] working groups, of which I am a member.

While the general designs of the LEP experiments were quite similar, the details varied significantly. In particular, the L3 BGO calorimeter stood prominently as the most accurate photon detector at LEP. Starting from 1997, the BGO calorimeter was precisely calibrated with the RFQ accelerator, which significantly improved its resolution and eliminated the resolution tails (see Chapter 5). The BGO energy resolution was about 1% for photons with energies above 10 GeV, at least three times as good as the resolution of any other electromagnetic calorimeter at LEP (see Section 4.2.3 p. 80).

In addition, the high-performance forward calorimeters of L3 allowed me to extend my single-photon selection to include photons with transverse momenta as low as 1.5 GeV (see Section 6.5). For comparison, the other LEP experiments had to apply a threshold cut of $P_t^\gamma \geq 5{-}7$ GeV. This resulted in L3 having a significantly higher sensitivity for detecting extra dimensions and pair-produced gravitinos.

For these reasons, the L3 experiment was the ideal place at LEP to search for new physics in photonic final states. As I will show below, the sensitivity of the

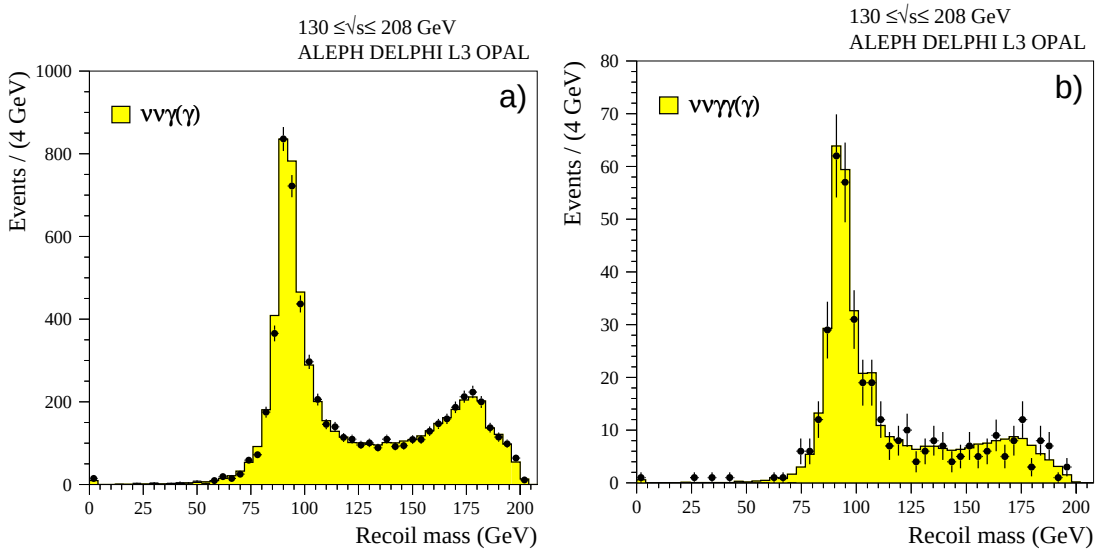

Figure E.1: Recoil mass spectra of the a) single-photon and b) multi-photon events selected by the four LEP experiments (points with error bars). The shaded histograms represent the Standard Model expectations.

LEP−combined searches for SUSY and extra dimensions was essentially the same as the sensitivity of my searches described in Sections 7.2 and 7.3. Moreover, the limits that I derived were almost always tighter than the limits obtained by combining the results from the other three LEP experiments.

E.1 The LEP Combined Event Samples

The combinations presented here are based on the results obtained with single- and multi-photon events selected by the four LEP experiments. These event samples have been selected in the data recorded during 1996-2000 from e^+e^- collisions at $\sqrt{s} = 161-208$ GeV, which corresponded to about 700 pb^{-1} per experiment. The only exception is the single-photon sample from OPAL which includes only events selected in about 250 pb^{-1} of data collected during 1996-1998 at $\sqrt{s} = 161 - 189$ GeV.[1] The combined single- and multi-photon samples consist of 6,282 and 392 events, respectively, with 6,424 and 406.3 events expected from Standard Model processes, mainly $e^+e^- \to \nu\bar{\nu}\gamma(\gamma)$. The corresponding recoil mass spectra are shown in Figure E.1.

[1] The OPAL experiment has not released any results from its single-photon analysis performed with 450 pb^{-1} of data collected in 1999-2000 at $\sqrt{s} = 192 - 208$ GeV.

$M_{\rm rec}$ [GeV]	Single-photon sample				Multi-photon sample			
	LEP		L3		LEP		L3	
	Data	MC	Data	MC	Data	MC	Data	MC
$0-70$	103	100.6	2	3.8	6	5.1	0	0.4
$70-110$	3272	3408.9	968	985.2	241	251.0	66	68.9
$110-160$	1350	1378.7	391	375.9	87	91.0	20	23.4
$160-210$	1557	1535.8	560	567.9	58	59.3	15	19.9
Total	6282	6424.1	1921	1932.7	392	406.3	101	112.7

Table E.1: Numbers of observed and expected events as a function of the recoil mass for the LEP−combined single- and multi-photon samples. For comparison, also given are the corresponding numbers for my samples selected using the L3 data collected at $\sqrt{s} = 189-208$ GeV.

Table E.1 gives the numbers of observed and expected events as functions of the recoil mass variable. For comparison, I also list the results of my single- and multi-photon selections performed using 619 pb^{-1} of data collected by L3 at $\sqrt{s} = 189-208$ GeV. In total, the L3 contributions represent about 35% and 30% of the LEP combined single- and multi-photon samples, respectively.

For the single-photon channel, there is good overall agreement between the LEP data and the Standard Model predictions. However, a noticeable deficit of events was observed in the region corresponding to the radiative return to the Z. In the bin $M_{\rm rec} = 70-110$ GeV, 3,272 events were found in the data while 3,408.9 were expected from the $e^+e^- \to \nu\bar{\nu}\gamma$ process. This corresponds to a deficit of about $-2.3\,\sigma$.

Much of this lack of data was caused by the contributions from DELPHI and OPAL, which both used the `KORALZ` Monte Carlo generator for the simulation of the $e^+e^- \to \nu\bar{\nu}\gamma$ process. However, the more advanced and precise `KKMC` program predicts 2 - 3% less events in the region of the Z-return peak (see Section 2.2.3). In addition, the DELPHI analysis suffered from significant systematic errors due to trigger inefficiencies and calorimeter calibration.[2] It should be noted that the ALEPH

[2]For the DELPHI analysis [216], the total systematic error on the measured cross section was about 5%, whereas for my analysis it was only about 1%.

and L3[3] single-photon analyses found a good agreement (within $0.5\,\sigma$) between the data and Monte Carlo in this region of the recoil mass spectrum. These two analyses were performed using the KKMC event generator and represented about 65% of the LEP−combined event sample.

The event statistics given in Table E.1 show that the other single-photon selections suffered from significantly higher backgrounds in the region of low recoil masses (high photon energies). Such background was mainly caused by the mismeasurement of events in the Z-return peak of the $e^+e^- \to \nu\bar{\nu}\gamma$ process. In my analysis, this source of background was found to be negligible because the RFQ calibration technique eliminated the BGO resolution tails (see Figure 5.9 p. 105). Only 3.8 $\nu\bar{\nu}\gamma$ events were expected in the bin $M_{\rm rec} < 70$ GeV, at least five times lower than for any other single-photon analysis performed at LEP. For this reason, the sensitivity of my searches for neutralino production processes in SUSY was substantially higher since such processes were expected to lead to events with energetic photons (see Sections 7.2.2 and 7.2.3).

For the multi-photon channel, good agreement between the data and Monte Carlo was observed for the entire recoil mass spectrum as shown in Figure E.1b. This combination is considered to be final since all four experiments provided their published results based on the full LEP2 data set.

E.2 Searches for SUSY Signatures

To perform combinations of LEP results on searches for Supersymmetry, the LEP SUSY working group adopted the following procedure. For a given signal hypothesis, each experiment provided the number of observed events, the number of expected background events, and the selection efficiency for this signal process. This information was then used to perform a multi-channel likelihood fit, and the cross section limits were derived using the *Fast Fourier Transform* method [257].

This procedure was suitable for the combination of results from other LEP ex-

[3]Here and in the following the L3 results refer to those described in this thesis.

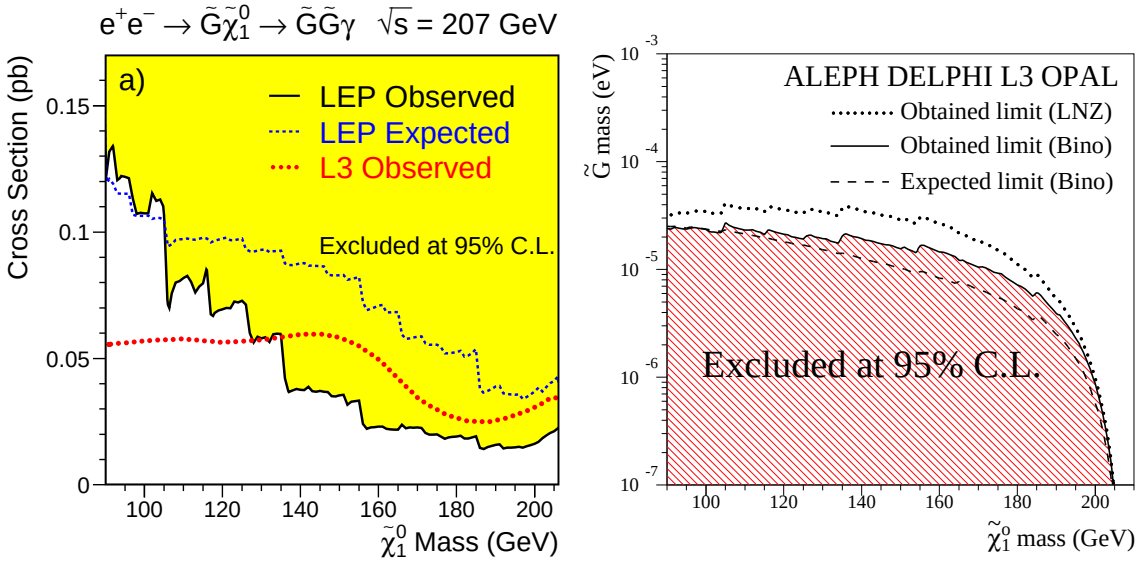

Figure E.2: **a)** Observed and expected upper limits on the production cross section of the reaction $e^+e^- \to \tilde{G}\tilde{\chi}_1^0 \to \tilde{G}\tilde{G}\gamma$, obtained from the LEP−combined search. The corresponding limits from my search are also shown. The limits were obtained at the 95% C.L. for $\sqrt{s} = 207$ GeV. Data collected at lower $\sqrt{s}$ were included assuming the signal cross section to scale according to the LNZ model [193]. **b)** Regions excluded in the $(m_{\tilde{\chi}_1^0}, m_{\tilde{G}})$ mass plane, under the assumptions of the LNZ model and a pure bino neutralino GMSB model with $m_{\tilde{e}_R} = 150$ GeV.

periments which employed event-counting methods [111, 215, 216]. However, my searches for new physics were based on likelihood fits to discriminating distributions as described in Section 7.2.1. In order to provide the required information, e.g., just one number of observed events, I had to apply additional cuts on the discriminating variables. Although I optimized the values of these cuts, for some mass hypotheses this led to a significant deterioration of the analysis performance. As a consequence, the sensitivity of the LEP−combined search could become lower than the sensitivity of my individual search.

Figure E.2a shows the observed and expected upper limits on the signal cross section obtained from the LEP−combined search for the $e^+e^- \to \tilde{G}\tilde{\chi}_1^0 \to \tilde{G}\tilde{G}\gamma$ process. For high neutralino masses $m_{\tilde{\chi}_1^0} \geq 110$ GeV, the obtained limits were found to be significantly better than expected. This effect was caused by a substantial deficit of data events observed by the ALEPH analysis [111] in the region of highest sensitivity,

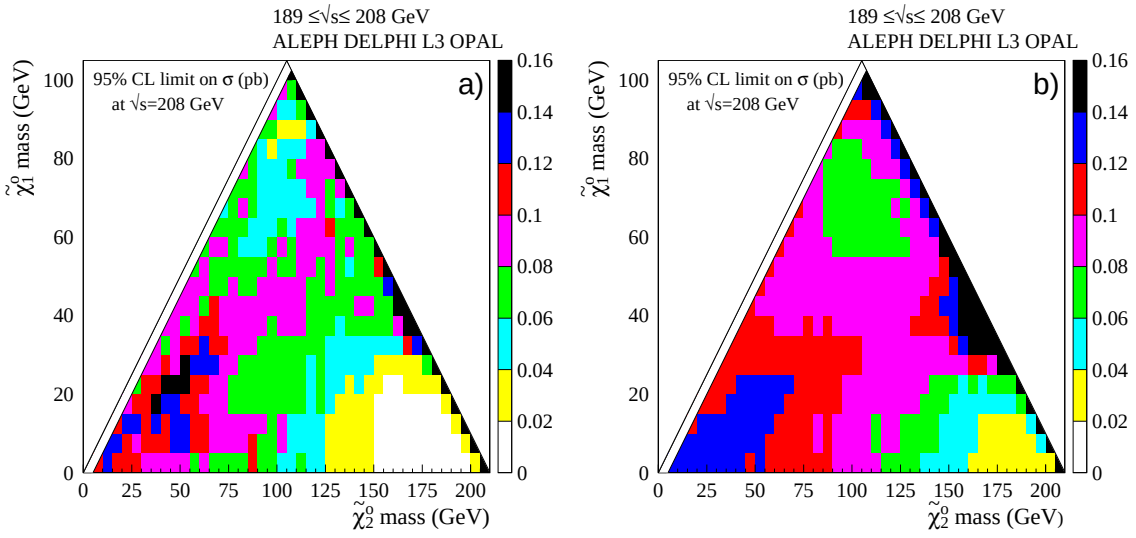

Figure E.3: a) Observed and b) expected cross section upper limits from the LEP−combined search for the process $e^+e^- \to \tilde{\chi}_2^0\tilde{\chi}_1^0 \to \tilde{\chi}_1^0\tilde{\chi}_1^0\gamma$. The limits were obtained at the 95% C.L. for $\sqrt{s} = 208$ GeV. The branching fraction for the $\tilde{\chi}_2^0 \to \tilde{\chi}_1^0\gamma$ decay was assumed to be 100%.

$M_{\rm rec} \lesssim 80$ GeV. Figure E.2a also shows the cross section limits that I derived in Section 7.2.2. The L3 and LEP−combined searches were found to have essentially the same sensitivity.

The no-scale SUGRA LNZ model has only two free parameters — the gravitino and the neutralino masses (see Section 3.2.4). Figure E.2b shows the exclusion region in the $(m_{\tilde{\chi}_1^0}, m_{\tilde{\rm G}})$ mass plane obtained from this combination of LEP results. Gravitino masses below 10^{-5} eV were excluded for neutralino masses below 185 GeV.

The LEP−combined search for the reaction $e^+e^- \to \tilde{\chi}_2^0\tilde{\chi}_1^0 \to \tilde{\chi}_1^0\tilde{\chi}_1^0\gamma$ was also performed. The observed and expected limits are shown in Figure E.3.

Multi-Photon Signatures

Figure E.4a shows the upper limits on the signal cross section obtained from the LEP−combined search for the $e^+e^- \to \tilde{\chi}_1^0\tilde{\chi}_1^0 \to \tilde{\rm G}\tilde{\rm G}\gamma\gamma$ process. In this case, the observed limits were in good agreement with the expectation. Figure E.4a also shows the limits on the $e^+e^- \to \tilde{\chi}_1^0\tilde{\chi}_1^0$ cross section that I derived from my search (Section 7.2.3). For neutralino masses above 85 GeV, the LEP−combined search was found to be more

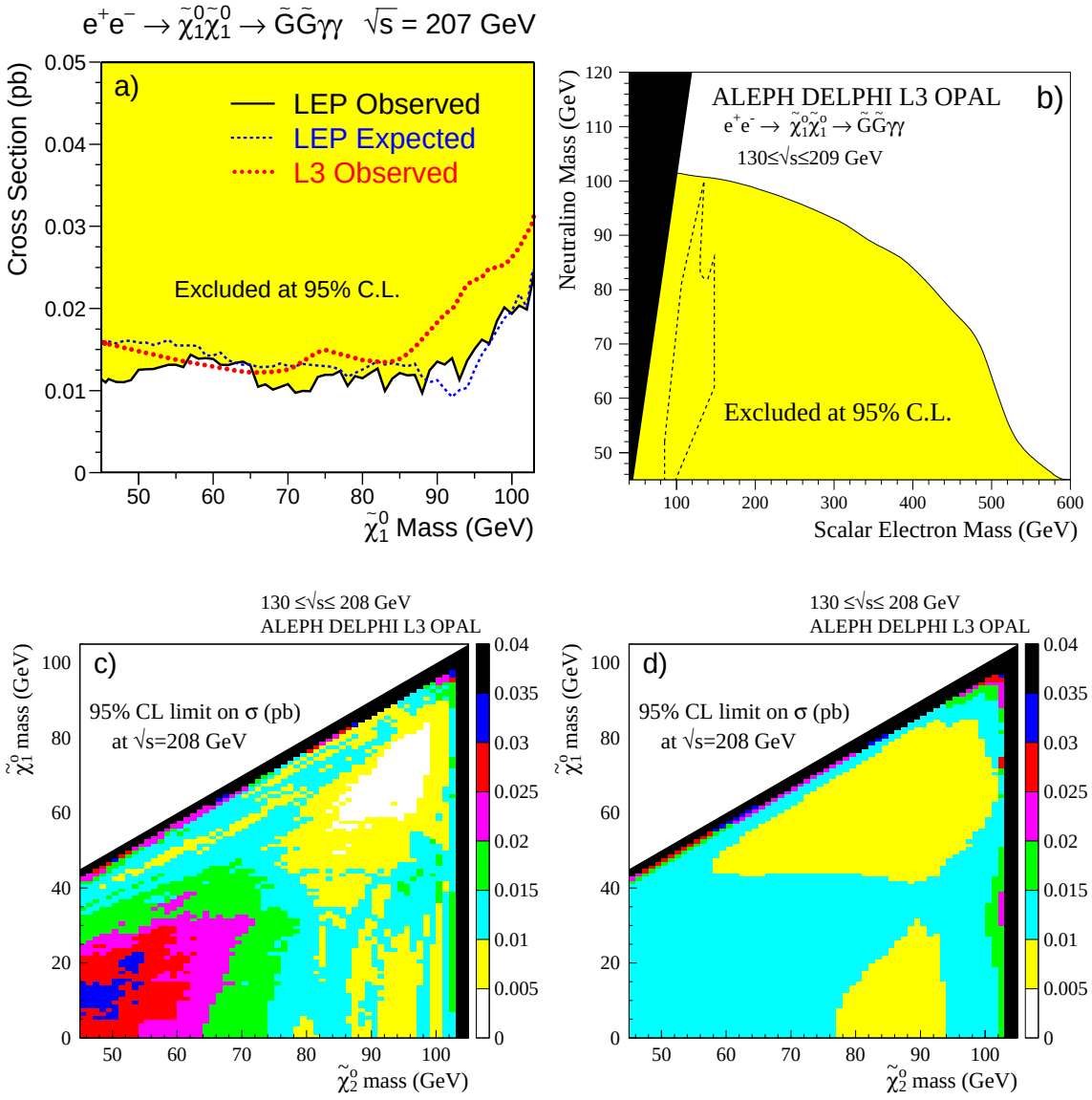

Figure E.4: **a)** Observed and expected upper limits on the production cross section of the reaction $e^+e^- \to \tilde{\chi}_1^0\tilde{\chi}_1^0 \to \tilde{G}\tilde{G}\gamma\gamma$, obtained from the LEP−combined search. The corresponding limits from my search are also shown. The limits were obtained at the 95% C.L. for $\sqrt{s} = 207$ GeV. Data collected at lower $\sqrt{s}$ were included assuming the signal cross section to scale according to the MGM model [194]. **b)** Region excluded for a pure bino neutralino model in the $(m_{\tilde{e}_R}, m_{\tilde{\chi}_1^0})$ mass plane. The region compatible with the GMSB interpretation of the CDF event [68] is also shown. **c)** Observed and **d)** expected cross section upper limits from the LEP−combined search for the process $e^+e^- \to \tilde{\chi}_2^0\tilde{\chi}_2^0 \to \tilde{\chi}_1^0\tilde{\chi}_1^0\gamma\gamma$. The limits were obtained at the 95% C.L. for $\sqrt{s} = 208$ GeV. The branching fraction for the $\tilde{\chi}_2^0 \to \tilde{\chi}_1^0\gamma$ decay was assumed to be 100%.

sensitive. The achieved improvement over the results of my analysis was equivalent to increasing the size of my data sample by about 50%. The region excluded at the 95% C.L. in the $(m_{\tilde{e}_R}, m_{\tilde{\chi}_1^0})$ mass plane is shown in Figure E.4b. The GMSB interpretation of the rare CDF event (Section 3.2.2) was ruled out by this combination of LEP analyses.

The LEP−combined search for the reaction $e^+e^- \to \tilde{\chi}_2^0\tilde{\chi}_2^0 \to \tilde{\chi}_1^0\tilde{\chi}_1^0\gamma\gamma$ was also performed. The observed and expected limits are shown in Figures E.4c,d.

E.3 Searches for Extra Dimensions

All four LEP experiments have searched for the emission of Kaluza-Klein gravitons via the reaction $e^+e^- \to \gamma G$. As discussed in Section 3.3.1, this reaction leads to a single-photon with missing energy signature since the gravitons would escape undetected. Its differential cross section is expected to peak at low photon energies and polar angles (see Figure 3.16 p. 59).

n	M_D (TeV)			
	ALEPH [111]	DELPHI [216]	L3 [230]	OPAL [215]
2	1.26	1.31	1.50	1.09
3	0.95	1.02	1.14	0.86
4	0.77	0.82	0.91	0.71
5	0.65	0.67	0.76	0.61
6	0.57	0.58	0.65	0.53

Table E.2: Lower limits at the 95% confidence level on the new gravity scale M_D for different numbers of extra dimensions n, derived by the four LEP experiments from the individual searches for graviton-photon emission. The L3 search was described in Section 7.3. The OPAL limits were obtained using only the data set recorded in 1998 at $\sqrt{s} = 189$ GeV.

Searches performed by ALEPH [111], DELPHI [216], and L3 (Section 7.3) used the highest center-of-mass energy and luminosity LEP data sets collected during 1998-2000 at $\sqrt{s} = 189 - 208$ GeV, which corresponded to an integrated luminosity of

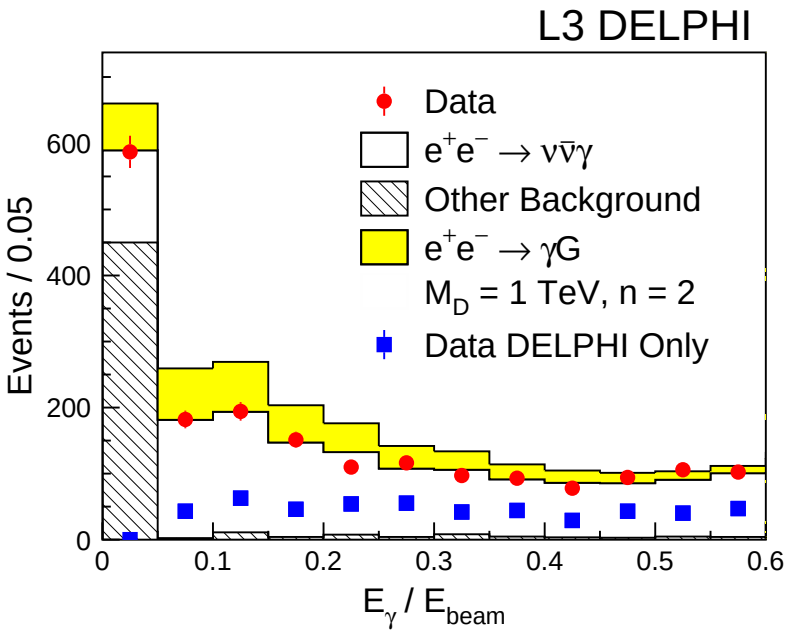

Figure E.5: Distribution of the ratio of the photon energy to the beam energy for the single-photon events selected by DELPHI and L3 together with the Standard Model prediction. Expected signal from the reaction $e^+e^- \to \gamma G$ is also shown for $M_D = 1$ TeV and $n = 2$. In addition, the individual contribution from DELPHI is shown as squares with error bars.

about 0.6 fb^{-1} per experiment. Since OPAL had analyzed only the data collected in 1998 at $\sqrt{s} = 189$, its results [215] were not considered for this combination.

Good agreement with the Standard Model prediction was observed by all experiments. In order to place limits on the new gravity scale M_D, each experiment performed a fit to its measured single-photon distributions under the assumption that the data contained a mixture of the signal and Standard Model background. The obtained limits are given in Table E.2.

The limits derived by my analysis are substantially tighter than those derived by DELPHI and ALEPH. This effect can be understood by examining Figure E.5, which shows the energy spectrum of the single-photon events selected by DELPHI and L3 together with the Standard Model prediction and the expected signal from the graviton-photon emission. This figure shows that in the region of highest sensitivity, $E_\gamma/E_{beam} < 0.2$, this sample was dominated by events from my single- and soft-photon selections (see Sections 6.3.8 and 6.5).

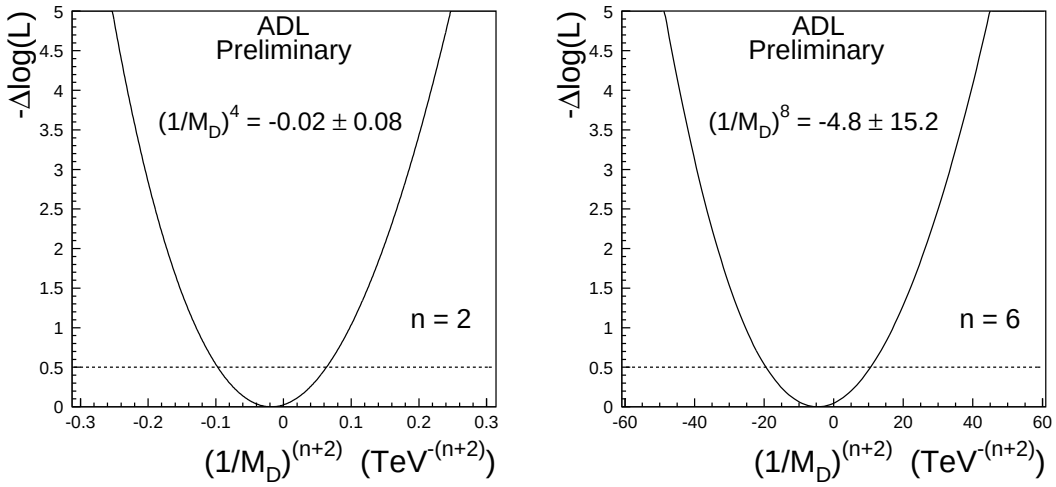

Figure E.6: The combined (ALEPH, DELPHI, and L3) negative log-likelihoods as functions of $(1/M_D)^{n+2}$ for $n = 2$ and $n = 6$. In each case, the minimum value was subtracted. The dashed line indicates $-\Delta \log \mathcal{L} = +0.5$.

Combination of the LEP Results

The combination was performed[4] using the likelihood functions derived by the ALEPH, DELPHI, and L3 individual analyses. Because the signal kinematic distributions were expected to change with the number of extra dimensions n, each experiment provided a separate log-likelihood function, $\log \mathcal{L}$, for each value of n. The systematic uncertainties were taken into account by each experiment separately. They were found to have no significant effect on the combined limits.

The individual $\log \mathcal{L}$ functions were added together, and the combined likelihoods were used to fit for the parameter $(1/M_D)^{n+2}$. This parameterization was chosen because, for a given n, the signal kinematic distributions were independent of M_D and the total cross section scaled as $(1/M_D)^{n+2}$. Figure E.6 shows that the combined $\log \mathcal{L}$ curves were close to parabolas.

The results of the fits are given in Table E.3, where the error on the parameter $(1/M_D)^{n+2}$ corresponds to a change in the negative log-likelihood with respect to its minimum of 0.5. The fitted values of $(1/M_D)^{n+2}$ were found to be in good agreement with the Standard Model expectation of zero.

[4] This work was done in collaboration with Dr. Stefan Ask (Lund University).

n	$(1/M_D)^{n+2}$	M_D (TeV)	R (mm)
2	-0.02 ± 0.08 TeV^{-4}	> 1.60	< 0.19
3	-0.09 ± 0.22 TeV^{-5}	> 1.20	$< 2.6 \times 10^{-6}$
4	-0.3 ± 0.8 TeV^{-6}	> 0.94	$< 1.1 \times 10^{-8}$
5	-0.9 ± 3.3 TeV^{-7}	> 0.77	$< 4.1 \times 10^{-10}$
6	-4.8 ± 15.2 TeV^{-8}	> 0.66	$< 4.6 \times 10^{-11}$

Table E.3: Fitted values of $(1/M_D)^{n+2}$ together with lower limits on the gravity scale (M_D) as functions of the number of extra dimensions (n). Upper limits on the size of the extra dimensions (R) are also given. All limits are LEP−combined (ADL) and are at the 95% confidence level.

Since no indication of a signal was found, limits on the new gravity scale were derived using the Bayesian likelihood method. At the 95% confidence level, a one-sided lower limits on M_D were obtained as

$$\mathrm{CL} = \frac{\int_0^{x_{95}} \mathcal{L}(x')dx'}{\int_0^{\infty} \mathcal{L}(x')dx'} = 0.95\,, \tag{E.1}$$

where $x = (1/M_D)^{n+2}$, $\mathcal{L}(x)$ is the combined likelihood function, and the integration is performed over the physical region $x > 0$. The derived limits are listed in Table E.3. The achieved improvement over the results of my analysis (Table E.2) roughly corresponds to increasing the size of my data sample by 50%.

The lower limits on the gravity scale can be converted into upper limits on the size of extra dimensions (R) using the following equation [80]:

$$G_N^{-1} = 8\pi R^n M_D^{n+2}\,, \tag{E.2}$$

where G_N^{-1} is Newton's constant of gravitation. Figure E.7 shows the radii of the extra dimensions as functions of the gravity scale M_D together with the obtained 95% C.L. upper limits on R. These limits are also listed in Table E.3.

The LEP−combined search for extra spatial dimensions excluded at the 95% C.L. gravity scales below between 1.6 TeV and 0.66 TeV for the number of extra dimensions

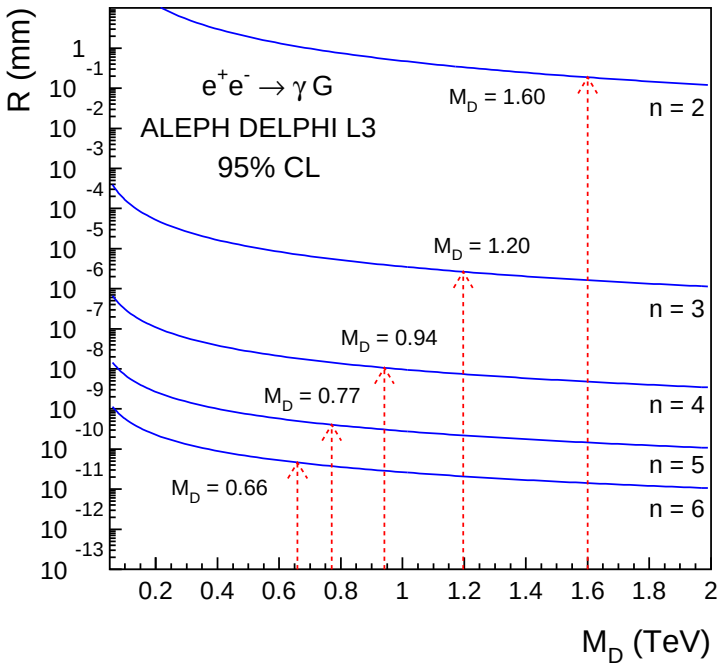

Figure E.7: The radii of the extra dimensions R as functions of the gravity scale M_D for $n = 2 - 6$. Arrows indicate the obtained upper limits on R.

between 2 and 6. The CDF and DØ experiments at the Tevatron $p\bar{p}$ collider have searched for the production of Kaluza-Klein gravitons in monojet events. The current CDF result excludes gravity scales below 1.0, 0.77, and 0.71 TeV for $n = 2, 4$, and 6, respectively [223]. The DØ experiment quoted slightly lower limits[5] [222]. Thus, for $n < 6$ the LEP limits are the best bounds to date on direct graviton emission in collider experiments. It should be noted that short-range tests of Newton's law [79] as well as astrophysical and cosmological constraints [78] provide similar or better bounds for the case of two extra dimensions. However, for $n > 2$ such bounds are relatively weak.

[5]The Tevatron results were obtained using the Run 1 data only. However, a preliminary analysis of the Run 2 data indicates that these limits will not be significantly improved at Run 2 [258].

Bibliography

[1] J. J. Thomson, Phil. Mag. **44**, 293 (1897);
J. J. Thomson, Nature **55**, 453 (1897).

[2] S.L. Glashow, Nucl. Phys. **22**, 579 (1961);
S. Weinberg, Phys. Rev. Lett. **19**, 1264 (1967);
A. Salam, *Elementary Particle Theory*, Ed. N. Svartholm *et al.*, 367 (1968).

[3] P.W. Higgs, Phys. Lett. **12**, 132 (1964);
P.W. Higgs, Phys. Rev. Lett. **13**, 508 (1964);
P.W. Higgs, Phys. Rev. **145**, 1156 (1966).

[4] H. Fritzsch, M. Gell-Mann, and H. Leutwyler, Phys. Lett. **B 47**, 365 (1973);
D.J. Gross and F. Wilczek, Phys. Rev. **D 8**, 3633 (1973).

[5] G. 't Hooft, Nucl. Phys. **B 33**, 173 (1971);
G. 't Hooft, Nucl. Phys. **B 35**, 167 (1971).

[6] Particle Data Group, S. Eidelman *et al.*, Phys. Lett. **B 592**, 1 (2004).

[7] CDF Collab., F. Abe *et al.*, Phys. Rev. **D 50**, 2966 (1994);
CDF Collab., F. Abe *et al.*, Phys. Rev. Lett. **74**, 2626 (1995);
D$\emptyset$ Collab., S. Abachi *et al.*, Phys. Rev. Lett. **74**, 2632 (1995).

[8] DONuT Collab., K. Kodama *et al.*, Phys. Lett. **B 504**, 218 (2001).

[9] L3 Experiment, *http://l3.web.cern.ch/l3/.*

[10] LEP Electroweak Working Group,
The current results can be found at *http://lepewwg.web.cern.ch/LEPEWWG/*

LEP Collaborations, *A Combination of Prelimifary Electroweak Measurements and Constraints on the Standard Model*, arXiv:hep-ex/0412015 (2004).

[11] LEP Collaborations, *Search for the Standard Model Higgs Boson at LEP*, Phys. Lett. **B 565**, 61 (2003).

[12] For recent reviews see, e.g.:
E. Roulet, *Beyond the Standard Model*, arXiv:hep-ph/0112348 (2001); C. Quigg, *Beyond the Standard Model in Many Directions*, arXiv:hep-ph/0404228 (2004); G. Altarelli, *The Electroweak Interactions in the Standard Model and Beyond*, arXiv:hep-ph/0406270 (2004).

[13] Super-Kamiokande Collab., S. Fukuda *et al.*, Phys. Rev. Lett. **85**, 3999 (2000);
Y. Fukuda *et al.*, Phys. Rev. Lett. **81**, 1562 (1998);
SNO Collab., Q.R. Ahmad *et al.*, Phys. Rev. Lett. **89**, 011301 (2002);
SNO Collab., Q.R. Ahmad *et al.*, Phys. Rev. Lett. **89**, 011302 (2002);
KamLAND Collab., K. Eguchi *et al.*, Phys. Rev. Lett. **90**, 021802 (2003).

[14] For recent reviews see, e.g.:
C. Giunti, *Status of Neutrino Masses and Mixing*, hep-ph/0309024 (2003);
K. Scholberg, *Neutrino Physics: Status and Prospects*, hep-ex/0308011 (2003);
H. Murayama, *Theoretical Neutrino Physics*, Eur. Phys. J. **C 33**, DOI 10.1140/epjcd/s2004-03-1697-8, (2004).

[15] A. Straessner, *Measurement of the W Boson Mass at LEP*, arXiv:hep-ex/0405005 (2004).

[16] Z. Berezhiani and A. Rossi, Phys. Lett. **B 535**, 207 (2002).

[17] `KKMC` version 4.19 is used:
S. Jadach, B.F.L. Ward, and Z. Was, Comput. Phys. Commun. **130**, 260 (2000).

[18] C. Mana, M. Martinez, and R. Miquel, *Radiative Corrections To The Neutrino Counting Experiment*, UAB-LFAE-89-07, Talk given at Ann Arbor Workshop

on QED Structure Functions, May 22-25, 1989;
ALEPH Collab., R. Barate *et al.*, Phys. Lett. **B 445**, 239 (1998).

[19] S. M. Bilenky, *Neutrinos*, arXiv:physics/0103091 (2001);
M. Shaevitz, *Neutrino Physics, Masses, and Oscillations*, in Proceedings of the 16th Lake Louise Winter Institute on Fundamental Interactions, 2002.

[20] G. Bonneau and F. Martin, Nucl. Phys. **B 27**, 381 (1971);
F. A. Berends and R. Kleiss, Nucl. Phys. **B 260**, 32 (1985);
O. Nicrosini and L. Trentadue, Nucl. Phys. **B 318**, 1 (1989);
M.E. Peskin, D.V. Schroeder, *An Introduction to Quantum Field Theory*, Addison-Wesley, 1995, pp. 173-174.

[21] G. Montagna *et al.*, Nucl. Phys. **B 452**, 161 (1995).

[22] `KORALZ` version 4.04 is used:
S. Jadach, B.F.L. Ward, and Z. Was, Comput. Phys. Commun. **79**, 503 (1994);
S. Jadach, B.F.L. Ward, and Z. Was, Comput. Phys. Commun. **124**, 233 (2000).

[23] Z. Was, private communication (2003).

[24] D.Y. Bardin *et al.*, Eur. Phys. J. **C 24**, 373 (2002).

[25] S. Jadach, B.F.L. Ward, and Z. Was, Phys. Rev. **D 63** (2001) 113009.

[26] D.Y. Bardin *et al.*, Comput. Phys. Commun. **59**, 303 (1990).

[27] `NUNUGPV` version 2.0 is used:
G. Montagna *et al.*, Nucl. Phys. **B 541**, 31 (1999);
G. Montagna, O. Nicrosini, and F. Piccinini, Comput. Phys. Commun. **98**, 206 (1996).

[28] Two-Fermion Working Group, M. Kobel *et al.*, arXiv:hep-ph/0007180 (2000).

[29] P.A.M. Dirac, Proc. Roy. Soc. Lond. **A 117**, 610 (1928).

[30] C.D. Anderson, Phys. Rev. **43**, 491 (1933).

[31] A review can be found for example in:
H.E. Haber and G.L. Kane, Phys. Rep. **117**, 75 (1985).

[32] R. Haag, J.T. Lopuszanski, and M. Sohnius, Nucl. Phys. **B 88**, 257 (1975).

[33] G. 't Hooft, in: G. 't Hooft *et al.*, eds., *Recent Developments in Field Theories*, Plenum Press, New York, 1980;
E. Witten, Nucl. Phys. **B 188**, 513 (1981);
R.K. Kaul, Phys. Lett. **B 109**, 19 (1982).

[34] J. R. Ellis, *Supersymmetry for Alp Hikers*, arXiv:hep-ph/0203114 (2002).

[35] U. Amaldi, W. de Boer, and H. Furstenau, Phys. Lett. **B 260**, 447 (1991).

[36] P. Fayet, Nucl. Phys. **B 90**, 104 (1975);
A. Salam and J. Strathdee, Nucl. Phys. **B 87**, 85 (1975).

[37] J. Ellis *et al.*, Nucl. Phys. **B 238**, 453 (1984).

[38] S. P. Martin, *A Supersymmetry Primer*, arXiv:hep-ph/9709356 (1997).

[39] G. Jungman, M Kamionkowski, and K. Griest, Phys. Reports **267**, 195 (1996).

[40] A.R. Liddle and D.H. Lyth, Phys. Reports **213**, 1 (1993).

[41] C.L. Bennett *et al.*, Astrophys. J. Suppl. **148**, 1 (2003).

[42] P. Gondolo, *Non-baryonic Dark Matter*, arXiv:astro-ph/0403064 (2004);
A.B. Lahanas, N.E. Mavromatos, and D.V. Nanopoulos, Int. J. Mod. Phys. **D 12**, 1529 (2003); V. Sahni, *Dark Matter and Dark Energy*, arXiv:astro-ph/0403324 (2003).

[43] J.F. Gunion, H.E. Haber, G. Kane, and S. Dawson, *The Higgs Hunter's Guide*, Frontiers in Physics **vol. 80**, Addison-Wesley, 1990.

[44] S.L. Glashow and S. Weinberg, Phys. Rev. **D 15**, 1958 (1997).

[45] S. Dawson, *The MSSM and Why It Works*, arXiv:hep-ph/9712464 (1997).

[46] K. Inoue *et al.*, Prog. Theor. Phys. **67**, 1889 (1982);
R. A. Flores and M. Sher, Annals Phys. **148**, 95 (1983);
J. F. Gunion and H.E. Haber, Nucl. Phys. **B 272**, 1 (1986) [Erratum-ibid. **B 402**, 567 (1993)].

[47] G. Degrassi *et al.*, Eur. Phys. J. **C 28**, 133 (2003).

[48] M. E. Peskin, *Beyond the Standard Model*, arXiv:hep-ph/9705479 (1997).

[49] J. Goldstone, Nuovo Cim. **19**, 154 (1961);
J. Goldstone, A. Salam, and S. Weinberg, Phys. Rev. **127**, 965 (1962).

[50] P. Fayet, Phys. Lett. **B 84**, 421 (1979);
P. Fayet, Phys. Lett. **B 86**, 272 (1979).

[51] S. Dreser and B. Zumino, Phys. Rev. Lett. **38**, 1433 (1977);
D.V. Volkov and V.A. Soroka, JETP Lett. **18**, 312 (1973).

[52] L.J. Hall, J. Lykken, and S. Weinberg, Phys. Rev. **D 27**, 2359 (1983).

[53] S.K. Soni and H.A. Weldon, Phys. Lett. **B 126**, 215 (1983);
Y. Kawamura, H. Murayama, and M. Yamaguchi, Phys. Rev. **D 51**, 1337 (1995).

[54] L.E. Ibanez, Phys. Lett. **B 118**, 73 (1982);
L.E. Ibanez and G.G. Ross, Phys. Lett. **B 110**, 215 (1982);
J.R. Ellis, D.V. Nanopoulos, and K. Tamvakis, Phys. Lett. **B 121**, 123 (1983);
J.R. Ellis *et al.*, Phys. Lett. **B 125**, 275 (1983);
L. Alvarez-Gaume, J. Polchinski, and M.B. Wise, Nucl. Phys. **B 221**, 495 (1983).

[55] M. Dine and A.E. Nelson, Phys. Rev. **D 48**, 1277 (1993);
M. Dine, A.E. Nelson, and Y. Shirman, Phys. Rev. **D 51**, 1362 (1995);
M. Dine *et al.*, Phys. Rev. **D 53**, 2658 (1996).

[56] G. F. Giudice and R. Rattazzi, Phys. Rept. **322**, 419 (1999).

[57] J.A. Bagger *et al.*, Phys. Rev. Lett. **78**, 1002 (1997);
S. Dimopoulos, S. Thomas, and J.D. Wells, Nucl. Phys. **B 488**, 39 (1997).

[58] D. Ruschmeier, *Search for New Physics in Electron-Positron Interactions with Photons in the Finals State*, Ph.D. thesis, Humboldt University, 1999.

[59] H. Baer *et al.*, *Simulating Supersymmetry with ISAJET 7.0 / ISASUSY 1.0*, arXiv:hep-ph/9305342 (1993).

[60] S. Ambrosanio *et al.*, Phys. Rev. **D 54**, 5395 (1996).

[61] J.A. Bagger *et al.*, Phys. Rev. **D 55**, 3188 (1997).

[62] A. Bartl, H. Fraas, and W. Majerotto, Nucl. Phys. **B 278**, 1 (1986);
S. Ambrosanio and B. Mele, Phys. Rev. **D 52**, 3900 (1995).

[63] J.R. Ellis and J.S. Hagelin, Phys. Lett. **B 122**, 303 (1983).

[64] J.H. Dann, *A Study of Single and Multi-Photon Events in* e^+e^- *Collisions at Center-of-Mass Energies of 161* GeV *and 172* GeV, Ph.D. thesis, UC Santa Cruz, 1998.

[65] S. Ambrosanio, G.D. Kribs, and S.P. Martin, Phys. Rev. **D 56**, 1761 (1997).

[66] `SUSYGEN` version 2.20 is used:
S. Katsanevas and P. Morawitz, Comp. Phys. Comm. **112**, 227 (1998).

[67] CDF Collab., F. Abe *et al.*, Phys. Rev. Lett. **81**, 1791 (1998).

[68] J.L. Lopez and D.V. Nanopoulos, Phys. Rev. **D 55**, 4450 (1997).

[69] S. Ambrosanio *et al.*, Phys. Rev. **D 55**, 1372 (1997).

[70] S. Ambrosanio and B. Mele, Phys. Rev. **D 55**, 1399 (1997);
H. Baer and T. Krupovnickas, JHEP **0209**, 038 (2002).

[71] E. Cremmer *et al.*, Phys. Lett. **B 133**, 61 (1983);
J. Ellis *et al.*, Nucl. Phys. **B 241**, 406 (1984);
J. Ellis *et al.*, Nucl. Phys. **B 247**, 373 (1984).

[72] A. Brignole, F. Feruglio, and F. Zwirner, Nucl. Phys. **B 516**, 13 (1998).

[73] J.L. Lopez, D.V. Nanopoulos, and A. Zichichi, Phys. Rev. **D 49**, 343 (1994);
J.L. Lopez, D.V. Nanopoulos, and A. Zichichi, Int. J. Mod. Phys. **A 10**, 4241 (1995).

[74] J.R. Ellis, J.L. Lopez, and D. V. Nanopoulos, Phys. Lett. **B 394**, 354 (1997).

[75] I. Antoniadis *et al.*, Phys. Lett. **B 194**, 231 (1987);
J. Ellis *et al.*, Nucl. Phys. **B 311**, 1 (1989).

[76] P. Fayet, Phys. Lett. **B 117**, 460 (1982);
O. Nachtmann, A. Reiter, and M. Wirbel, Z. Phys. **C 27**, 577 (1985);
A. Brignole, F. Feruglio, and F. Zwirner, Nucl. Phys. **B 501**, 332 (1997).

[77] N. Arkani-Hamed, S. Dimopoulos, and G.R. Dvali, Phys. Lett. **B 429**, 263 (1998); I. Antoniadis, N. Arkani-Hamed, S. Dimopoulos, and G.R. Dvali, Phys. Lett. **B 436**, 257 (1998); N. Arkani-Hamed, S. Dimopoulos, and G.R. Dvali, Phys. Rev. **D 59**, 086004 (1999).

[78] For recent reviews see, e.g.:
J. Hewett and M. Spiropulu, Ann. Rev. Nucl. Part. Sci. **52**, 397 (2002);
F. Feruglio, Eur. Phys. J. **C 33**, S114 (2004), hep-ph/0401033;
S. Mele, Eur. Phys. J. **C 33**, S919 (2004).

[79] J.C. Long and J.C. Price, Comptes Rendus Physique **4**, 337 (2003).

[80] G.F. Giudice, R. Rattazzi, and J.D. Wells, Nucl. Phys. **B 544**, 3 (1999).

[81] E. Mirabelli, M. Perelstein, and M.E. Peskin, Phys. Rev. Lett. **82**, 2236 (1999);
T. Han, J.D. Lykken, and R.J. Zhang, Phys. Rev. **D 59**, 105006 (1999).

[82] R. Sundrum, Phys. Rev. **D 59**, 085009 (1999);
A. Dobado and A.L. Maroto, Nucl. Phys. **B 592**, 203 (2001).

[83] J.A.R. Cembranos, A. Dobado, and A.L. Maroto, Phys. Rev. Lett. **90**, 241301 (2003); J.A.R. Cembranos, A. Dobado, and A.L. Maroto, Phys. Rev. **D 68**, 103505 (2003).

[84] J. Alcaraz *et al.*, Phys. Rev. **D 67**, 075010 (2003).

[85] M. Bando *et al.*, Phys. Rev. Lett. **83**, 3601 (1999).

[86] D. Brandt *et al.*, Rep. Prog. Phys. **63**, 939 (2000).

[87] L3 Collab., B. Adeva *et al.*, Nucl. Inst. Meth. **A 289**, 35 (1990).

[88] ALEPH Collab., D. Decamp *et al.*, Nucl. Instrum. Meth. **A 294**, 121 (1990).

[89] OPAL Collab., K. Ahmet *et al.*, Nucl. Instrum. Meth. **A 305**, 275 (1991).

[90] DELPHI Collab., P. Aarnio *et al.*, Nucl. Instrum. Meth. **A 303**, 233 (1990).

[91] LEP Design Report, **Vol. 1**, *The LEP Injector Chain*, CERN–LEP/TH/83–29, CERN, (1983).

[92] UA1 Collab., G. Arnison *et al.*, Phys. Lett. **B 122**, 103 (1983).

[93] UA2 Collab., M. Banner *et al.*, Phys. Lett. **B 122**, 476 (1983).

[94] K. Schindl, *The Injector Chain for the LHC*, in Proceedings of the 9th LEP-SPS Performance Workshop, Chamonix, France, ed. J. Poole, CERN/PS 99-018.

[95] LEP Collaborations, CERN-EP/2000-153, arXiv:hep-ex/0101027 (2000).

[96] R.W. Assmann, *LEP Operation and Performance with Electron-Positron Collisions at 209 GeV*, in Proceedings of 11th LEP-SPS Performance Workshop, Chamonix, France, CERN-SL-2001-003-DI.

[97] P. Brown *et al.*, *Ultimate Performance of the LEP RF System*, in Proceedings of IEEE Particle Accelerator Conference, Chicago, USA, CERN-SL-2001-018-HRF.

[98] L. Arnaudon *et al.*, Phys. Lett. **B 284**, 431 (1992).

[99] LEP Energy Working Group, R. Assmann *et al.*, Eur. Phys. J. **C 6**, 187 (1999).

[100] A.A. Sokolov and I.M. Ternov, Dokl. Akad. Nauk. SSSR **153**, 1052 (1963).

[101] J. Prochnow, *The LEP Energy Spectrometer*, Diploma thesis, RWTH Aachen, 2000, PITHA 00/10.

[102] P. B. Renton, *Measurement of the Beam Energy at LEP 2*, in Proceedings of ICHEP 2000, Osaka, Japan, **Vol. 1** 687.

[103] LEP Energy Working Group, R. Assmann *et al.*, Eur. Phys. J. **C 39**, 253 (2005).

[104] ALICE Experiment, CERN/LHCC/96-71 (1996), *http://alice.web.cern.ch/Alice*

[105] A. P. Colijn, *Measurement of the Tau Lepton Lifetime*, Ph.D. thesis, NIKHEF, 1999.

[106] H. Anderhub *et al.*, Nucl. Instrum. Meth. **A 515**, 31 (2003).

[107] M. Acciari *et al.*, Nucl. Instrum. Meth. **A 351**, 300 (1994).

[108] R. Wigmans, *Calorimetry Energy Measurement in Particle Physics*, Clarendon Press, Oxford, 2000, pp. 26-109.

[109] J.A. Bakken *et al.*, Nucl. Instrum. Meth. **A 275**, 81 (1989).

[110] C. Tully, *Baryon Production in Z decay*, Ph.D. thesis, Princeton University, 1997.

[111] ALEPH Collab., A. Heister *et al.*, Eur. Phys. J. **C 28**, 1 (2003).

[112] P. Huntemeyer, *A Determination of the Electroweak Quark Couplings using Final State Photon Emission in Z Decays*, Ph. D. thesis, University of Hamburg, 2001.

[113] DELPHI Collab., P. Abreu *et al.*, Eur. Phys. J. **C 17**, 53 (2000).

[114] G. Bastl *et al.*, Nucl. Instrum. Meth. **A 374**, 293 (1996).

[115] S. Laplace, *Bhabha Event Selection in the EGAP Detector*, L3 Note 2813, September 1998.

[116] U. Uwer, *The L3 Scintillation Counter System: Description and Status*, L3 Note 2003, November 1997.

[117] O. Adriani *et al.*, Nucl. Instrum. Meth. **A 300**, 493 (1991).

[118] A. Robohm, *Measurement of the Muon Pair Production with the L3 Experiment*, Ph.D. thesis, ETH Zurich, 1998.

[119] M. Chemarin *et al.*, Nucl. Instrum. Meth. **A 349**, 345 (1994).

[120] G. Grenier, *Recherche de Particules Supersymétriques à l'aide de Photons avec le Détecteur L3 à LEP200*, Ph.D. thesis, University of Lyon, 2000.

[121] B.F.L. Ward *et al.*, Phys. Lett. **B 450**, 262 (1999).

[122] I.C. Brock *et al.*, Nucl. Instrum. Meth. **A 381**, 236 (1996).

[123] R. Bagnaia *et al.*, Nucl. Instrum. Meth. **A 324**, 101 (1993);
Y. Bertsch *et al.*, Nucl. Instrum. Meth. **A 340**, 309 (1994);
S.P. Beingessner *et al.*, Nucl. Instrum. Meth. **A 340**, 322 (1994).

[124] C. Luci, *DAQ and Trigger Status Report*, L3 Note 2616a, September 2000.

[125] R. Bizzarri *et al.*, Nucl. Instrum. Meth. **A 317**, 463 (1992).

[126] F. James, *Monte Carlo Theory and Practice*, in *Experimental Techniques in High Energy Physics*, ed. T. Ferbel, Addison-Wesley Publishing Company Inc., 1987, pp. 627-677.

[127] R. Brun *et al.*, GEANT3, CERN-DD/EE/84-1 (Revised), 1987.

[128] L3 Collab., *The Construction of L3*, April 1985.

[129] L3 Collab., M. Acciarri *et al.*, Phys. Lett. **B 407**, 351 (1997).

[130] J.A. Bakken *et al.*, Nucl. Instrum. Meth. **A 254**, 535 (1987);
J.A. Bakken *et al.*, Nucl. Instrum. Meth. **A 280**, 25 (1989).

[131] J.A. Bakken *et al.*, *Calibration of the L3 Electromagnetic Calorimeter in Electron Beam*, L3 Note 1712, March 1995.

[132] M. Merk, *Study of Bhabha Scattering at the Z^0-Resonance using the L3 Detector*, Ph.D. thesis, University of Nijmegen, 1992.

[133] C.W. Fabjan and F. Gianotti, Rev. Mod. Phys. **75**, 1243 (2003).

[134] Y. Karyotakis, *The L3 Electromagnetic Calorimeter*, LAPP-EXP-95.02, Contributed to 1994 Beijing Calorimetry Symposium.

[135] P. Deglon, *Etude de la diffusion Bhabha avec le Détecteur L3 au LEP*, Ph.D. thesis, University of Geneva, 2002.

[136] C. Green, *An Investigation into the Temperature Fitting and Correction System for the BGO Calorimeter*, L3 note 1677, November 1994.

[137] J. Fay, *The L3 Electromagnetic Calorimeter*, in Proceedings of CALOR 1999, Lisbon, Portugal, 212.

[138] A. Bay *et al.*, Nucl. Instrum. Meth. **A 321**, 119 (1992).

[139] J. Wenninger, *Mesure de Paramètres Électro-faibles du Z^0 avec la Réaction* $e^+e^- \to e^+e^-(\gamma)$, Ph.D. thesis, University of Geneva, 1992.

[140] A. Balandras, *Recherche de Supersymétrie dans les Canaux avec Un ou Deux Leptons avec le Détecteur L3 à LEP*, Ph.D. thesis, LAPP, 2000.

[141] Y. Kubota *et al.*, Nucl. Instrum. Meth. **A 320**, 66 (1992).

[142] T. Bohringer *et al.*, Phys. Rev. Lett. **44**, 1111 (1980);
G. Mageras *et al.*, Phys. Rev. Lett. **46**, 1115 (1981).

[143] Y. Chan *et al.*, IEEE Trans. Nucl. Sci. **25**, 333 (1978);
M. Oreglia *et al.*, Phys. Rev. **D 25**, 2295 (1982);
R. Partridge, *A Study of the* $\Psi''(3370)$ *using the Crystal Ball Detector*, Ph.D. thesis, Caltech, 1984.

[144] J. M. Bauer [BABAR Collab.], *Absolute Energy calibration with the Neutron-activated Liquid-source System at BaBar's CsI(Tl) Calorimeter*, arXiv:physics/0312128 (2003); M. Kocian [BABAR Collab.], *Performance and Calibration of the Crystal Calorimeter of the BABAR Detector*, SLAC-PUB-10170, in Proceedings of CALOR 2002, Pasadena, California, 167.

[145] G. Gratta, H. Newman, and R.Y. Zhu, Ann. Rev. Nucl. Part. Sci. **44**, 453 (1994).

[146] A. Aloisio *et al.*, *Calibration of the KLOE Electromagnetic Calorimeter*, in Proceedings of CALOR 2002, Pasadena, California, 388.

[147] K. Miyabayashi, *Monitoring and Calibration of the BELLE Electromagnetic Calorimeter*, in Proceedings of CALOR 2002, Pasadena, California, 394.

[148] J. A. Bakken *et al.*, Nucl. Instrum. Meth. **A 343**, 456 (1994).

[149] R.Y. Zhu *et al.*, Nuclear Physics **B** (Proc. Suppl.) **44**, 109 (1995);
U. Chaturvedi *et al.*, IEEE Trans. Nucl. Sci. **47**, 2101 (2000);
A. Favara *et al.*, Nucl. Instrum. Meth. **A 461**, 376 (2001).

[150] H. Ma *et al.*, Nucl. Instrum. Meth. **A 274**, 113 (1989).

[151] W. Lu, *A Study of Bhabha Scattering at the Z Resonance*, Ph.D. thesis, Caltech, 1997.

[152] R.A. Lee, *Radiative Decays of the A Study of the Ψ' to All-photon Final States*, Ph.D. thesis, Stanford University, 1985.

[153] T.W. Bonner and J.E. Evans, Phys. Rev. **73/7**, 666 (1948).

[154] R.Y. Zhu, *EGS Study on the BGO Calibration by Using Low Energy Photons*, L3 Internal Report, December 1985.

[155] R.Y. Zhu, Nucl. Instrum. Meth. **A 306**, 145 (1991).

[156] `BHWIDE` version 1.03 is used:
S. Jadach, W. Placzek, and B.F.L. Ward, Phys. Lett. **B 390**, 298 (1997).

[157] `GGG` Monte Carlo Program:
F.A. Berends and R. Kleiss, Nuclear Physics **B 186**, 22 (1981).

[158] L3 Collab., M. Acciarri *et al.*, Phys. Lett. **B 475**, 198 (2000);
L3 Collab., P. Achard *et al.*, Phys. Lett. **B 531**, 28 (2002).

[159] M. Gataullin *et al.*, *L3 BGO Calorimeter Calibration using an RFQ Accelerator*, in Proceedings of CALOR 1999, Lisbon, Portugal, 417.

[160] D. Duchesneau, private communication (2003).

[161] P. Achard, *Production inclusive de hadrons dans les collision de deux photons au sein de l'expérience L3*, Ph.D. thesis, University of Geneva, 2003.

[162] L3 Collab., O. Adriani *et al.*, Phys. Lett. **B 286**, 403 (1992).

[163] M. Sanders, *Pion (Non-) Correlations in Hadronic Events at the Z Resonance*, Ph.D. thesis, University of Nijmegen, 2002.

[164] D. Barney, *A Pedagogical Introduction to the CMS Electromagnetic Calorimeter*, CMS Conference Report 1998/004.

[165] D. Bailleux *et al.*, *ECAL Monitoring Light Source at H4*, CMS Internal Note 2003/045.

[166] R. Paramatti, *Calibration of the CMS Electromagnetic Calorimeter*, CMS Conference Report 2003/002; D. Futyan, *In-Situ Calibration of the CMS Electromagnetic Calorimeter*, CMS Conference Report 2003/005.

[167] Annual Report to the DOE, Caltech HEP Division, 2004.

[168] `TEEGG` version 7.1 is used:
D. Karlen, Nucl. Phys. **B 289**, 23 (1987).

[169] `EXCALIBUR` version 1.11 is used:
F.A. Berends, R. Pittau, and R. Kleiss, Comput. Phys. Comm. **85**, 437 (1995).

[170] `DIAG36` Monte Carlo:
F.A. Berends, P.H. Daverfeldt, and R. Kleiss, Nucl. Phys. **B 253**, 441 (1985).

[171] L3 Collab., P. Achard *et al.*, CERN-PH-EP/2005-01, (2005).

[172] D. Kirkby, *A Study of Final-State Radiation in Hadronic Z Decays*, Ph.D. thesis, Caltech, 1996.

[173] G. Raven, *Measurement of Invisible Z Decays*, Ph.D. thesis, University of Utrecht, 1995.

[174] National Institute of Standards and Technology, Physical Reference Data, *http://physics.nist.gov/PhysRefData/*.

[175] J. Alcaraz, J. Casaus, and C. Palomares, *Measurement of the Photon Conversion Probability at Low Polar Angles at LEP2* , L3 Note 2106, March 1997.

[176] L3+C Collab., P. Achard *et al.*, Phys. Lett. **B 598**, 15 (2004).

[177] L3+C Collab., O. Adriani *et al.*, Nucl. Instrum. Meth. **A 488**, 209 (2002).

[178] L3 Collab., M. Acciarri *et al.*, Phys. Lett. **B 470**, 268 (1999).

[179] L3 Collab., M. Acciarri *et al.*, Phys. Lett. **B 431**, 199 (1998).

[180] R. Barlow, *Systematic Errors: Facts and Fictions,* arXiv:hep-ex/0207026 (2002); The BaBar Statistics Working Group, *Recommended Statistical Procedures for BaBar,* BaBar Analysis Document 318 (2001).

[181] OPAL Collab., K. Ackerstaff *et al.*, Eur. Phys. J. **C 8**, 23 (1999).

[182] S. Blyth, private communication (2003).

[183] L3 Collab., M. Acciarri *et al.*, Eur. Phys. J. **C 16**, 1 (2000).

[184] See for example: G. Cowan, *Statistical data analysis*, Clarendon Press, 1998.

[185] A. Shvorob, *A Study of W Boson Properties with Four-Jet W^+W^- events at LEP*, Ph.D. thesis, Caltech, 2000; S. Villa, *Measurement of the Triple Gauge Couplings of the W Boson at LEP2*, Ph.D. thesis, Northeastern Univ., 2000.

[186] C. Parkes, *Practicalities of combining analyses: W physics results at LEP*, in Advanced statistical techniques in particle physics, Durham, pp. 211-214, 2002; L. Lyons, D. Gibaut, and P. Clifford, Nucl. Instrum. Meth. **A 270**, 110 (1988).

[187] CDF and D$\emptyset$ Collaborations, Phys. Rev. **D 70**, 092008 (2004).

[188] A. Favara and M. Pieri, *Confidence level estimation and analysis optimisation*, Preprint DFF-278/4/1997, arXiv:hep-ex/9706016 (1997).

[189] L3 Collab., M. Acciarri *et al.*, Phys. Lett. **B 411**, 373 (1997);
L3 Collab., M. Acciarri *et al.*, Phys. Lett. **B 495**, 18 (2000).

[190] LEP Collaborations, *Lower bound for the Standard Model Higgs boson mass from combining the results of the LEP experiments*, CERN-EP/98-046, (1998).

[191] A. Read, *Modified Frequentist Analysis of Search Results (The CLs Method)* in "Workshop on Confidence Limits", eds. F. James, L. Lyons and Y. Perrin, CERN 2000-05, p. 81.; T. Junk, Nucl. Instrum. Meth. **A 434**, 435 (1999).

[192] R.D. Cousins and V.L. Highland, Nucl. Instrum. Meth. **A 320**, 331 (1992).

[193] J.L. Lopez, D.V. Nanopoulos, and A. Zichichi, Phys. Rev. **D 55**, 5813 (1997).

[194] S. Dimopoulos, S. Thomas, and J.D. Wells, Phys. Rev. **D 54**, 3283 (1996).

[195] L3 Collab., A. Arefiev *et al.*, Nucl. Instrum. Meth. **A 285**, 403 (1989);
L3 Collab., O. Adriani *et al.*, Nucl. Instrum. Meth. **A 302**, 53 (1991).

[196] A. Boucham, *Recherche de Neutralinos avec le Détecteur L3 au LEP*, Ph.D. thesis, LAPP, 1996.

[197] "Interpretation of Neutralino and Scalar Lepton Searches in the Minimal GMSB Model", M. Gataullin *et al.*, L3 Note 2777, October (2003).

[198] `ISAJET` version 7.51 is used:
F.E. Paige *et al.*, arXiv:hep-ph/0312045 (2003).

[199] L3 Collab., P. Achard *et al.*, Phys. Lett. **B 545**, 30 (2002).

[200] L3 Collab., P. Achard *et al.*, Phys. Lett. **B 597**, 145 (2004).

[201] W.J. Stirling and A. Werthenbach, Phys. Lett. **B 466**, 369 (1999).

[202] L3 Collab., M. Acciarri *et al.*, Phys. Lett. **B 467**, 171 (1999);
L3 Collab., P. Achard *et al.*, Phys. Lett. **B 586**, 151 (2004).

[203] A. Hill and J.J. van der Bij, Phys. Rev. **D 36**, 3463 (1987);
R. Casalbuoni *et al.*, Nucl. Phys. **B 282**, 235 (1987).

[204] S. Godfrey, *Quartic Gauge Boson Couplings*, Proc. International Symposium on Vector Boson Self-Interactions, UCLA, February 1995.

[205] G. Belanger and F. Boudjema, Phys. Lett. **B 288**, 201 (1992).

[206] G. Bélanger *et al.*, Eur. Phys. J. **C 13**, 283 (2000).

[207] G. Montagna *et al.*, Phys. Lett. **B 515**, 197 (2001).

[208] L3 Collab., P. Achard *et al.*, Phys. Lett. **B 527**, 29 (2002).

[209] L3 Collab., P. Achard *et al.*, Phys. Lett. **B 540**, 43 (2002).

[210] W.J. Stirling and A. Werthenbach, Eur. Phys. J. **C 14**, 103 (2000).

[211] *Triple Gauge Couplings*, G. Gounaris *et al.*, in *Physics at LEP 2*, Report CERN 96-01 (1996), eds. G. Altarelli, T. Sjöstrand, F. Zwirner, Vol. 1, p. 525.

[212] A. Jacholkowska, J. Kalinowski, and Z. Wąs, Comp. Phys. Comm. **124**, 238 (2000).

[213] A. Jacholkowska, J. Kalinowski, and Z. Wąs, Eur. Phys. J. **C 6**, 485 (1999).

[214] L3 Collab., M. Acciarri *et al.*, Phys. Lett. **B 461**, 397 (1999);
L3 Collab., P. Achard *et al.*, Phys. Lett. **B 517**, 67 (2001).

[215] OPAL Collab., G. Abbiendi *et al.*, Phys. Lett. **B 602**, 167 (2004);
OPAL Collab., G. Abbiendi *et al.*, Eur. Phys. J. **C 18**, 253 (2000).

[216] DELPHI Collab., J. Abdallah *et al.*, Eur. Phys. J. **C 38**, 395 (2005).

[217] OPAL Collab., R. Akers *et al.*, Z. Phys. **C 65**, 47 (1995).

[218] CDF Collab., D. Acosta *et al.*, Phys. Rev. Lett. **89**, 281801 (2002).

[219] CDF Collab., D. Acosta *et al.*, Phys. Rev. **D 71**, 031104 (2005).

[220] DØ Collab., V.M. Abazov *et al.*, Phys. Rev. Lett. **94**, 041801 (2005).

[221] OPAL Collab., G. Abbiendi *et al.*, Phys. Rev. **D 70**, 032005 (2004).

[222] DØ Collab., V.M. Abazov *et al.*, Phys. Rev. Lett. **90**, 251802 (2003).

[223] CDF Collab., D. Acosta *et al.*, Phys. Rev. Lett. **92**, 121802 (2004).

[224] CMS Experiment, CERN/LHCC/94-38, *http://cmsdoc.cern.ch/cms.html*

[225] ATLAS Experiment, CERN/LHCC/94-43, *http://atlas.web.cern.ch/Atlas/*

[226] I. Fleck, Eur. Phys. J. **C 34**, S185 (2004);
K. Hoepfner, Eur. Phys. J. **C 34**, S161 (2004).

[227] F.E. Paige, *SUSY signatures in ATLAS at LHC*, arXiv:hep-ph/0307342 (2003).

[228] B. Zhou, Eur. Phys. J. **C 34**, S241 (2004);
L. Vacavant, Eur. Phys. J. **C 33**, S924 (2004).

[229] O.J.P. Eboli *et al.*, Phys. Rev. **D 69**, 095005 (2004).

[230] L3 Collab., P. Achard *et al.*, Phys. Lett. **B 587**, 16 (2004).

[231] LEP SUSY Working Group: *http://lepsusy.web.cern.ch/lepsusy/*
Single Photons 130-208 GeV, Note LEPSUSYWG/04-10.1 (2004);
Acoplanar Photon Pairs 130-208 GeV, Note LEPSUSYWG/04-09.1 (2004).

[232] LEP Exotica Working Group: *http://lepexotica.web.cern.ch/LEPEXOTICA/*
Combination of LEP Results on Direct Searches for Large Extra Dimensions, Note LEPExWG/2004-03 (2004).

[233] F.A. Berends *et al.*, Nucl. Phys. **B 301**, 583 (1988).

[234] M.E. Peskin, D.V. Schroeder, *An Introduction to Quantum Field Theory*, Addison-Wesley, 1995, pp. 202-208.

[235] O. Nicrosini and L. Trentadue, *Structure Function Techniques In* e^+e^- *Collisions*, CERN-TH-5437/89, in Proceedings of the Workshop on Electroweak Radiative Corrections for e^+e^- Collisions, Ringsberg, Germany, 1989.

[236] E.A. Kuraev and V.S. Fadin, Sov. J. Nucl. Phys. **41**, 466 (1985);
G. Altarelli and G. Martinelli, *Physics at LEP*, CERN Report 86–02, J. Ellis and R. Peccei, eds. (Geneva, 1986); O. Nicrosini and L. Trentadue, Phys. Lett. **B 196**, 551 (1987) and Z. Phys. **C 39**, 479 (1988).

[237] S. Ambrosanio *et al.*, Nucl. Phys. **B 478**, 46 (1996).

[238] K.M. Hamilton, *Radiative Corrections, New Physics Fits and* $e^+e^- \to ? \to f\bar{f}$, hep-ph/0311322 (2003).

[239] D.R. Yennie, S.C. Frautschi, and H. Suura, Annals Phys. **13**, 379 (1961).

[240] S. Jadach and B.F.L. Ward, Phys. Rev. **D 38**, 2897 (1988);
A. Schalicke, F. Krauss, R. Kuhn, and G. Soff, JHEP **0212**, 013 (2002).

[241] Bear Project, *http://nis-www.lanl.gov/groups/nis-4/proj/bear.shtml*

[242] Air Force 2025, Chapter 3b, *http://www.au.af.mil/au/2025/*

[243] E. Speth, Rep. Prog. Phys. **52**, 57 (1989).

[244] *http://www.accsys.com/*

[245] K.N. Leung, Rev. Sci. Instrum. **59/3**, 453 (1988);
K.N. Leung, Rev. Sci. Instrum. **62/1**, 100 (1991).

[246] K. Saadatmand, Rev. Sci. Instrum. **66/6**, 3438 (1995);
K. Saadatmand, Rev. Sci. Instrum. **67/3**, 1318 (1996).

[247] M. Weiss, *Radio-Frequency Quadrupole*, in Advanced Accelerator Physics Course, Rhodes, Greece, 1993, **Vol. 2** 959.

[248] J.M. Potter, *A Parallel Planar Triode Array High Power Rf System For Accelerator Applications*, in Proceedings of EPAC 1990, Nice, France, **Vol. 1** 991.

[249] M. Hanada, Rev. Sci. Instrum. **75/5**, 1813 (2004).

[250] H. Tawara and A. Russek, Rev. Mod. Phys. **45/2** 178 (1973).

[251] D. Zahnow *et al.*, Z. Phys. **A 351**, 229 (1995); K.N. Mukhin, *Experimental Nuclear Physics*, Mir Publishers, Moscow, 1987, **Vol. 1** pp. 559-562.

[252] E.I. Sirotinin *et al.*, Nucl. Instrum. Meth. **B 4**, 337 (1984).

[253] I. Kominis and I. Nemenman, *BGO Dead Crystal Correction and Shower Fitting*, L3 note 2157, November 1997; F. Filthaut, *Shower Fitting in the L3 BGO Calorimeter*, L3 note 2240, March 1998.

[254] L. Xia, *Search for Scalar Leptons at LEP with the L3 Detector*, Ph.D. thesis, Caltech, 2002.

[255] P. A. Movilla Fernandez, Nucl. Phys. Proc. Suppl. **74**, 384 (1999).

[256] S. Rosier, private communication (2004).

[257] H. Hu and J. Nielsen, *Analytic Confidence Level Calculations Using the Likelihood Ratio and Fourier Transform*, in "Workshop on Confidence Limits", eds. F. James, L. Lyons, and Y. Perrin, CERN 2000-05, p. 190.

[258] D$\emptyset$ Collab., *Search for large extra spatial dimensions in Jets + Missing E_T topologies*, D0−CONF 4400 (2004).